Development of a Fabry-Pérot Etalon Spectrometer for High-resolution Aerosol Observations in the Oxygen A-Band

Alexander Gordon Geddes

Supervisors: Hartmut Bösch, Steve Ball

Earth Observation Science Group
Department of Physics and Astronomy
The University of Leicester

February 2, 2015

Declaration

I hearby declare that no part of this thesis has been previously submitted to this or any other University as part of the requirement for a higher degree. The work described herein was conducted by the undersigned except for contributions from colleagues as acknowledged in the text.

Alexander G. Geddes
February 2, 2015

Contents

List of Figures

List of Tables

List of Abbreviations

AA	Apparent Absorption
ABC	Atmospheric (or Asian) Brown Cloud
ACE	Aerosol Characterisation Experiment
ACOS	Atmospheric CO_2 Observations from Space
ADC	Analogue/Digital Converter
AERONET	Aerosol Robotic Network
AOD	Aerosol Optical Depth
Ar	Argon
ARM	Atmospheric Radiation Measurement
ASTER	Advanced Spacebourne Thermal Emission and Reflection Radiometer
ATOMFS	Aerosol Time-Of-Flight Mass Spectrometry
A-Train	Afternoon Constellation
AVIRIS	Airborne Visible / Infrared Imaging Spectrometer
BE	Best Estimate
CALIPSO	Cloud-Aerosol LIDAR and Infra-red Pathfinder Satellite
CCD	Charge-Coupled Device
CCN	Cloud Condensation Nuclei
CH_4	Methane
CNES	Centre National dEtudes Spatiales
CNRS	Centre National de la Recherche Scientifique
CO_2	Carbon Dioxide
COD	Cloud Optical Depth
CSIRO	Commonwealth Scientific and Industrial Research Organisation
DAQ	Data Acquisition Device

DMA/DPMA	Differential (Particle) Mobility Analyser
DoF	Degrees of Freedom
ECMWF	European Centre for Medium-Range Weather Forecasts
EPS	EUMETSAT Polar Sustem
ERF	Effective Radiative Forcing
ESA	European Space Agency
EUMETSAT	European Organisation for the Exploitation of Meteorological Satellites
FoV	Field of View
FPE	Fabry-Pérot Etalon
FPE-G	FPE - Groundbased
FSR	Free Spectral Range
FTS	Fourier Transform Spectrometer
FWHM	Full Width at Half Maximum
GOME	Global Ozone Monitoring Experiment
GOSAT	Greenhouse Gas Observing Satellite
GOSAT-G	GOSAT - Groundbased
H_2O	Water
HALOE	Halogen Occultation Experiment
ILS	Instrument Line Shape
InGaAs	Indium Gallium and Arsenide Detector
IR	Infra-Red
JAXA	Japan Aerospace Exploration Agency
LAOD	Layer Aerosol Optical Depth
LIDAR	Light Detection and Ranging
LIDORT	Linear Discrete Ordinate Radiative Transfer Model
MAAP	Multi-Angle Aerosol Photometer
MIPAS	Michelson Interferometer for Passive Atmospheric Sounding
MISR	Multiangle Imaging SpectroRadiometer
MODIS	Moderate-resolution Imaging Spectrometer
N_2	Molecular Nitrogen
NASA	National Aeronautics and Space Administration
NIR	Near Infra-Red

NO_2	Nitrogen Dioxide
O_2	Molecular Oxygen
O_3	Ozone
OCO	Orbiting Carbon Observatory
OMI	Ozone Monitoring Instrument
OSIRIS	Optical Spectrograph and Infrared Imager System
PALMS	Particulate Analysis by Laser Mass Spectrometry
PC	Personal Computer
PCC	Pearsons Correlation Coefficient
PEA	Piezo Electric Actuator
PHOTONS	PHOtomtrie pour le Traitement Oprationnel de Normalisation Satellitaire
POLDER	POLarization and Directionality of the Earth's Reflectances
PSAP	Particulate Soot Absorption Photometer
RADAR	Radio Detection and Ranging
RF	Radiative Forcing
RIMA	Red Ibrica de Medida fotomtrica de Aerosoles
RT	Radiative Transfer
S-5 P	Sentinel-5 Precursor
SA	Solar Azimuth
SAGE	Stratospheric Aerosol and Gas Experiment
SCIAMACHY	SCanning Imaging Absorption spectroMeter for Atmospheric CHartographY
SMPS	Scanning Mobility Particle Sizer
SNR	Signal-to-Noise Ratio
SO_2	Sulphur Dioxide
SSA	Single Scattering Albedo
SWIR	Shortwave Infra-Red
SZA	Solar Zenith Angle
TCCON	Total Carbon Column Observing Network
TIR	Thermal Infra-Red
TOA	Top of Atmosphere
UoL-FP	University of Leicester - Full Physics Retrieval Algorithm

USA	United States of America
UV	Ultraviolet
VA	Viewing Azimuth
VIS	Visible
VOC	Volatile Organic Compound
VZA	Viewing Zenith Angle
WHO	World Health Organisation

Publications

Geddes, A., & Bösch, H. (2014). Tropospheric Aerosol Profile Information from High Resolution Oxygen A-Band Measurements from Space. *Atmospheric Measurement Techniques Discussions*, 7, 6021-6063.

Geddes, A., & Bösch, H. (2013). CarbonSat Earth Explorer 8 Candidate Mission - Potential Aerosol and Surface Pressure Secondary Products. *Proceedings of the ESA Living Planet Symposium*

Acknowledgements

This work was funded by the UK Centre of Earth Observation Instrumentation (CEOI). Special thanks to J.Landgraf (SRON) and C. ODell (CSU) for help regarding Sentinel-5 P and OCO-2, respectively as well as the ESA CarbonSat Earth Explorer 8 Candidate Mission Level-2 and Level-1B Requirements Consolidation Study. In addition I would like to thank colleagues at the Univ. of Leicester, Earth Observation Science group, particularly my supervisor Hartmut Böesch for his support and guidance and all the PDRAs in the GHG group for their help with this project and in the production of this thesis. A big shout out to the library crew, Lara and Sian ,my fellow postgrads and all my other friends for their encouragement and for keeping me entertained. I'd also like to thank my family for putting up with me, particularly over the last few months whilst I have been living at home. Lastly and most importantly I want to thank A.G.Barr plc. for producing Irn Bru, which I estimate I have drunk over 300 litres of during the course of this PhD.

Abstract

Aerosols are an important factor of the Earth climatic system and they play a key role for air quality and public health. Observations of the Oxygen A-Band at 760 nm can provide information on the vertical distribution of aerosols from passive sensors, that can be of great interest for operational monitoring applications with high spatial coverage if the aerosol information is obtained with sufficient precision, accuracy and vertical resolution. To address this issue, retrieval simulations of the aerosol vertical profile retrieval from Oxygen A-Band observations by GOSAT, the upcoming OCO-2 and Sentinel 5-P mission and the proposed CarbonSat mission have been carried out. These simulations suggest that such observations will be useful in the measurement of uplifted aerosols such as volcanic plumes and forest fires. Retrievals from GOSAT were also undertaken that showed promising results in challenging conditions, warranting further study. The Fabry-Pérot Etalon spectrometer provides a compact, robust and affordable alternative to grating or Fourier transform spectrometers. Such an instrument was designed and optimised for the measurement of aerosol in the Oxygen A-Band and its performance simulated in comparison to GOSAT, where it competed well despite its low cost. Initial calibrations of the instrument were undertaken and showed promising results in the instrument operation concept. Following on from this simulations were used to study the performance of groundbased observations showing that using and combining a range of viewing angles would contribute significantly to the vertical information content whereas polarisation proved not to be useful except possibly in extreme circumstances.

Chapter 1

Introduction

1.1 The Earth's Atmosphere and Climate Change

The Earth's atmosphere contains a number of constituents, ranging from the populous molecular nitrogen (N_2, 78%), oxygen (O_2, 21%) and argon (Ar, 0.6%) to the trace gases such as carbon dioxide (CO_2), methane (CH_4), ozone (O_3) and nitrogen dioxide (NO_2) as well as the ever variable water vapour (H_2O), which can in cases make up 4% of the air mass. In addition to these molecular species, particles are suspended in the atmosphere that are known as clouds and aerosols. Taken together, the changes in each quantity drive the processes of climate change, air quality and the ozone hole depletion (Seinfeld and Pandis, 2012). Recently, the issue of man made climate change through the emission of 'greenhouse gases' such as CO_2 and CH_4 has become increasingly important, and a big source of uncertainty in this is the role of aerosols (Stocker et al., 2013).

The fundamental idea used to describe climate change is that of radiative balance. Radiative balance is in essence the theory of conservation of energy. In radiative balance the energy entering the Earth's atmosphere from the Sun must be balanced by the amount radiated back into space. This radiated energy can either

be sunlight that is scattered back into space by interaction with particles within the atmosphere and the Earths surface, or it can be absorbed and then re-emitted in the thermal infra-red (TIR) by the surface. Certain gases within the atmosphere also absorb in the infra-red (IR) and then re-emit in all directions, thereby effectively trapping energy within the lower region of the atmosphere, therefore increasing the temperature, this is known as the greenhouse effect. Gases that contribute to this, are most importantly CO_2, CH_4 and water vapour amongst others.

Aerosols on the other hand are predominantly scattering bodies, they reduce the amount of radiation reaching the lower atmosphere and surface, thus cooling the Earth and mitigating the effects of the greenhouse gases; this effect is known as the direct effect and is discussed in Section 1.2.1. However aerosols are not perfect scattering bodies, they also absorb radiation, most notably by high carbon species such as black carbon, the impact of these absorbing aerosols is similar then to the greenhouse gases, they act to warm the air around them through re-emission of radiation. Aerosols also play a key role in the cloud inhibition known as the semi-direct effect, highlighted in Section 1.2.4, as well as cloud formation and lifetime in the in-direct effect (Section 1.2.3). Lastly they can impact the radiative balance by acting as a heterogeneous catalyst for chemical reactions in the atmosphere. Thereby playing a significant role in the depletion and formation rates of key radiative balance molecules such as ozone, as well as in air quality and composition, briefly discussed in Section 1.2.5. To illustrate these processes the radiative transfer (RT) budget is shown in Figure 1.1. The RT budget shows the input and output radiation fluxes and the various associated sources and sinks and is a useful guide to the radiative balance of the atmosphere.

We can from this figure see that the reflection of radiation by clouds and aerosols accounts for 76 Wm^{-2}, or approximately 22% of the incoming radiation. Coupled

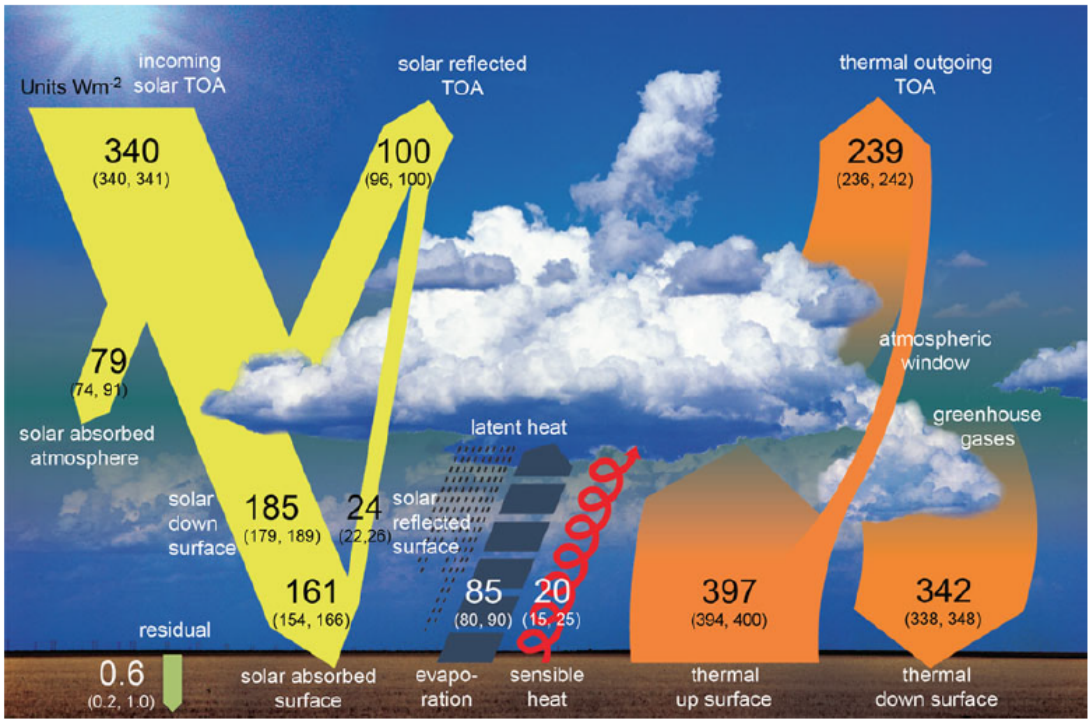

Figure 1.1: Global mean radiative transfer budget under present day conditions, numbers stated are energy fluxes in Wm^{-2}. Numbers in parentheses represent the uncertainty range for each process. (Wild et al., 2013)

with this the absorption by aerosols and gases accounts for a further 79 Wm^{-2} reduction. Therefore any changes to either the cloud or aerosol distribution will have a significant impact upon the radiative balance of the atmosphere. To quantify the effects of these warming and cooling processes we often use the term radiative forcing.

Radiative forcing represents the change in radiative flux relative to a reference point, typically taken to be 1750, i.e. the pre-industrial era, where anthropogenic emissions of greenhouses gases were minimal, or at least stable. A negative value of the radiative forcing indicates a cooling process, such as the direct effect of aerosols, while positive forcing is indicative of a warming process, like the greenhouse effect of CO_2. The latest estimates of the various radiative forcings (RF) are shown in Figure 1.2, where the effective radiative forcing (ERF) is also included. This adjustment

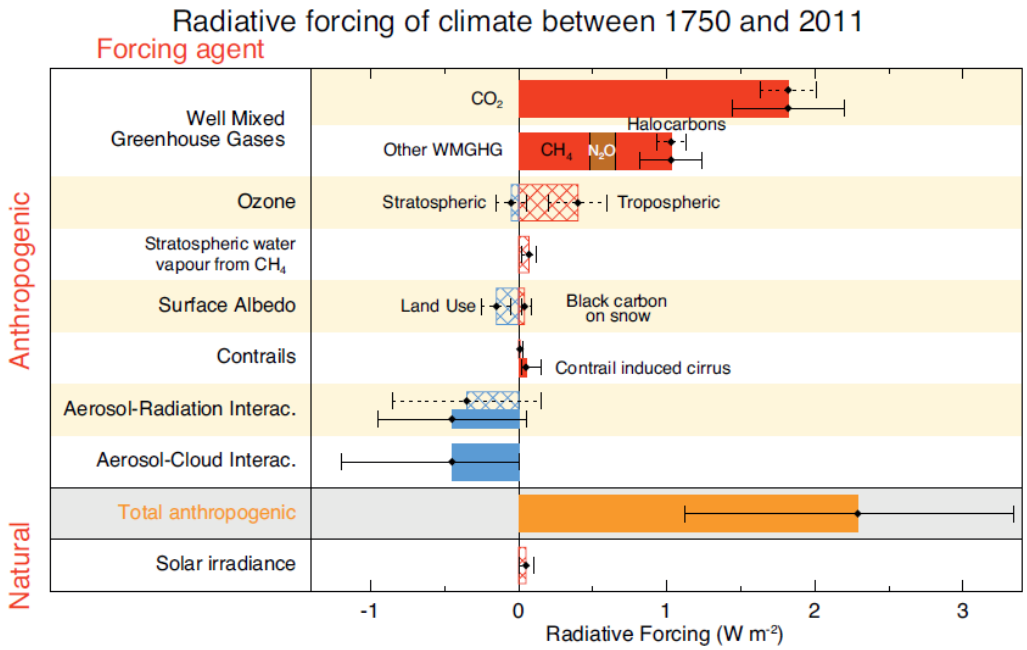

Figure 1.2: Bar chart for RF (hatched) and ERF (solid) for the period 1750-2011. Uncertainties (5 to 95% confidence range) are given for RF (dotted lines) and ERF (solid lines). (Stocker et al., 2013)

allows for additional adjustment of atmospheric parameters compared to RF, this requires more complex calculations but the additional rapid adjustments provide a better indicator of the impact on global temperature, particularly for aerosols.

As can be seen the biggest contribution to positive forcing, i.e. heating, comes from greenhouse gases such as CO_2 and CH_4. However the cooling effect of aerosols largely compensates for their effects. Unfortunately, as can be seen, there are large uncertainties on the effect of aerosols. Therefore it is vital to constrain this through increased observation of the the global aerosol distribution and the microphysical properties of aerosols to further quantify their effect through scattering, absorption, cloud processes and chemistry.

1.2 The Importance of Aerosols

Aerosols are important for a number of reasons, playing a large role in the radiative balance of the atmosphere. They do this through four processes; the direct, semi-direct and indirect effects as well as aerosol chemistry. The tendency of aerosols to cool the atmosphere can be seen as a beneficial effect for tackling climate change but aerosols also have a significant negative impact upon air quality and therefore health (WHO, 2009). In addition their scattering nature also causes uncertainties in the remote sensing of other atmospheric constituents.

1.2.1 Direct Effect

The direct effect of aerosol relates to any change of radiative forcing in the atmosphere by the scattering and absorption properties of aerosol due to anthropogenic emissions and changes in the optical properties (Abel et al., 2005; Bates et al., 2006; Bellouin et al., 2005). Increasing the amount of aerosol in the atmosphere leads to a negative forcing dependent upon the relative abundances of the different aerosol types and their absorbing and scattering properties, with the direct effect of aerosols amounting to a radiative forcing of between -0.9 and +0.1 Wm^{-2}. The large uncertainty here illustrates the challenge of aerosols, with differing aerosols producing vastly differing effects, making accurately quantifying their role as a whole, a challenge.

An example of a strongly contrasting effect is the atmospheric (or Asian) brown cloud (ABC). The ABC is a large layer of air pollution that often occurs in the early part of the year over South Asia and heavily obscures satellite imagery. The reflecting properties of the ABC mask up to 50% of the global greenhouse gas forcing (Ramanathan et al., 2005), however its high carbon content means that the air can be warmed around it and enhance lower atmospheric heating by around 50%

Ramanathan et al. (2007). This plays a significant role in temperature sensitive regions like Tibet and Himalayas, where the deposition of black carbon, from events such as the ABC, has significantly contributed to the retreat of glaciers Xu et al. (2009), which further exacerbates the heating effect by lowering the surface albedo. Both the heating and cooling effects are incorporated into the direct effect and as a result the wide ranging effects cause a high degree of uncertainty. For this reason it is important to quantify aerosols in order to improve our understanding of climate change. Key parameters in the impact of each aerosol type in the direct effect are the aerosol optical depth (AOD), single scattering albedo, asymmetry factor and Angström coefficient amongst others. These are discussed in detail in Section 2.1.1 as it is the direct effect that is studied in depth in this thesis.

1.2.2 Aerosol-Cloud Interactions

Aerosol-cloud interactions refer to processes by which aerosols alter the production and lifetimes of clouds (Hobbs, 1993). The amount and lifetime of clouds are important in climate from a radiative forcing point of view because they can act as a high albedo surface above the surface of the Earth, and therefore reflect large amounts of radiation back out of the atmosphere. This is predominantly true for low altitude clouds but high altitude thin clouds can act to trap some of the outgoing radiation and so warm the atmosphere, though taken together, the net effect is to cool the atmosphere. If low altitude clouds are formed more readily and have an extended lifetime, they will amplify their forcing. The processes by which the production and lifetime are moderated can be grouped into two effects, the indirect and semi-direct effects (Andreae and Rosenfeld, 2008), and their net effect is a forcing of -1.3 and 0 Wm^{-2}.

1.2.3 Indirect Effect

The indirect effect of aerosols relate to the formation and lifetime of clouds (Lohmann and Feichter, 2005). Aerosols aid the formation of clouds by acting as cloud condensation nuclei (CCN). Water typically needs to be cooled to below 14° with a supersaturation of less than 1%. In warmer conditions however the air would need to be supersaturated to over 400% for clouds to form, however in a non-gaseous surface can be used to make this transition from vapour to liquid. As such, aerosols can act as CCN, but their effectiveness is dependent on size (ideally greater than 0.1 μm) and composition. For instance sulphates and sea salt are good CCN as they readily absorb water. Black carbon and minerals do not absorb water and so are poor CCN, however they can act as CCN for ice clouds in higher, colder parts of the atmosphere. The lifetime of clouds is also dependent upon CCN. Higher numbers of CCN reduce droplet size by distributing the water mass over more CCN. The result of this is that precipitation is suppressed, thus extending the lifetime of clouds. This can be considered as a climate feedback as it has a strong impact upon the hydrological cycle but can be considered as a negative forcing (Ramanathan et al., 2001a).

1.2.4 Semi-Direct Effect

In the semi-direct effect tha absorption of radiation by aerosols such as soot, results in a reduction of cloud cover and can inhibit new cloud growth (Hansen et al., 1997; Ackerman et al., 2000). By reducing cloud cover the radiative balance is altered significantly, resulting in a positive forcing due to reduction of high albedo clouds. In addition there can be a second influence upon the hydrological cycle by altering the trade-wind cumulus layer (Ramanathan et al., 2001a,b).

1.2.5 Chemistry

Aerosols play a crucial role in atmospheric chemistry by acting as heterogeneous catalysts. This means that the catalyst is of a different phase to the reactants; in the case of aerosol, the reactants are gases and the aerosol is a solid or liquid particle. Gas particles are adsorbed to the surface of the aerosol via physisorption, a Van der Waals attraction, or by chemisorption which involves the sharing of electrons between the aerosol (adsorbent) and gas molecule (adsorbate). The reaction then proceeds when the two reactants interact as a result of proximity or collision, with often various intermediate steps, before desorbing. The aerosol is necessary here as it often ionises one or more of the reactants, promoting an otherwise unlikely reaction.

One of the most important such reactions is the hydrolysis of dinitrogen pentoxide, N_2O_5 (Dentener and Crutzen, 1993). In the absence of sunlight, this reaction is a major sink of NO_x, and proceeds far more rapidly with the addition of wet surface aerosols than it would otherwise. NO_x is important for a number of reasons, it reacts readily with ammonia, moisture, volatile organic compounds (VOCs) and other species to form variety of products which pose a significant health risk and in addition can deplete the ozone layer. As such it is of great importance to understand its behaviour and the role aerosols play within this. During the night, N_2O_5 and NO_3 are formed via the following mechanisms;

$$NO_2 + O_3 \rightarrow O_2 + NO_3 \tag{1.1}$$

$$NO_3 + NO_2 + M \leftrightarrow N_2O_5 + M \tag{1.2}$$

with M representing a catalyst, which in this case is the aerosol. During the day, the build up of these two species is largely reduced by the rapid photolysis of NO_3

and to a lesser extent N_2O_5, and would be reduced further by reactions with OH radicals formed again by photolysis. At night their formation can continue largely uninhibited, in addition a strong seasonality would be observed with the drop in the abundance of OH during winter. This is not observed due to the presence of an additional loss mechanism which is the adsorption of N_2O_5 and/or NO_3 species on to wet aerosol surfaces;

$$N_2O_5 + H_2O \xrightarrow{aerosol} 2\,HNO_3 \tag{1.3}$$

Other important heterogeneous reactions involving aerosols include SO_2 oxidation by cirrus clouds (Clegg and Abbatt, 2001), halogen oxidation in the marine boundary layer (Vogt et al., 1996) and HO_2 uptake in the troposphere (Martin et al., 2003).

1.2.6 Health and Air Quality

The impacts of aerosol are not limited to radiative and chemical effects, but they are also associated with a wide range of health issues. Studies have shown a clear link between cardiovascular morbidity, decreased lung function, hospital admissions and overall mortality to increases in chemical and particulate air pollution, with a range of effects associated with different particle types (Kelly, 2003). Indeed, the World Health Organisation estimates that 0.9 million people die per year as a direct result of air pollution, of which aerosols are a major factor (WHO, 2009). They do this directly through things like inhalation of carcinogenic smoke, but also indirectly through the transportation of more dangerous chemicals into the lungs which can lead to increased risk of lung diseases and cardiovascular / pulmonary complications (Seaton et al., 1995; Pope III and Dockery, 2006). The composition of the particles, as previously highlighted plays a substantial role in the impact upon

health, however though it is known to play a part, the exact mechanism by which it does is unclear with another key factor being the particle size (Harrison and Yin, 2000). Particle size is important because smaller particles are able to penetrate deeper into the respiratory system and reduce lung function further than larger particles perhaps would (Peters et al., 1997). Therefore accurate measurements of not only the amount of aerosol, but also the size distribution and composition are crucial in furthering our understanding of the role of aerosols within health. As the landscape has become increasingly urbanised, the need to accurately measure local aerosol has in turn become increasingly important to help shape emission policy, civil planning and healthcare.

1.2.7 Remote Sensing

Not only is it important to understand aerosols for their effects on climate and health, but also in remote sensing applications. As aerosols can have an impact across the visible (VIS) and near infra-red (NIR) and ultraviolet (UV) ranges of the electromagnetic spectrum, they are present in regions associated with absorption by gases. The impact of this is to introduce uncertainty in the measurement of the gas because of aerosol scattering changing the path length of the radiation. This aerosol effect needs to be corrected, and can be done through dedicated aerosol measurements, from for instance radiometers and lidars or through simultaneous measurements in the Oxygen A-Band.

Another important remote sensing effect is in the determination of surface albedo. In many ways the surface behaves similarly to an aerosol layer, it absorbs and reflects radiation dependent upon its albedo. Therefore when an aerosol layer is at low altitude it is almost indistinguishable from the surface and depending upon the surface albedo and the optical depth of the aerosol, either increases or decreases the

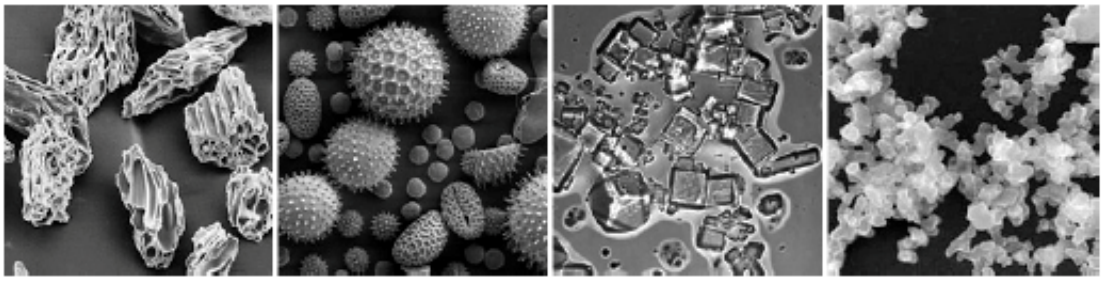

Figure 1.3: Examples images of aerosols from scanning electron microscopes courtesy of USGS, UMBC (Chere Petty) and Arizona State Univeristy (Peter Buseck). Aerosols shown, from right to left, are; volcanic ash, pollen, sea salt and soot.

apparent surface albedo. The result is that accurate retrieval of surface albedo is challenging without knowledge of the aerosol distribution, and conversely the same is true of aerosol retrievals even before non-Lambertian surfaces are considered.

1.3 Aerosol Types, Sources and Sinks

Aerosols are particles suspended in the atmosphere that can have a wide range of properties, shapes and sizes, from sub to several microns (Figure 1.3). Aerosol is categorised into four groups, natural and anthropogenic aerosol, and primary and secondary aerosols (Seinfeld and Pandis, 2012). Natural primary aerosols include mineral aerosols, sea salt, volcanic dust and organic aerosols. Anthropogenic primaries are industrial dust, black carbon and carbons from non-industrial sources such as biomass burning, vehicle emissions and. The secondary aerosols, both natural and man-made, are primarily driven by sulphates formed from SO_2 emissions (volcanoes, burning of fossil fuels) and biogenic gases such as dimethyl sulphide from marine phytoplankton (Haywood and Boucher, 2000). Other secondary aerosols include organic aerosols formed by VOCs and nitrates formed by the emission of NO_x. An additional source of anthropogenic aerosols which can affect various aerosol types is land use change.

The impact of each aerosol type upon the radiative forcing can vary substantially. For instance, black carbons formed by fossil fuel burning are highly absorbing and can therefore introduce a strong positive forcing (Jacobson, 2001), which is estimated to be +0.4 (+0.05 to 0.8) Wm^{-2}. Sulphate aerosols are almost entirely scattering, and so have a strong negative forcing of -0.4 (-0.6 to -0.2) Wm^{-2}. Furthermore, there are aerosol sources that contain mixtures of scattering and absorbing particles, such as biomass burning, which contains absorbing black carbon and the predominantly scattering organic aerosols (Bond et al., 1999; Bond, 2001). In such cases the impact is far more uncertain, with even the sign of the forcing called into question (Kasischke and Penner, 2004). Current estimates place this at -0.0 (-0.2 to +0.2) Wm^{-2}. The different impacts of anthropogenic aerosols are highlighted in more detail in Figure 1.4. The global emission rates of these aerosol types are highly variably and often not well constrained for instance, the global emission of sea spray is thought to be between 2 and 20 Tg yr^{-1} (Gantt et al., 2011) and mineral dust is estimated to be anywhere from 0.5 Tg yr^{-1} in South America to 2800 Tg yr^{-1} in North Africa (Huneeus et al., 2011). Secondary organics are thought to be produced at a rate of 50 to 380 Tg yr^{-1} (Spracklen et al., 2011). Sources such as biomass burning (Heald and Spracklen, 2009) and natural precursors are far less well known and are poorly constrained, with datasets only available for a few species in the case fothe latter, such as isoprene and monoterpenes (Müller et al., 2008; Guenther et al., 2012).

In contrast to greenhouse gases who have a long lifetime within the atmosphere, aerosols have a much shorter lifetime, typically between hours and days. As a result, and due to their often highly localised source, aerosols are not very well mixed, resulting in strong regional variations, which in turn depends upon the meteorological conditions and vertical distribution.

Aerosols are removed from the atmosphere by dry or wet deposition. The dry

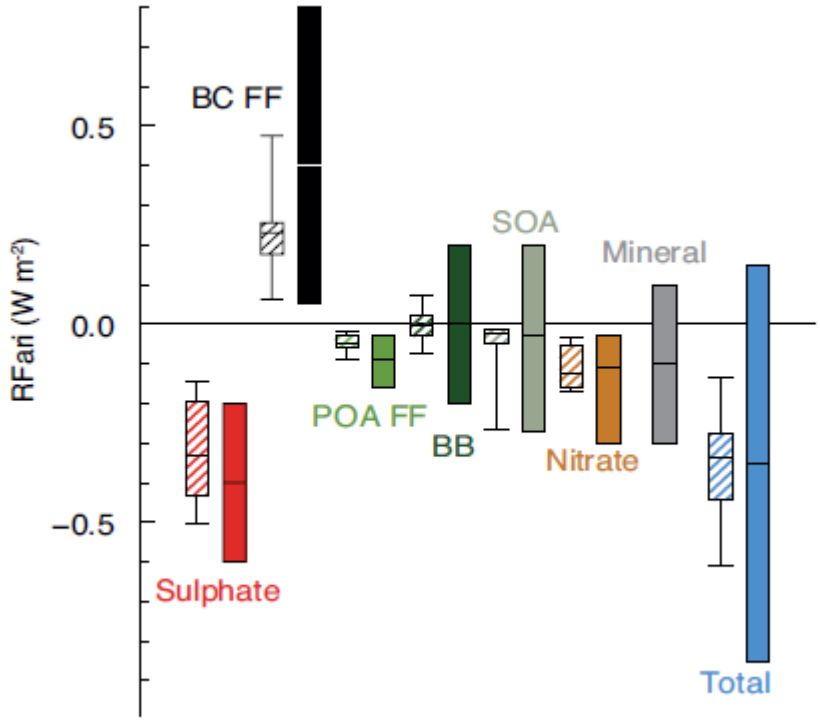

Figure 1.4: Annual mean top of the atmosphere radiative forcing due to aerosol radiation interactions (RFari) due to anthropogenic aerosol types; sulphate, black carbon from fossil fuels and biofuels (BC FF), primary organic aerosols from fossil fuels and biofuels (POA FF), biomass burning aerosols (BB), secondary organic aerosol (SOA), nitrates and minerals. Solid boxes show the AR5 best estimates and 90% uncertainty ranges, hatched box and whiskers show the results from AeroCom II models (Myhre et al., 2013). (Stocker et al., 2013)

deposition velocity, or rate, is dependent upon several factors including the size, shape and density of the aerosol as well as the surface type, for instance a hard smooth surface that promotes particles bouncing off will reduce the rate.

1.3.1 Size Distribution

One of the challenges of aerosols is the sheer diversity of sizes from ultra fine particles of only several nanometres to several hundred micron, a roughly 4 orders of magnitude size range. In the ideal world, one would have a list of all the different

aerosol particles with their dimensions and so be able to calculate any chosen parameter. However such a dataset, that would vary with time, would be incredibly hard to handle and is not practical. Instead what is needed is a set of distributions that describe the number of particles, surface area and volume as a function of the particle size. This is known as the size distribution, and typically follows a log-normal distribution;

$$n_n(D) = \frac{1}{\sqrt{2\pi} D \ln \sigma_g} \exp\left[-0.5\left(\frac{\ln(D/\tilde{D}_n)}{\ln \sigma_g}\right)^2\right] \tag{1.4}$$

This relationship gives the number density of particles, n_n, as a function of diameter, D. With σ_g being the geometric standard deviation (often defined as ln σ_g) and $\tilde{D}_n$ is the median diameter. If then the particles are assumed to be spherical, the second moment provides the surface area as a function of diameter whilst the third moment gives the volume. These different distributions are illustrated in Figure 1.5 which also highlights widely used size distributions of aerosol, nucleation ($10^{-3}\mu$m - $10^{-2}\mu$m, Aitken ($10^{-2}\mu$m - 0.1 μm), accumulation (0.1 μm - 1 μm) and coarse (>1 μm) modes and emphasises the various formation and processes involved in each mode.

1.3.2 Aerosol Formation and Growth

One of the keys to an understanding of the aerosol size distribution is the evolution of aerosol particles; from their initial formation to their growth (O'Dowd et al., 2002). As already discussed, secondary particles are formed from chemicals present in the atmosphere which are subsequently converted to a vapour (Kroll and Seinfeld, 2008). From here the particles grow via homogeneous nucleation or condensation followed by coagulation. Homogeneous nucleation is driven by the supercooling and resulting supersaturation of a vapour, leading to the spontaneous formation of larger particles.

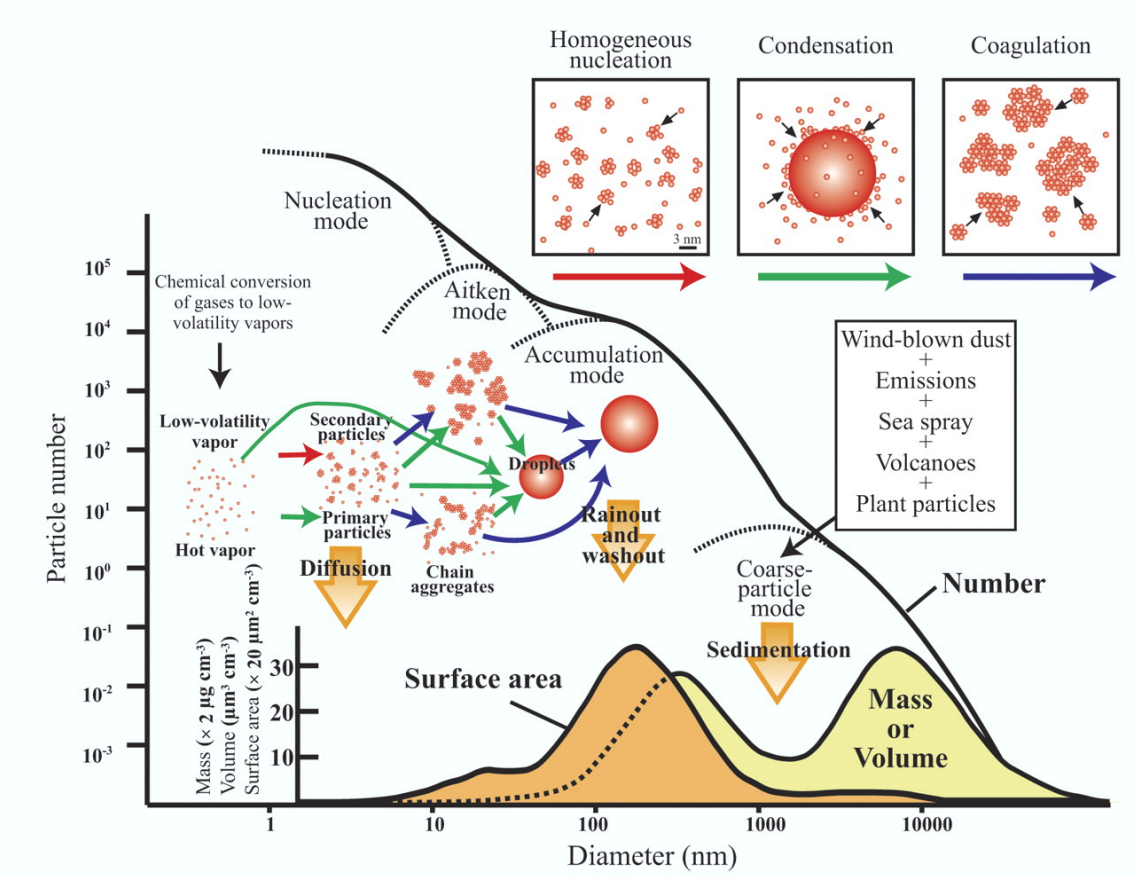

Figure 1.5: Detailed figure showing the number, mass, volume and surface area size distributions of aerosols along with their designated modes. Also describes the size relevant formation and loss processes (Buseck and Adachi, 2008).

Condensation involves the growth of particles either by the condensation of the same species onto larger atomic / molecular clusters, such as water droplets in clouds, or from an additional gaseous species such as the condensation of water vapour onto aerosol particles. Coagulation is the result of the collision of droplets and particles which as a result coalesce or aggregate, to form denser or larger particles. These processes are highlighted and described in terms of particle size in Figure 1.5, and also shows the increase in the surface area distribution and decrease in number density as the particles continue to grow. The larger primary aerosols are also noted here where growth procedures are less pronounced due to the already large size and faster depletion rates.

1.4 Measurement of Aerosols

Aerosols can be measured with in-situ measurements, where they are directly measured from a sample of air for instance, or by remote sensing. Remote sensing uses changes in solar, or terrestrial radiation (passive remote sensing) or its own radiation (active) to infer aerosol information in the atmosphere. Remote sensing can be applied from the ground, aircraft, or from space, allowing vast coverage without the user having to come into direct contact. The advantages and disadvantages of these methods are detailed in the following sections.

1.4.1 In-situ Measurements

In-situ measurements of aerosol offer the chance to study aerosol properties in great detail providing a single point measurement but often to a high levels of accuracy and precision. There are a number of methods available that count, size, and analyse the various properties. Aerosol sizers and counters typically consist of a laser system whose beam is disrupted by the presence of an aerosol particle, the resulting scattered light is then detected. The frequency of this disruption and detection serves to count the aerosol particles flowing through the beam. The size of the particles can be deduced from the intensity of the scattered light, examples include the passive and active cavity aerosol spectrometer probes (PCASP and ACASP, Liu et al. (1992); Ferrare et al. (1998); Liu and Daum (2000)) and the GRIMM dust detector (Namdeo et al., 1999). Another technique is to use the principles of inertia; whereby different size particles are accelerated by different amounts as the incoming airflow is accelerated, an example is the TSI Aerodynamic Particle Sizer (Peters and Leith, 2003; Peters et al., 2006). Mobility sizers, is a non-optical method which analyses the mobility of a particle within an electric field such as the Scanning Mobility Particle Sizer (SMPS, Van Gulijk et al. (2004)) and Differential (Particle) Mobil-

ity Analysers (DMA/DPMA Birmili et al. (1999). Aerosols can also be collected by a filter and deposited onto a substrate before being analysed with optical techniques such as photometers. Typically this is done for optically absorbing particles such as black carbon and are in general called aethalometers (Hansen et al., 1984) with variants such as the Particulate Soot Absorption Photometers (PSAP, Bond et al. (1999) and Multi-Angle Aerosol Photometer (MAAP, Petzold and Schönlinner (2004)). Several instruments also use a mass spectrometer in order to measure the chemical composition of the particles (Murphy et al., 1998). Sampled particles are typically collimated into a beam, vaporised and then ionised before being fed into the mass spectrometer. Examples of this are the Aerodyne aerosol mass spectrometer (Jimenez et al., 2003; Canagaratna et al., 2007), Particle Analysis by Laser Mass Spectrometry (PALMS, Murphy et al. (1998, 2006)) and Aerosol Time-Of-Flight Mass Spectrometry (ATOMFS, Prather et al. (1994); Angelino et al. (2001)). All in-situ measurements, however accurate and detailed, are limited by their single point nature. As such they are often used in conjunction with remote sensing techniques, which provide greater coverage but at an often lower accuracy without much information on composition.

1.4.2 Groundbased Remote Sensing

Groundbased measurements of aerosol began with the use of simple hand held photometers by Volz (1959). Photometers are relatively simple devices that measure the intensity of direct sunlight and by employing a range of filters, can infer total column AOD through application of the Beer-Lambert Law. With advances in technology such devices have increased in accuracy dramatically and can operate autonomously (Schmid et al., 1997; Ehsani et al., 1998). In addition, by measuring the spectral sunlight at specific angular distances from the Sun it is possible to perform inver-

sions to estimate microphysical properties of aerosol (Nakajima et al., 1983, 1986, 1996; Tanre et al., 1988; Kaufman, 1994; Shiobara et al., 1991). With a wide range of instruments and techniques, a need for a standardised measurement network was identified and fulfilled by the Aerosol Robotic Network (AERONET, Holben et al. (1998))

The AERONET network was established by NASA and the PHOTONS group (Univ. of Lille, CNES and CNRS-INSU) and now involves a range of additional collaborators worldwide. Including various affiliated networks (e.g. ARM, RIMA, CSIRO), the number of measurement sites reaches well above 500 globally. Figure 1.6 shows the average AOD at 500nm from a handful of AERONET sites ($\sim$ 80) spread across the globe, identifying regional variations in AOD with a mean standard deviation of 0.083 (37%).

The weakness of the photometers is the lack of vertical information. This can be remedied by the use of Light Detection and Ranging systems (LIDAR) (Fernald et al., 1972). The principle is similar to that of RADAR, light is emitted in a highly coherent, narrow beam and as it encounters particles in its path, i.e. aerosols, a fraction of the light is scattered back to the system. The timing of which indicates the location of the scattering body, and its intensity relates to the AOD. In addition by measuring multiple wavelengths and / or polarization, LIDAR can infer information on aerosol type (Marenco et al., 1997; Raes et al., 2000). However, their substantial cost and complexity has limited their widespread use from the ground although they are frequently used for characterisation and validation, notably the Aerosol Characterisation Experiments (ACE-1,2) (Bates et al., 1998; Raes et al., 2000).

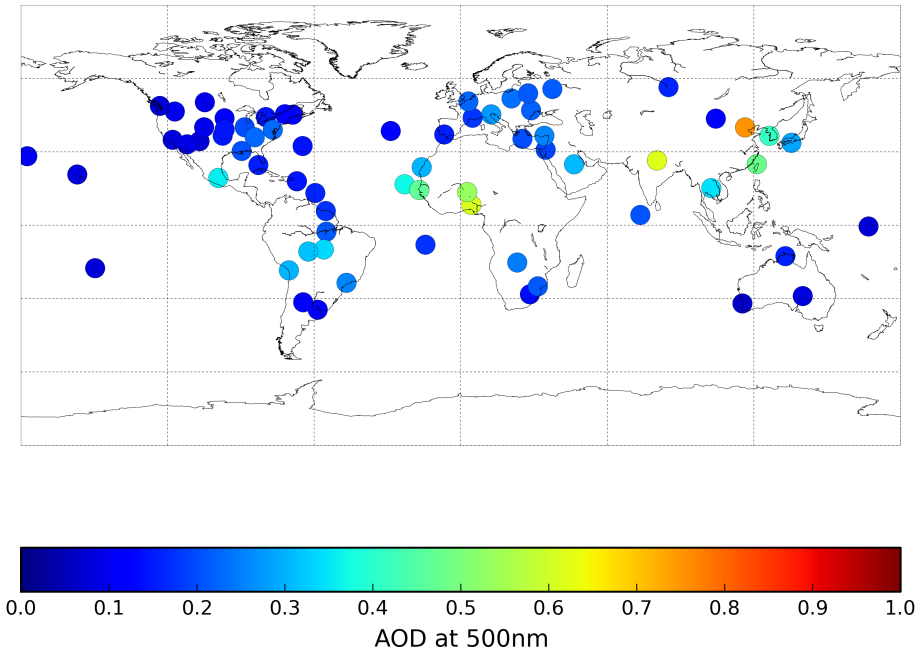

Figure 1.6: Average AOD at 500nm for a selection of AERONET sites

1.4.3 Spacebased Remote Sensing

The inherent disadvantage of groundbased, and to a lesser extent airborne measurements is the lack of global coverage. As a result, several satellites have been flown with this task in mind, as summarised in Table 1.1. The NASA satellite Terra operates amongst others, two instruments that have aerosol capabilities, the MODerate-resolution Imaging Spectroradiometer (MODIS) and the Multiangle Imaging SpectroRadiometer (MISR). As spectroradiometers they both operate similarly to groundbased photometers, with the exception that incident light is reflected from Earth's surface rather than directly from the Sun. Lack of vertical information is an issue, there are however some passive instruments that can obtain vertical information such as Solar occultation instruments (e.g. HALOE or SAGE, (Mauldin III

Mission / Instrument	Organisation	Timeline	Details
A(A)TSR	ESA	Various, 1991-	Imaging Radiometer (Llewellyn-Jones et al., 2001)
ACE	CSA	2003-	Solar occultation FTS (Bernath et al., 2005)
CALIPSO	NASA	2006-	LIDAR
GOME(2)	DLR	Various, 1995-	UV Scanning imaging spectrometer (Burrows et al., 1999)
GOSAT	JAXA	2009-	O_2 A-Band FTS
HALOE	NASA	1991-2005	Solar occultation radiometer
MERIS	ESA	2002-2012	Imaging spectrometer (Bezy et al., 2000)
MIPAS	ESA	2002-2012	FTS
MISR	NASA	2000-	Multi-angle imaging spectroradiometer
MODIS	NASA	2000-	Imaging spectroradiometer
OCO-2	NASA	2014-	O_2 A-Band grating spectrometer
OMI	NASA / NIVR / FMI	2004-	Scanning imaging spectrometer
OSIRIS	SSC / CSA / CNES / TEKES	2001-	Limb sounding imaging radiometer
POLDER	CNES	2004-2009	Imaging radiometer
SAGE	NASA	Various, 1979-	Solar occultation radiometer
SCIAMACHY	ESA	2002-2012	Scanning imaging spectrometer
SEVIRI	EUMETSAT	2004-	Imaging radiometer (Aminou, 2002)

Table 1.1: Summary of existing and recent aerosol missions with references given for those not described in the text.

et al., 1985; Russell et al., 1993; Hervig and Deshler, 2002) or limb scanners (e.g. MIPAS Fischer et al. (2008) and OSIRIS Llewellyn et al. (2004)), albeit limited to measurements of the stratosphere and upper troposphere. Multi-angle observations can also provide some estimate of the height of an aerosol layer from stereo-image techniques if the aerosol layer is sufficiently thick and high (Martin et al., 2010) and has been achieved in certain conditions with MISR (Kahn et al., 2007). In addition the use of polarization and UV observations in constraining aerosol height has been used with some success by instruments such as POLDER and OMI respectively (Dubuisson et al., 2009; Satheesh et al., 2009).

The NASA mission Cloud-Aerosol LIDAR and Infra-red Pathfinder Satellite Observations (CALIPSO, Hunt et al. (2009); Winker et al. (2009)) is an example of a spacebased LIDAR that provides information on the vertical distribution of scatterers as well as information that allows classification of the aerosol type. However, space based LIDAR suffer from a very small swath and therefore truly global coverage is not possible with such an instrument. In addition, space-based LIDARs are expensive and large instruments which are limiting factors for operational monitoring or for combined payloads on satellite platforms. Figure 1.7 demonstrates the

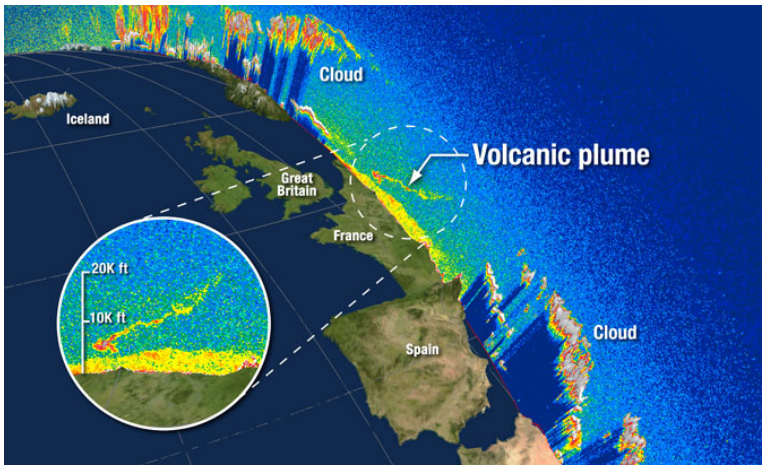

Figure 1.7: CALIPSO measurements for the Icelandic ash cloud 17th April 2010. Credit: NASA/Kurt Severance and Tim Marvel

power of LIDAR measurements by showing measurements made by CALIPSO of the ash cloud resulting from the Eyjafjallajökull volcano eruption in April 2010. The vertical resolution is clearly demonstrated with CALIPSO easily locating clouds, aerosols and importantly the ash plume in this case as it progresses over mainland Europe with the yellow layer near the surface believed to be air pollution. However, the lack of horizontal resolution is obvious, particularly when compared to the similar measurement by MISR shown in Figure 1.8 where aerosol height is estimated through stereo-imaging. The result is a much larger coverage but with far less vertical resolution, indeed it is clearly visible that clouds in this case have to flagged out.

Many important applications related to air quality and climate monitoring, however, require separation of boundary layer and free tropospheric aerosol with errors for AOD of less than 0.02 to 0.05 and a vertical resolution of 1 to 2 km (Hicks, 1994; Siddans et al., 2007).

Several recent and upcoming missions make use of the O_2 A-Band spectral region (Section 2.2). It contains a well understood and contamination free spectrum with a number of absorption lines. This allows for accurate retrievals of aerosol properties

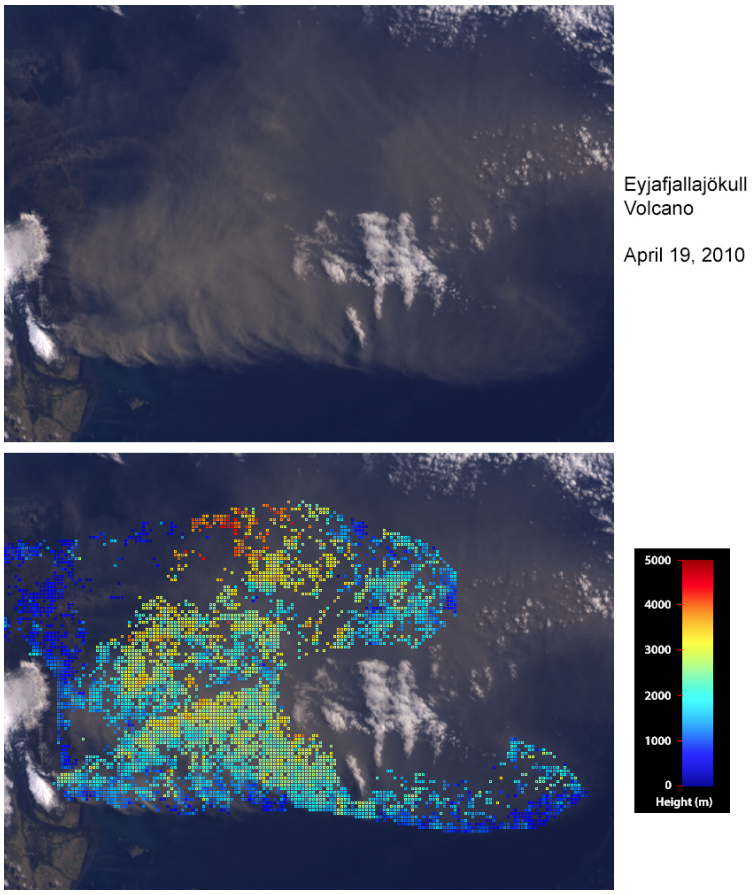

Figure 1.8: MISR image (top) and height calculations (bottom) for the Icelandic ash cloud 19th April 2010. Credit: NASA/GSFC/LaRC/JPL, MISR Team

and crucially contains information of the aerosol distribution, not just its optical depth. As such an O_2 A-Band spectrometer could make up for some of the short comings of a sunphotometer whilst not being as expensive or complex as a LIDAR instrument.

1.5 Thesis Overview

The motivation for this work is to improve the understanding of aerosols in through the assessment and development of space and ground based instrumentation. The aim of this thesis is then to develop a low cost, compact and reliable instrument

for the measurement of aerosol as well as investigate the capabilities of an aerosol retrieval from the O_2 A-Band from ground and space. There are three main spectrometer types, Fourier transform, grating and Fabry-Pérot Etalon (FPE). The latter, though not prevalent, is increasing in popularity due to its low cost and low complexity, whilst still providing high resolution measurements with high signal-to-noise ratios (SNR). Such a technique has already been promisingly applied to measurements of CO_2. If applied to aerosols, low cost, reliable and accurate measurements might be possible, being particularly useful in the measurement of point sources such as volcanoes and industrial sites, especially in under-developed areas of the world where expensive stations such as AERONET are not possible.

The aim of the thesis can be broken down into three steps;

1) To understand the capabilities of current and upcoming missions in the retrieval of aerosol from the O_2 A-Band, and how might the aerosol retrieval be improved upon.

2) To develop a FPE spectrometer through the coupling of a realistic instrument model to the retrieval simulations, and assess its performance theoretically and experimentally.

3) Investigate the intricacies of groundbased retrievals in the O_2 A-Band, including the effects of polarisation and viewing angle for a realistic FPE and other conventional instruments.

Chapter 2 address the theoretical detail needed, including the radiative role of aerosols in much greater depth, as well as the spectroscopy of the O_2 A-Band. Lastly this chapter will outline the forward model and retrieval algorithm used to investigate the above problems. Chapter 3 addresses thesis step one by conducting aerosol retrieval simulations of the Greenhouse Gas Observing Satellite (GOSAT), Orbiting Carbon Observatory 2 (OCO-2), CarbonSat, and Sentinel-5 Precursor (S-5 P),

all of which make use of the O_2 A-Band for path length correction in the observation of greenhouse gases. Chapter 3 also will address the role of surface albedo, surface pressure, aerosol type, multiple aerosols and chlorophyll fluorescence upon the retrieval. The second part of Chapter 3 will show early attempts at applying the retrieval algorithm to GOSAT spectra for a case study of Lamont (Oklahoma, USA). Chapter 4 covers the development of a mathematical framework of an FPE and describes the causes and nature of a variety of inaccuracies that must be accounted for. This is built upon in Chapter 5 where a design is finalised through an optimisation process and the initial calibration of the instrument is undertaken along with simulations of expected performance in comparison to Chapter 3. Chapter 6 takes the finalised FPE model and simulates its performance from the ground along with GOSAT for comparison, and will also explore possibilities in improving the ground based retrieval through polarisation and varying and combined viewing angles. Lastly Chapter 7 summarises the findings of the various studies and discuses the various avenues for future research.

Chapter 2

Key Concepts

2.1 Remote Sensing

2.1.1 Radiative Transfer

Passive instruments measuring in the near infra-red (NIR), visible (VIS) and ultra-violet (UV) measure the intensity of radiation from the Sun that has, in the case of groundbased instruments, passed through the atmosphere, or in the case of space borne instruments, passed through the atmosphere and reflected or scattered back into space. Along its path the beam of radiation can under go several processes that can alter its intensity. It is these changes from the initial intensity at the top of the atmosphere (TOA) that inform us of the composition and properties of the atmosphere. Such processes include the absorption of radiation, scattering out of the direct path, scattering into the direct path (both single and multiple scattering events) and emission of radiation into the path. In the NIR this last process can largely be ignored, as the emission of radiation from the Earth's surface and atmosphere, whose wavelength (or energy) distribution is dependent upon temperature, occurs at much longer wavelengths in the thermal infra-red (TIR).

The radiative transfer equation represents these variations in the intensity of the beam for a specific wavelength, $\mathbf{dI}_\lambda$ over a given distance, $\mathbf{ds}$. In its simplest form it can be given as the sum of the various contributions and reductions in intensity as;

$$\mathbf{dI}_\lambda = -\mathbf{dI}_{\mathbf{SO},\lambda} - \mathbf{dI}_{\mathbf{AO},\lambda} + \mathbf{dI}_{\mathbf{SI},\lambda} + \mathbf{dI}_{\mathbf{MI},\lambda} \tag{2.1}$$

The first two components on the right hand side of the above equation are reductions in intensity due to scattering out of the beam and absorption respectively. More formally these terms are described as;

$$Scattering, \mathbf{dI}_{\mathbf{SO},\lambda} = \mathbf{I}_\lambda \sigma_{\mathbf{s},\lambda} \mathbf{ds} \tag{2.2}$$

$$Absorption, \mathbf{dI}_{\mathbf{AO},\lambda} = \mathbf{I}_\lambda \sigma_{\mathbf{a},\lambda} \mathbf{ds} \tag{2.3}$$

Where $\mathbf{I}_\lambda$ is the intensity at the wavelength λ, and σ_s and σ_a are the scattering and absorption extinction coefficients. The solution to these first two terms in isolation is described by the Beer-Lambert law which depicts the exponential decay in intensity along the absorbing / scattering path. The Beer-Lambert law can be written as;

$$I = I_0 e^{-\tau} \tag{2.4}$$

where I and I_0 are the final and incident intensities and τ is the optical depth. The optical depth is defined as the attenuation over the path length, given by the sum of the absorption and scattering coefficients (extinction coefficient) integrated over the path length. The single scattering contribution is given by the third term in Equation 2.1 and is depicted for a solar source by;

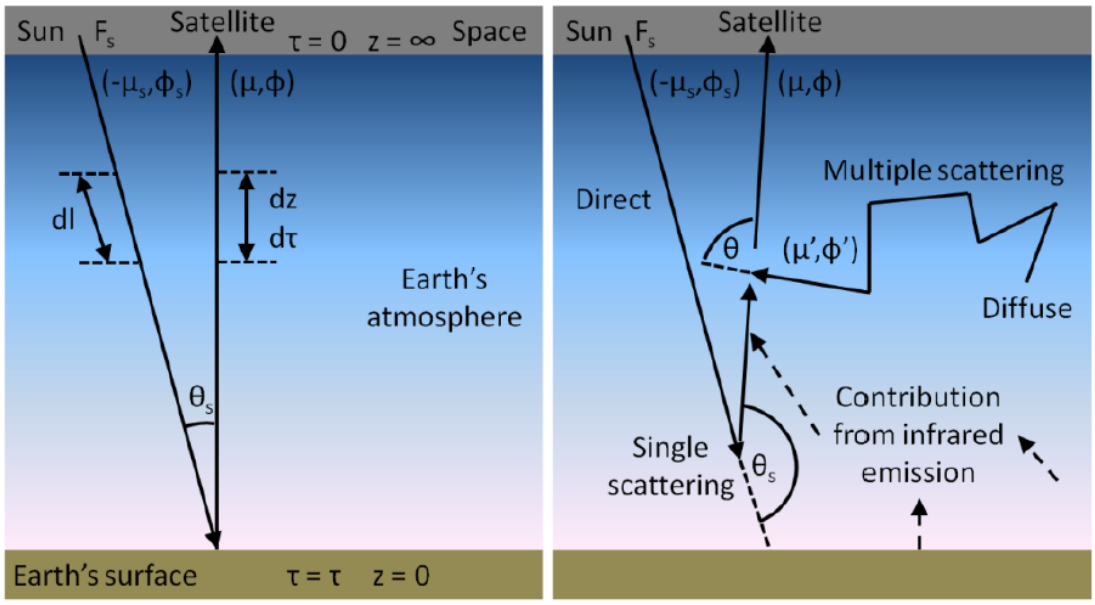

Figure 2.1: Radiative transfer diagram showing the non extinction case (left) and multiple scattering case (right). θ and θ' are the solar zenith angles of the direct and scattered beam with ϕ being the corresponding azimuth. μ is defined to be positive for upwelling radiation and negative for downwelling. Adapted from Jacobson (2001); Liou (2002); Cogan (2012)

$$\mathbf{dI_{SI,\lambda}} = \left[\sum_{\mathbf{k}} \left(\frac{\sigma_{\mathbf{s,k},\lambda}}{4\pi}\mathbf{P_{s,k,\lambda,\mu,-\mu_s,\phi,\phi_s}}\right)\right]\mathbf{F_{s,\lambda}}\mathbf{e}^{-\frac{\tau_\lambda}{\mu_\mathbf{s}}}\mathbf{ds} \tag{2.5}$$

In the above equation, **k**, denotes individual particles, P is the scattering phase function which describes the angular dependence of the scattering, F is the initial irradiance level at the top of the atmosphere with the Beer Lambert law included. The scattering geometry, described by ϕ (solar azimuth) and μ (cosine of solar zenith), is further detailed in Figure 2.1. Lastly the contribution of multiple scattering events to the intensity is given by:

$$\mathbf{dI_{MI,\lambda}} = \left[\sum_{\mathbf{k}} \frac{\sigma_{\mathbf{s,k},\lambda}}{4\pi}\int_{\mathbf{0}}^{\mathbf{2\pi}}\int_{\mathbf{-1}}^{\mathbf{1}} \mathbf{I_{\lambda,\mu',\phi'}P_{s,k,\lambda,\mu,\mu',\phi,\phi'}d\mu' d\phi'}\right]\mathbf{ds} \tag{2.6}$$

By combining Equations 2.4-2.6 we can then reproduce Equation 2.1 in its full

form;

$$\frac{\mathbf{dI}_{\lambda,\mu,\phi}}{\mathbf{ds}} = -\mathbf{I}_{\lambda,\mu,\phi}(\sigma_{\mathbf{s},\lambda} + \sigma_{\mathbf{a},\lambda}) + \left[\sum_{\mathbf{k}} \left(\frac{\sigma_{\mathbf{s},\mathbf{k},\lambda}}{\mathbf{4\pi}} \mathbf{P}_{\mathbf{s},\mathbf{k},\lambda,\mu,-\mu_{\mathbf{s}},\phi,\phi_{\mathbf{s}}}\right)\right]$$

$$.\mathbf{F}_{\mathbf{s},\lambda}\mathbf{e}^{-\frac{\tau_\lambda}{\mu_{\mathbf{s}}}} + \left[\sum_{\mathbf{k}} \frac{\sigma_{\mathbf{s},\mathbf{k},\lambda}}{\mathbf{4\pi}} \int_{\mathbf{0}}^{\mathbf{2\pi}} \int_{\mathbf{-1}}^{\mathbf{1}} \mathbf{P}_{\mathbf{s},\mathbf{k},\lambda,\mu,\mu',\phi,\phi'} \mathbf{d}\mu' \mathbf{d}\phi'\right] \mathbf{ds} \tag{2.7}$$

Here, the contributions of single and multiple scattering introduce additional uncertainty in the solution. For instance in the case of a groundbased instrument looking directly at the Sun, the contributions of these last two terms would be minimal in comparison to the scattering out of the path and absorption terms, thus Equation 2.7 would be easily solvable.

However when this is not the case, a more complex method is required to deduce aerosol parameters or indeed any other parameters. The three main solution classes are Monte-Carlo methods which attempt to simulate the multiple scattering processes directly, discrete ordinate methods which divide all coordinates including wavelength and angle into grid cells and use iterative approaches to solve the equation, or lastly by Moment methods which treat the angular and frequency domains in terms of their moments.

2.1.2 Scattering

When light is incident upon a particle it can react in a number of ways depending upon the particles size, refractive index and wavelength of the incident light. The three different scattering regimes possible are geometric, Mie and Rayleigh scattering (Liou, 2002). Geometric scattering occurs when the wavelength of the incident light is small compared to the particle size, often several orders of magnitude smaller, in such cases, scattering is highly dependent upon the refractive index. Geometric scattering occurs in the presence of raindrops and is responsible for phenomena such

as rainbows. Rayleigh scattering is the elastic scattering of radiation by particles much smaller than the wavelength. Characteristics of Rayleigh scattering are a strong wavelength dependence (4th power) and a near uniform circular phase function. In the visible and NIR this corresponds to scattering by gas molecules, with an example being the sky's blue colour. Of most relevance for aerosol retrieval is Mie scattering, occurring when the size of particle and incident wavelength are comparable. It is characterised by a strong forward scattering phase function and has a relatively weak dependence upon wavelength, typically to the power of -1. We can quantify the scattering type of a given particle for a particular wavelength by defining a size parameter x, which is defined as;

$$x = \frac{2\pi r}{\lambda} \tag{2.8}$$

with r being the particle radius (assuming it is spherical), λ is the wavelength of the light being scattered. If $x \ll 1$, Rayleigh scattering occurs, where as $x \gtrsim 1$ is true of Mie scattering.

2.1.2.1 Rayleigh Scattering

Named after the British physicist Lord Rayleigh, Rayleigh scattering can be described by the induction of an oscillating dipole in a polarisable particle by incident radiation (the history of which is described in Young (1981)). The particles that this applies to are small in comparison to the wavelength of the incoming light. As mentioned previously, the scattering cross section of Rayleigh scattering (C_{rs}) depends roughly on λ^{-4} but more accurately can be defined as;

$$C_{rs} = \frac{8\pi r^6}{3}\left(\frac{2\pi n}{\lambda}\right)^4\left(\frac{m^2-1}{m^2+2}\right)^2 \tag{2.9}$$

where r is the radius of the particle, n is the refractive index of the medium

in question, air, and m is the ratio of the refractive index of the particle to the refractive index of the medium, n. The dependence on the radius of the particle is to the sixth power, meaning that larger particles have a larger cross section as well as being inversely proportional to wavelength. The result of this is that the cross section of Rayleigh scattering is small in the longer wavelengths of the NIR. It also implies all air molecules will scatter to some extent, meaning that with increasing atmospheric path length the extinction due to scattering will increase.

The phase function (P) of Rayleigh scattering for unpolarised light for scattering angle Ω is described by:

$$P(\Omega) = \frac{3}{4}(1 + \cos^2 \Omega), \tag{2.10}$$

and when the anisotropy of the polarisability is considered the equation becomes:

$$P_a(\Omega) = 0.7629.(1 + 0.9324 \cos^2 \Omega). \tag{2.11}$$

This modification is typified by a reduction in the forward and back scattered radiation and an increase in scattering perpendicular to the incident direction. More generally Rayleigh scattering is typified by equally forward and back scattered intensities.

2.1.2.2 Mie Scattering

Mie scattering occurs when r is comparable to the λ. If r is not negligible compared to the λ, i.e. a size parameter $\mathbf{x} \gtrsim 1$, interference effects have to be taken into account. Mie theory describes the solution to this kind of scattering for homogeneous, isotropic spheres and was developed by Gustav Mie and others in the early part of the 20th Century (Mie, 1976). A brief and by no means complete overview of the general approach is given here, with full treatment given in texts such as Born and

Wolf (2002). The method concerns the finding the solutions of Maxwell's equations describing the electromagnetic fields resulting from a plane monochromatic wave that interacts with a spherical surface. The interaction causes the sphere to radiate the waves of itself and are not generally isotropic. The outgoing wave is expanded and linked to the incoming wave through the use of vector spherical harmonics, which in turn involve the use of Legendre polynomials and Bessel functions, and by applying boundary conditions for electric and magnetic fields at the edge of a sphere. The result is that the extinction coefficient (scattering and absorption) is given by:

$$\sigma_{ext} = \frac{2\pi}{k^2} \sum_{n=1}^{\infty} (2n+1) \mathrm{Re} \left\{ a_n + b_n \right\}, \tag{2.12}$$

where $k = 2\pi/\lambda$ is the wavenumber, and a_n and b_n are expansion coefficients for the outgoing wave given by the expansion through vector spherical harmonics,known as scattering coefficients. The larger r compared to the λ being considered, the more terms have to be incorporated into the sum, where the size parameter x is approximately 1, the number of terms that need to be considered is roughly equal to x. However with increasing particle size compared to the wavelength, the computational time needed to solve this can become large. To this end an array of models exist to calculate phase functions and extinction coefficients for a wide range of aerosol types and size distributions (discussed in Section 2.1.4) such as those developed by Wiscombe (1980), Grehan and Gouesbet (1979) and Du (2004).

The Henyey-Greenstein parameterisation is an example of an analytical expression for the phase function in which the computational cost is reduced and depends only on a handful of parameters:

$$P(\Omega) = \frac{1 - g^2}{2(1 + g^2 - 2g\cos\Omega)^{\frac{3}{2}}} \tag{2.13}$$

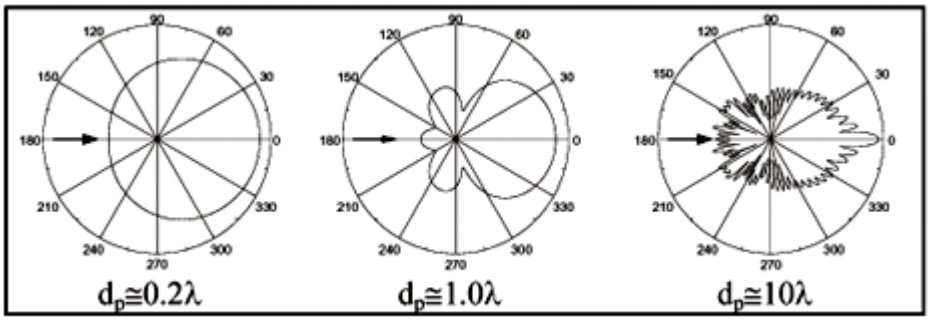

Figure 2.2: Phase function as a function of particle diameter d_p. As the ratio decreases the function becomes more isotropic, exhibiting Rayleigh scattering. As the ratio increases the forward scattering increases in accordance with Mie scattering (Jensen, 2004).

Noting that his is normalised over 4π, the beauty of this is its dependence on only Ω and g, known as the asymmetry factor;

$$g = \frac{1}{2}\int_{-1}^{1} P(\Omega)\cos\Omega d\Omega. \tag{2.14}$$

The key differences between Mie and Rayleigh scattering is the far stronger forward scattering component of Mie, as highlighted in Figure 4.3, and its size / wavelength dependence. Mie scatterings weaker dependence on λ also means that it plays a greater role in the NIR radiation balance than Rayleigh scattering.

2.1.2.3 Single Scattering Albedo

The single scattering albedo (SSA, ω) is a useful quantity in describing the nature of different aerosol types. It is defined as the ratio between the scattering extinction coefficient to the total extinction, i.e.;

$$\omega = \frac{\sigma_s}{\sigma_s + \sigma_a} \tag{2.15}$$

If the SSA is equal to one, then all of the extinction is a result of scattering,

conversely when it is zero, it is a purely absorbing aerosol. The SSA is often a product of the Mie codes previously discussed and is frequently referred to when describing the aerosol type. Examples of the SSA are shown for a range of particle types and mixtures that are relevant to this thesis in section 2.3.6.

2.1.2.4 Optical Depth and Ångström Coefficient

The total level of extinction is often described by the aerosol optical depth (τ or AOD if dealing with aerosols specifically), which is simply the integral of extinction by each particle over a given path length. It is necessary to break the path length into sub sections to take into account any non-uniformities in the distribution of aerosol particles.

$$\tau = \sigma_{total} \int_0^l \sum dz, \tag{2.16}$$

where σ_{total} is the sum of the absorption and scattering coefficients, l is the total path length being considered and z is the subdivision used. One can relate the optical depths of an aerosol at different wavelengths to each other via the Ångström coefficient, α;

$$\alpha = -\frac{\log\left(\frac{\tau_1}{\tau_2}\right)}{\log\left(\frac{\lambda_1}{\lambda_2}\right)}. \tag{2.17}$$

α is inversely related to the size of the particle such that the smaller the particle, the larger the value. As such it is often used to characterise the sizes of aerosols as well as their wavelength dependencies.

2.1.3 Absorption

Though the majority of attenuation of radiation by aerosols is attributed to scattering, some aerosols absorb light by converting it to heat, this is determined by the SSA of the particle and is calculated by Mie theory. As such the main absorbers of solar radiation are those with a low SSA, carbonaceous particles such as black carbon; a product of incomplete combustion, and organic carbons which are a mixture of natural and anthropogenic sources. As a result, such aerosols can cause a local warming, particularly in the lower atmosphere where they are more abundant. For instance the radiative forcing due to black carbon aerosols from fossil and bio fuels is as mentioned, estimated at +0.40 (+0.05 to +0.80 Wm^{-2}, (Stocker et al., 2013)).

The other absorption process present in the atmosphere is the molecular absorption of radiation by gases. This is discussed in more detail in Section 2.2 but here briefly is described. Atoms and molecules absorb radiation at discrete energy levels based upon their electronic and molecular structures. Absorption that occurs is described by the nature of the change it causes, either electronic, rotational or vibrational, or indeed a combination. Energy associated with each individual transition corresponds exactly to the wavelength of the absorbed radiation. The cumulative effect of the absorption of various gases is profound, a wide range of wavelengths are reduced in intensity, including potentially harmful ones such as those in the UV, as well as contributing in the infrared radiation to the greenhouse effect.

2.1.4 Polarisation

The polarization state of an electromagnetic wave is a useful way of characterising the scattering behaviour of aerosols. It is described by four linear quantities called the Stokes parameters:

$$I = E_P E_P^* + E_S E_S^*, \tag{2.18}$$

$$Q = E_P E_P^* - E_S E_S^*, \tag{2.19}$$

$$U = E_P E_S^* + -E_S E_P^*, \tag{2.20}$$

$$V = -i(E_P E_S^* - E_S E_P^*). \tag{2.21}$$

I,**Q**,**U** and **V** denote the total intensity of the beam, the two linear polarizations and the circular polarization. $*$ indicates the complex conjugate and i is the $\sqrt{-1}$. The wave itself is described by the electric field **E**, and its being parallel (**P**) or perpendicular (**S**) to the plane of incidence. The plane of incidence describes the plane in which the scattering event occurs. These four parameters are then combined into the Stokes vector;

$$\mathbf{I} = \begin{matrix} I \\ Q \\ U \\ V \end{matrix} \tag{2.22}$$

For example, as used in Chapter 6, a stokes vector of $(1, 0, 0, 0)$ describes unpolarized light, perfectly **P** by $(1, 1, 0, 0)$ and perfectly **S** by $(1, -1, 0, 0)$. The degree of polarization, $\mathbf{D}_P$, follows on from this and is given by;

$$\mathbf{D_P} = \frac{\sqrt{Q^2 + U^2 + V^2}}{I}. \tag{2.23}$$

Or for the degree of linear polarization $\mathbf{D}_{LP}$;

$$\mathbf{D_{LP}} = \frac{\sqrt{Q^2 + U^2}}{I} \text{or} \frac{-Q}{I} \text{if} U \ll Q \tag{2.24}$$

2.2 Spectroscopy of the Oxygen A-Band

A promising method for inferring information on the vertical aerosol distribution from passive instruments is the measurement of the absorption spectrum of molecular oxygen. The O_2 A-Band, an absorption band at 765 nm, first found interest in the sixties for the measurement of cloud top height or apparent surface pressure (Hanel, 1961; Yamamoto and Wark, 1961a; O'Brien and Mitchell, 1992; Rozanov and Kokhanovsky, 2004), and more recently for the retrieval of aerosol profiles (Heidinger and Stephens, 2000). The reason for this is due to two key aspects: firstly the atmospheric distribution of O_2 is well known throughout the atmosphere and there are no other contaminating species within the same spectral region thus the absorption lines directly provide information on atmospheric scattering, as there are no other species affecting the path length and optical depth. The profiling capability relies on the large range of optical depths of the absorption lines from space in the O_2 A-Band with light from strong absorption lines originating from the upper atmosphere while light for very weak lines will more likely have passed through the atmosphere and be reflected by the surface.

2.2.1 Spectroscopic Basics

Molecular oxygen exhibits absorption spectra consisting of rotation-vibration of several electronic transitions. Of the resulting bands, several are active in the visible and near infrared regions of the electromagnetic spectrum, known as the atmospheric bands. The O_2 A-Band is prominent as it does not overlap with other gases species such as water vapour. The A-Band itself is formed by the electronic transition;

$$X^3\Sigma_g^- \rightarrow b^1\Sigma_g^+ \tag{2.25}$$

Change in the first indices from 3 to 1 relates to a change in the quantum spin number, **S** of 1 to 0. Selection rules for an electronic transition state that this is forbidden for $\Delta\mathbf{S} = 0$. For this transition to occur one of two processes must take place; either magnetic dipole transitions or electronic quadrupole transitions which are 10^5 and 10^8 times more unlikely to happen (Herzberg, 1950). In short, this transition will occur but at a far lower probability than if it was a conventional electronic transition, resulting in a much weaker absorption spectrum. However, due to the sheer quantity of oxygen present in the atmosphere, the net effect is still strong.

Rotational excitation leads to the fine structure of the O_2 A-Band, splitable into three branches based upon the change in rotational excitation. The P and R branch correspond to a decreasing and increasing rotational excitation respectively, the Q branch is observed when the rotational state is constant. These branches are labelled in the top panel of Figure 2.3 where an example O_2 spectra is displayed.

The Q branch is missing due to rotational symmetry selection rules forbidding its existence. One can observe distinct pairs of lines. The rotational levels are defined by the rotational and total angular moments N and J, and individual transitions are described by changes in these numbers by P, Q and R for changes of -1, 0 or +1 followed by the initial values of N and J. The allowed transitions are illustrated in Figure 2.4 where it is worth noting that the initial N must be odd and final be even for $^{16}O_2$.

The results are absorption pairs, which for the P branch are separated by approximately 2 cm^{-1}, R branch pairs are separated by 2-4.5 cm^{-1}. The P and R pairs themselves are separated by 6-10 cm^{-1} from other pairs. Separation of pairs is non-linear due to rotation not acting as a rigid rotor; as the rotational energy increases, the bond begins to stretch which alters the energy levels of the transitions.

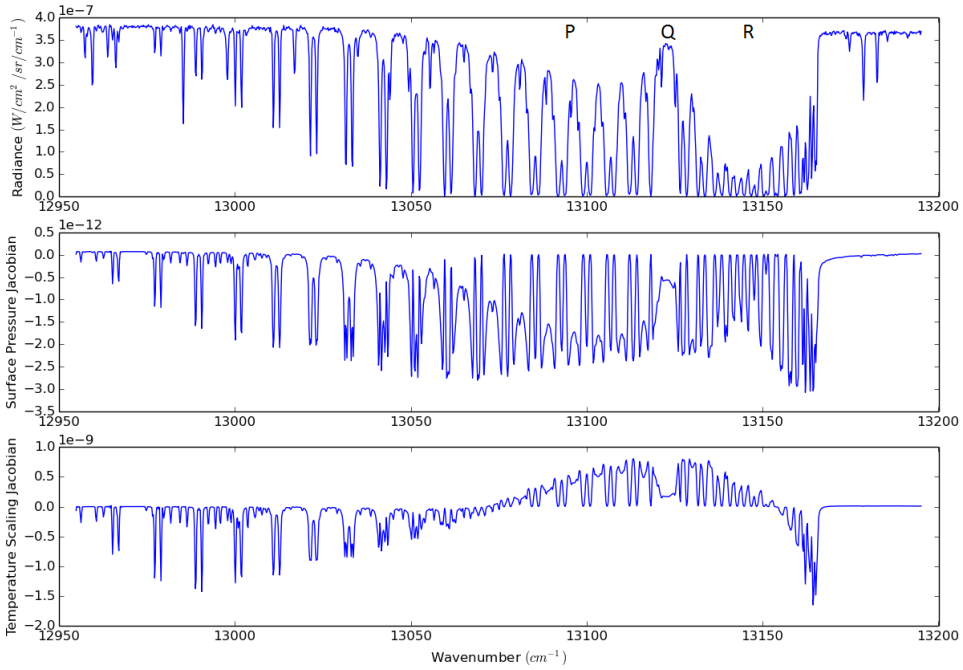

Figure 2.3: Example spectrum with the bands highlightes (top), along with surface pressure and temperature scaling Jacobians taken from GOSAT, note the varying magnitude of the Jacobians within the absorption lines with the change in line strength.

The effect of this upon instrument design is noted later.

2.2.2 Absorption Line Dependences on Temperature and Pressure

Temperature and pressure play key roles in determining the absorption line strength (depth) and shape of the absorption lines of the O_2 A-Band. Line strength, S_i is dependent on the occupation of the initial state and the transition probability. Occupation of the initial state is highly dependent upon the temperature through the Boltzmann energy distribution. As a result lower energy states are occupied more at lower temperatures compared to the occupation of higher energy states. It

follows directly then that absorption lines of lower energy states are stronger than those of higher energies at lower temperatures.

Temperature also plays a small role through the process of Doppler broadening, in which the thermal motion of absorbing molecules causes a shift in the absorbing frequency. When in thermal equilibrium, the velocities are defined by Maxwell's law and result in a Gaussian line shape (Demtröder, 1982). The full width at half maximum (FWHM) of this Gaussian varies with square root of the temperature and for oxygen at 296 K is approximately 0.028 cm^{-1} (Funk, 2000). This process is dominant high in the atmosphere, due to pressure broadening being far weaker in the lower pressure, high altitude environments.

Pressure broadening is the result of molecular collisions causing variation in energy levels. If the collision duration is short relative to the time between collisions, the effect is characterised by a sudden change in the phase of the wave which results in a Lorentzian line shape. Under standard conditions, the FWHM of a pressure broadened line is 0.08 cm^{-1} (Funk, 2000).

To illustrate this, an example spectrum from GOSAT is shown in Figure 2.3 alongside the Jacobians for surface pressure and temperature scaling. The Jacobians show the sensitivity of the measured spectra to the temperature or pressure and mostly describe an increase in the total column of O_2, the mathematics of which are discussed later.

Temperature and pressure profiles are combined to form the Voigt profile by their convolution, shown in Figure 2.5.

2.2.3 Dicke Narrowing

It was found that in applying Voigt profile to O_2 lines a slight residual was left over (Ritter and Wilkerson, 1987). The cause of this is collision Dicke narrowing

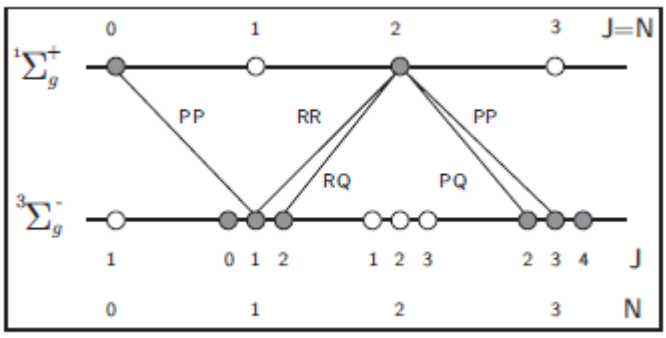

Figure 2.4: Possible transitions for the Oxygen A-Band ($^{16}O_2$). Filled circles indicate rotational levels with positive symmetry. In the final state, J=N (Funk, 2000).

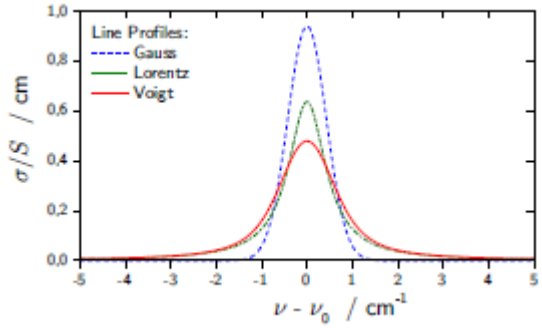

Figure 2.5: Normalized Gauss, Lorentz and Voigt line shapes. The Gauss and Lorentz lines have the same full width at half maximum (1 cm^{-1}), the resulting Voigt line is broader at 1.5cm^{-1} (Funk, 2000).

(Dicke, 1953), with the theory being that collisions cause velocity changes of the O_2 molecules but the phase change is negligible. When taken into account and including small phase changes, by assuming that many collisions are need to change the velocity, one arrives at the Galatry profile. This extension is a minor improvement and is only required when an accuracy of greater than 5% is needed, as shown in Figure 2.6, where the figure also shows the strong impact of narrowing in the core of the absorption lines.

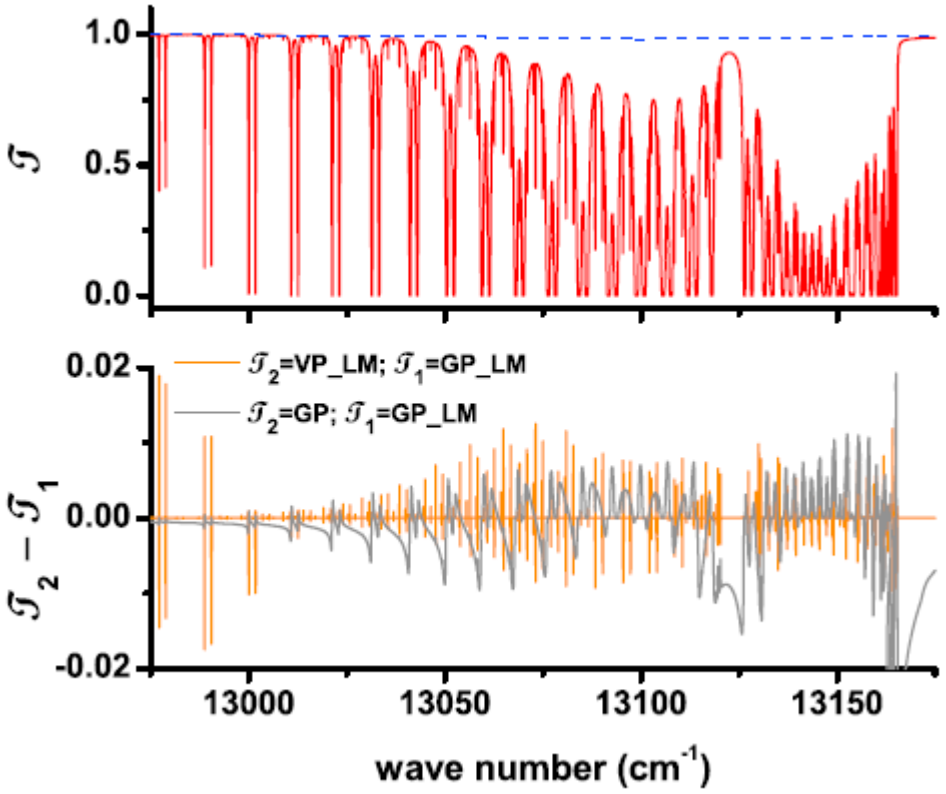

Figure 2.6: (top) Calculated transmission spectrum of the O_2 A-Band with LM and CIA (GP LM, solid red line). CIA contribution shown in blue.(bottom) Contribution of Dicke Narrowing (orange) and LM (grey) both including CIA (Long and Hodges, 2012).

2.2.4 Collision Induced Absorption and Line Mixing

Two more effects that alter the absorption spectra of the O_2 A-Band are collision induced absorption (CIA) and line mixing (LM). Collision induced absorption results from collisions between O_2 and O_2 or N_2 resulting in a short lived electric dipole. The effect of this extra dipole on the spectrum is an additional broad absorption profile. Line mixing occurs when spectral lines are merged with each other. Collisions alter the populations of different transition states, particularly affecting the absorption line strength. Figure 2.6 shows firstly (top) an example spectrum of the O_2 A-Band including LM and CIA in red and the contribution of CIA in blue. The

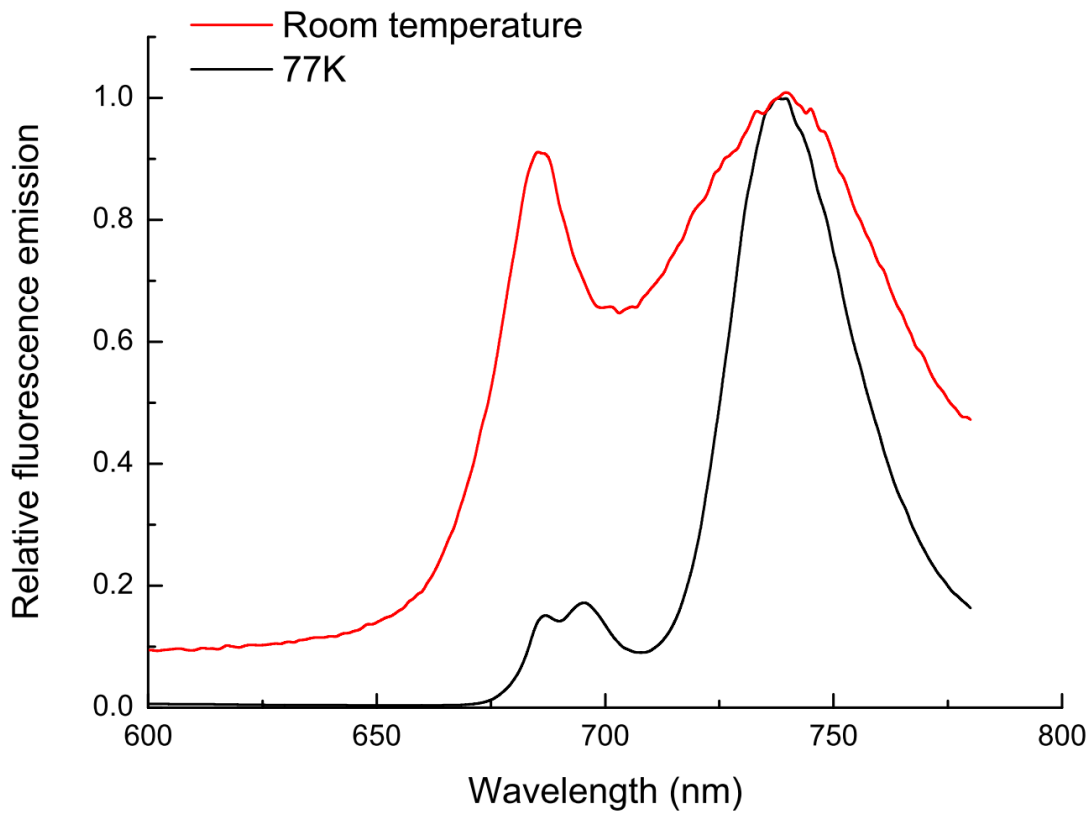

Figure 2.7: Fluorescence emission of a leaf measured at room temperature or in liquid nitrogen, spectra have been normalised to the peak at 748 nm (Atwell et al., 1999).

bottom panel shows the difference between this and other line profiles, firstly in orange is the contribution of Dicke narrowing and in grey is the line mixing. We can see then CIA is in general a broad spectral feature where as LM is highly variable within and around the absorption lines. The retrieval utilizes tabulated spectroscopic parameters for O_2 taken from v3.2 of the OCO line lists (Crisp et al., 2012).

2.2.5 Fluorescence in the Oxygen A-Band

Chlorophyll fluorescence is the process by which plant leaves re-emit radiation after being absorbed by chlorophyll molecules (Maxwell and Johnson, 2000). Plants use

the energy provided by the absorption to drive photosynthesis. If however there is too much energy, for instance if photosynthesis is inefficient, then the leaf can be damaged. As a result this excess energy is either radiated as heat or as fluorescence. Measuring the fluorescence of plants is an interesting means of assessing plant physiology and processes. This emitted radiation is present in, but not limited to the O_2 A-Band and so spectra of this band can provide information on fluorescence levels with the intensity ratios of different wavelengths indicating chlorophyll content. This interferes with the retrieval of aerosols and needs to be accounted for as the emitted radiation acts as an additional source from the surface. The fluorescence profile is shown in Figure 2.7, its relatively broad features mean that modelling of fluorescence as a spectrally constant offset to the TOA radiance is a reasonable approximation, as is done in this thesis. A more accurate method would be to measure a spectral gradient in addition to a constant offset. These parameters are discussed with respect to the measurement of aerosols in Section 2.3.5.4.

2.3 Retrieval Algorithm

The University of Leicester full physics (UoL-FP) retrieval algorithm was developed primarily to retrieve column CO_2 from GOSAT shortwave infra-red (SWIR) spectra and utilises the O_2 A-Band to correct for the effects of aerosol (Bösch et al., 2006, 2011; Connor et al., 2008; Crisp et al., 2012; Parker et al., 2011). This band can be used independently for the retrieval of aerosols.

2.3.1 Forward Model

Firstly we define a state vector $\mathbf{x}$, the elements of which are the atmospheric properties we wish to measure, such as aerosol profile, surface albedo, temperature scaling. The forward model of the retrieval algorithm takes the state vector and from that

simulates the resulting spectrum $\mathbf{y}$, of an atmosphere based upon the forward function F:

$$\mathbf{y} = \mathbf{F}(\mathbf{x}, \mathbf{b}) + \mathbf{e} \tag{2.26}$$

where $\mathbf{b}$ represents any other parameters that influence the measured spectra but are assumed to be known, such as surface pressure and aerosol type. The $\mathbf{e}$ term is simply the measurement error associated with the measurement $\mathbf{y}$ (Rodgers et al., 2000a).

The forward model contains three key components, a radiative transfer (RT) model, a solar model, and an instrument model. The solar model described by Bösch et al. (2011) was applied, containing several thousand absorption lines with their associated wavelength, strength and width. These absorption lines are convolved with the Planck function of the Sun to obtain a solar spectrum. The solar model is assumed to be time independent but allows for variation in the continuum radiance due to the varying Earth-Sun distance.

The RT model is used to calculate the transfer of radiation from the incident beam of radiation through the atmosphere based on a priori knowledge of the state of the atmosphere and surface. The linearised discrete ordinate radiative transfer model (LIDORT, Spurr et al. (2001); Spurr (2008)) is used to calculate backscattered intensities for pseudo-spherical, multi-layered and multiple-scattering atmospheres, as well as producing a set of atmospheric variations for any given elevation angle. To speed up an otherwise computationally expensive process, only two orders of scattering were used in addition to the low-streams interpolation method (O'Dell, 2010). This method uses low accuracy line-by-line RT calculations which are modified by a correction curve derived by the ratio of low and high accuracy RT calculations at a number of wavelengths. Absorption by the Earths atmosphere in the RT model

comes from tables of spectroscopic parameters of each gas. Of most relevance is O_2 which includes line-mixing and is taken from v3.2 of the OCO linelists (Crisp et al., 2012).

The instrument model convolves the modelled high resolution spectrum with the instrument line shape function (ILS) which is defined by the instrument specifications. In addition the model also provides the noise spectrum to accompany the instrument spectrum.

2.3.2 The Jacobian

If the forward model is linear within the error bounds we can derive the following;

$$\mathbf{y} - \mathbf{F}(\mathbf{x_0}) = \frac{\delta \mathbf{F}(\mathbf{x})}{\delta \mathbf{x}}(\mathbf{x} - \mathbf{x_0}) + \mathbf{e} \tag{2.27}$$

with $\mathbf{x}_0$ the linearised state, and the partial derivative $\delta F/\delta x$ the sensitivity of the forward model to a change in the state vector $\mathbf{x}$. This is known as the Jacobian $\mathbf{K}$, and is typically a rectangular matrix consisting of m forward model elements (the number of measurements) and n state vector elements. When m exceeds n the retrieval is said to be over-constrained, conversely when the opposite is true the retrieval is under-constrained. In our case where the measurement vector typically consists of hundreds of spectral points, the retrieval is over-constrained.

Examples of Jacobians are shown throughout this thesis, particularly when studying the merits of polarisation and multiple angles. They are useful because they can directly relate spectral measurements to the aerosol retrieval and allow us to discern where in the atmosphere are we particularly sensitive to, and so provide a means of determining the impact of different measurement schemes.

2.3.3 Inverse Method

In the case of under-constrained retrievals, where the number of unknown state parameters exceeds the number of measurements, a priori information is needed to constrain the retrieval as it would not otherwise be possible to solve the retrieval for $\mathbf{x}$. When the retrieval is over-constrained it may also be desirable to constrain the retrieval. This because in most cases no one solution agrees perfectly with all the measurements due to the inherent error of each measurement. As such all retrievals benefit from a priori information, applied through optimal estimation to find the best solution.

The optimal solution is obtained in two ways. Firstly the most probable state where $\mathrm{d}\mathbf{P}(\mathbf{x},\mathbf{y})/\mathrm{d}\mathbf{x} = 0$ or the expected state $\hat{x}$, which is the mean state averaged by its probability density function (PDF):

$$\hat{\mathbf{x}} = \int \mathbf{x}\mathbf{P}(\mathbf{x}|\mathbf{y})d\mathbf{x}. \tag{2.28}$$

If the PDF is assumed to be Gaussian, the PDF is symmetric about its maximum, i.e. the most probable state equals the expected state.

To find the most probable state one must minimise the cost function. This cost describes the difference between measured and modelled spectra, in addition to the the differences between the state and a priori vectors. It is written as;

$$\chi^2 = (\mathbf{y} - \mathbf{K}\mathbf{x})^{\mathbf{T}}\mathbf{S}_{\epsilon}^{-\mathbf{1}}(\mathbf{y} - \mathbf{K}\mathbf{x}) + (\mathbf{x} - \mathbf{x_a})^{\mathbf{T}}\mathbf{S}_{\mathbf{a}}^{-\mathbf{1}}(\mathbf{x} - \mathbf{x_a}), \tag{2.29}$$

with $\mathbf{x}_a$ the a priori estimate of the state vector and S_y the measurement error. From this the most probable state, in the case of a linear problem, can then be written as:

$$\hat{\mathbf{x}} = \mathbf{x_a} + (\mathbf{K^T S_\epsilon^{-1} K} + \mathbf{S_a^{-1}})^{-1} \mathbf{K^T S_\epsilon^{-1}} (\mathbf{y} - \mathbf{K x_a}). \tag{2.30}$$

To ensure that the most probable state found is close to the truth an iterative approach is used for non-linear problems, with each iteration re-computing the forward model. The Gauss-Newton scheme (Rodgers et al., 2000b) can be used to find the minimum of the cost function by re-calculating the Jacobians and spectra at each step. However this method struggles if the retrieval is too non-linear or if the solution is too far from the truth resulting in the iteration getting trapped in false minima. To combat this there are several methods that significantly alter the state in order to arrive at a solution closer to the truth; one such example is the Levenberg-Marquardt method (Rodgers et al., 2000b). This method uses an extra factor, γ, to minimise the cost function. After each iteration γ is varied by an arbitrary amount depending upon the cost function. If the cost function is increased, γ is increased and the iteration is repeated. If the function decreases γ is also decreased, the state vector updated and the next iteration is undertaken. This sequence is repeated until the retrieval converges. The iterative solution for the Levenberg-Marquardt method is as follows, with the only difference between it and the iterative Gauss-Newton being the inclusion of the $(1 + \gamma)$ term:

$$\mathbf{x_{i+1}} = \mathbf{x_i} + \left[(\mathbf{1} + \gamma)\mathbf{S_a^{-1}} + \mathbf{K_i^T S_\epsilon^{-1} K_i}\right]^{-1} \left[\mathbf{K_i^T S_\epsilon^{-1}} (\mathbf{y} - \mathbf{F}(\mathbf{x_i})) - \mathbf{S_a^{-1}} (\mathbf{x_i} - \mathbf{x_a}). \right. \tag{2.31}$$

The convergence criteria are as follows; firstly the ratio of the updated and previous iterations cost function to the forecast and previous cost function is taken. If it is greater than 0.75 then it has said to have converged (Rodgers et al., 2000b). Secondly the error variance derivatives $\mathrm{d}\sigma^2$, of the updated and previous iterations

are compared. Convergence is achieved if the difference is less than or equal to the length of the state vector. $\mathrm{d}\sigma^2$ is computed by;

$$d\sigma_i^2 = dx_{i+1}^T \hat{S}^{-1} dx_{i+1}. \tag{2.32}$$

With $\hat{S}$ the covariance of the retrieved state. Lastly the chi squared (χ^2) of the fit is used to assess the quality of the retrieval; where less than 1 would be a good fit, between 2 and 10 would be an acceptable fit, and greater than 10 is regarded as poor (Rodgers et al., 2000b). Once convergence has been achieved we can then calculate the a posteriori covariance matrix $\hat{S}$. This method is referred to as full end-to-end retrievals and is used in the latter parts of Chapter 3, where the biases of extra aerosol layers, different types, temperature and surface pressures are assessed. In addition it is also used in the retrieval of aerosol from real GOSAT spectra in the second part of Chapter 3.

2.3.4 Simulation Method

For simulations, we can calculate $\hat{\mathbf{S}}$ directly from the forward modelled Jacobian, a priori covariance matrix, $\mathbf{S}_a$, and the spectral noise covariance $\mathbf{S}_\epsilon$ by linear error analysis, thus negating the iteration process. We can do this if we assume that the retrieval has indeed converged to the best solution. In either case, $\hat{\mathbf{S}}$ is calculated according to;

$$\hat{\mathbf{S}} = (\mathbf{K}^T \mathbf{S}_\epsilon^{-1} \mathbf{K} + \mathbf{S}_\mathbf{a}^{-1})^{-1}. \tag{2.33}$$

The averaging kernel matrix which characterises the ability of the retrieval to reproduce changes in state vector elements is then given by

$$\mathbf{A} = \hat{\mathbf{S}} \mathbf{K}^T \mathbf{S}_\epsilon^{-1} \mathbf{K}. \tag{2.34}$$

The diagonal elements of **A** gives the degree of freedom (DoF) for the signal which represents the number of independent pieces of information that can be retrieved. In the case of aerosol, the radiance relevant retrieved quantity is aerosol extinction per level. A more commonly used quantity is the AOD as discussed is the integrated extinction, and so is a layer quantity rather than a level. To calculate total AOD from the retrieved aerosol extinction profile (which is defined in terms of pressure rather than kilometres), we have applied an operator **h** to the state vector **x** such that:

$$AOD = \mathbf{h}^T \mathbf{x} \tag{2.35}$$

where **h** is defined as follows:

$$\mathbf{h} = [0.5\,\Delta P_{(0,1)},\ \Delta P_{(1,2)} \ldots \Delta P_{(n-2,n-1)},\ 0.5\,\Delta P_{(n-1,n)}], \tag{2.36}$$

with $\Delta P_{(i,i+1)}$) representing the pressure difference between two adjacent levels down to the lowest level n (i.e. surface pressure). To calculate the AOD for a certain height range, the same operation has been used but with elements of **h** being set to zero outside of the selected height range, with 0.5 elements marking the upper and lower extents of the heights used. When using individual AOD layers, which consist of the minimum two extinction levels, we use the term layer AOD (LAOD) to differentiate it from the integrated and total AODs.

The error σ on AOD is then given by:

$$\sigma^2 = \mathbf{h}^T \hat{\mathbf{S}}\ \mathbf{h}. \tag{2.37}$$

2.3.5 State Vector and A Priori Covariance

The state vector includes a number of parameters that are retrieved. This includes aerosol parameter as well as atmospheric and surface parameters that aren't sufficiently well known, such as albedo, temperature scaling and fluorescence.

2.3.5.1 Aerosol

In this thesis aerosol extinction is retrieved, unless otherwise stated, as a profile of 39 equally spaced pressure levels (spaced by 26.25 mb, lowest altitude used is 997.5 mb or 0.02 km). In all simulations the profile is created assuming a Gaussian distribution about a centre height, with a FWHM typically of 1 km, though 2 km is used in some cases. The a priori covariance matrix has been constructed using constant uncertainties for each level and a correlation length of 2 km to infer the non-diagonal values of the covariance matrix. The values for a priori uncertainties for each level have been chosen so that a priori uncertainty for the total AOD is one. For the 4 top-most levels the a priori uncertainty has been set to very small values so that these levels are effectively not retrieved.

An additional retrieval scheme for aerosol is also used named the parameter retrieval, where the aerosol profile is parameterised by a Gaussian-shaped profile. In this case, the 39 state vector elements representing the aerosol extinction profile are replaced with the 3 elements: total AOD, layer centre height and layer width. The a priori uncertainty for total AOD is 1, for centre height 5km and for width the uncertainty is highly constrained, so we are effectively not retrieving it.

2.3.5.2 Surface Albedo

The surface is assumed to be Lambertian, i.e. the apparent brightness of the surface is the same regardless of viewing geometry, or in other words its luminance is

isotropic. It is also defined as being constant across the spectral window used. Its a priori covariance unless stated it is set to 1 and so is largely unconstrained. The importance of this constraint with regards to the retrieval of aerosol is studied in Chapter 3, the assumption of a spectrally flat and isotropic albedo is not studied in this thesis.

2.3.5.3 Temperature Scaling

The temperature scaling parameter is an additive offset to the atmospheric temperature profile provided by atmospheric a priori information discussed in Section 2.3.6.1. Its a priori uncertainty is set to 5 K. The temperature profile used is shown in Figure 2.8 along with the atmospheric composition. Additionally the impact of biases in low altitude temperature on the retrieval of aerosol is also studied in Chapter 3.

2.3.5.4 Continuum Intensity Offset

A continuum intensity offset is included to account for the effects of chlorophyll fluorescence. It is highly unconstrained with an uncertainty of 5% of the continuum value. It is also assumed to be spectrally constant over the band whilst fluorescence is in no way included in the forward model. This approximation is used not in an attempt to retrieve fluorescence, but as a means of mitigating the impact of fluorescence upon the retrieval and assessing the effects upon the retrieval of aerosol.

2.3.6 Non-Retrieved Parameters

Non-retrieved parameters, denoted as $\mathbf{b}$ in Equation 2.26, relate to parameters that are well defined but are still relevant to the forward model. Such parameters could be defined by solar geometry, meteorological or atmospheric models. Firstly, the surface

Aerosol Type	Relative Abundance	Characteristic Radius (μm)	SSA
Accumulated Dust	0.39	0.47	0.91
Coarse Dust	0.19	1.90	0.73
Sulphate	0.29	0.08-0.1	1.0
Sea Salt	0.13	0.35-0.61	1.0

Table 2.1: Aerosol base types and their properties, SSA listed at 675 nm for aerosol mixture 2b (Kahn et al., 2001).

pressure is not retrieved and a value of 1000 mb is used. The impacts of a bias in surface pressure is studied in Chapter 3. Aerosol type is not retrieved for simplicity and is fixed at Kahn type 2b (Kahn et al., 2001) which relates to a mixture of four base aerosols with properties calculated as in Cogan (2012), these are summarised in Table 2.1 with this aerosol mixture corresponding to a dusty maritime and coarse dust mixture. Aerosol properties can be retrieved, particularly when using multiple viewing angles as discussed in Frankenberg et al. (2012), but as the focus of this research is the ability to obtain vertical distribution information, this was omitted in favour of added clarity. Though the effects of incorrect assumptions of aerosol mixture are also studied in Chapter 3 with resulting errors in AOD and aerosol layer height being as high as 45% for cases where the Ångström coefficient is vastly different to the modelled aerosol.

2.3.6.1 Atmospheric Composition

The atmospheric composition is based upon a European Centre for Medium-Range Weather Forecasts (ECMWF) model for Darwin Australia in September 2009 and consists of H_2O, CO_2, CH_4 and O_2 as well as a temperature profile. These profiles are shown as a reference in Figure 2.8.

It is important to note that though these gases are present, they are not optically active within the O_2 A-Band and are shown purely for context. We identify the tropopause location as the minimum of the temperature profile at approximately 12

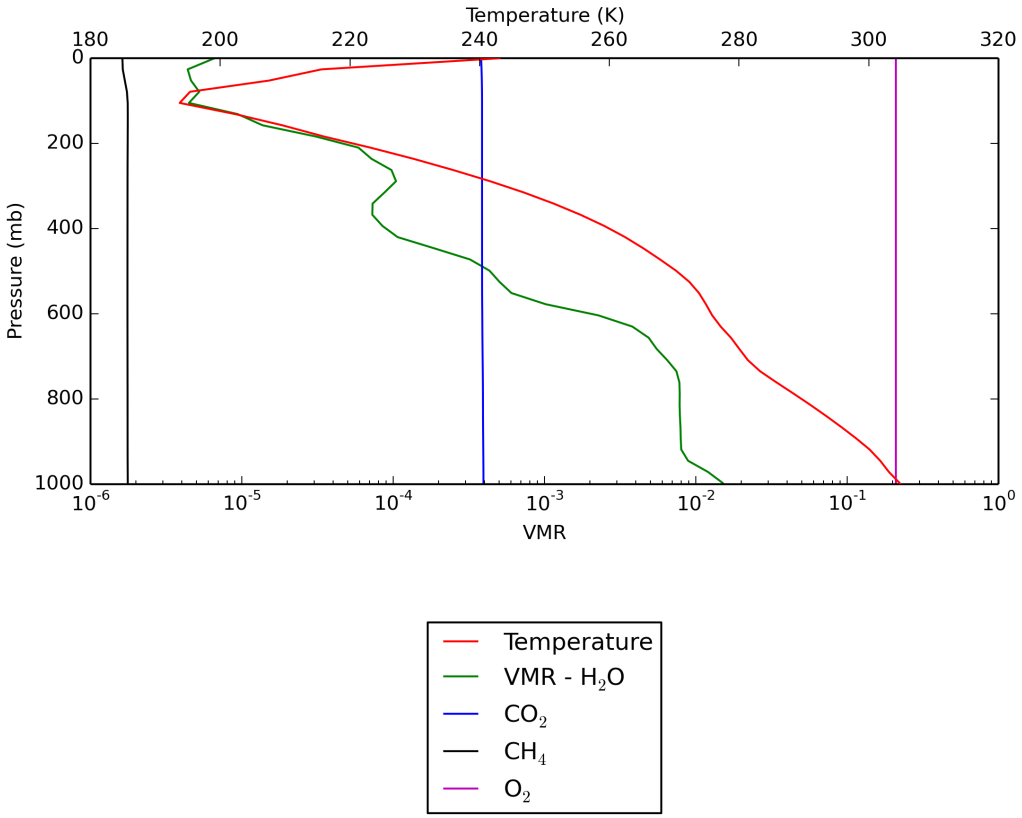

Figure 2.8: VMR profile of H_2O, CO_2, CH_4 and O_2 and the temperature profile used for retrieval simulations. Taken from ECMWF for Darwin, Australia, September 2009.

km, and we can estimate the boundary layer height to be approximately 900 mb (800 m) from the drop in H_2O. This profile was chosen largely at random, though as only the O_2 and temperature profiles are actually used, and given that a temperature scaling retrieval is also used, the impact on the validity of the results is negligible.

2.3.6.2 Viewing Geometry

The viewing geometry is defined by four angles; the solar zenith (SZA, θ_i) and azimuth (SA, ϕ_i) and the corresponding instrument or viewing zenith (VZA, θ_r) and azimuth (VA, ϕ_r). These angles are described in Figure 2.9. In the simulations used throughout this thesis the VZA is 0° (nadir viewing) in the case of spacebased

simulations, and zenith viewing in the case of groundbased measurements. The two azimuths are set to 0° and 180° for the SA and VA respectively so that the measurement plane is aligned with the illumination.

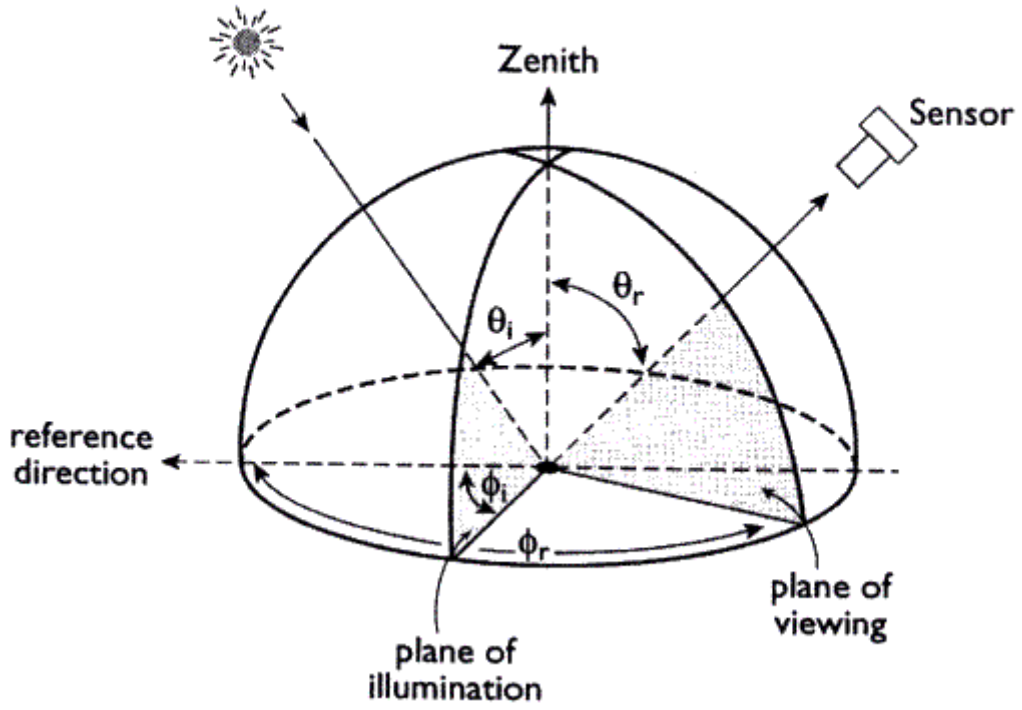

Figure 2.9: Viewing geometry used with relevant associated angles, adapted from (Kriebel, 1976)

2.4 Summary

This chapter introduced a number of important concepts that were broken down into three sections. The first of which Section 2.1.1, focused upon the radiative properties of aerosol in the atmosphere, this included an outline of radiative transfer in general before detailing the various scattering and absorption processes relevant to aerosol. Key quantities defined here that relate to the aerosol properties are the

AOD, SSA and Ångström coefficient which describe the optical thickness, scattering properties and wavelength dependence respectively. The second section (2.2) gave an overview of the spectroscopy and relevance of the O_2 A-Band including the effects of temperature, pressure and fluorescence. The final part of this chapter(2.3) discussed the retrieval algorithm used to deduce aerosol properties. The roles of the radiative transfer, solar and instrument models in the forward model were described and the inverse and simulation methods that are integral to this thesis were highlighted in detail. The section ends with a description of the various parameters that make up the state vector and forward model.

With this in place the next stage is to assess the performance of several upcoming and existing instruments in the retrieval of aerosols from the O_2 A-Band. This will be done within the structure of simulations as they allow all instruments to be compared to each other in a systematic and concise way. Following on from this then would be to test the retrieval described here on the presently available spectra from GOSAT.

Chapter 3

Tropospheric Aerosol Profile Information from High Resolution Oxygen A-Band Measurements from Space

A promising method for inferring information on the vertical aerosol distribution from passive instruments is the measurement of the absorption spectrum of molecular oxygen (O_2). The atmospheric distribution of O_2 is well known throughout the atmosphere and thus the absorption lines directly provide information on the optical path length and thus on atmospheric scattering. Traditionally, the O_2 A-Band in the near-infrared at 765 nm is used for cloud top pressure (or apparent surface pressure) retrievals (Hanel, 1961; Yamamoto and Wark, 1961b; O'Brien and Mitchell, 1992). More recently, the use of O_2 A-Band measurements for vertical profiling of aerosols has been studied by Heidinger and Stephens (2000). This profiling capability relies on the large range of optical depths of the absorption lines in the O_2 A-Band with light from strong absorption lines originating from the upper atmosphere while light

for very weak lines will more likely have passed through the atmosphere and be reflected by the surface.

However, as concluded from theoretical studies by Heidinger and Stephens (2000), the vertical resolution will be limited and measurements need to be obtained with a spectral resolution of about 0.5 cm^{-1} and with an accuracy of 2% or better. Simulations of O_2 A-Band spectra for the SCIAMACHY instrument by Corradini and Cervino (2006) showed that a maximum of 3 aerosol layers can be resolved and that aerosols near the surface cannot be retrieved if the surface is bright. They have also pointed out that knowledge of aerosol properties such as single scattering albedo and phase function are of great importance. Retrieving such properties simultaneously along with the profile is difficult but can be enhanced through the combination with a LIDAR, (Heidinger and Stephens, 2000), polarization as in Boesche et al. (2008) or by using multiple angles as discussed by Frankenberg et al. (2012). In the latter, they show that it is possible to retrieve a number of aerosol type parameters along with one aerosol profile centre height and width showing an increase of 2-4 degrees of freedom (DoF) with the addition of 2 viewing angles compared to the strictly nadir view only.

Hollstein and Fischer (2014) assessed the role of spectral resolution and instrument noise upon the retrieval of aerosol optical depth and height from the O_2 A-Band using a fast forward operator based upon lookup tables. They conclude that while performance generally increases with improved spectral resolution, particularly above values of 0.1nm, performance can degrade with increased resolution due to SNR requirements. They also discuss the impact of aerosol type with the conclusion that the retrieval is largely immune to such changes, with AOD more strongly affected compared to height.

The O_2 A-Band is susceptible to chlorophyll fluorescence as discussed by Franken-

berg et al. (2011). They state that this effect can introduce significant biases in retrieved aerosol parameters if not taken into consideration. They advocate the use of solar lines to retrieve an intensity offset caused by fluorescence, otherwise disentangling the effects of aerosols and fluorescence in the O_2 A-Band would be difficult. Sanders and De Haan (2013) use the fact that the O_2 A-Band has a number of solar lines and they retrieve a fluorescence value simultaneously with aerosol with a minimal detrimental impact upon the accuracy of the aerosol retrieval.

There are a number of satellite instruments that are either currently in orbit, will be launched in the next 1-2 years or are proposed which provide measurements of the O_2 A-Band and will provide valuable information on aerosols. The Greenhouse Gas Observing SATellite (GOSAT) which was launched in 2009, Orbiting Carbon Observatory-2 (OCO-2) in 2014 and the Sentinel 5-Precursor (S-5 P) mission which will be launched within the next 1-2 years and the ESA Earth Explorer 8 candidate mission CarbonSat is a proposed mission for launch around 2020. In the first part of this chapter, we present a synthetic study to assess the capability of these four instruments with largely different instrumental characteristics to retrieve the information on the vertical distribution of aerosols. The second part focuses on the aerosol capabilities of GOSAT using real observed spectra.

3.1 Theoretical Studies

Section 3.1.1 provides a brief description of the four instruments included in this study, with a focus on their characteristics within the O_2 A-Band followed by an overview over the simulation and retrieval methods in Section 3.1.2. In Section 3.1.3, we present the results obtained from profile retrievals of aerosols for the four instruments for simple (single aerosol layer) and more complex (two aerosol layers) scenarios. Following on from this, we will discuss the effect of introducing additional

constraints on the aerosol retrieval by imposing a parameterised shape on the aerosol profile or assuming a priori knowledge on surface albedo. An assessment of systematic errors caused by inaccurate knowledge of aerosol mixtures, surface pressure and temperature on the retrieval of aerosol parameters is given in Section 3.1.5.

3.1.1 Instrumentation

Four space-based instruments are included in this study that provide measurements in the O_2 A-Band range with a wide variety of spectral resolutions and signal-to-noise characteristics.

GOSAT launched by the Japanese Space Agency in 2009 is equipped with the TANSO-FTS instrument; a Fourier Transform Spectrometer that provides spectrally resolved radiance measurements in the three shortwave infrared (SWIR) bands and a thermal-infrared (TIR) band (Kuze et al., 2009). GOSAT has a 3-day repeat cycle and TANSO-FTS nominally performs a cross-track scanning pattern with a ground pixel 10.5 km in diameter. Until August 2010, the standard mode consisted of five cross-track points separated by 158 km which has been changed to three points to reduce pointing errors (Crisp et al., 2012).

The OCO-2 mission launched in the summer of 2014 into the afternoon constellation (A-train) orbit (Crisp et al., 2004, 2008). The OCO-2 payload consists of a high-resolution grating spectrometer that covers 3 spectral bands in the SWIR. OCO-2 uses a narrow nadir swath width of 10 km with ground pixels of area 3 km^2 and an orbit with a 16-day repeat cycle.

The S-5 P mission is a gap-filler and a preparatory programme for the EUMETSAT Polar System (EPS) Second Generation programme (Ingmann et al., 2012). The planned launch date of S-5 P is in March 2015 and it will fly in formation with the U.S. NPP mission. The S-5 P instrument has 4 bands in the UV-visible range, 2

	GOSAT	OCO-2	S-5 P	CarbonSat
Agency	JAXA	NASA	ESA/GMES	ESA
Launch Year	2009	2014	2016	2018
Spectral Range (nm)	756-775	757-775	755-775	757-773
Resolution/FWHM (nm)	0.03	0.044	0.5	0.1
Sampling per FWHM	2.5	2.5	2.5	3.0
Number of Pixels	1584	1016	100	480

Table 3.1: Assumed instrument parameters in the O_2 A-Band range for the four instruments used in this study. Resolution is defined by the FWHM of an assumed Gaussian distribution for OCO-2, CarbonSat and S-5 P. GOSAT is as in Kuze et al. (2009)

bands in the near infrared (NIR) and 1 SWIR band with moderate spectral resolution. The instrument measures a wide swath of 2600 km with a spatial resolution of 7×7 km^2 and it achieves daily global coverage. The instrument parameters for S-5 P used in this study represent a baseline performance given in Buscaglione and Maresi (2011) and changes, particularly in the spectral sampling and resolution, could alter the results.

CarbonSat is a satellite mission that has been selected by the European Space Agency (ESA) as one of two candidate missions for ESAs Earth Explorer 8 (EE8) programme, with one to be launched around the end of the decade ($\sim$2020). CarbonSat is an imaging spectrometer that will cover three spectral bands in the NIR and SWIR with moderate to high spectral resolution. CarbonSat has a high spatial resolution with ground pixels with an area of 2×2 km^2 and good spatial coverage via continuous imaging across a 240 km swath width (goal: 500 km) (Bovensmann et al., 1999; Buchwitz et al., 2013).

There are a number of satellite instruments that provide measurements of the O_2 A-Band such as SCIAMACHY, GOME and GOME-2 that are not included in this study. Their spectral resolution is comparable to that of S-5P and comparisons are possible with the help of Figure 3.3.

Table 3.1 gives an overview of the assumed instrument parameters of the four

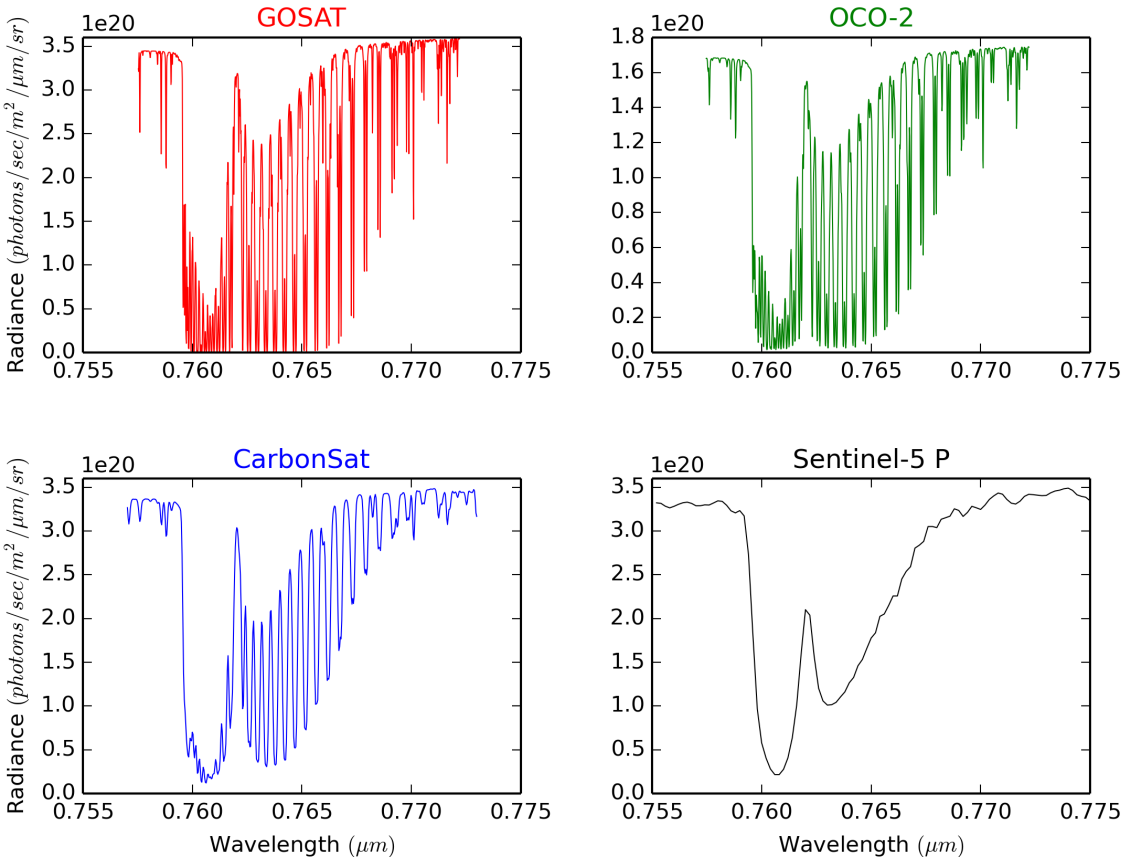

Figure 3.1: Simulated spectra for GOSAT, OCO-2, CarbonSat and S-5 P for a solar zenith angle of 30°and a surface albedo of 0.5. An aerosol layer with optical depth of 0.3 at a height of 1 km with a width of 1km is assumed.

instruments for the O_2 A-Band range. Simulated example spectra for the four instruments are shown in Figure 3.1. GOSAT and OCO-2 acquire O_2 A-Band spectra with high spectral resolution which the separation of individual absorption lines. The structure of the absorption lines is still visible in the CarbonSat spectra, while the resolution of S-5 P is too low to observe the line structure of the O_2-Band. OCO-2 observes roughly half the radiance levels of the other instruments since it measures only one polarization component of the signal. In this study, we have not considered polarization explicitly and we halved the simulated intensity levels for OCO-2 to take into account this effect.

The assumed signal-to-noise (SNR) characteristics of the four instruments are

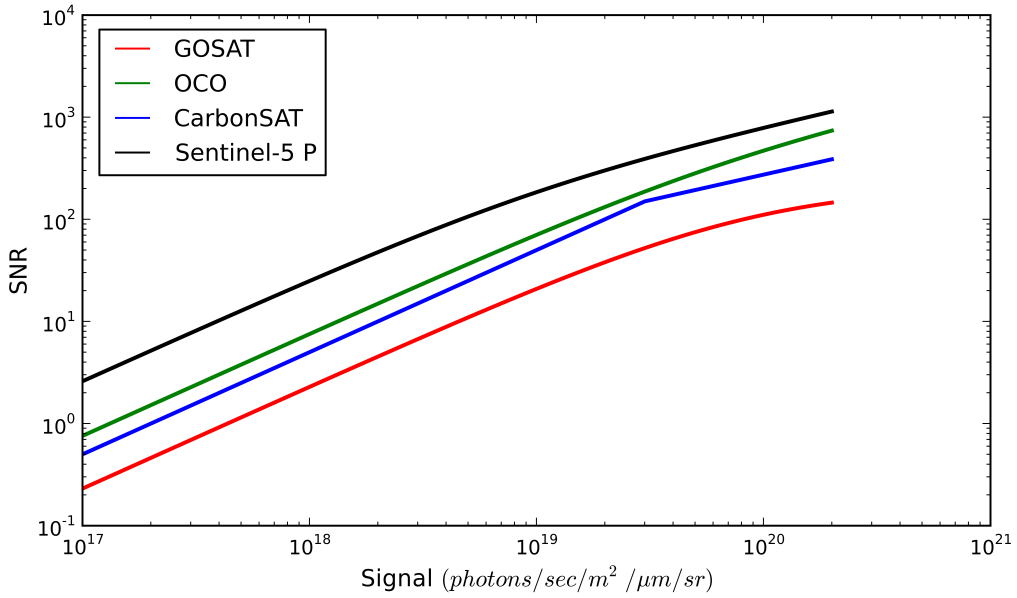

Figure 3.2: Assumed signal-to-noise (SNR) models for the four instruments GOSAT, OCO-2, CarbonSat and S-5 P.

given in Figure 3.2 and are based on instrument noise requirements or provided calibration data. The instrument with lowest spectral resolution tends to have the highest SNR and vice versa, except that OCO-2 has a better SNR than CarbonSat despite its higher resolution. For S-5 P and OCO-2, we have assumed a dependence of the SNR with the square root of the radiance. For CarbonSat, we have assumed a linear dependence with radiance for low radiance levels and a square root dependence for higher radiance levels. For GOSAT, we have assumed a weak radiance dependence on the measurement noise with a linear relationship.

The instrument line shape (ILS) function used for OCO-2, CarbonSat and S-5 P is a Gaussian function defined by the full width at half maximum (FWHM) given in Table 3.1. GOSAT uses ILS function which was obtained from the JAXA ILSF

model (Kuze et al., 2009).

3.1.2 Simulation Framework

To assess the aerosol retrieval capabilities for the four instruments we have carried out a series of retrieval simulations based on the instrument configurations as described previously using the framework discussed in Section 2.3 of the previous chapter though some additional specifics are described here.

We have simulated spectra of the O_2 A-Band for a range of geophysical scenarios described in Table 3.2. Albedos of 0.05 and 0.5 have been chosen as extreme values that represent ocean and heavily vegetated land respectively, higher albedo scenarios were found to behave similarly to the 0.5 case and so were not studied in detail (as highlighted later in Figure 3.9). An aerosol extinction profile with a Gaussian-shaped (in height rather than pressure) vertical distribution has been assumed for all scenarios using nadir-viewing geometry only for consistency and we expect that the retrieval performance will vary for off-nadir geometry. In reality a more likely profile is a boundary layer aerosol that decays exponentially with height, however this approximation allows for a consistent and systematic approach.

The retrieval setup described here is referred to as profile retrieval. In the latter part of this section we use an alternative aerosol retrieval called the parameter retrieval where the aerosol profile is parameterised by a Gaussian-shaped profile. In this case, the 39 state vector elements representing the aerosol extinction profile are replaced with 3 elements: total AOD, layer centre height and layer width. The a priori uncertainty for total AOD is 1 and for centre height 5 km. A very small value for the a priori uncertainty of width has been chosen so that this parameter is highly constrained and it is effectively not retrieved, we do this as the width is otherwise poorly retrieved.

Variables	Values
SZA	30°, 70°
Surface Pressure	1000 mb
Surface Albedo	0.05, 0.5
Atmosphere	09/09 - Darwin, Aus.
Aerosol Scenario	AOD, Height, Width
Scenario A:	
Boundary Layer Aerosol	0.3, 1 km (850 mb), 1 km
Scenario B:	
Elevated Aerosol i.e. dust	0.3, 3 km (700 mb), 1 km
Scenario C:	
Cirrus Layer	0.1, 10 km (250 mb), 2 km

Table 3.2: Geophysical parameters used for the retrieval simulations. The aerosol profiles are setup as a Gaussian shaped distribution for the given value of AOD, height and width with approximate pressure levels.

To study systematic effects of incorrect assumptions on aerosol profile, surface pressure and aerosol mixture (Sections 3.1.4.1 and 3.1.5), a full end-to-end retrieval of the parameterised aerosol retrieval was used instead of directly calculating the a posteriori error covariance matrix as described previously. Systematic errors have then been estimated from the difference of retrieved and true values for the aerosol parameters. These biases will additionally be driven by biases in offset and albedo (which will be minimised by correct a priori information), the results however are studied purely as a function of the stated assumptions.

3.1.3 Aerosol Profile Retrieval

3.1.3.1 Single Aerosol Layer Scenarios

The information content of the aerosol profile retrieval from the O_2 A-Band is primarily determined by the SNR and the spectral resolution of the instrument. To better understand the dependence on these two instrument parameters, we have carried out simulations for a range of SNRs and resolutions for a generic instrument

based on the noise model of S-5 P.

For the simulations we have used a surface albedo of 0.5, a SZA of 30°and aerosol scenario A. We have kept the number of spectral pixels constant for all configurations which results in a high spectral oversampling for configurations with low spectral resolution; this has been done so as not to confuse loss of information with loss of spectral pixels (Frankenberg et al., 2012).

The left panels of Figure 3.3 show the error for the total AOD and the DoF as a function of the spectral resolution and continuum SNR for a retrieval without an intensity offset. Note that the DoFs are calculated with respect to the a priori covariance matrix described in Section 2.3 and thus they do not necessarily reflect the true DoFs with respect to the atmospheric variability. Instead, they provide a meaningful relative measure for characterizing the ability of different instrumental setups to provide information on the vertical aerosol distribution.

From Figure 3.3 we find that a precise, low error, retrieval of total AOD does not necessarily require high spectral resolution but high SNR. For high values of SNR, the errors tend to be smaller for lower resolution. This is due to the SNR model limiting the usefulness of the higher resolution and therefore lower signals, particularly within the absorption lines and the fact that we have kept the number of spectral points constant for all values of resolution. However, for very high spectral resolution (0.03 nm), increasing resolution leads to smaller AOD errors regardless of SNR.

As expected, vertical information, shown by the DoFs, shows a clear dependence on the spectral resolution as the vertical information is inferred from the absorption lines of the O_2 A-Band. For low values of SNR (<200), the noise is limiting the information that can be obtained from the absorption lines and the effect of spectral resolution becomes weak. Consequently, large values for DoF require very high

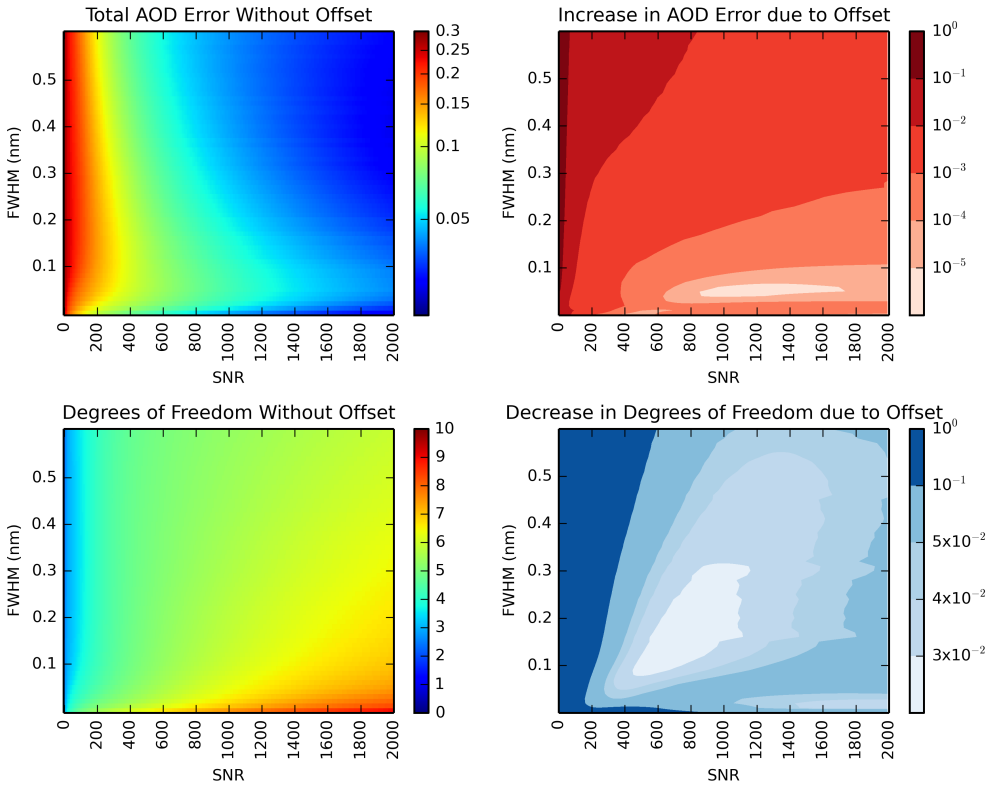

Figure 3.3: Total AOD error (top left panel) and DoF (bottom left panel) for the aerosol profile retrieval for scenario A, SZA 30°and albedo 0.5 as a function of continuum SNR and spectral resolution (as given by the FWHM of the ILS) without including an intensity offset in the retrieval. The panels on the right show the change in total AOD error and DoF when including an offset.

spectral resolution combined with very high SNR.

The impact of including an intensity offset in the retrieval is shown in the right hand side of Figure 3.3. The increase in the error for total AOD is typically small with an average value of 5×10^{-3}. The largest increase is observed for low SNR, and the smallest effect is found for high resolution and modest-to-high SNR. For DoF, we observe a small decrease of 0.05 on average. Again at low SNR the loss in information is more substantial and can be up to a 50% decrease in DoFs for very low values of SNR.

Based on Figure 3.3, we can make several tentative predictions for the perfor-

mance of the four instruments described in Section 3.1.1. Firstly, we expect S-5 P to behave somewhat differently from the other three instruments due to it operating in the low resolution and high SNR regime that should result in low total AOD errors but also low DoFs. OCO-2 has high spectral resolution and high SNR, so it should achieve high DoFs together with small total AOD errors. GOSAT has very high spectral resolution but lower SNR such that the values for DoFs will be lower and for the total AOD error higher. CarbonSat has lower spectral resolution but higher SNR than GOSAT, which should lead to a similar performance. All four instruments should not be substantially affected by the inclusion of an intensity offset in the retrieval. It can be expected that DoFs will be around 4 to 5 and AOD errors might exceed a value of 0.05, especially for GOSAT and CarbonSat.

We now study the performance of the four instruments described in Table 3.1 and Figure 3.2. Simulations are shown in Figures 3.4 and 3.5 for scenarios A and B as described in Table 3.2.

The LAOD error, shown in the top row of Figures 3.4 and 3.5, is typically between 0.02 and 0.04 between 200 and 800 mb for layers representing roughly 26 mb each with typically smallest errors for OCO-2 and largest errors for S-5 P. For scenario A, errors tend to increase significantly below 800 mb due to correlations between surface albedo and the aerosol residing near the surface.

However, instruments with low spectral resolution (S-5 P) tend to show a much weaker increase in error towards the surface, especially for large SZA, compared to higher resolution instruments. For the high resolution instrument, the aerosol weighting functions will change their shape between low and high altitude due to saturation effects near the line centres for low altitude which is not the case for the lower resolution instrument with an example shown in Figure 3.6. In this figure the weighting functions have had a delta value applied to convert them to radiance space,

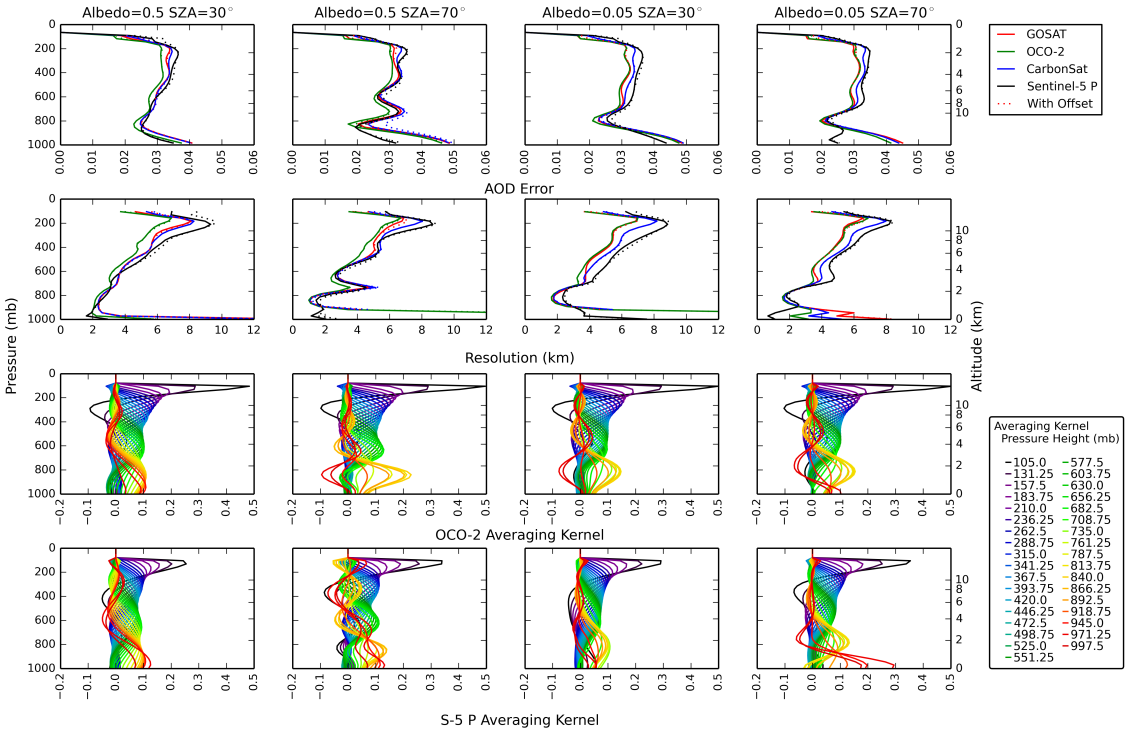

Figure 3.4: Error of LAOD (top panel) and vertical resolution (middle panel) as a function of pressure for the aerosol profile retrieval for scenario A for surface albedos of 0.05 and 0.5 and SZAs of 30°and 70°for the four instruments without an intensity offset. The results for a retrieval with intensity offset is shown by the dotted lines. The bottom two rows of panels show the averaging kernels for OCO-2 and S-5 P for the profile retrieval with intensity offset. Note that the top four pressure levels are not shown.

so as to allow direct comparison between the noise and the resulting intensities.

For scenario B, such a clear increase in error with decreasing altitude is not observed as the bulk of the aerosol in this simulation is in the free troposphere, resulting in less saturation of the Jacobians and weaker correlations to the surface albedo.

The impact of including an intensity offset is fairly minor. A slight increase in errors can be observed, which is most pronounced for CarbonSat and S-5 P using scenario A.

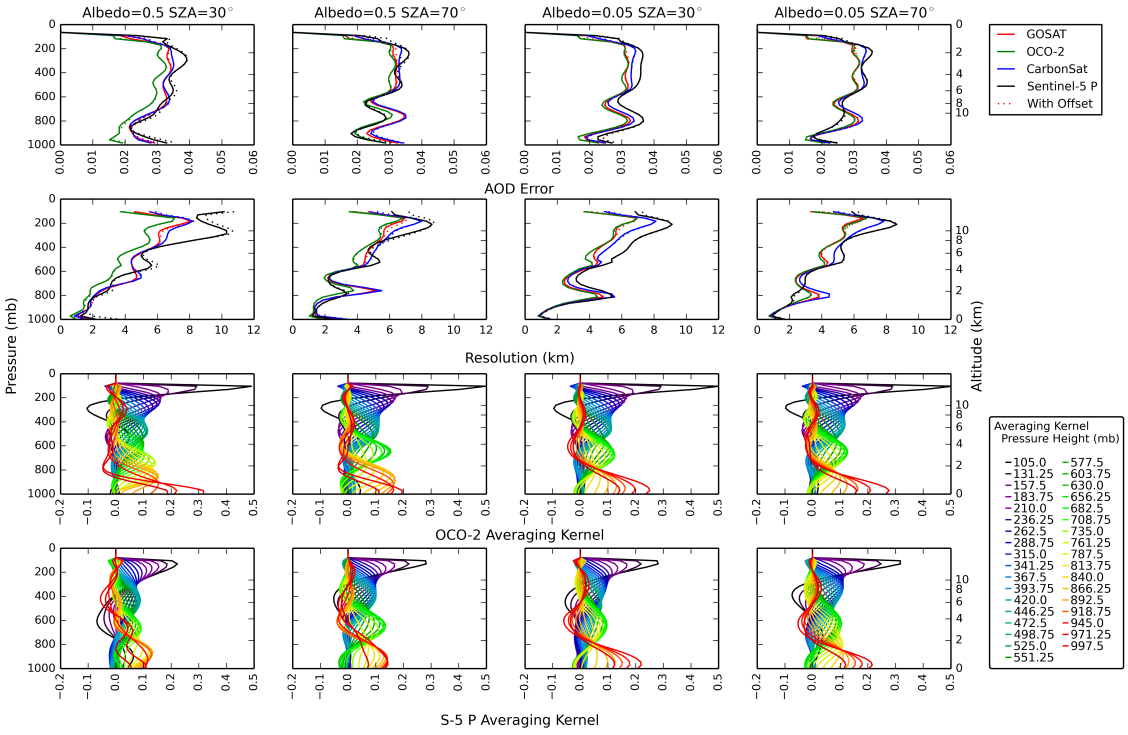

Figure 3.5: As Figure 3.4 but for scenario B.

The middle panels of Figures 3.4 and 3.5 show the vertical resolution of the aerosol profile retrieval as a function of altitude, where we define the resolution by the reciprocal of the trace of the averaging kernels multiplied by the pressure grid and converted into kilometres as in Purser and Huang (1993), the impact of varying the aerosol height upon the vertical resolution is shown by comparing the two and is discussed in further detail later.

On average the resolution is 4.5 km with the resolution becoming substantially poorer for high altitude. For scenario A, the vertical resolution increases from 2 km at 800 mb to 6-10 km at 200 mb pressure for all four instruments. For S-5 P the resolution remains similar near the surface, while for the other instruments the resolution decays rapidly at low altitude. For scenario B, the best resolution is observed near the surface with values approaching 1 km for all instruments and the

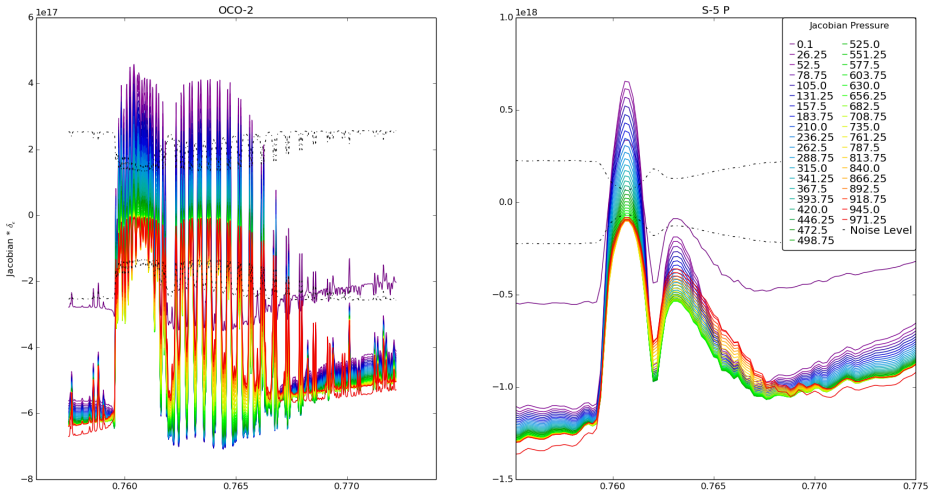

Figure 3.6: Aerosol weighting function multiplied $\delta = 1\text{x}10^{-5}$ for scenario A, SZA 30° for OCO-2 and S-5 P with the measurement noise (positive and negative) also shown

average resolution improves to 4 km.

Similar to the LAOD errors, OCO-2 has typically the highest vertical resolution in the free troposphere. S-5 P typically outperforms all other instruments near the surface but often shows the worst vertical resolution near the free and upper troposphere.

The averaging kernels for the aerosol profile retrieval for OCO-2 and S-5 P are given in the bottom panels of both figures. As expected, the averaging kernels are relatively broad which reflects the limited vertical resolution. Between 200 and 600 mb, the peak roughly corresponds to the associated pressure height while below and above we often find that averaging kernels overlap. Overall, the averaging kernels suggest that it may be possible to resolve 3-4 layers within the atmosphere. The also further demonstrate the increase in sensitivity nearer to the surface for S-5 P, particularly at higher SZA. As the effect of an intensity offset is small in both scenario A and B, all further retrieval simulations include intensity offset in the retrieval as

it will provide a more realistic assessment of aerosol retrievals over vegetated land.

For a more quantitative comparison, we have integrated the LAOD profile over the height range between 0 and 2 km(∼1000-750 mb) to represent roughly the range of the boundary layer, over 2 to 5 km (∼750-500 mb) to represent the lower free troposphere and over the full atmosphere to obtain total AOD. The AOD errors and DoFs for the three height ranges are given in Figures 3.7 and 3.8 for the scenarios A and B, respectively. Scenarios labelled A+B, A+C or B+C include two aerosol layers and they will be discussed in Section 4.2.

For scenario A (Figure 3.7), we find that AOD errors for the 0-2 km range are consistently lowest for S-5 P with errors between 0.09 and 0.21. The superior retrieval performance of S-5 P is most pronounced for large SZAs, whereas for lower SZAs the errors for the four instruments become more similar, with errors for OCO-2 approaching those obtained for S-5 P. DoFs range from 0.62 (CarbonSat for SZA of 30°and albedo of 0.05) to 1.35 (S-5 P for SZA of 70°and albedo of 0.5) but are mostly slightly less than one which means that AOD for this height range cannot be independently retrieved.

For the 2-5 km range, we find a different picture with lowest errors and largest DoFs for OCO-2, with errors between 0.11 and 0.13 and DoFs close to 1. For S-5 P, errors are particularly large for the low albedo cases. As expected, we find that results for CarbonSat and GOSAT are similar to each other. For total AOD, the retrievals for the four instruments compare in a similar manner as for the 0-2 km range, with errors ranging from 0.06 up to 0.29. This represents a significant reduction in error compared to the a priori uncertainty of 1 for all cases. Note that the errors for total AOD are often smaller than the errors for the 0-2 km or 2-5 km height range owing to the presence of negative correlations between layers. The DoFs for the full range is between 3.3 to 4.7, with the highest values for OCO-2 and

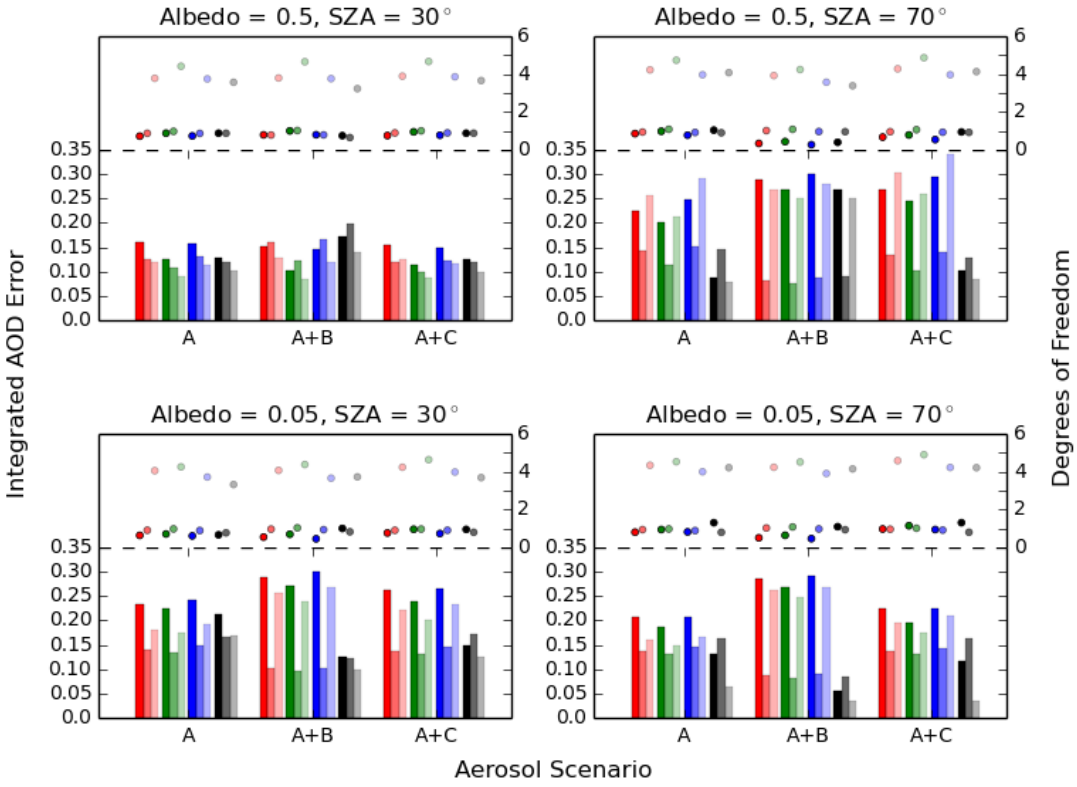

Figure 3.7: AOD error and DoF for the aerosol profile retrieval for surface albedos of 0.05 and 0.5 and SZAs of 30°and 70°for the four instruments. Errors are integrated over the 0-2 km and 2-5 km ranges as well as the total column (which are described by differing shades of the instrument colour) for aerosol scenario A and combined aerosol scenarios A+B and A+C. Intensity offset is included.

the lowest values for S-5 P and CarbonSat.

As has been discussed above, the retrieval of aerosol vertical information depends on the surface albedo. At low albedo, aerosols act to shorten the path length and at high albedo they will lead to a lengthening of the path length. Therefore, at a specific albedo, aerosols will have no impact on the path length. We find that aerosol weighting functions are becoming small for a surface albedo of 0.2 with largest retrieval errors but, due to the modulation of this surface effect with the O_2 absorption, the weighting functions still differ from zero. This effect is illustrated in Figure 3.9 where the Jacobians at 918 mb are shown for OCO-2 and S-5P for

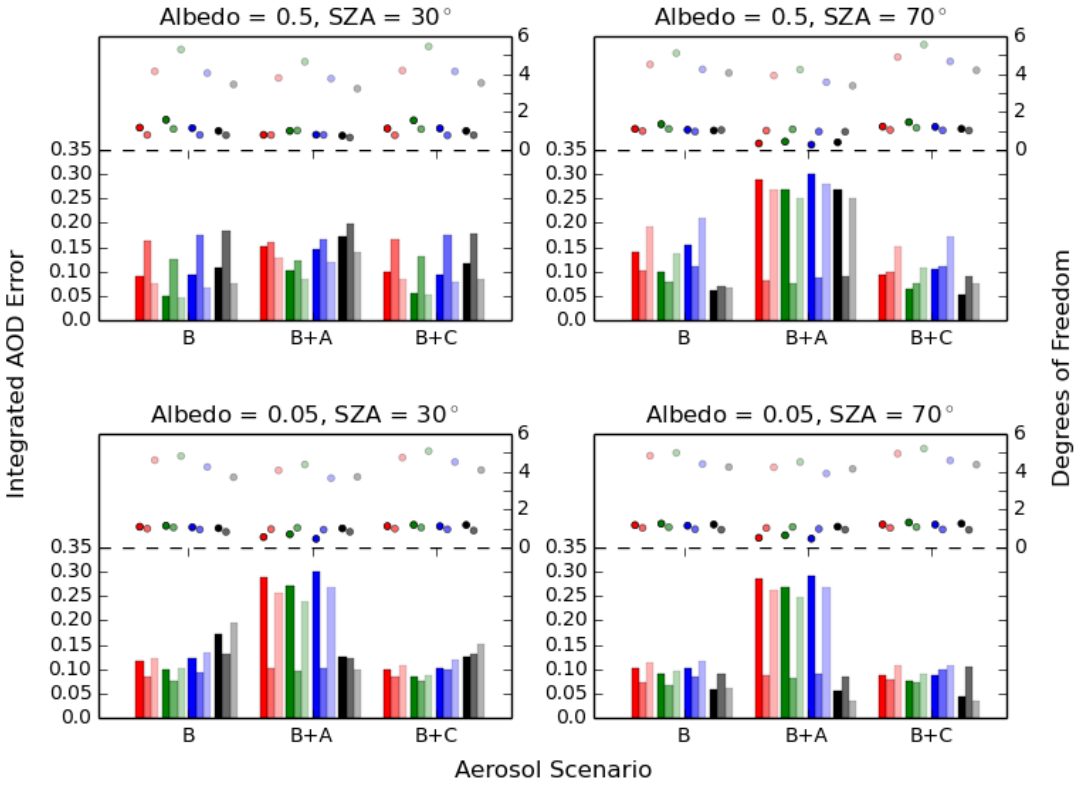

Figure 3.8: As Figure 3.7 but for the aerosol scenario B and combined aerosol scenarios B+A and B+C. Note that scenario B+A is identical to A+B from Figure 3.7.

scenario A as a function of albedo.

As a result the retrieval errors will increase as the weighting functions become smaller as is evidenced in Figure 3.10 which also shows the corresponding errors and DoFs for the SZA 70°. This figure also highlights the point previously made that higher albedos are not studied because the effects of them compared to 0.5 are relatively minor, especially at low SZA.

For scenario B (Figure 3.8), the AOD error for the 0-2 km and the 2-5 km range tend to be much smaller for all instruments compared to scenario A, with the exception of the case of high albedo and low SZA. The retrieval performance for S-5 P varies largely with SZA, with lowest errors of around 0.05 for SZA of 70°and

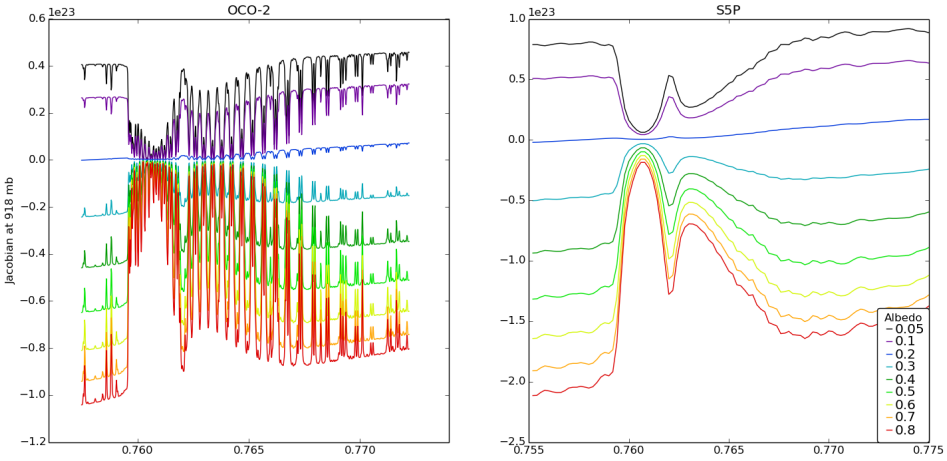

Figure 3.9: Aerosol weighting function (at 918 hPa) for OCO-2 (left) and S5-P (right) for surface albedos between 0.05 and 0.8 and a SZA of 30° and scenario A.

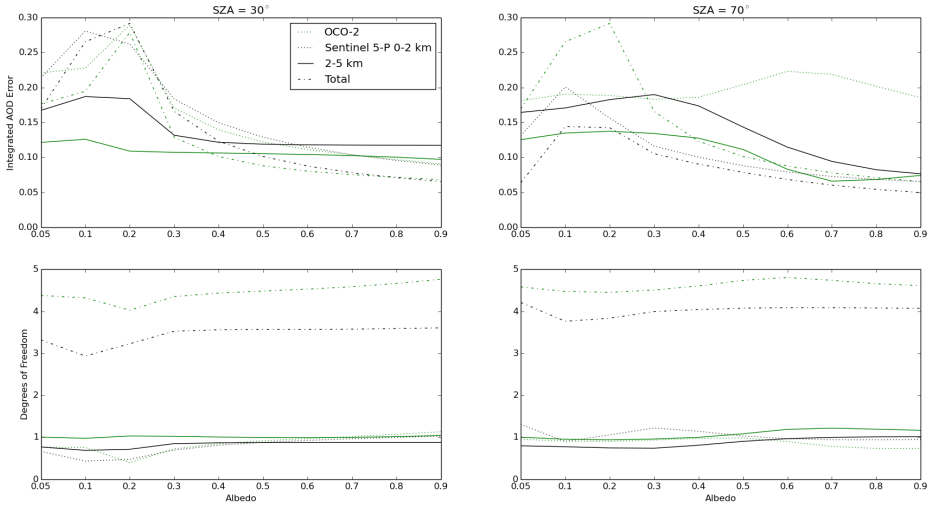

Figure 3.10: Integrated AOD errors for scenario A using OCO-2 and S-5 P as a function of SZA and surface albedo.

highest errors with values between 0.1 and 0.18 for SZA of 30°. For the low SZA case, OCO-2 gives smallest AOD errors for the 2-5 km height range where the bulk of the aerosol resides in these simulations, with values ranging from 0.08 to 0.12.

To illustrate the effect of the height of the aerosol layer on the aerosol retrieval,

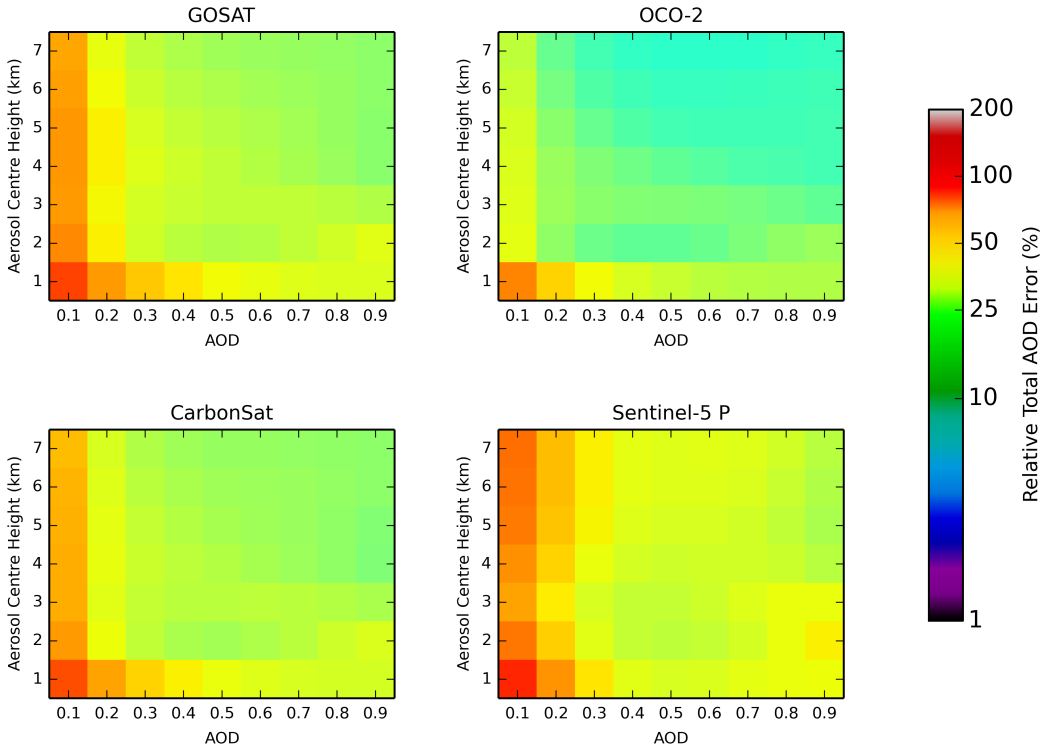

Figure 3.11: Total AOD error (given as a relative error) as a function of aerosol centre height and AOD for the four instruments for a SZA of 30°and albedo of 0.5. Intensity offset is included in the retrieval.

the error of the total AOD has been calculated as a function of centre layer height ranging from 1 to 7 km ($\sim$ 850-400 mb) and the total AOD ranging from 0.1 to 0.9 for the case of SZA of 30°and albedo of 0.5. As shown by Figure 3.11, a clear decrease in relative error with increasing total AOD and with increasing height can be observed. As the AOD increases to much higher values, the errors tend to then increase again. This is caused by two opposing effects: an increase in sensitivity of the aerosol retrieval with aerosol weighting functions showing larger values with increasing AOD and a decrease in SNR with increasing AOD due to the high surface albedo.

This figure further emphasises the difficulty in retrieving aerosol that is present

near the surface. Errors can be around 100 % for typical values of background AOD (∼0.1). OCO-2 tends to perform significantly better than the other three instruments with errors in the range of 20-25 % if the centre height is 2 km or higher. With increased layer height, the observed AOD error from GOSAT and CarbonSat are also smaller than those from S-5 P. Note that for a scenario with large SZAs, the performance of S-5 P would improve considerably compared to the case shown in Figure 3.11.

The AOD errors will be a composite of the error due to the measurement noise and the so-called smoothing error which reflects the errors introduced by the limited vertical resolution of the observations and the smoothing of the a priori constraint (Rodgers et al., 2000b). We have estimated the smoothing errors for the different instruments using the a priori covariance matrix to represent the atmospheric variability of an ensemble of scenes via;

$$\mathbf{S_{sm}} = (\mathbf{I} - \mathbf{A})\mathbf{S_a}(\mathbf{I} - \mathbf{A})^{\mathbf{T}}, \tag{3.1}$$

with $\mathbf{I}$ being the identity matrix and $\mathbf{S}_{sm}$ as the smoothing error, with the results shown in Figure 3.12 . This will certainly lead to an overestimation of true smoothing errors for most scenarios as the assumed uncertainty of the aerosol a priori covariance matrix is very large with a standard deviation of the total AOD of one (see section 3.1.2). For scenario A, the estimated smoothing errors are significant with values of about 35% to 55% of the total AOD error for GOSAT, OCO-2 and CarbonSat and 30% to 40% for S-5 P. The estimated smoothing errors significantly decrease for scenario B with values of 13% to 30% for GOSAT, OCO-2 and CarbonSat and larger values of 32% to 42% for S-5 P.

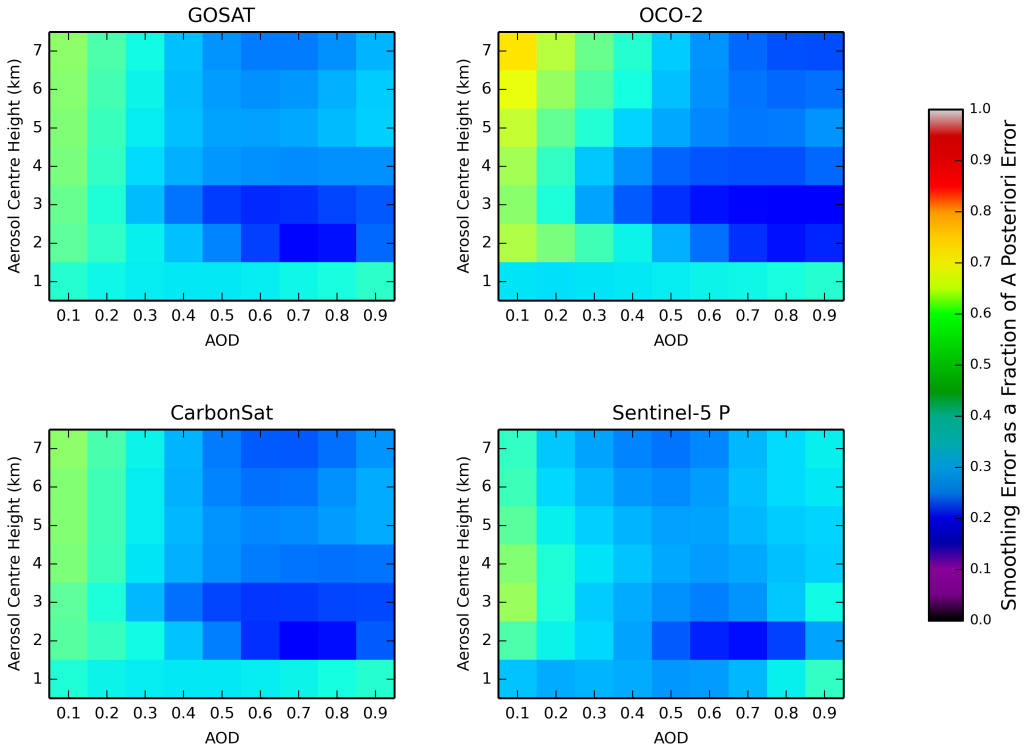

Figure 3.12: Smoothing error as a fraction of the retrieved error as a function of aerosol centre height and AOD for the four instruments for a SZA of 30°and albedo of 0.5. Intensity offset is included in the retrieval.

3.1.3.2 Double Aerosol Layer Scenarios

So far we have only included scenarios with a single aerosol layer in the atmosphere, but in reality multiple aerosol layers will often be present, such as an elevated dust layer present above boundary layer aerosol. Furthermore, a high altitude cirrus layer can be present above an aerosol layer, especially in the tropics. Here, we study the performance of the aerosol profile retrieval for the four instruments, for scenarios that combine an aerosol layer in the boundary layer (scenario A), an elevated layer in the free troposphere (scenario B) and a cirrus cloud layer (scenario C).

Figure 3.7 shows the AOD error for the 0-2 km and 2-5 km ranges, as well as the total AOD error for the combined scenarios A+B and A+C.

Compared to scenario A, the additional layer of scenario A+B leads to an increase in the AOD error of 0.05-0.1 for the 0-2 km range for GOSAT, OCO-2 and CarbonSat, except for the low SZA and high albedo case where little change is seen. A very significant increase in the AOD error for the 0-2 km range is also found for S-5 P for high albedo whereas the opposite behaviour is found for low albedo with a large decrease in the AOD error by ∼50 %, this an be simply described by the SNR decreasing and increasing in each case respectively, whereas for the other instruments, they are again hampered by Jacobian saturation.

The errors for the 2-5 km range are reduced for all instruments to values between 0.07-0.12 except for the low SZA and high albedo case.

Adding a high altitude cirrus cloud (scenario C) has less impact on the AOD retrieval than adding the free tropospheric aerosol layer (scenario B). For the scenario A+C, the error for the 0-2 km range increases by up to 0.05 for GOSAT, OCO-2 and CarbonSat. For S-5 P, we find that the AOD error for the 0-2 km range is slightly decreased for low albedo and is almost unchanged for high albedo, which might reflect a weaker sensitivity of S-5 P to the upper atmosphere.

Figure 3.8 demonstrates the impact of additional aerosol layers for scenario B, noting that scenario B+A is the same as scenario A+B shown in Figure 3.7. Comparing scenario B+A to scenario B we see that the additional aerosol layer has far less impact than in the previous case, where an additional aerosol layer was added to scenario A.

The most noticeable variations for the 2-5 km range occur for the high albedo cases where the error reductions, and in the case of S-5 P, error increases, are between 0.001 and 0.025. In contrast, the total AOD error varies substantially in comparison to the single aerosol for the scenario B+A case (0.05-0.2), producing a greater relative change than in the previous example. The addition of an extra

layer does not significantly effect the DoFs within the 2-5 km range, where values are consistently 1, though a drop is noticeable for the 0-2 km and total column.

For scenario B+C we see very little increase in errors for all instruments, and typically a minor reduction in 0-2 km range and total error particularly at high albedo and SZA whereas the 2-5 km range does not show the same degree of variability. S-5 P shows the greatest reduction of the four, particularly at low albedo and high SZA. The DoFs mirror this behaviour by only very slight fluctuations across all ranges, instruments and scenes. The impact of a cirrus layer is clearly weaker when the aerosol is higher in the atmosphere and thus more disentangled from the surface.

3.1.4 Constraining the Aerosol Retrieval

3.1.4.1 Parameter Retrieval

An alternative method for the aerosol retrieval is to retrieve a small number of parameters of an assumed profile shape instead of retrieving a full extinction profile. This means that we replace the soft constraint on the aerosol profile imposed by the a priori covariance matrix with a hard constraint given by an assumed profile shape. We assume a Gaussian function for the vertical distribution of aerosol optical depth that is defined by the total AOD, centre height and width so that the 39 parameters related to the aerosol extinction profile are replaced with two retrieved parameters only (note that width is effectively not retrieved). Accordingly, the retrieval precision for the two parameters will be higher compared to the 39 parameters of the full profile retrieval.

We have calculated the errors on the retrieved AOD and centre height for the four instruments for the same scenarios as before.

Comparing the AOD error of the parameter retrieval (Table 3.3) to the total AOD error from the profile retrieval (Figures 3.7 and 3.8), we find that errors are

much reduced in almost all cases for scenario B, whereas for scenario A, the errors are comparable for high albedo but much increased for scenarios with low albedo with errors up to 0.57. This is not surprising, as the extinction that is retrieved as a profile is collapsed into the total AOD which corresponds to a single parameter, whereas for the parameterised retrieval two parameters are obtained. Interestingly, the AOD error for the parameterised retrieval for the boundary layer scenario (scenario A) with low albedo even exceeds the AOD error for the 0-2 km range from the profile retrieval. Similar to the profile retrieval, for scenario A the AOD errors are smallest for S-5 P, except for low SZA and high albedo. AOD errors for scenario A tend to be large and only for S-5 P (for large SZA) and OCO-2 (for low SZA and high albedo) do errors approach a value of 0.05 or less. AOD errors for scenario B are well below 0.05 for GOSAT and OCO-2 as well as for CarbonSat except for low SZA and high albedo, where for S-5 P errors tend to be much higher.

The error for the centre height tends to be correlated with the AOD error and errors for the centre heights are typically small with values around a few hundred meters. For scenario A and low albedo, the errors can exceed 1 km with the largest errors being found for CarbonSat and GOSAT.

Figure 3.13 shows the AOD error for the four instruments as a function of aerosol centre height and AOD for a SZA of 30°and albedo of 0.5 similar to the profile retrieval in Figure 3.11. As discussed, the structure is caused by increasing information content and decreasing SNR with increasing AOD and with decreasing sensitivity to the 3-4 km when the aerosol is above or below this height.

For this high albedo case shown in the figure, we find that the AOD error from the parameterised retrieval yields significantly smaller errors compared to the profile retrieval, especially if the aerosol centre height is 2 km or higher. AOD errors for the parameterised retrieval remain small even for low AODs with errors less than

	AOD Error			
	GOSAT	OCO-2	CarbonSat	S-5 P
Scenario A				
Albedo = 0.5, SZA = 30°	0.082	0.029	0.084	0.117
Albedo = 0.5, SZA = 70°	0.266	0.150	0.258	0.057
Albedo = 0.05, SZA = 30°	0.502	0.426	0.571	0.275
Albedo = 0.05, SZA = 70°	0.375	0.288	0.369	0.053
Scenario B				
Albedo = 0.5, SZA = 30°	0.045	0.025	0.070	0.112
Albedo = 0.5, SZA = 70°	0.032	0.018	0.035	0.055
Albedo = 0.05, SZA = 30°	0.026	0.019	0.035	0.064
Albedo = 0.05, SZA = 70°	0.021	0.018	0.037	0.023

	Height Error (km)			
	GOSAT	OCO-2	CarbonSat	S-5 P
Scenario A				
Albedo = 0.5, SZA = 30°	0.265	0.095	0.259	0.371
Albedo = 0.5, SZA = 70°	0.651	0.367	0.671	0.157
Albedo = 0.05, SZA = 30°	1.442	1.225	1.649	0.838
Albedo = 0.05, SZA = 70°	1.005	0.774	0.987	0.175
Scenario B				
Albedo = 0.5, SZA = 30°	0.177	0.060	0.179	0.319
Albedo = 0.5, SZA = 70°	0.270	0.156	0.334	0.441
Albedo = 0.05, SZA = 30°	0.242	0.183	0.434	0.376
Albedo = 0.05, SZA = 70°	0.216	0.168	0.364	0.090

Table 3.3: Errors of retrieved AOD (top) and height (bottom) for the parameterized aerosol retrieval for aerosol scenarios A and B. Intensity offset is included.

10 % for OCO-2 for aerosols with centre heights above 1-2 km. In particular for S-5 P, the AOD errors in the parameterised and profile retrievals converge if the the aerosols are near the surface.

The parameterised retrieval assumes a certain shape of the aerosol profile and any deviations from the assumed profile shape can result in biases in the retrieved AOD and centre height. To assess this effect, we have simulated scenarios that include two aerosol layers or one aerosol layer and a cirrus cloud, and then retrieved

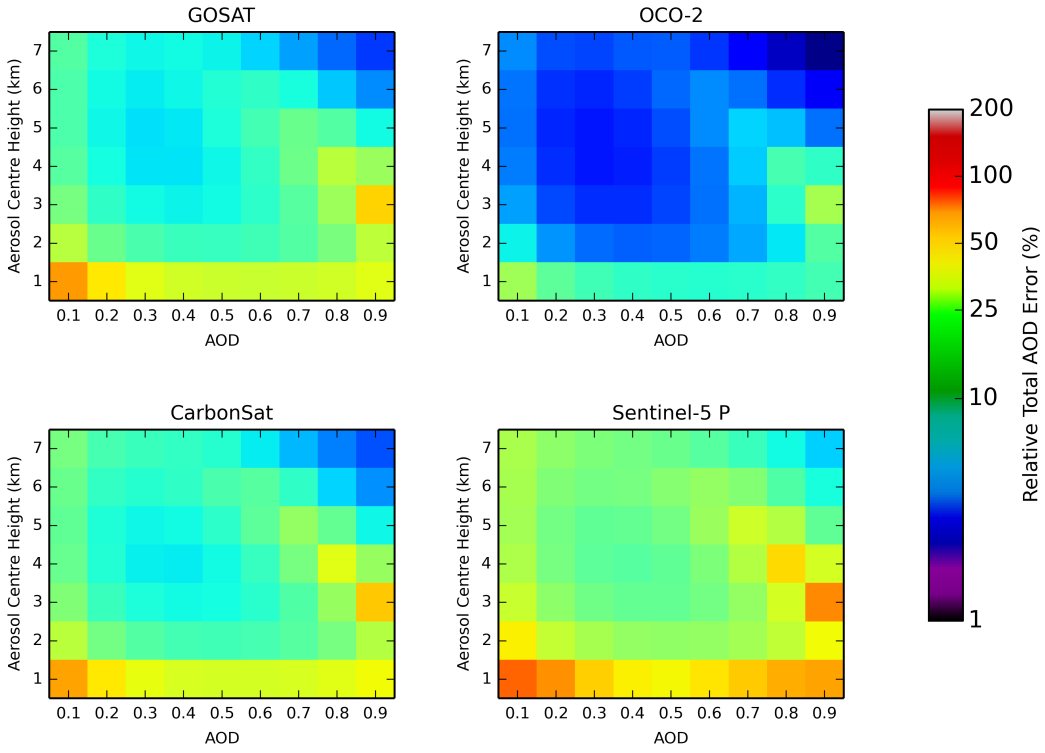

Figure 3.13: Relative AOD error as a function of aerosol centre height and AOD for the parameterised aerosol retrieval for a SZA of 30°and albedo of 0.5. Intensity offset is included.

them with the parameterised retrieval for a single aerosol layer using the full end to end retrieval. The a priori information for the retrieval has been taken from the lower aerosol layer of each simulated scenario.

Figure 3.14 shows the retrieved AODs and centre heights for simulated scenarios A+B, A+C and B+C.

The total AOD for Scenario A+B is 0.6 with layers at 1 and 3 km, which appears to be well reproduced by all instruments for the high albedo and low SZA case. The retrieved height is around 2 km representing the mean of the two aerosol layers in the simulation. For all other cases, OCO-2, GOSAT and CarbonSat appear mostly sensitive to the upper aerosol layer, and thus the total atmospheric AOD is

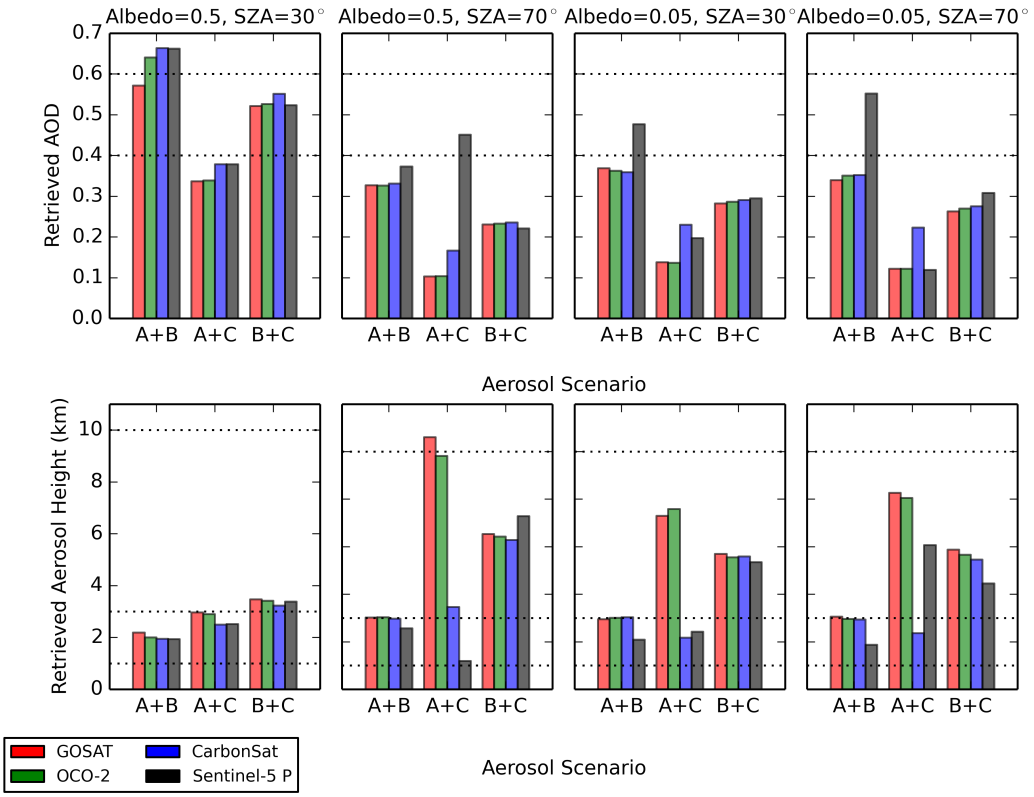

Figure 3.14: AOD and height errors for the parameterised aerosol retrievals for the combined aerosol scenarios A+B, A+C and B+C. In the top row the horizontal lines indicate the true AOD values for each case, i.e. the sum of both layers. In the bottom row they show the heights of each individual layer as a reference noting that the prior value for each scenario is the lowest layer height.

underestimated. S-5 P shows some sensitivity to the lower layer and retrieved AOD values are consistently larger and retrieved heights lower compared to the other three instruments.

For the scenario A+C that combines boundary layer aerosol with a cirrus cloud, we find that retrieved AOD and height vary substantially from case to case and for the different instruments. Again, for the high albedo and low SZA case, the retrieved AOD reproduces approximately the true AOD of 0.4 and the retrieved height represents roughly a weighted average value of the two layers in the simulation. For all other cases, a centre height and AOD resembling those of cirrus layer is observed

for instruments with high spectral resolution (OCO-2 and GOSAT), while for S-5 P and CarbonSat the retrieved height and AOD are more variable with sensitivity to both layers.

For scenario B+C, we find that results for all four instruments are very similar to each other with a tendency to overestimate the total AOD for high albedo and low SZA, and to underestimate AOD for all cases. The retrieved height tends to represent or somewhat overestimate the average height except for the high albedo and low SZA case, where the retrieved height is the height of the lower layer.

3.1.4.2 Albedo Constraints

For the aerosol retrieval, we have imposed only a very weak constraint on surface albedo with an a priori uncertainty of 1. As already discussed in the previous sections, the errors for the AOD retrieval are especially large when the aerosol is near the surface due to strong correlations between AOD near the surface and surface albedo. Imposing a much tighter constraint on surface albedo will help to reduce these correlations, which will then lead to an improved precision of the AOD retrieval.

To investigate the potential benefit of albedo constraints, a series of retrieval simulations with varying levels of albedo constraint have been carried out.

The inferred errors of the total AOD for scenario A are shown in Figure 3.15. As expected, we find that the error for the AOD retrieval decreases with increasing constraint on the surface albedo, but significant improvements in the errors are only obtained once the assumed albedo a priori uncertainty falls below a certain threshold. In the high albedo case for OCO-2, CarbonSat and GOSAT, this threshold is around 0.1 (or 20 %) for a SZA of 70°, though it reduces to 0.01 (or 2 %) for a SZA of 30°. Again, we find that S-5 P behaves differently and a stronger constraint on the surface albedo is needed for the high albedo cases. For the low albedo case, the threshold

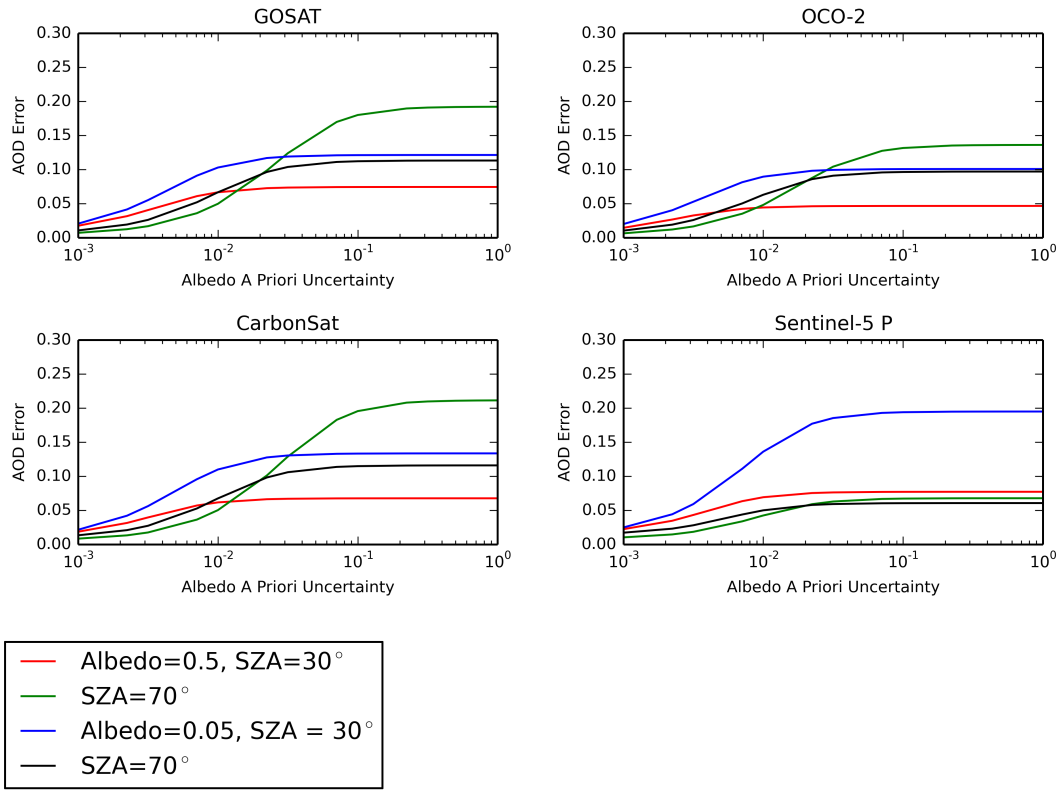

Figure 3.15: Total AOD error for the aerosol profile retrieval for scenario A for different albedo constraints given by the a priori uncertainty.

is between 0.01 and 0.03 (20 % to 60 %).

Overall, we find that constraining the surface albedo will help to reduce the errors of the AOD retrieval, but the required level of a priori knowledge on the surface albedo is very variable and can be very high for some scenarios.

3.1.5 Retrieval Assumptions

3.1.5.1 Surface Pressure and Temperature

In the retrieval simulations so far, we have assumed that the surface pressure is sufficiently well known and would not need to be retrieved. To assess the impact of a potential bias in surface pressure on the retrieved aerosol parameters, we have

simulated spectra for scenario A with a surface albedo of 0.5 and a SZA of 30°. The spectra have then been retrieved using the full end to end retrieval, with the parameterised aerosol retrieval as described in Section 3.1.2, but with a systematic bias in surface pressure of 2 mb noting that in this simple test, hydrostatic balance was not maintained. The resulting biases in AOD and height are shown in Table 3.5.

Overall, we find that instruments with higher spectral resolution couple with SNR are less sensitive to biases in surface pressure. A 2 mb bias in surface pressure results in a 0.1 (30 %) bias in retrieved AOD for S-5 P, CarbonSat and GOSAT and of 0.07 (23 %) for OCO-2. The bias in height is typically less. For a 2 mb surface pressure bias, a 200 m or more bias in retrieved height is obtained for S-5 P, CarbonSat and GOSAT, whilst a bias of only 70 m is obtained for OCO-2.

Temperature scaling is a retrieved parameter but the retrieval of aerosol is still subject to potential errors caused by a systematic difference in the atmospheric temperature profile. To assess this effect, a perturbation of 1 Kelvin has been added to the bottom kilometre of the assumed atmospheric profile before performing the retrieval. The inferred biases in AOD and height for the same scenario as above are given in Table 3.5. Overall, we find that biases are small and with the largest bias for S-5 P of 0.02 for AOD and of 74m for height. Similarly to surface pressure, we find that instruments with high resolution are far less affected and biases are an order of magnitude smaller compared to S-5 P.

3.1.5.2 Aerosol Mixture

All retrieval simulations so far have assumed that the aerosol mixture is known. Usually this is not the case and wrong assumptions on the aerosol mixture can result in systematic errors in the retrieved aerosol parameters. This is the case because we also retrieve the surface albedo and differing aerosol properties can have an effect

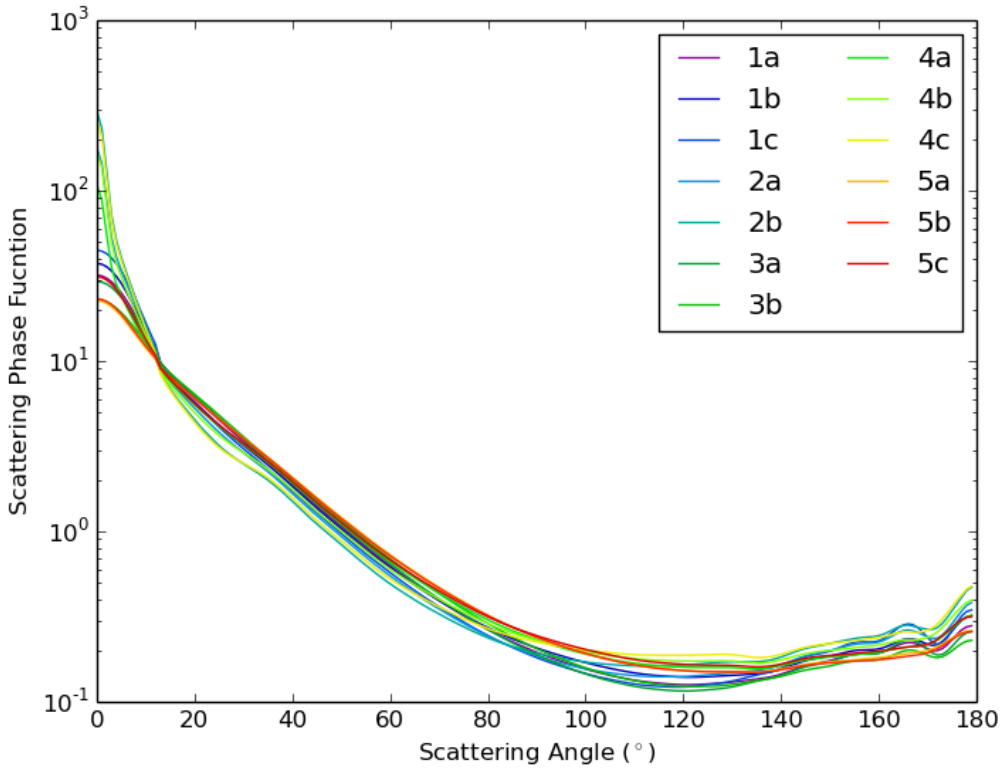

Figure 3.16: Phase functions of the 13 aerosol mixtures calculated at 770 nm.

upon the simultaneous retrieval due to their differing scattering and absorption properties. Again, we have simulated spectra for scenario A for a surface albedo of 0.5 and a SZA of 30°. We have used the full end to end retrieval to retrieve the simulated spectra generated using the dusty maritime and course dust mixture (mixture 2b) and carried out the retrieval for each of the other 12 aerosol mixtures from Kahn et al. (2001).

These 12 mixtures typically represent smaller particles with Ångström coefficients as high as 1.16 for the continental carbonaceous and black carbon mixture (mixture 5a). The single scattering albedos range from 0.856 for the carbonaceous and continental black carbon mixture (mixture 5b) to 0.978 for the carbonaceous and dusty maritime mixture (mixture 1a). These mixtures are summarised in Table

Mixture	Description	SSA	Ångström Coefficient
1a	Carbonaceous	0.980169	0.926372
1b	+ Dusty Maritime	0.955016	0.690861
1c		0.973486	0.571918
2a	Dusty Maritime	0.96626	0.532647
2b	+ Course Dust	0.941893	0.193452
3a	Carbonaceous	0.931148	0.954577
3b	+ Black Carbon Maritime	0.881402	1.004232
4a	Carbonaceous	0.955967	0.950471
4b	+ Dusty Continental	0.93908	0.573087
4c		0.927494	0.220487
5a	Carbonaceous	0.912448	1.188148
5b	+ Black Carbon Continental	0.856353	0.963949
5c		0.89961	0.908768

Table 3.4: Aerosol mixture properties calculated for the O_2 A-Band for all 13 types (Cogan et al., 2012).

3.4 and the corresponding phase functions are shown in Figure 3.16. The phase functions are particularly varied at low scattering angles where mixture types 3 and 4 exhibit a much greater forward scattering component than the other types.

The key results are shown in the bottom half of Table 3.5 and more generally in Figure 3.17. The biases observed for the AOD retrieval are all negative which means that the AOD has been underestimated. Largest biases of ∼45% are found for the instruments with high resolution for mixtures with largest Ångström coefficient reflecting smaller particles (carbonaceous and black carbon continental mixtures, mixtures 5a - 5c; carbonaceous and dusty continental, mixture 4a; carbonaceous and black carbon maritime, mixtures 4a - 4b; carbonaceous and dusty maritime, mixture 1a).

AOD biases found for OCO-2, GOSAT and CarbonSat are all very similar, while AOD biases for S-5 P are much smaller with the largest AOD biases of less than 30% but with the same trend with Ångström coefficient.

For the high resolution instruments OCO-2, GOSAT and CarbonSat we find an

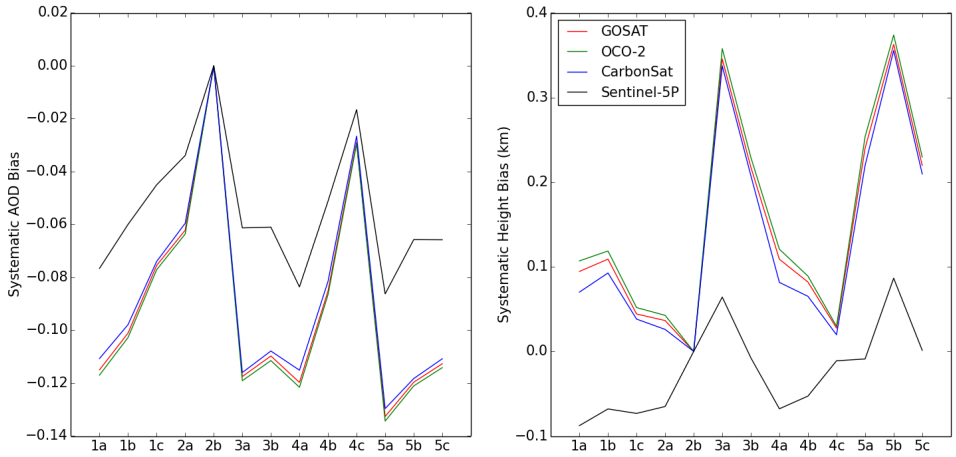

Figure 3.17: Bias in the retrieved AOD and height as a function of retrieved aerosol type with respect to the truth modelled with 2b (Retrieved - Truth).

overestimation of the aerosol layer height with a tendency for mixtures with small particles to result in larger biases. However, the trend with Ångström coefficient (or particles size) is much weaker compared to the AOD biases and we find the largest biases for aerosol mixtures with the lowest value of the scattering phase function for a scattering angle of 120° (carbonaceous and black carbon maritime, mixture 3a) or the lowest single scattering albedo (carbonaceous and black carbon continental, mixture 5b). Again the biases for height are significantly smaller for S-5 P compared to the instruments with high resolution with biases not exceeding 100m.

3.1.6 Summary and Conclusions

We have assessed the ability of space-based instruments to infer information on the aerosol vertical profile from the O_2 A-Band with a series of retrieval simulations for the existing GOSAT mission, the upcoming OCO-2 and S-5 P missions and the proposed CarbonSat mission. The aerosol profiles used, although largely non-physical, allow for a systematic approach to assessing the performance of the instruments and

Surface Pressure and Temperature	AOD and Height (km) Bias			
	GOSAT	OCO-2	CarbonSat	S-5 P
ΔP_{surf} = 2 mb				
AOD	-0.099	-0.069	-0.106	-0.106
Height	.195	0.070	.246	.270
ΔT_{0-1km} = 1 K°				
AOD	-0.002	-0.001	-0.002	-0.020
Height	0.003	0.002	0.005	0.074
Aerosol Mixture	GOSAT	OCO-2	CarbonSat	S-5 P
AOD				
Max Bias (5a)	-0.132	-0.134	-0.130	-0.086
Min (4c)	-0.029	-0.030	-0.027	-0.017)
Mean	-0.091	-0.092	-0.088	-0.054
Height				
Max Bias (5b)	0.363	0.374	0.356	0.087
Min (4c)	0.028	0.030	0.020	0.001
Mean	0.145	0.154	0.133	-0.022

Table 3.5: Relative systematic biases in retrieved AOD and height due to a surface pressure bias (ΔP_{surf}) of 2 mb, 0-1 km temperature bias (ΔT_{0-1km}) of 1 K and assumptions in aerosol mixture. The aerosol mixture is given in parenthesis using the nomenclature from Kahn et al. (2001). The reference aerosol mixture used in the simulations is mixture 2b.

represent cases for which the instruments are more likely to be able to measure, as low altitude aerosol that decays with altitude will, as has been shown, be a challenge.

From the aerosol profile retrieval simulations for a range of different instrument spectral resolutions and signal-to-noise ratios, we find that high instrument resolution does not necessarily lead to lower errors in the total AOD. In fact, for small AOD errors low resolution combined with high SNR can be preferable, in agreement with Hollstein and Fischer (2014). This low AOD error will, however, come at the expense of vertical information. This behaviour is confirmed by simulations for OCO-2 and S-5 P which represent these two differing regimes.

Retrieving boundary layer aerosols with sufficiently small errors of around 0.05-0.1 and vertical resolutions of 1-2 km appears difficult for any of the studied four instruments, with best results often obtained from S-5 P. The retrieval errors for aerosols in the free troposphere are sufficiently smaller, and higher spectral resolution instruments such as OCO-2 allow far better retrievals compared to lower resolution instruments. Though in all cases the surface albedo is a significant cause of low altitude AOD error through increasing correlations, the resolution of the instruments plays a substantial role through the saturation of Jacobians and thus weaker sensitivity to low altitude aerosols for higher resolutions.

One major difficulty is the separation of reflection from the surface and scattering by aerosols near the surface which results in the high retrieval errors for AOD in the boundary layer. Imposing a stricter a priori constraint on the surface albedo will help to improve the retrieval precision but we find that the required a priori uncertainty on surface albedo needs to be very low to have a significant impact on the aerosol retrieval and can be as small as 2 % for some scenarios which is not feasible. Still, making use of a priori knowledge of surface albedo can result in improvements of the aerosol retrieval, especially for low albedo and/or high SZA scenarios where the required level of uncertainty on surface albedo is higher.

Since the vertical resolution of the aerosol profile retrieval is low, a suitable (and more robust) alternative to the profile retrieval will be to retrieve only the height and optical depth of an aerosol layer with a pre-defined shape. Although this retrieval does not result in a more precise AOD retrieval if the aerosol is in the boundary layer (nor will it truly represent it), it allows very precise retrievals of AOD and height for elevated aerosol layers. Retrieving only a single aerosol layer if there are multiple layers or if the aerosol has a substantially different shape, will result in misleading and erroneous retrievals with the result strongly dependent on the

vertical sensitivity of the instrument. Retrieving simultaneously two aerosol layers or different shapes can help to mitigate this effect but this has not been further investigated in this study.

Typical assumptions for the aerosol retrieval from the O_2 A-Band are that surface pressure and aerosol mixture are known. Both assumptions can introduce very significant additional errors of up to 30-40 % in the aerosol retrieval. Surface pressure could be retrieved jointly with aerosols but this would increase the random retrieval error. Some mitigation of the errors from aerosol mixture should be possible by either using information from co-located dedicated aerosol sensors (e.g. A-train instrument for OCO-2) or by using aerosol models. The effect of low altitude temperature bias was also investigated, resulting in errors of less than 8 %, this could be further minimised through combination with meteorological data.

We find that the use of current or upcoming O_2 A Band satellite sensors to monitor boundary layer aerosols will be limited but, nevertheless, observations from these instruments could provide a powerful way of observing, and in the case of S-5 P or CarbonSat, of mapping uplifted plumes of aerosols e.g. from forest fires, dust storm or volcanic plumes.

For the analysis of 'real' space-based observations, imperfect knowledge of spectroscopy or uncertainties in the instrument calibration can lead to poorer results as presented in this study. The need for good calibration and improvements to the spectroscopy of the O_2 A-band is widely recognized (Long and Hodges, 2012) and efforts are under way to obtain improved spectroscopic data.

3.2 Aerosol Retrievals from GOSAT Spectra

This section describes early attempts at aerosol retrievals from GOSAT alone, as it is the only instrument that is in operation or for which there is an appreciable

time series. The retrieval will use many of the elements of the simulation in order to attempt to validate its performance and provide a real test of the algorithm. To do this, a validation site was chosen in order to provide aerosol validation data, and was Lamont (Oklahoma, USA). Lamont has regularly been used for GOSAT validation as it is one of the sites that make up the Total Carbon Column Observing Network (TCCON), however it is also host to a part of the Atmospheric Radiation Measurement (ARM) programme. The ARM programme, ran by the US. Department of Energy, consists of a number of sites across the USA which operate a wide range of atmospheric instrumentation, including crucially a suite of radiometers and lidars for the measurement of aerosol. It is to the data provided by these instruments that comparisons will be made to assess the performance of GOSAT and the retrieval algorithm.

3.2.1 Retrieval Framework

The algorithm itself largely follows that described in Chapter 2 and Chapter 3. With the parametrised form being used but with the inclusion of a second high altitude cirrus layer rather than a single aerosol layer. The a priori for which are an AOD, height and width of 0.05, 2 km and 1 km for the aerosol layer and 0.01, 9.2 km and 1 km for the cloud layer, the a priori errors fo which are 100% for both AODs and 5 km for the height. Such a low value for cloud optical depth (COD) was chosen so as to avoid biasing the retrieval when no cloud is present. The albedo was fixed at 0.275 with an error of 0.1. The co-location criteria for the GOSAT soundings and ARM measurements were within $\pm$ 5° and ARM data only at 1pm was taken, in order to coincide with GOSAT overpass times.

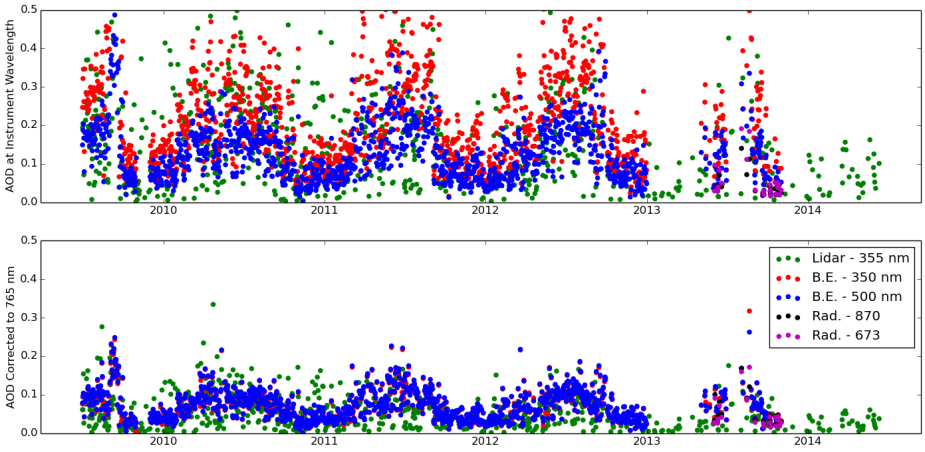

Figure 3.18: Raw and wavelength corrected (to 765nm) ARM data

3.2.2 ARM Measurements

The ARM measurements used consist of three instruments; four radiometers (at 350, 500, 673 and 870 nm) and a Raman LIDAR (355 nm). All five instruments produce a quality flagged AOD product which is shown in Figure 3.18 which consists of two Best Estimate (BE) data sets taken from the two low wavelength radiometers, two small direct data sets from the higher two and the LIDAR data. The Best Estimate sets contain almost exclusively radiometer data but will use the LIDAR data amongst others when unavailable, though to avoid confusion these cases are screened out. In the top panel of Figure 3.18 the raw data is displayed and as can be seen there are large differences between the datasets, this is caused by the measurements being at different wavelengths. The bottom panel corrects this by using the Ångström coefficent as measured by the radiometers, where now all AODs are calculated for a wavelength of 765 nm.

As can be seen there is strong seasonal cycle with peaks of 0.1-0.2 occuring during the summer months, with very low AOD during the winter. Unfortunately the more relevent datasets of 673 and 870 nm are confined only to a small section of 2013,

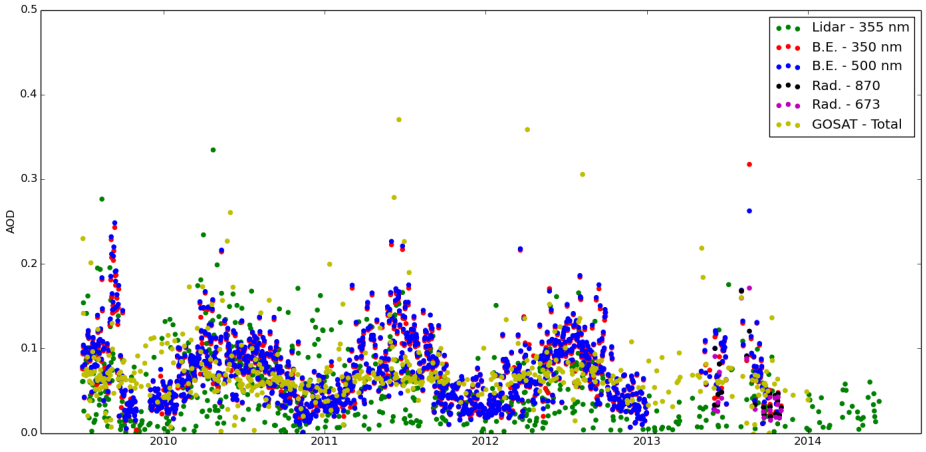

Figure 3.19: Corrected ARM data compared to the total optical depth retrieved from GOSAT

meaning that the lower wavelength data sets must be used for comparison. This is not ideal as using the Ångström coefiicient to convert AODs over such a large wavelength range is very ambitious, it should still provide a means of assessing the general capability of GOSAT by providing an approximate reference. By comparing back to the simulations studies, we know at low AOD retrievals of the AOD itself are problematic but hopefully the higher AODs of 0.1-0.2 will hopefully prove sufficient for GOSAT.

3.2.3 GOSAT Retrieval Comparisons

Figure 3.19 displays the first attempt of the retrieval of AOD from GOSAT compared to the ARM data sets where the two aerosol layers from GOSAT are combined to form a total AOD.

The seasonal cycle is largely reproduced but by and large, the variability of the AOD observed in the ARM measurements is not replicated in the GOSAT data. Indeed if we plot the datasets against each other (Figure 3.20) we can see that there is very little correlation between GOSAT and ARM, with Pearson's correlation

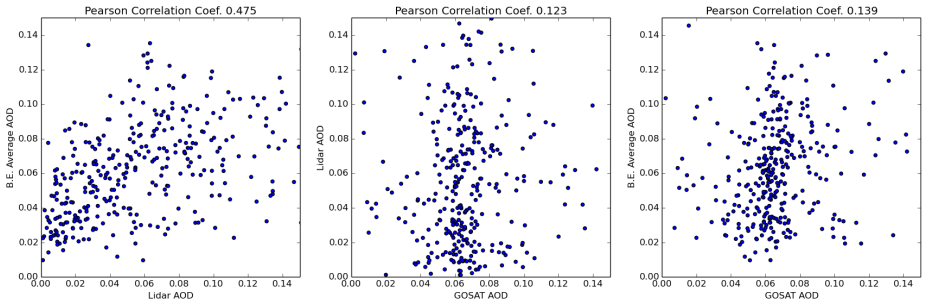

Figure 3.20: Correlation between the ARM datasets and GOSAT.

coefficients (PCC) of only 0.123 and 0.139 between GOSAT and the Lidar and best estimate data respectively. Also displayed is the correlation between these two ARM measurement, 0.475, surpassing this would therefore be ideal.

3.2.3.1 Correlations to Surface Albedo

One explanation for the low correlation between GOSAT and ARM is strong correlations between the optical depths and heights to the surface albedo, shown in Figure 3.21. The top row displays the correlation between the optical depth of both layers and the surface albedo. We can see that in the vast amount of cases, the aerosol optical depth is highly positively correlated to the surface albedo, with most of the variation in optical depth occurring here.

This is unsurprising as if the two are highly correlated, the optical depth will be highly sensitive to the measured albedo. Conversely at low correlation we see very little variation in the optical depth, suggesting that the a priori value of 0.05 isn't far from the truth, as can bee seen from Figure 3.19. The cirrus layer is far less correlated to the surface albedo and has high variability in its optical depth at low

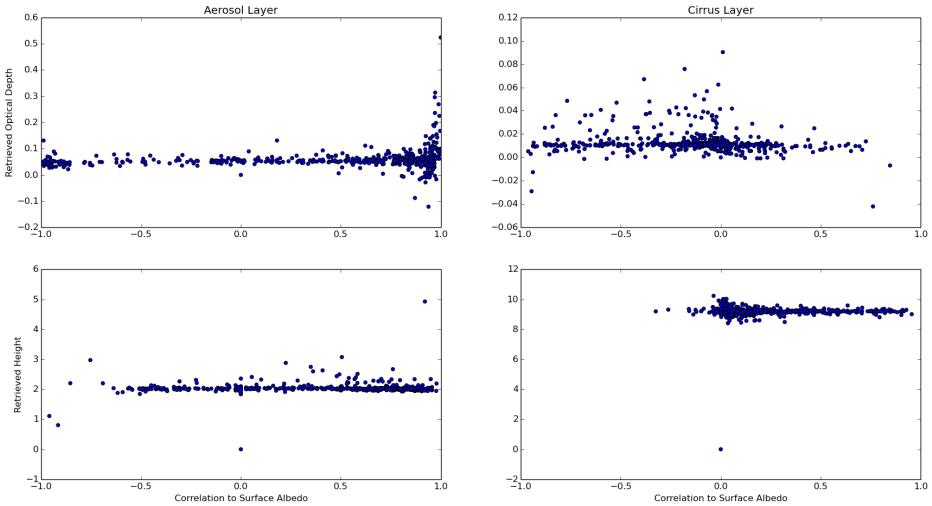

Figure 3.21: Correlation between the retrieved optical depths and heights to the surface albedo for GOSAT.

correlation, indicating that whilst the a priori isn't a bad one, cleary when there is cirrus present it is below the true amount. This makes sense as the a priori for the cirrus layer was deliberately chosen to be low so as not to add a bias into the total AOD when cirrus was not present and the layer was struggling to be retrieved. Retrieved height presents a similar picture with the cirrus layer far less correlated to the surface than the aerosol layer. With the exception that cirrus height is almost exclusively positively correlated whereas the optical depth was negatively so. The aerosol layer height though follows the pattern of its optical depth and is largely positively correlated. However the lack of variability across both layers would suggest that though there might not be as strong correlations, the error reduction in the height might be minimal, leading to the retrieved value sticking to the a priori assumption.

We know from the simulations that any aerosol near the surface will struggle to be retrieved due to the these strong correlations and so in real retrievals it often results in a bias in surface albedo and AOD. We can quantify the impact of an

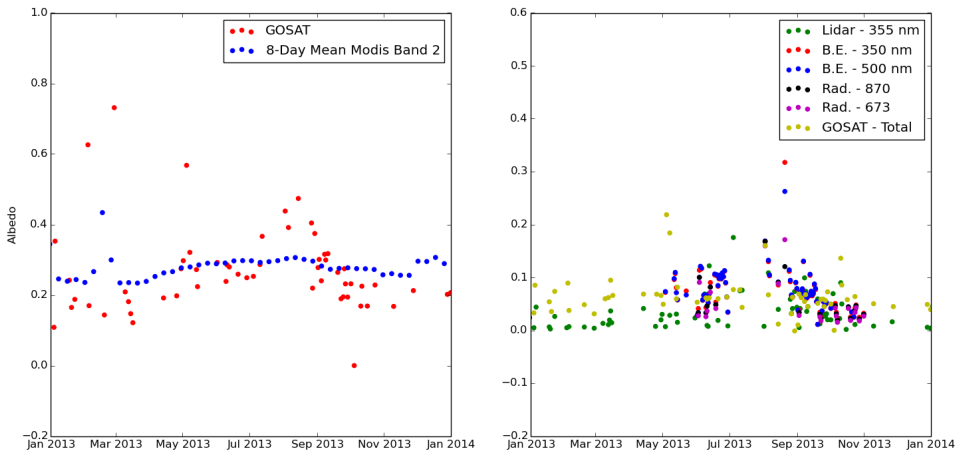

Figure 3.22: Left Panel; GOSAT retrieved surface albedo compared to the 8 day mean measured from band to of MODIS, Right Panel; Retrieved GOSAT total AOD and ARM data for 2013.

incorrect surface albedo on the retrieved AOD by performing similar simulations as those performed for temperature and surface pressure bias. In this case instead of retrieving the surface albedo, we assume it is known but retrieve the AOD with a small bias in the surface albedo. The results of this are shown in Table 3.6 where the SZA is 30° and AOD is 0.3 for GOSAT.

The results here clearly demonstrate that any error in the retrieved albedo with have a large impact upon the retrieved AOD. What is also apparent from the changing signs between true surface albedos is the differing role of aerosol in each case, with the aerosol darkening the scene in the case of the high albedo, and brightening for the low albedo case. This is the reason for retrieving the AOD and albedo simultaneously but also it demonstrates the challenge of this, particularly for low altitude aerosol. In a simultaneous retrieval the two competing effects will have to be balanced and its therefore clearly possible that erroneous value of both AOD and surface albedo could well be retrieved.

This is demonstrated in the retrieved surface albedo (left panel of Figure 3.22)

	AOD Bias	
	Scenario A	Scenario B
True Albedo = 0.5		
$\Delta_{albedo} = +0.01$	+0.091	+0.074
$\Delta_{albedo} = -0.01$	-0.084	-0.076
True Albedo = 0.05		
$\Delta_{albedo} = +0.01$	-0.212	-0.201
$\Delta_{albedo} = -0.01$	+0.203	+0.173

Table 3.6: Relative systematic biases in retrieved AOD due to a surface albedo bias (Δ_{albedo}) of 0.01 for scenarios A and B and with respect to a high and low surface albedo.

which varies substantially when compared to the albedo measured by MODIS in 2013, particularly in the latter part of the year. The albedo during the year shown also offers an explanation to part of the reason for such high correlations, the albedo is within the 0.2-0.3 range which we know from the simulations will cause substantial uncertainty. The right panel shows the retrieved total optical depth for the same period compared to the ARM data. We can crudely observe that when the albedo is roughly correct the GOSAT optical depth improves relative to the non similar albedo cases, notably in June and September, otherwise when there is an offset in albedo we see an offset in AOD. It could therefore be possible to either use the MODIS albedo as an a priori estimate with an appropriate constraint or as a means of filtering out poor retrievals. The MODIS albedo used here is taken from band 2 (841-876 nm) and therefore does not correspond exactly to the 765 nm used by GOSAT. The impact of this will be an over or under estimation of the surface albedo, the extent of which is determined by the surface type.

Figure 3.23 shows the albedo as a function of wavelength for a number of land classifications from the Advanced Spaceborne Thermal Emission and Reflection Radiometer (ASTER) and the Airborne Visible / Infrared Imaging Spectrometer

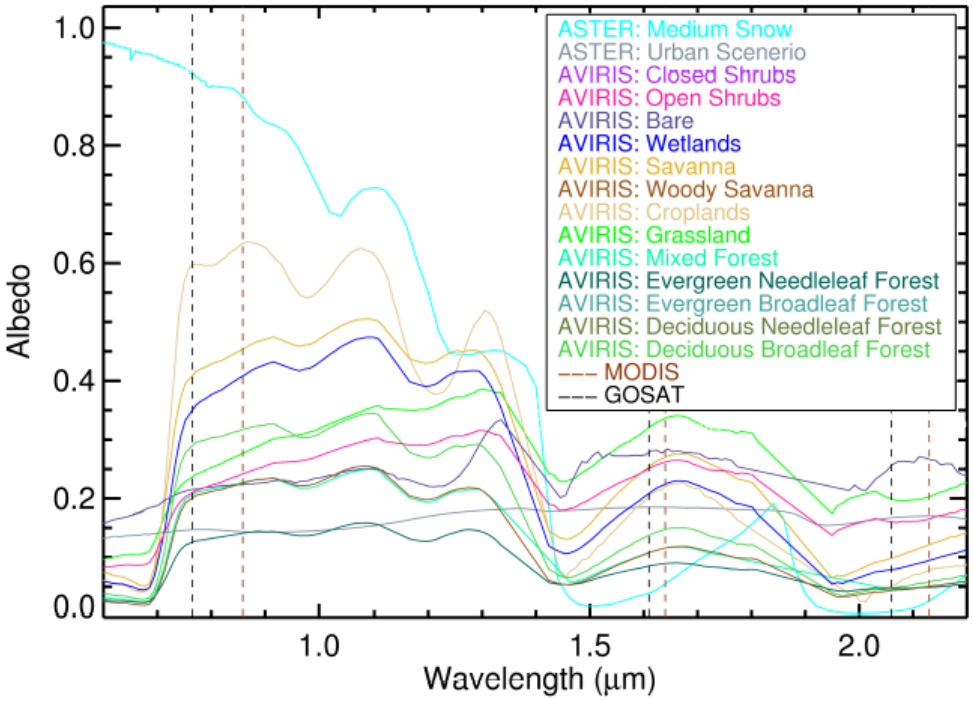

Figure 3.23: Spectral dendence of surface albedo for different land types from ASTER and AVIRIS with GOSAT and MODIS bands shown (Cogan, 2012).

(AVIRIS) along with the band centres of GOSAT and MODIS. This allows us to see the variation in albedo between the GOSAT and MODIS bands and assess the impact that might have. Typically we see that the differences are within 10% and are especially small for the forest classifications. In general the MODIS values are higher than those of GOSAT with the only case to the contrary being for medium snow. With such small variations between bands we can assume that the MODIS albedo will be a good approximation for the O_2 A-Band albedo as either an a priori estimate of filter.

However there is a large variation in albedo both temporaly and spatially as evidenced in Figure 3.24 where the MODIS band 2 albedo is displayed for the co-location area in January and July.

As can be seen, particularly in January there is a very high variation in albedo across the scene. Given the land classifications in Figure 3.23 we can identify snow

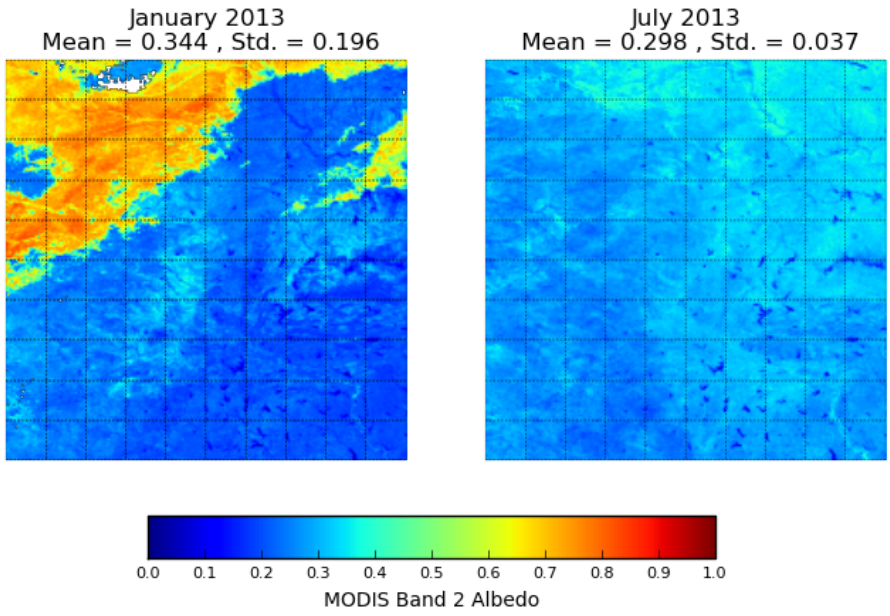

Figure 3.24: 8 day mean surface albedo for the first week of January and July 2013 from MODIS band 2. Data is shown over the co-location area of Lamont with lines indicating 1° increments

in the northern half of the January scene where as the rest of the scene is more consistent between months with values between 0.2 and 0.4. The previous retrievals used a fixed value for the surface albedo a priori, using MODIS data would provide a more realistic albedo however the high variability of the surface albedo means that a tight constraint on the albedo is not possible, nor would not retrieving the albedo. The result is that it would not be possible to counter the high correlations between surface albedo and AOD and improve the agreement between GOSAT and ARM. The other use for MODIS, as a filter could well be useful but the reduction in data as will be high as shown in Figure 3.22 which shows the monthly mean retrieved surface albedo and work would have to be done to ensure correct filtering within the

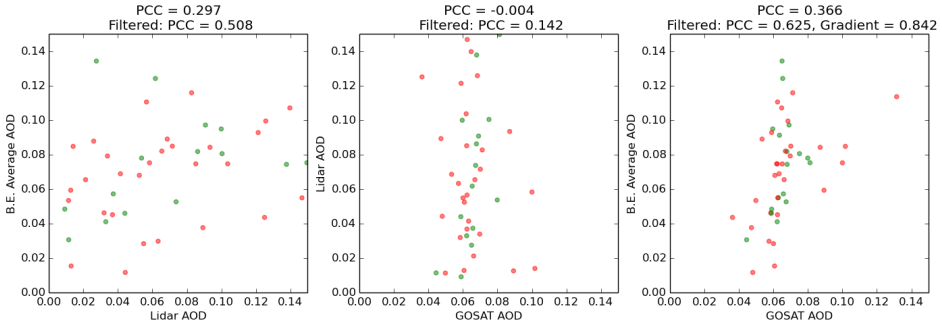

Figure 3.25: Correlation between the ARM datasets and GOSAT when data is filtered down to albedo correlations of less than 0.5

realms of the associated uncertainty in the MODIS data.

3.2.3.2 Improving the Data

An alternative means to improve the quality of the data set is to simply filter out all cases were strong correlation to the surface albedo is present. Ignoring the colour, Figure 3.25 shows the correlation between data sets when GOSATs two optical depths have been filtered down simultaneously to below 0.5. The results show a remarkable improvement in their PCCs (top number) if we compare to the previous correlation attempts (Figure 3.20) indeed they surpass the correlation between the LIDAR and the ARM best estimate average which is a promising result. Furthermore, if we exclude data that has not shown error reduction greater than 50%, we can further improve data quality.

The results of this additional filtering are indicated by the colour of the points in Figure 3.25 with the corresponding PCC and gradient (assuming an intercept at 0). Red denotes points at which the COD has failed to show enough error reduction with the AOD passing and vice versa for the blue points. Green points then show the cases where both have been successful. An even greater correlation between

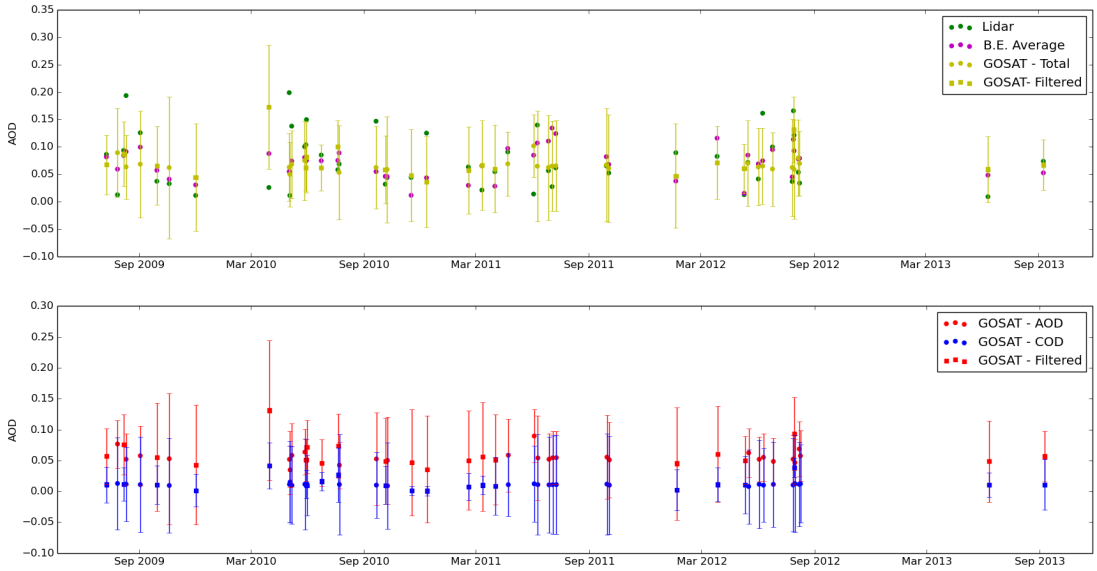

Figure 3.26: Filtered GOSAT and ARM data to AOD-albedo correlations of less than 0.5, total AOD (top panel) individual AODs (bottom), squares denote the error reduction in each layers optical depth is greater than 50%.

the data sets is observed for this filter with a PCC of 0.625 between GOSAT and the B.E. average, the gradient is also promising with a value of 0.842 with 1 being the ideal. This shows that when the conditions are right for GOSAT, an accurate retrieval is possible using the existing method. However this clearly substantially reduces the data points, in this case from above 400 before any filtering, to 20.

This is made clearer in Figures 3.26 3.27 which show the albedo correlation filtered (circles) and the additional error reduction filtering (squares) for the retrieved AOD and height over the 4 year period in Lamont.

Considering firstly Figure 3.26 we can see that although in real terms the retrieval performance has improved, the associated errors are still high, caused by strong correlations between the two retrieved optical depths. Averaging the data will reduce this but given the sparsity of the data it is unwise. The filters provide the most amount of data during the spring and early summer, due to the lessened variability

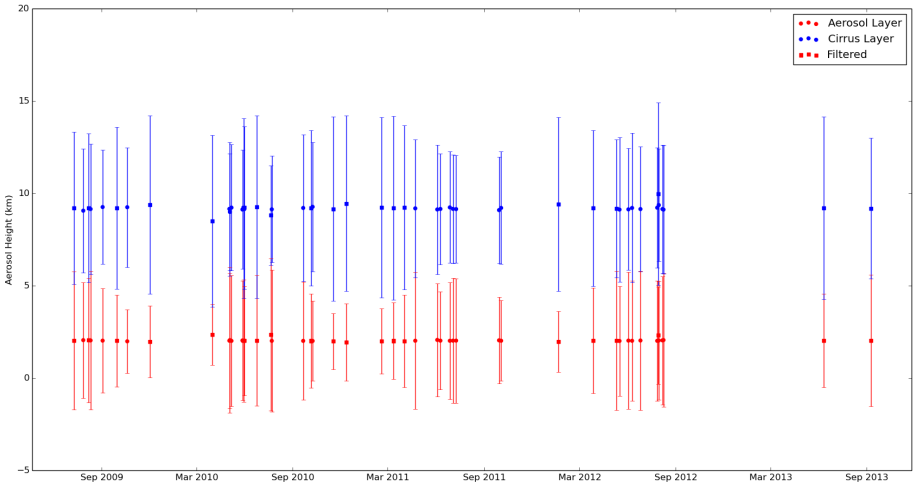

Figure 3.27: Filtered GOSAT data to AOD-albedo correlations of less than 0.5, retrieved height of the aerosol and cirrus layers, squares denote the error reduction in each layers optical depth is greater than 50%.

in the surface albedo during these months. The retrieved height in Figure 3.27 shows only a minor improvement in terms of variability and error reduction although the optical depth error reduction filtered data typically show a reduction in error for the aerosol layer atleast.

3.2.4 Summary and Conclusions

Early attempts at the retrieval of aerosol from GOSAT have proved challenging but are promising. Strong correlations to the surface albedo have consistently hampered the retrieval resulting in poor correlations between the retrieved AOD to the AOD measured by the ARM suite of instruments. These correlations are a result of low altitude aerosols and the albedo being in the region of 0.2-0.3, which was previously found to cause high uncertainty. Any small variation in albedo will result in retrieved albedo will result in a substantially different AOD as noted previously.

However when the cases with high AOD to albedo correlations have been removed

from the data set the GOSAT/ARM correlations improve drastically (excluding the LIDAR data), and further are improved by filtering out cases with poor error reduction.

Height was poorly retrieved with little or no variation and error reduction, however further validation with an instrument such as CALIPSO is needed to fully assess this. LIDAR profile information from the ARM site would have been ideal but was not available. This would have allowed a direct assessment of the scenes likelihood of being a case which GOSAT could retrieve an accurate aerosol profile from.

The filtering process however resulted in very few data points, and therefore this study needs to be expanded to a global scale in order to improve the statistics. At a global scale with more ideal albedos, such as over the ocean (low albedo), with uplifted aerosols (above the 0-2 km boundary layer), and with higher AODs, the performance of GOSAT should drastically improve. In addition data from other ARM or AERONET sites along with CALIPSO could be used to further validate the retrieval. This would help to identify any potential biases and provide a better assessment of the ARM/GOSAT comparison.

Lastly data from OCO-2 will soon be available and as we know OCO-2 should provide a much more accurate and precise means of retrieving aerosol in the O_2 A-Band, particularly at low altitudes.

Chapter 4

Spectrometer and FPE Theory

4.1 An Introduction to Spectrometer Design

There are three main spectrometer systems for measuring the atmospheric spectrum: these are grating spectrometers, Fourier Transform spectrometers (FTS) and lastly the Fabry-Pérot Etalon (FPE). These three instruments have a number of advantages and disadvantages over each other and will be briefly described here to make the argument for the use of a FPE for the measurement of aerosols within the O_2 A-Band.

Grating spectrometers such as those used by OCO-2, CarbonSat and Sentinel 5-P have significant advantages in SNR at high signal levels whilst in general delivering poorer spectral resolutions to that of GOSAT, an FTS. The reason for the limitation of the spectral resolution is the nature of dispersion harnessed by grating spectrometers (Hutley, 1982). Incoming light is incident on a grating surface, it is then diffracted according to the wavelength and grating spacing; the result is a series of interference orders corresponding to different path lengths. The radiation is then measured by a detector array (Charge-Coupled Device (CCD) or semi-conductor array. The resolving power R is dependent only on the order of the interference m

and the number of illuminated grating lines N;

$$R = \frac{\lambda}{\Delta\lambda} = mN \tag{4.1}$$

As the number of grating lines is constant (equally spaced lines with a finite sized grating), the resolving power is only increased by sampling higher orders of diffraction, which in turn corresponds to higher diffraction angles and thus a progressively larger instrument. This spatial limitation is the primary reason for lower spectral resolutions in grating spectrometers than in a FTS with the benefits of higher SNR coming from higher bandwidths and the the short comings of other techniques.

Fourier transform spectrometers are a contrasting technique that produces an interferogram as a result of the interference of two beams (Born and Wolf, 2002). This interferogram is then related to the radiance via a Fourier transform. Figure 4.1 shows an ideal FTS in which a beam of light passes through an absorbing medium before being split into two wave fronts. These waves are then reflected back on themselves by two mirrors and recombined and headed towards the detector. The difference in path length of each wave front, which is varied by the moveable mirror, results in an interferogram and a Fourier transform pair which can be solved for the spectral distribution. Fourier transform spectrometers are therefore multiplex instruments.

The multiplex (or Fellgett) effect (Fellgett, 1949) is the result of measuring different wavelengths simultaneously by the same detector and can be an advantage or disadvantage depending on the scenario. When a measurement is made using a multiplex instrument like a FTS, where the noise is primarily from the detector, an improvement is made in the SNR in proportion to the square root of the number of samples compared to the non-multiplex case of the grating spectrometer. It is important to note that where a CCD or linear array is used for a grating spectrom-

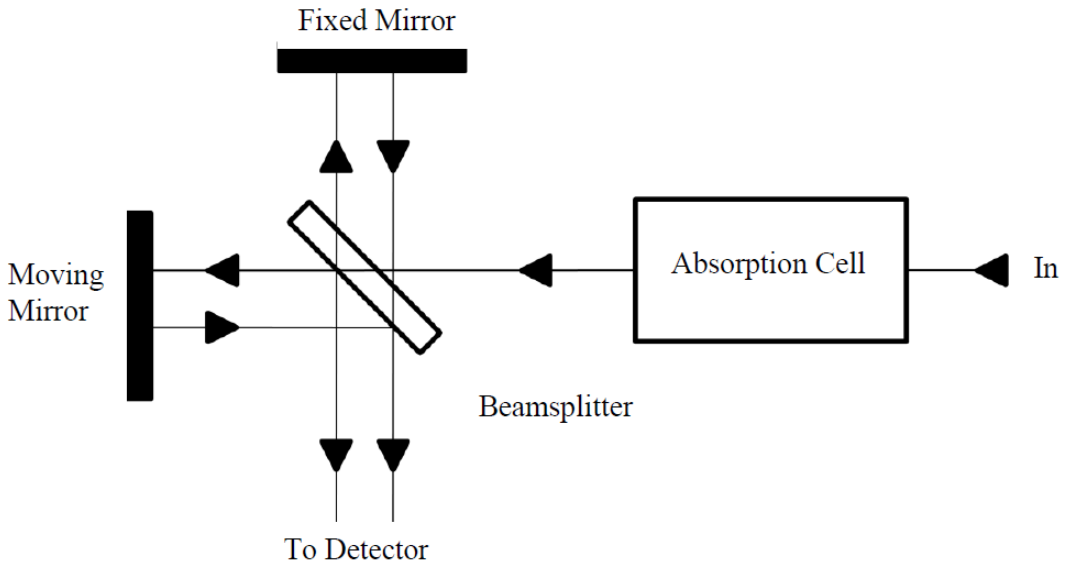

Figure 4.1: Idealised and simplified Fourier Transform Spectrometer design (Born and Wolf, 2002)

eter, the instrument in effect becomes a multiplex instrument through the shared noise of the detectors. The impact of this is that noise can be said to be spread out more evenly over the spectrum. If the signal of interest is a strong emission line for instance, this is ideal as the noise will be reduced at the peak intensity. However if the signal that is of most interest is an absorption line or weak signal, the noise will be increased relative to a grating spectrometer. In the case of a shot noise limited instrument, where the noise is dependent on the square root of the signal, the noise of a multiplex instrument will be proportional to the square root of the number of sampling points and thus offsets the previous advantage exactly. The Jacquinot advantage (White, 1989) is the effect of having a circular aperture as in an FTS or FPE instead of a slit aperture as is the case for a grating spectrometer. This advantage is simply that a circular aperture allows a higher throughput, or signal, than a slit would. A limitation of the FTS is the need for a moving mirror, which can be a

source of uncertainty, particularly when controlled by an electric motor which can decay over time. This is largely solved by the introduction of static optical components that produce analogous inteferograms, such as Wollaston prisms (Padgett and Harvey, 1995; Courtial et al., 1996), resulting in static FTS instruments, although the resolution of such instruments are highly size dependent due to the imaging of the interferogram.

Fabry-Pérot Etalon spectrometers are an alternative to both of these techniques and make use of some of the advantages and corresponding disadvantages of both of them. The core principle is similar to that of a FTS, an interferogram is produced by varying the path difference between successive beams of light (Hernández, 1988). The resulting reflected and transmitted beams are then recombined using a lens and the integrated signal focused on a detector as shown in Figure 4.2. The key difference compared to the FTS is that the interferogram consists of very high resolution peaks of radiation amongst almost zero transmission, meaning only certain wavelengths are multiplexed together. This reduces the advantages and disadvantages that come with a fully multiplexed instrument. The FPE can in addition be made to be very small and compact whilst still providing high resolutions and it can be designed not to include any moving parts and thus reduce uncertainty. However the performance of the etalon is susceptible to environmental effects such as temperature and pressure, as the path length is highly dependent on the refractive index of the spacing material. These limitations are discussed more fully in Section 4.3 when dealing with instrument design.

The argument for the use of a FPE over a grating or Fourier transform spectrometer, on a purely theoretical basis, is that the FPE can achieve very high spectral resolutions with high signal-to-noise ratios whilst not suffering from the multiplex disadvantage in the shot noise regime to the extent an FTS would. At the same

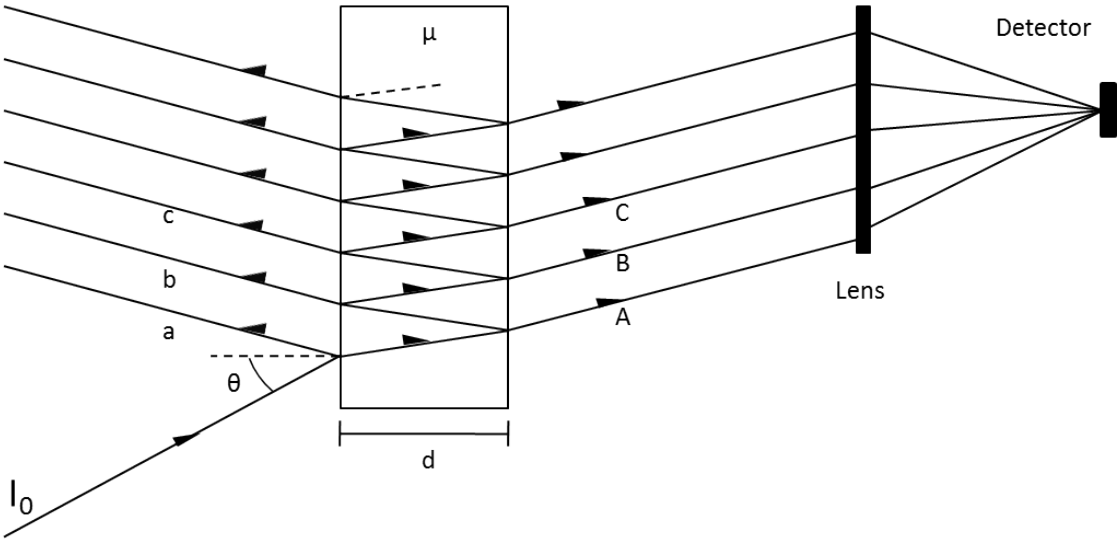

Figure 4.2: Idealised and simplified Fabry Pérot Etalon design (Hernández, 1988)

time a FPE can be designed to be substantially smaller and more robust than its counterparts, reducing uncertainty and unreliability. To test this more rigorously, and more specifically for the retrieval of aerosols, a mathematical framework will need to be developed and implemented for simulated spectra in the O_2 A-Band.

4.2 Mathematical Framework

4.2.1 The Ideal Fabry-Pérot Etalon

Returning to Figure 4.2 and considering two semi-transparent surfaces separated by a distance d by a medium of refractive index μ, this is known as the etalon. A beam of monochromatic light of intensity I_0 is then incident on the surface at an angle θ to the normal. The light is then reflected and transmitted successively down the length of the etalon. The transmitted lines are then gathered and superimposed by a lens to create an integrated interference signal. The phase difference, ϕ, between successive transmitted lines, such as A and B, is given by;

$$\phi = \frac{4\pi\mu d\cos\theta}{\lambda} \tag{4.2}$$

where λ is the wavelength of the incident radiation. The reflective surfaces can be defined by their complex reflection and transmission and amplitude coefficients r_i and t_i such that r_1 (t_1) is the case where a wave is travelling from the surrounding medium into the etalon and r_2 (t_2) represents a wave travelling from the etalon towards the medium. In this case, each successive transmitted amplitude for a unit incident amplitude ($I_0 = 1$) are;

$$t_1t_2,\ t_1t_2r_2^2e^{i\phi},\ t_1t_2r_2^4e^{2i\phi}\ , ... \tag{4.3}$$

As these beams are combined by the lens, the total transmitted amplitude is the sum of the individual amplitudes;

$$A_t(\phi) = t_1t_2 + t_1t_2r_2^2e^{i\phi} + ... = \tau(1 - Re^{i\phi})^{-1} \tag{4.4}$$

where we have defined that;

$$t_1t_2 = \tau,$$
$$r_1^2 = r_2^2 = R,$$

The transmitted intensity is calculated by multiplying the amplitude with its complex conjugate;

$$Y_t(\phi) = A_t(\phi)A_t^*(\phi) = \tau^2(1 + R^2 - 2R\cos\phi)^{-1} \tag{4.5}$$

Since τ can be expressed as a combination of absorption/scattering and reflectivity coefficients A and R via $R+\tau+A = 1$, the transmitted intensity can be shown to be;

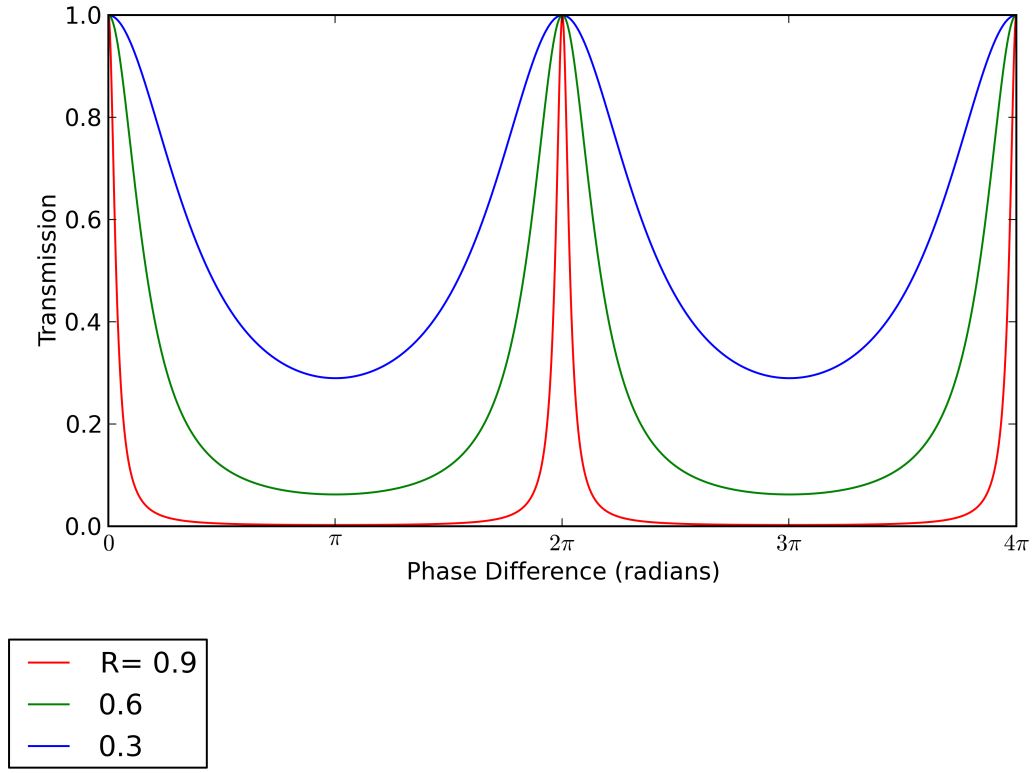

Figure 4.3: Transmission of an ideal FPE as function of phase difference and reflectivity with no absorption or scattering, i.e. A=0

$$Y_t(\phi) = (1 - A(1-R)^{-1})^2(1-R)^2(1 + R^2 - 2R\cos\phi)^{-1} \tag{4.6}$$

Figure 4.3 shows how the transmission varies as a function of the phase difference and reflectivity. In this case the absorption/scattering coefficient, A, is set to zero which is often the case as non-absorbing mediums are often used.

As can be seen, when the phase difference is an even multiple of π the transmission is maximal, whereas at odd multiples, it is minimal, which is purely an effect of the cosine term. The reflectivity, R, then determines not the position of the peaks, but their width in other words the resolution, with the lower the value of R the wider the peak. The peak height is in this case determined by the absorption/scattering

coefficient, A, that has been set to zero. If A is increased, the peak transmission would drop according to the first term in equation 4.6. We can quantify the impact of the reflectivity on line shape by deducing the FWHM of the transmission lines. This can be shown to be;

$$\text{FWHM} = 2\pi^{-1} \sin^{-1}((1-R)(2R^{1/2})^{-1}) \tag{4.7}$$

FWHM is given as a fraction of the 2π period, this period is known as the free spectral range or FSR, and is itself dependent on a number of factors. Taking the phase difference from equation 4.2, different orders, n, of peak transmission can be defined;

$$n = \frac{\phi}{2\pi} = 2\mu d\lambda^{-1} \cos\theta \tag{4.8}$$

The separation between orders is the FSR. This can be expressed as a variation in any one of the variables, however, it is often convenient to consider the FSR as the difference in wavelength or wavenumber, σ;

$$\Delta\lambda_{FSR} \approx \frac{\lambda^2}{2\mu d \cos\theta} \tag{4.9}$$

$$\Delta\sigma_{FSR} = \frac{1}{2\mu d \cos\theta} \tag{4.10}$$

The FSR is then dependent on the distance between the surfaces, d, the refractive index, μ and the angle of incidence, θ. In the case of wavelength, FSR itself is dependent on the wavelength which is an unnecessary complication, hence throughout the rest of this thesis, the wavenumber form will be used to remove this non-linearity. Figure 4.4 shows the transmission as a function of wavenumber and reflectivity with a FSR of 10 cm^{-1}, which corresponds to a spacing d of 0.5 mm with a refractive index of 1 and zero angle of incidence. Here we can see the transmission

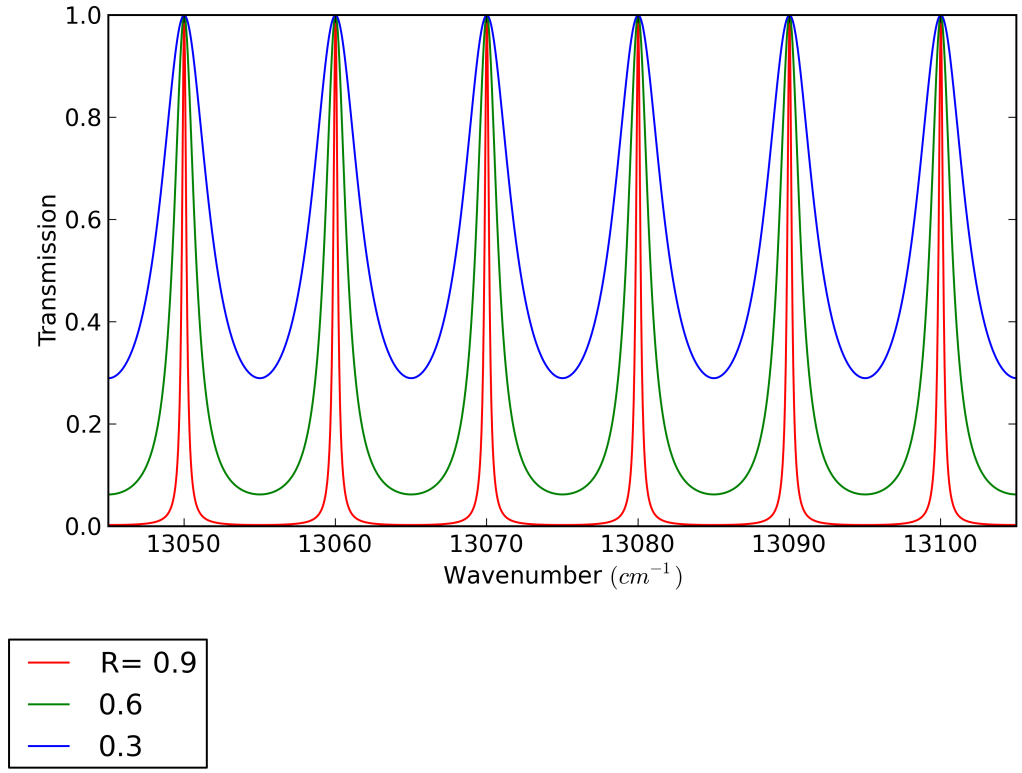

Figure 4.4: Transmission of an ideal FPE as function of wavenumber and reflectivity with no absorption or scattering, i.e. A=0 and a free spectral range of 10cm^{-1} (d = 0.5mm, $\mu = 1$, $\theta = 0$)

lines separated by the FSR of 10 cm^{-1}. It also helps to visualise one of the key ideas of the FPE, that multiple wavelengths are measured simultaneously with the values outside of the peaks substantially reduced.

However just having a fixed set of transmission lines isn't enough to produce a workable spectrum that is constrained enough to perform an accurate retrieval. In a conventional spectrometer, this would mean as many resolved spectral points as possible, whereas for an FPE of this type it would mean as many combinations of wavelengths. Therefore the lines need to be varied in some way to alter the combination of lines and create a scanned or pseudo spectrum, and the FSR thus

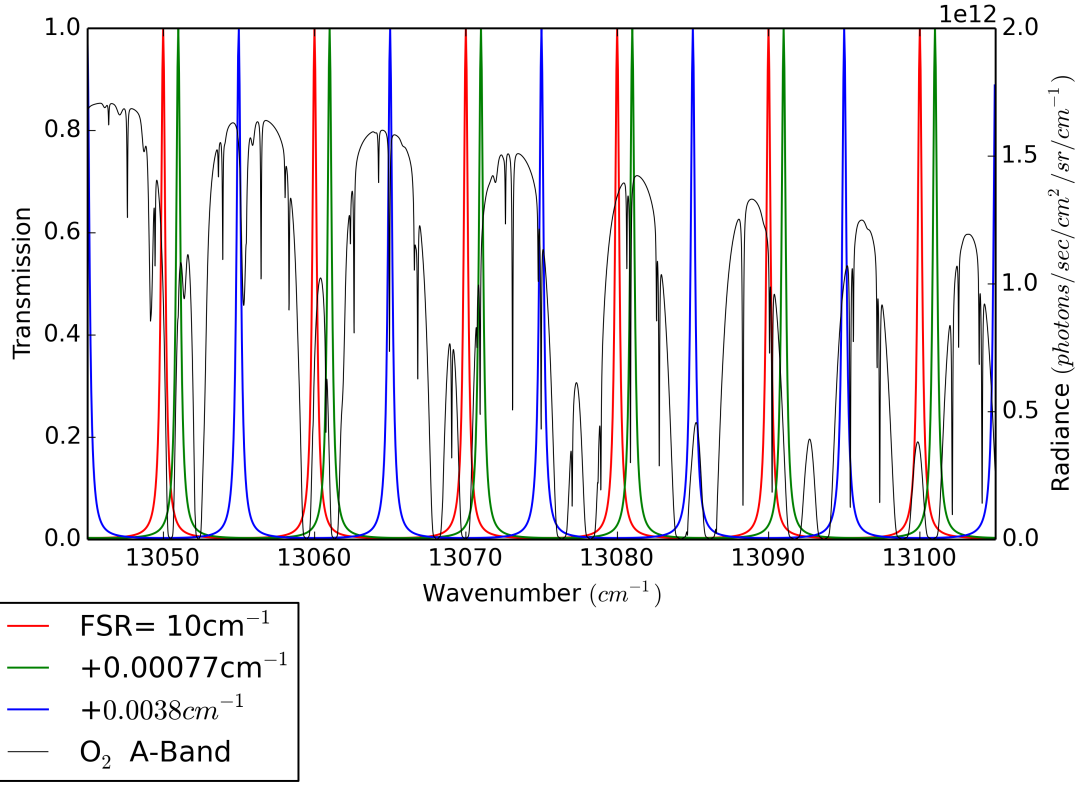

Figure 4.5: Transmission of an ideal FPE as function of wavenumber and FSR. Slight increases in FSR showing the scanning pattern, shift of 0.00077 corresponds to a shift in transmission centres of approximately one tenth of the initial FSR, and 0.0038 of half of the FSR. R=0.9, A=0. The black line and right hand axis show an example spectra of the O_2 A-Band from the forward model described earlier, SZA= 30°, albedo = 0.5, Scenario A.

needs to be controlled. If the FSR is increased by a small amount by varying one of its parameters, the transmission lines will shift slightly creating a similar transmission profile as previously but with a different set of peak wavenumbers, as seen in in Figure 4.5 along with a segment of the O_2 A-Band to illustrate the effect on the measured spectra

As a result, one can build up a pseudo-spectrum by increasing the FSR until it has shifted by one full FSR, one full order in terms of the initial wavenumbers. Once shifted by a full FSR the FSR will have increased, in this case by 7.6x10^{-3} cm^{-1}, which is well within the FWHM of the transmission lines, meaning that the

initial transmission and the full FSR shifted transmissions are almost identical. The result of this is that the number of unique combinations of transmission lines are dependent entirely on the resolution of the lines as given in equation 4.7. Taking the reciprocal of this and given R as 0.9, the number of resolvable lines (or number of combinations) that can fit into one FSR, analogous to the finesse, is approximately 30. This means that the pseudo-spectrum will comprise 30 integrated transmission spectra. Different combinations could of course be obtained if the FSR was increased by a substantial amount, though this is not always practical or desirable as the gain in information can be offset by integration time.

Figure 4.6 shows the convolved and integrated spectra observed by such a scanning FPE, where the scan involved covers three FSRs. Multiple FSRs are scanned to further emphasise the repeating nature of a FPE but also to demonstrate the subtle variations over several FSRs. This repeating structure can also be used to self-calibrate the FSR as will be discussed later. What is also evident is the high degree of structure observed, which not only relates to the maximum and minimum observable signals, but also the fine detail of the O_2 A-Band. When a large number of transmission lines correspond to the continuum of the spectrum, a maximum in the integrated signal will occur, conversely, when the majority of the lines match up with absorption lines, a minimum will occur. The additional structure comes from various combinations of absorption lines with continuum signals. However, in order to de-convolve the spectra and make use of it, in our case for aerosol retrievals, accurate knowledge of the transmission profile, or instrument line shape (ILS) is necessary.

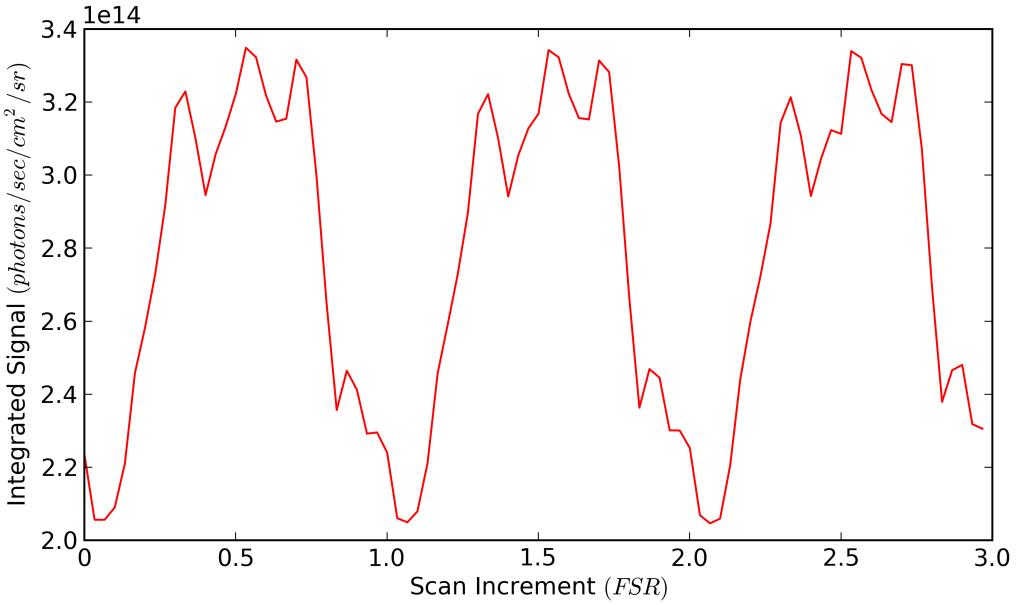

Figure 4.6: Integrated signal for a FPE scanned across three FSR of the section of the O_2 Band shown in Figure 4.5

4.2.2 Non-Ideal Fabry-Pérot Etalon

Thus far we have presented a mathematical treatment of an idealised FPE, however there are several factors that can alter the instrument line shape from the ideal. These alterations generally take the form of a reduction in peak transmission, a broadening of the transmission line and on occasion, a shift in peak position.

The first of which is the impact of non-collimated light incident on the FPE. Previously the light incident on the FPE has been considered to be collimated, meaning the FSR remains constant. However, with a range of angles this is not the case as a number of different FSRs are produced via the cosine term in equation 4.10. To visualise the effect of a divergent beam we can average the transmission over the incident angles for several fields of view, as shown in Figure 4.7

As can be seen the peak broadens and lowers with increasing field of view (FoV). There is also a strong bias to the right with increasing wavenumber in broadness and

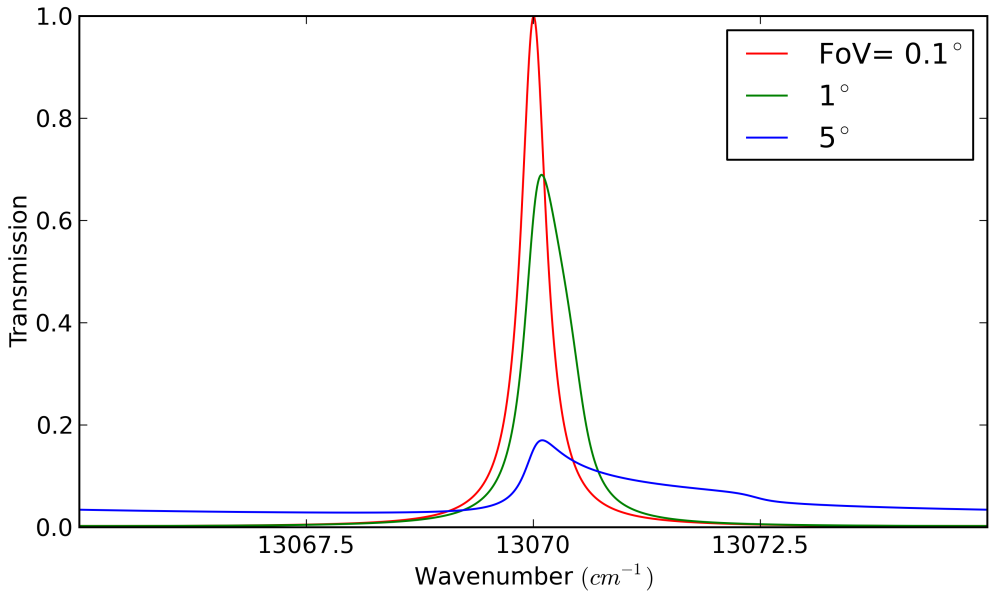

Figure 4.7: Transmission as a function of field of view (FoV) and wavenumber for a single transmission line. R = 0.9, A = 0, initial FSR = 10 cm^{-1}, FoV is centred about an angle of incidence of zero. Peak locations are 13070, 13070.09 and 13070.1 for red, green and blue respectively.

peak location, this comes from the symmetric nature of the cosine term about zero favouring a higher wavenumber transmission. If the divergence was centred about a non-zero angle of incidence, the effect is enhanced with the rapidly decreasing cosine function. We can readily conclude that the best performance is obtained with an angle of incidence of zero, and as small a range of divergence/FoV as possible, with 0.1°providing near ideal performance.

The field of view is easily controlled and adjusted, though other non-ideal effects are a result of spectrometer construction. The two main sources of error in this case are the two surfaces of the FPE not being parallel with each other, and irregularities in the coating. The first example is described by a tilt between surfaces which in simple terms changes the phase difference depending on the location upon the FPE ($\delta\phi_{tilt}$), non-flatness or curvature, $\delta\phi_{flat}$ is similarly defined, in polar co-ordinates

these are;

$$\delta\phi_{tilt} = 2\pi tr\cos(\beta) \tag{4.11}$$

$$\delta\phi_{flat} = 2\pi f(r^2 - 0.5) \tag{4.12}$$

where r is the normalised radius of the circular etalon, and t is the tilt parameter, usually defined in terms of a fraction of wavelength along with the flatness parameter, f. When a tilt is present, the phase difference will be largest at $\beta = 0°$which corresponds to the largest separation of the surfaces, zero phase difference is then at 90°and the largest decrease corresponding to the smallest separation occurring at 180°. This methodology ignores the slight variation in phase with each successive reflection compared to the parallel case, the effect of this is essentially a drift in the FSR as the light reflects its way through the FPE. Typically this phase drift is very small due to the finite size of the etalon limiting the number of reflections, low incident angles constraining the reflections and typical tilt angles being very minor. The initial difference in surface separation is then the dominant source of error in the case of etalon tilt. The effect of tilt is to reduce and broaden the peak transmission.

The flatness defect represents all other non-uniformities by modelling it as a curvature relative to the mean spacing of the etalon. It lowers and broadens the transmission peak as well as shifting it. Figure 4.8 shows the exaggerated effects of flatness and tilt, with f equal to 1/10 and t of 1/20 (these typically will be of order 1/100 wavelengths). Depending on the control mechanism used, FPE tilt could be controlled to minimise the effect on the transmission, non-flatness however can not be actively controlled.

With a finite size etalon, the number of reflections available becomes a significant

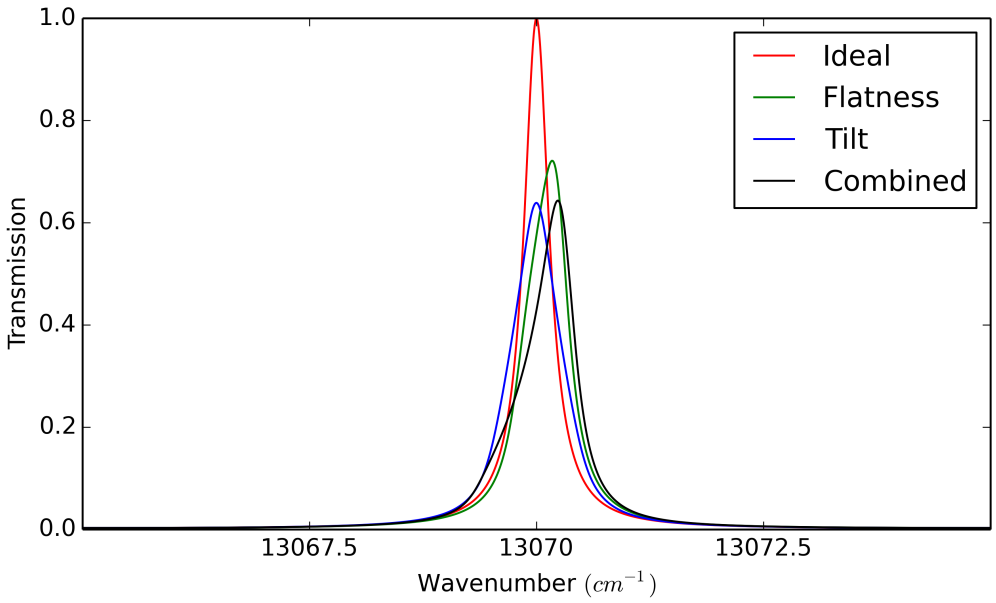

Figure 4.8: Transmission as a function of wavenumber for a single transmission line and different instrumental defects. R = 0.9, A = 0, FSR = 10 cm^{-1}, f = 1/20 wavelengths, t = 1/20 wavelengths at 765nm

factor in the design process, particularly when tilt and divergence are considered. Figure 4.9 demonstrates the affect of this upon the transmission function for increasing numbers of reflections (or effective size). While the broad shape is maintained, low sizes contain additional oscillations which don't smooth out until a large number (>100) of reflections are made. For incident light perpendicular to the etalon, the effective size in the absence of tilt is infinite. As soon as the angle of incidence moves away from the perpendicular the reflections will begin to propagate through the FPE, eventually escaping at the edge. In the non-tilt case the number of reflections is easily obtained via geometry;

$$\Delta l = 2d\tan(\theta),$$
$$n = L/\Delta l$$

where Δl is the distance traversed between reflections and L being the initial distance between the point of incidence and exit in the direction of propagation. The

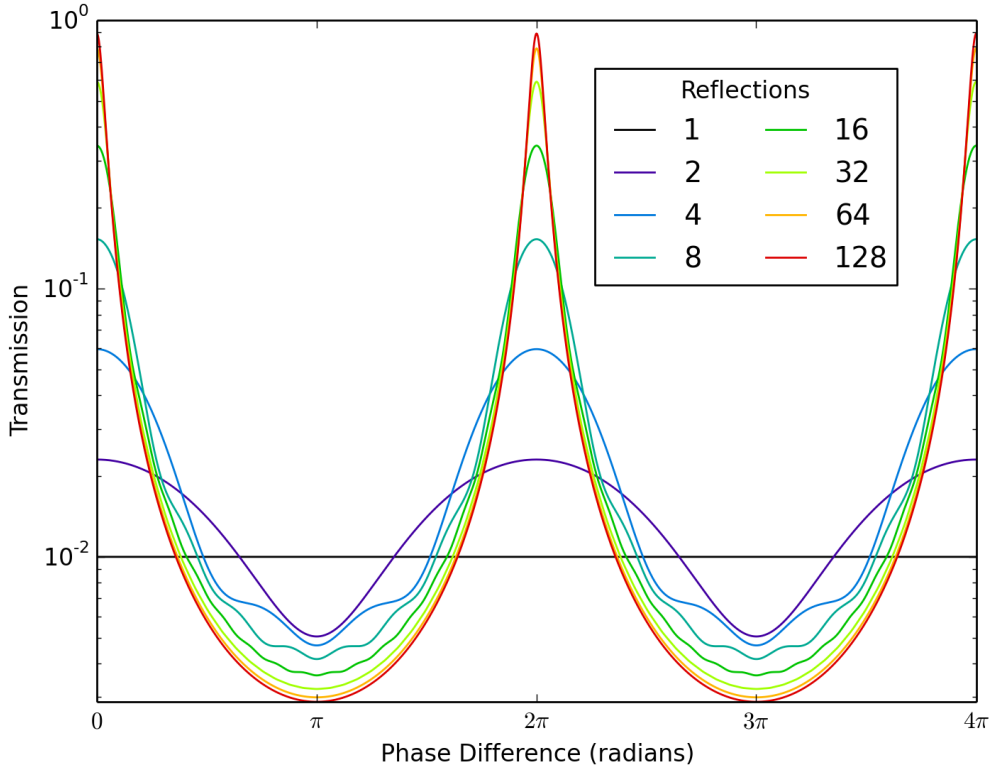

Figure 4.9: Transmission as a function of phase difference and number of reflections

first panel of Figure 4.10 demonstrates this for a divergence of 1° in both the x and y planes for an FPE with a radius of 2 mm broken down into a number of individual areas or FPEs. The reflections vary as one would expect, in such a simple case the average number of reflections for the field of view decreases as the sub-area moves closer to the edges. This picture changes dramatically if a tilt is introduced. The remaining panels of Figure 4.10 show the same geometry but now with a constant tilt of increasing magnitude, we can see that not only are the number of reflections reduced, but also the peak of reflection counts shifts towards the point of minimum distance. This is due to the tilt countering the differing angles of incidence. However one can also see that even with tilt, the number of reflections is typically well above 100, the exception being the case of extreme tilt and even in that case, only at the very edge of the etalon. We can conclude then that with a tight FoV of 1° and

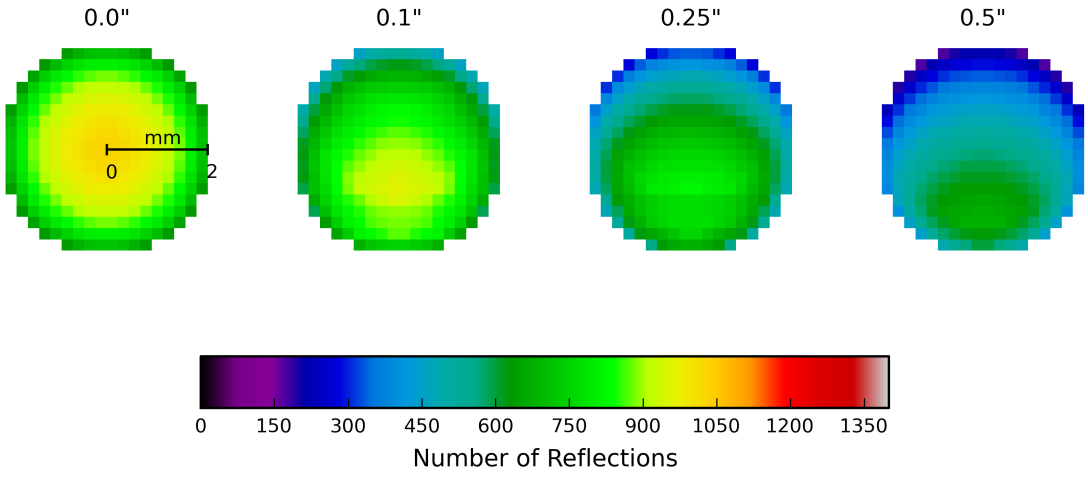

Figure 4.10: Number of available reflections for an FPE of radius 2mm and spacing 0.5mm with a FoV of 1°

allowing for even extreme tilt, the limited size of the FPE should not be a factor.

4.3 FPE Control

Aside from the physical properties of the FPE itself, the scanning mechanism is a significant cause of error. In the ideal scenario the FPE is scanned by varying the FSR precisely. The three controllable parameters in the FSR are the spacing, angle of incidence and the refractive index, varying any one of these will produce a scan effect and are known as mechanical, spatial and refractive index scanning respectively (Heaps and Kawa, 2002).

A simple example suggested by Jacquinot and Dufour (1948) for refractive index scanning was to place the etalon in an air tight container, and vary the refractive index by varying the pressure. Despite various improvements to pressure control (Hernandez, 1980; Rank and Shearer, 1956; Helbert et al., 1977) refractive index FPEs will always be limited by the linearity of the refractive index to pressure relationship, sensitivity to temperature variations, and the range of pressure needed

to obtain the required refractive index change. As such refractive index FPEs are not ideal for field work as unless highly insulated, variations in temperature will introduce errors and the pressure vessel would add weight and complexity.

Spatial scanning as mentioned involves the use of a varying angle of incidence upon the FPE. This can be achieved with variations in the aperture size and location, however this relies on precise control and knowledge of the optical arrangement (Shepherd et al., 1965). One can rely on relative movement of the light source and the FPE provided there is significant contrast with the background. An example of this would be a nadir viewing FPE on board an aircraft flying over a strong radiation source, the movement of the aircraft would alter the angle of incidence as it flies over the source, producing the scan. The final concept is to use a detector array rather than a single photodiode and thereby simultaneously measure the signal of multiple angles of incidence (Heaps and Kawa, 2002). The benefit here is the lack of any physical scanning, the drawback is that the light has to be sufficiently well mixed to avoid spatial variations, and the limited pixel density causing the mixing of angles of incidence / FSRs. A complex optical arrangement is again non-ideal for field work and the usefulness of relative motion is limited. The detector array system clearly has its benefits, and if combined with mechanical scanning, could be used for imaging (Atherton et al., 1982). The problem for this project would be the cost and complexity required.

The remaining (and most simple method) is mechanical scanning, which is promising because to scan one FSR the spacing needs only be varied by $\lambda/2$ as can be derived from Equation 4.8, making scanning over wide ranges more feasible than spatial or refractive index scanning. Numerous techniques have been used ranging from simple mechanical spring arrangements, electromagnetic scanning, thermal and even magnetic scanning (Jacquinot and Dufour, 1948). But by far the most

prominent method is the use of piezo eletric actuators (PEA).

4.3.1 Piezo Electric Actuators

PEAs vary the spacing between the two FPE surfaces in the order of micrometers by expanding when a voltage is applied. The benefit of this is that the voltage requirement is often low (several volts per FSR) and is highly controllable. In addition their structure affords high mechanical stability, making them ideal for rugged work. Their are however a number of flaws; hysteresis, non-linearity, latency and creep (Uchino, 1997).

4.3.1.1 Hysteresis and Creep

Hysteresis is an effect that occurs when a voltage is removed and the PEA relaxes back to its initial state. The polarization of the crystalline structure is not always fully randomised, leaving a remnant polarization. The result is that when the same voltage is applied again, the absolute displacement is not the same, demonstrated in Figure 4.11 (Choi et al., 1997; Al-Bender et al., 2005).

Figure 4.11 we see the voltage increasing to a maximum before decreasing, during the decrease the displacement does not follow the same path and at zero voltage there is a significant remnant. The result is that if we were to continually scan the FPE forward and backwards we would observe a significant hysteresis.

Creep occurs due to the same material properties as hysteresis but describes when a PEA is exposed to a steady voltage for a long period of time. This results in a drift away from the assumed spacing the speed of which speed decays logarithmically with time.

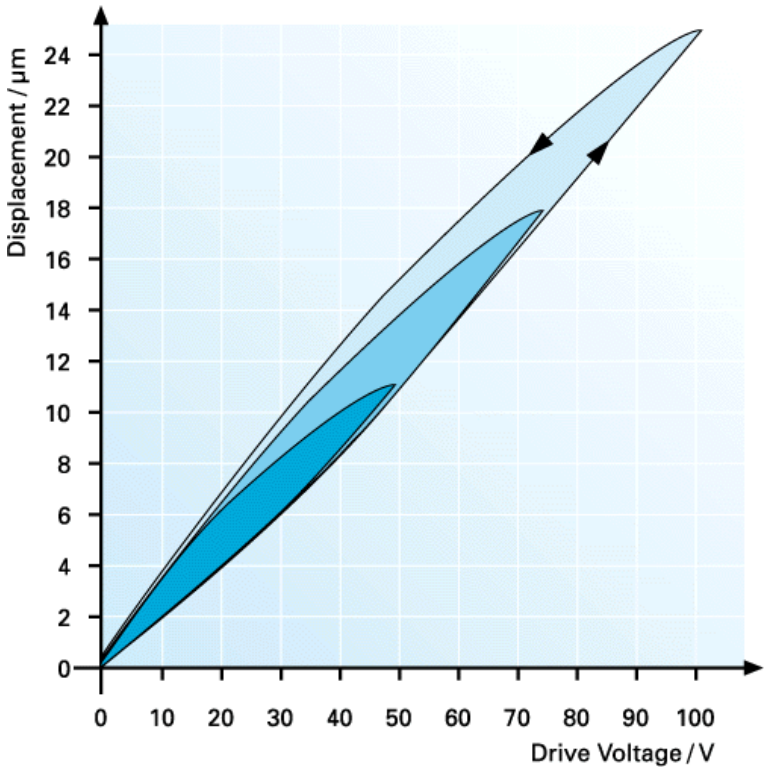

Figure 4.11: Example of PEA hysteresis and non-linearity for various peak voltages. Credit: Physik Instrumente

4.3.1.2 Non-Linearity and Latency

Another issue is the latency and the associated non-linearity. When the voltage is applied to the PEA the expansion is not immediate, meaning there is a lag or latency between applying the voltage and arriving at the required separation. Coupled to this is non-linearity, which in short means that the spacing at any given point whilst undergoing expansion is non-linear which in turn means that one cannot accurately determine the transmission profile, also highlighted in Figure 4.11. However both of these aren't an issue if the expansion rate is fast and voltage steps were used instead of continuous monitoring.

4.3.1.3 Spacing Control and Monitoring

As such it is of great importance to be actively measure the spacing, by means of a capacitor for example (Kaizuka and Siu, 1988; Gittins et al., 1998), known as closing the loop. If not possible, regular calibration would be required. Calibration in this sense would mean scanning the FPE until a known signal is reached, i.e. a peak intensity for which the wavelength is accurately known, thus allowing the spacing to be characterised. This is readily achieved with a laser for example and is a common means of calibration for stable control systems, although for PEA FPEs real time instability limits the effectiveness of calibration and as such would ideally use active monitoring.

The challenge in the example of the O_2 A-Band, and indeed any other absorption spectra, is that the spectrum is not composed of any one peak or trough that can be used to close the loop, it is an integrated signal composed of many lines measured simultaneously. The solution that was previously hinted at is to scan the FPE over multiple FSRs producing a repeating signal as seen in 4.5. The peak and minimum signals can only occur at certain FPE configurations, or spacings, meaning the spacing can be constrained. Scanning in small voltage steps will allow secondary maxima and minima to be used and by covering several FSRs the hysteresis can be identified, allowing a more accurate conversion from voltage space to FSR space. Using large FSRs (i.e. single transmission line in the spectral window) causes problems with PEA FPEs whereby the the start point of the scan must be reached and then maintained for a long period of time due to the lag between voltage and displacement caused by large voltage / displacement shifts (Bailey, 2013), though the effect of this is minimised by using multiple transmission lines.

4.4 Contemporary FPEs

Several relevant FPEs have already been mention with regards to there control methods, but a more detail discussion of them is warranted. Within remote sensing, FPEs have been used several times in recent years for the measurement of CO_2 and cloud properties, within which there are two main approaches. Firstly to measure the depth of a limited number of absorption line, thereby ascertaining the optical depth. This is done by filtering down using several FPEs or additional filters, as is the case in the FPE proposed by Yee et al. (2004), where three successively narrower FPEs are used in conjunction which are tuned by piezo electric actuators, which is done in the O_2 B-Band for cloud properties and provides imaging capabilities from geostationary orbit. Similarly the design by Kobayashi et al. (2010) uses one FPE, but multiple transmission peaks to sweep through a single absorption line for CO_2 measurements using a temperature controlled FPE. An alternative is to split the incident radiation in to two streams, one of which is measured in its entirety whilst the other is convolved with an FPE that is tuned to sit on , or as close to, a number of absorption lines. By taking the ratio of the two an optical depth can be calculated. Such an approach is used in various designs (Heaps and Kawa, 2002; Wilson et al., 2007) where the FPE is pressure tuned. A less common technique is to use a large FSR FPE with a single high resolution line which is swept across the whole spectrum as in (Bailey, 2013) with any discrepancy caused by the scanning process made up for by line matching, although this is not without its drawbacks as previously mentioned.

4.5 Detectors

Another consideration to make is the sensitivity and performance of the detectors used in the instrument. An ultra-fine resolution FPE for instance would need a detector capable of detecting the smallest of changes in the transmitted intensity. The basic principles of photo diode detectors are briefly discussed here. The idea behind them is that incident radiation causes electrons within the semiconductor surface to be displaced, leaving behind an electron hole. The liberated electron then moves towards to the cathode where as the hole moves towards the anode, thus generating a photocurrent. The scale of this current is dependent on the intensity of the incident radiation and the responsitivity of the diode, which varies with wavelength. The discrete nature of the photoelectrons means that it is subject to shot noise, which describes the statistical noise of the measured intensity. The SNR in this case increases with the square root of the number of photoelectrons.

Thermal (Johnson) noise describes the process by which electrons are liberated and thereby adding an additional noise current. This is particularly relevant for longer wavelength detectors such as germanium and indium gallium arsenide (InGaAs) detectors, where the latter are often cooled to below 0° C. Silicon photodiodes on the other hand do not need to be cooled to the same extent for observations in the visible spectrum.

Also to be taken into account is the dark current, which describes any additional background current and is therefore a source of noise. It relates to the random generation of charges within the diode and its rate is dependent on crystallographic defects within the diode.

4.6 Summary

The reasoning behind the use of an FPE for aerosol retrievals has been discussed and a mathematical framework within which to simulate FPEs has been described. In this the framework the key parameters are the FSR and reflectivity which govern the spacing of transmission lines and their FWHM respectively. Building upon this, several non-ideal factors were introduced in order to present a more realistic picture of FPE performance, these included non-collimated light, tilt, surface defects and finite radius. In the latter part of the chapter various control methods were discussed, in particular mechanical scanning by PEAs. This method was chosen for its simplicity and availability though it is not without its flaws as discussed in Section 4.3.1. The result of this is that we are now in a position to use the afore mentioned framework to tailor the design of the FPE to the challenge of aerosol retrievals in the O_2 A-Band and construct models to simulate its performance.

Chapter 5

Design, Optimization and Testing of the FPE

5.1 Design

Figure 5.1 shows the general design of the proposed FPE. The input optics consist of a telescope feeding a fibre optic bundle, which is then split into a 5:1 ratio, with the bulk of the signal passing to the FPE. The remainder will feed an additional detector and act as a reference. With the use of a lens arrangement, the output of the FPE fibre is collimated, passed through the FPE and refocused (if needed) on to detector 1. Detectors 1 and 2 will output an analogue signal to the analogue/digital converter (ADC) and onto the PC, where it is used to actively control the FPE via the ADC and power supply. As can be seen, this design is a simple one. By minimising the use of complex optics and by adopting fibre optics, the design can be made to be very compact, stable and cheap whilst not compromising performance. For further stability the apparatus will be housed in a sealed and insulated container that has active temperature control to minimise any environmental effects. Using fibres will be an advantage here by allowing the FPE to be indoors, away from the

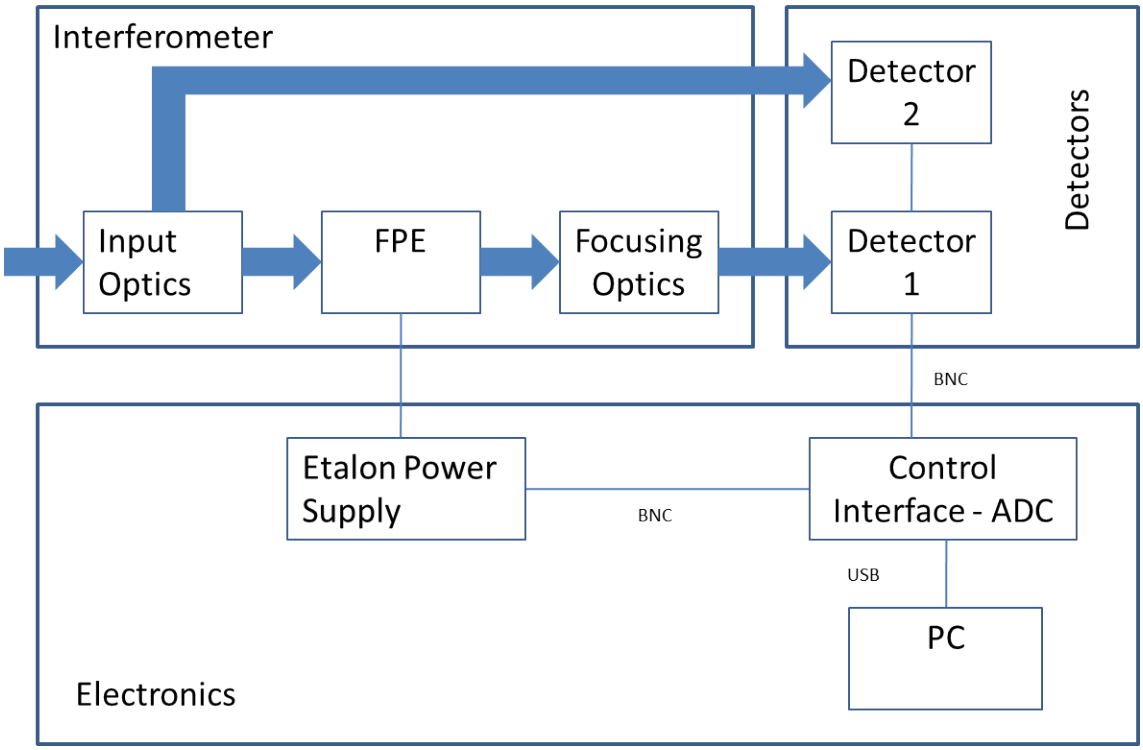

Figure 5.1: Schematic of the FPE Design

telescope if needed.

5.2 Optimization

With a mathematical framework and a simple instrument design in place, we can now look towards a FPE that is tailored to the O_2 A-Band and aerosol retrievals. To optimize the design of the etalon itself we must first consider the spectral range over which to measure. If the range is too large and as such includes a large continuum contribution towards the measured spectrum, the signal from the absorption lines is masked. If the range is too small on the other hand, vertical information will be lost. In short a balance needs to be struck between acceptable signal levels and information content, which is why the range 13045 cm^{-1} - 13105 cm^{-1} is used. If

the lower limit was extended then the signal would contain a large contribution from continuum radiation, as for the upper limit, if this was extended then it would add noise in the form of the saturated R branch. The remaining spectral range consists of seven absorption pairs, which provide valuable vertical information. This spectral range is important for the optimization of the FPE design for aerosol retrievals, although it could readily be extended to incorporate more absorption lines or solar lines. More practically the wavelength range used will be determined by the available filters. They are readily available within the O_2 A-Band often with a larger FWHM than we would ideally use, therefore in practice, some additional noise is inevitable, as the spectral information will be reduced by the spectral dependence of the reflectivity.

The two crucial parameters to the design of the FPE are the reflectivity and the free spectral range. In the case of reflectivity, which determines the resolution of the transmission lines, we can predict that increasing the reflectivity will increase the accuracy. FSR however is more of a problem, as it is not immediately obvious what the optimum value is for aerosol retrievals. To confirm the behaviour of the reflectivity and understand the impact of FSR we couple them to a simulated aerosol retrieval, much as in Chapter 3.

Figure 5.2 shows the impact of FSR and SNR upon the simulated retrieval of a boundary layer aerosol of optical depth 0.3, height and width 1km (Scenario A), from a groundbased and space-borne FPE. The number of channels used is kept constant throughout at 60 as this is determined by the reflectivity and corresponds to a scan over 2 FSRs. The noise model in this case is simplified as a fixed SNR for each channel, where the noise for each spectral point within that channel is given by the total signal divided by the SNR. Again as in Chapter 3, the absolute values displayed are not overly important as the instrument model is simplified and all

results are intimately tied to the covariances used. The trends however are of great importance as they indicate the key relationships between the instrument design and its performance.

Figure 5.2 shows firstly the total AOD error for the aerosol profile for both viewing cases. As one would expect, increasing the SNR leads to an improved performance, for the space-borne example, where errors can improve by an order of magnitude regardless of FSR. In the groundbased case this improvement is limited to 50% reduction in error at best, and is negligible at low FSR. This contrast is driven by the surface albedo. In the space-borne case the surface albedo is retrieved along with the aerosol, with high correlations between then two. As such SNR plays a vital role in disentangling the the two, whereas in the ground based case the albedo is not retrieved and plays a very weak role in the retrieval of aerosol.

The FSR, which is our priority here, exhibits a high degree of variation which is consistent between viewing geometries and antisymmetric between AOD and DoF, this is driven by the varying degree to which the transmission lines match up with the absorption lines. A key point to remember here is that although reflectivity drives the resolution, this resolution as given by equation 4.7 is relative to the FSR itself, so in absolute terms the resolution decreases with increasing FSR. Thus the general trend favours lower resolutions in both AOD and DoF with the poorest performance occurring at 0.1 cm^{-1} where the AOD error is more than an order of magnitude higher than the lower resolution cases. Below this peak the higher resolution appears to pay off somewhat, though not enough to eclipse the FSRs between 1 cm^{-1} and 100 cm^{-1}. As the FSR approaches 100 cm^{-1} we can see a subtle increase in AOD and decrease in DoF, this is much more noticeable in the space-borne, this is presumably the impact of loss of information due to the poorer resolution. This 'goldilocks' region around 10 cm^{-1} was chosen for the instrument

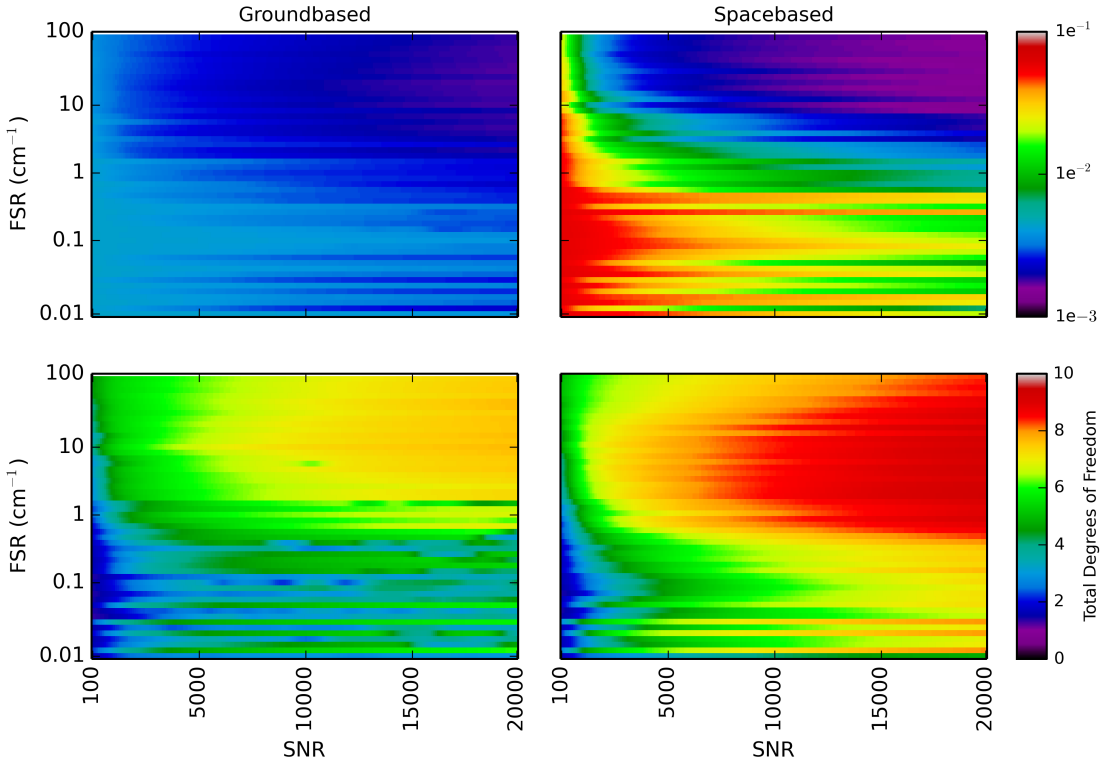

Figure 5.2: Total AOD error and degrees of freedom for a ground (zenith viewing) and space (nadir viewing) based FPS as a function of FSR and SNR, aerosol of optical depth 0.3, height 1km, width 1km, profile retrieval including continuum offset (SZA 30°, albedo 0.5).

as it affords a degree of variation without loss in performance, this variation from the production process would significantly harm larger FSRs (smaller spacings).

To optimize the reflectivity we must first think about its role within the retrieval and how it impacts the convolved signal. The reflectivity determines the broadness of the transmission lines, as such it significantly varies the convolved spectra. The key to a useful convolved signal is the variability, the difference between the maximum and minimum signal and the associated noise. With a high reflectivity and therefore fine lines, the maximum difference in the signal across the scan may be large, but

could well have a poorer SNR. In contrast at low reflectivity the variation would be small but the noise would be low due to the higher signal level. A compromise must be drawn between the two competing effects. To do this we convolve a simulated high resolution O_2 A-Band spectra with a FPE transmission profile of FSR 10cm^{-1} and scan over one full FSR. This is then repeated for different reflectivity values. From each scan the maximum and minimum signals are taken, from which an apparent absorption (AA, τ_a) can be calculated and from that a psuedo SNR (S_p) can be found;

$$\tau_a = \log I_{min} + \log I_{max} \tag{5.1}$$

$$S_p = \tau_a / d\tau_a \tag{5.2}$$

Where $d\tau_a$ is given by Gaussian error propagations. The result of this is shown in Figure 5.3. The SNR here is the relative SNR compared to the peak of the space-borne SNR. It shows firstly that the groundbased instrument will observe half the SNR of the space-borne, though unsurprisingly both have the same form. The peak SNR is at 0.65 with reflectivity above this being penalised, though less harshly in absolute terms for the groundbased case. From this we can say that the optimum SNR is given by the peak value of 0.65, however as previously discussed, any additional broadening from field of view, surface defects etc. will lower this significantly. As such, given the limited penalisation of higher reflections, it makes sense to opt for a reflectivity of about 0.9, which will reduce down to a more optimum value.

To summarise then we have opted for a free spectral range of 10 cm^{-1} and a reflectivity of 0.9. These two parameters should provide the optimum performance within the O_2 A-Band regardless of whether it is for space or groundbased applications. However choosing, a parameter is one thing, getting that back from the

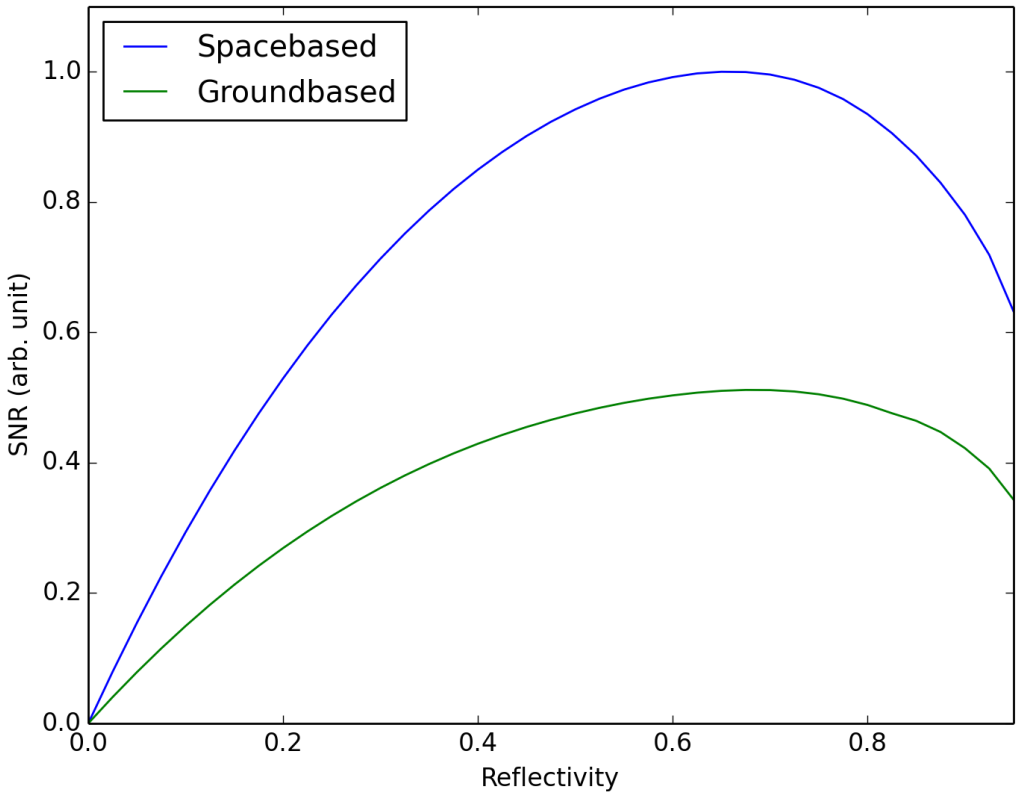

Figure 5.3: Pseudo SNR as a function of reflectivity for a space-borne and ground-based FPE

manufacturer is another; such highly customised components always come with a degree of uncertainty. Fortunately from our analysis we have shown that we should be able to cope with any slight discrepancies.

5.3 The Real FPE

The FPE was supplied with two important pieces of calibration data; the FPE coating performance and the spacing. The spacing data describes the separation of the two surfaces over the dimensions of the FPE, this is detailed in Figure 5.4 where the variation is relative to the minimum separation of 502.208 μm. From this

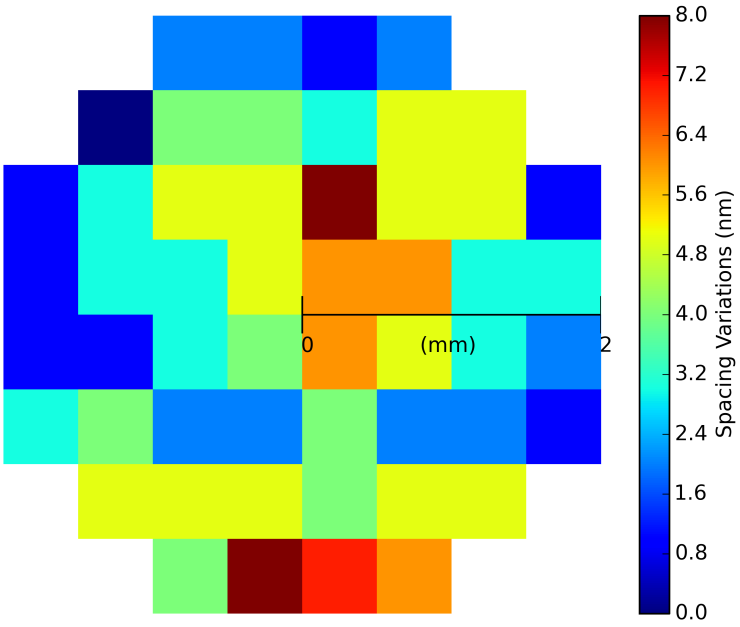

Figure 5.4: Variation in FPE spacing relative to 502.208 μm, as provided by the suppliers

data we are able to then compute the FPE transmission for each sub area, and by averaging produce an overall transmission profile. In addition we could also describe the variations in the form of tilt and curvature as discussed earlier. Discerning a tilt is not possible, since there are no strong trends in any particular direction. The curvature can however be inferred as it is an approximation that really describes variations rather than any actual curvature. Looking at the data we can see that the average variation from the minimum is 4 nm or approximately 1/200 λ. The overall transmission profile however corresponds much more to a value in the order of 1/50 λ. This discrepancy comes from the curvature model favouring smaller variations. The model could be adjusted to better suit the true distribution of variations, but in reality it is not much more computationally expensive just to use the overall transmission model that averages the transmission from the different sub areas.

The reflectivity data provided comes in the form of coating transmission as a

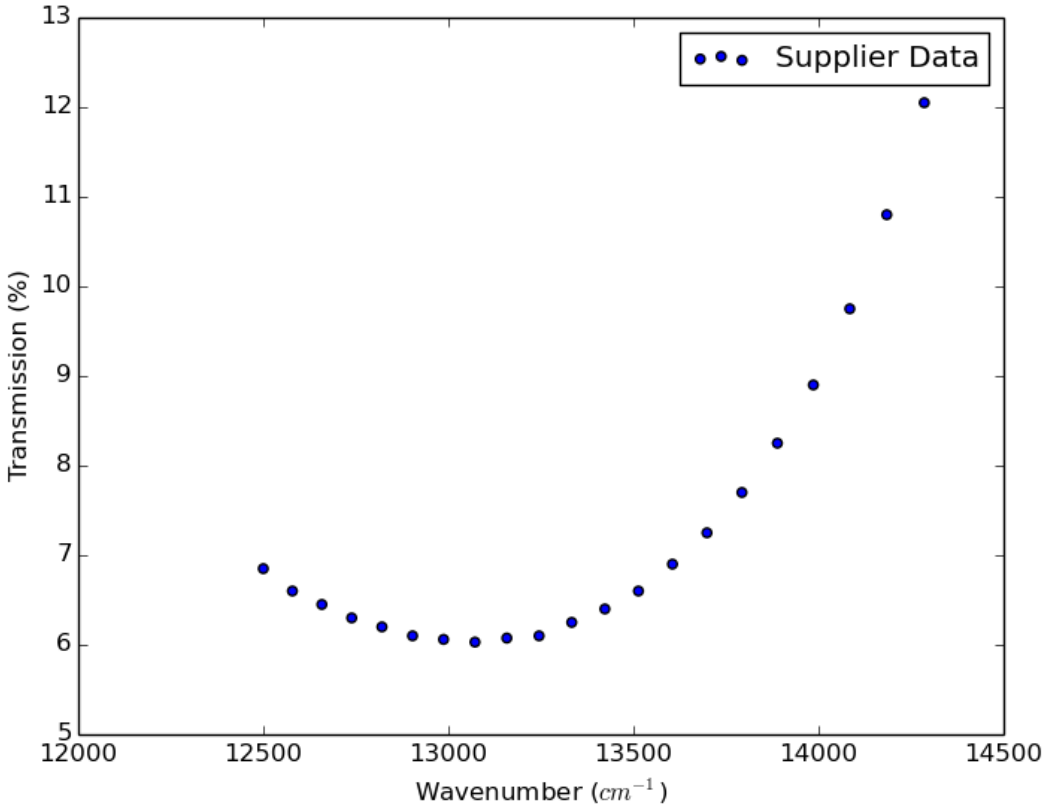

Figure 5.5: Coating transmission as a function of wavenumber, as provided by the suppliers

function of wavelength and is shown in Figure 5.5. The transmission of the FPE is optimised such that it is lowest, i.e. has the highest reflectivity, across the O_2 A-Band, although across a wider range the transmission is still well below 10% (reflectivity greater than 0.9). However, this plot is purely the performance of the coating, once further line broadening owing to defects and field of view, is taken into account, the reflectivity will effectively be lowered thus moving into a more favourable regime as in Figure 5.3.

We can take these optimizations and estimations of the FSR and reflectivity and use them to create a realistic transmission function for use in simulations. Figure

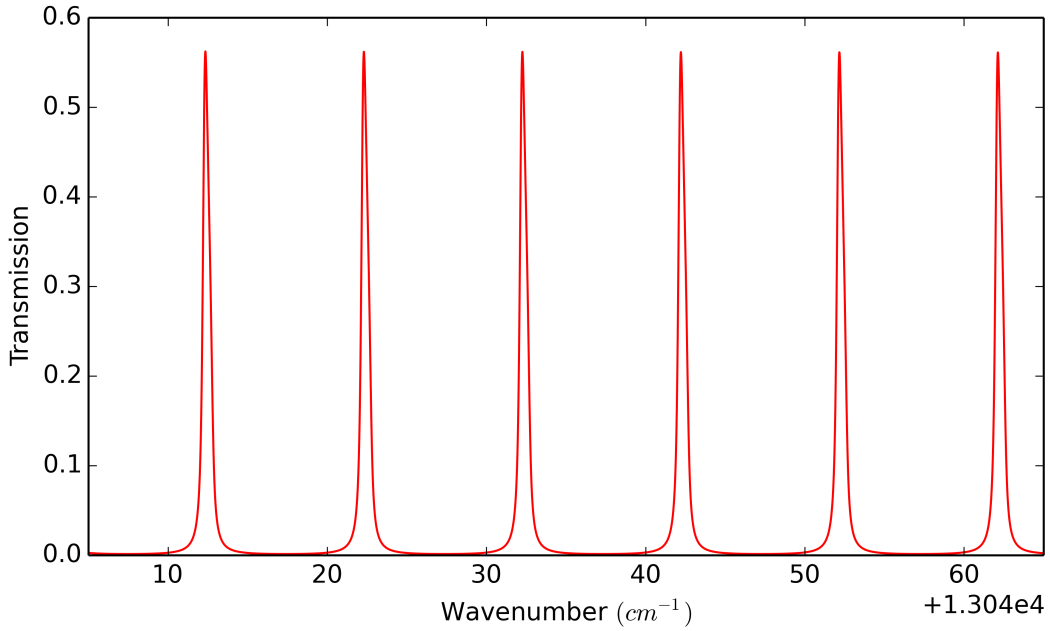

Figure 5.6: Finalised transmission function, taking into account supplier information on FSR and reflectivity

5.6 shows this finalised transmission function. From this figure one can clearly see that compared to the ideal cases displayed earlier, the peak transmission is reduced to just below 0.6 and the FWHM is slightly broadened. These are both results of divergence (1° is assumed) and surface defects. As the FWHM is broader it is is possible to reduce the sampling, or steps, down from the initial figure used of 30, however a degree of oversampling is always acceptable and will help in constraining the ILS as the spacing is varied.

5.4 Detectors and Noise

The detector used is a low cost silicon diode detector from ThorLabs. Its noise is primarily driven by the detector itself, rather than by the shot noise, i.e. the square root of the photoelectrons generated. The result is that the SNR as a function of radiance is linear with a maximum SNR of 5000. The ADC used is 12 bit and the voltage over which this is applied can be programmed, the resulting SNR of the ADC is given by;

$$S_{ADC} = \frac{S_i}{S_n} = \frac{2^{N-1} q \; 2^{-1/2}}{q \; 12^{-1/2}} \tag{5.3}$$

where N is the number of bits and q is the voltage range over which they are applied and Si and Sn are the signal and noise respectively. Thus the SNR (S_{ADC}) is independent of the range over which the bits are used, as both signal and noise are equally dependent. The net result of these noise sources is shown in Figure 5.7 with a comparison to GOSAT, OCO-2, CarbonSat and Sentinel-5 P for reference. Although in some cases the FPE will apparently have a lower SNR, the radiance received is often higher, by an order of magnitude in some cases, due to integration of the signal. This model however does not however include a background noise value, assumes the same 4 second integration time and viewing geometry as GOSAT, and assumes a relatively large telescope aperture size of 30 cm diameter. Thus it is in this case only an approximation and is deliberately made similar to GOSAT so that reasonable comparisons can be drawn when conducting simulations, particularly from space.

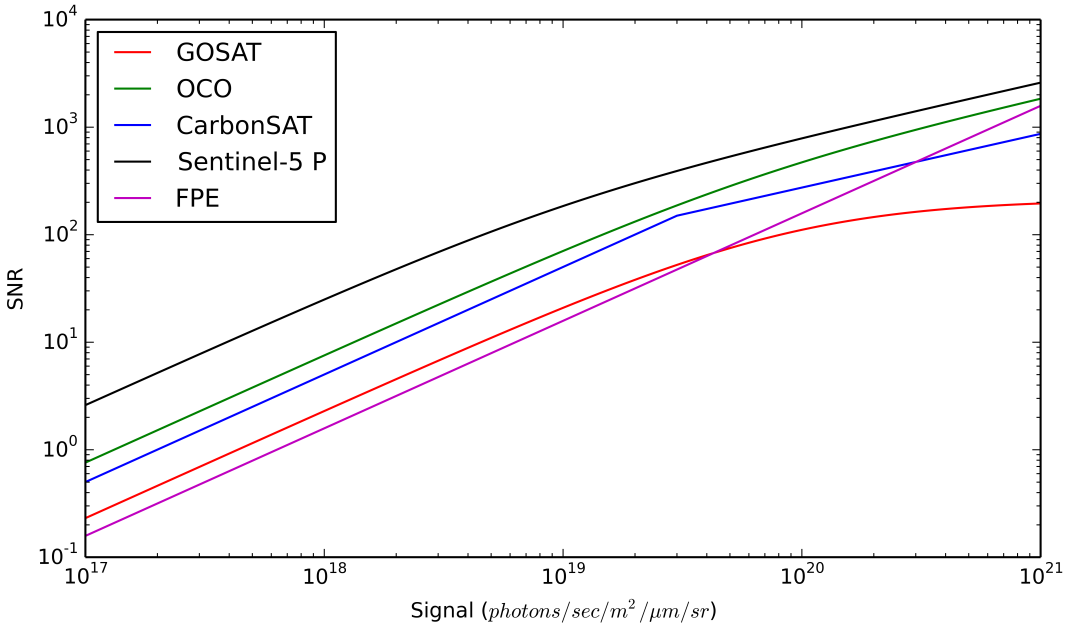

Figure 5.7: SNR comparisons of the four instruments discussed in Chapter 3 with the FPE

5.5 Simulations

Simulations have been conducted for the retrieval of aerosol from space using the FPE as described, following the procedures and scenarios set out in Chapter 3. Profile retrievals of scenarios A and B are shown in Figures 5.8 and 5.9, to reiterate, scenario A is an aerosol layer of optical depth 0.3, height 1 km and width 1 km, whereas B is moved to a height of 3km.

As is clear in both figures, the outlook is mixed. Firstly in terms of LAOD (top panels), high in the atmosphere, above 400 mb and particularly above 200 mb, the performance of the FPE is fairly similar to GOSAT, with LAOD errors

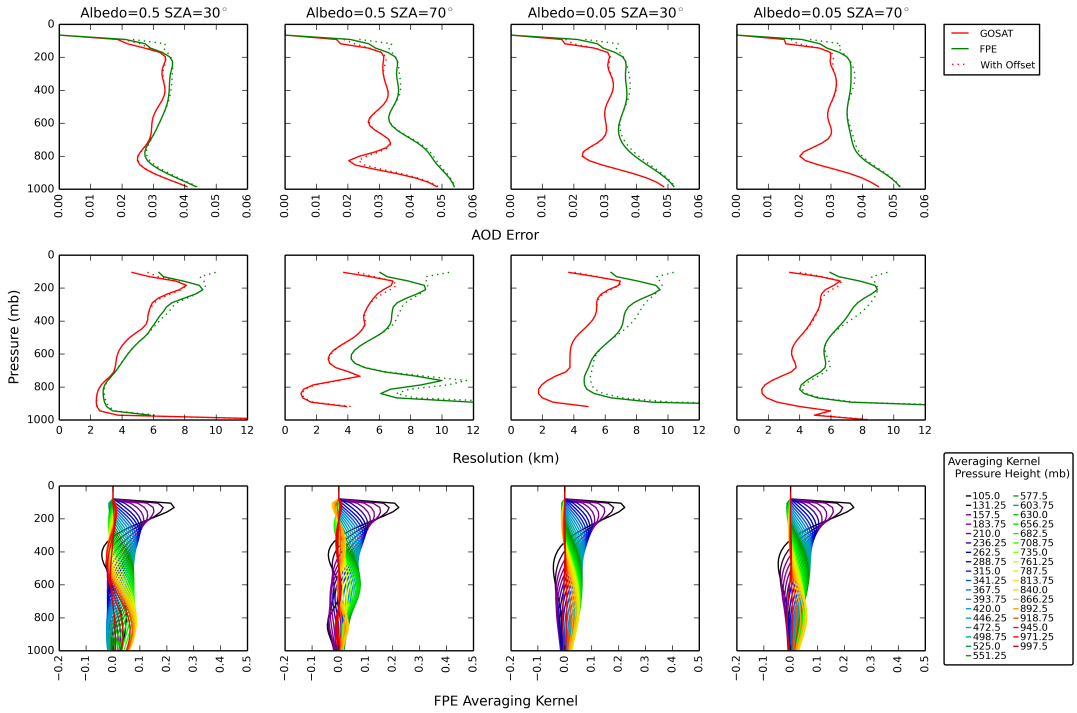

Figure 5.8: Error of LAOD (top panels) and vertical resolution (middle) as a function of pressure using the aerosol profile retrieval of scenario A for GOSAT and the FPE, the effect of an intensity offset is shown by the dotted lines. The bottom row displays the corresponding averaging kernels for the FPE. Note the top four pressure levels are not shown.

of less than 0.04. However as we move further down, in all but the case of 0.5 albedo and SZA 30° the FPE falls rapidly away from 600mb onwards. In scenario A however, very close to the surface, the gap closes due to GOSAT's weakness at low altitude, though this is more a case of both being poor rather than the FPE improving. Vertical resolution (middle) is a similar story, the FPE is comparable to GOSAT at higher altitudes but towards the surface the resolution degrades, the resolution is typically 6km though there are large fluctuations, especially below 600 mb, or whenever it reaches the aerosol layer. Over high surface albedo and low SZA the performance is far more promising. The resolution is further explained by

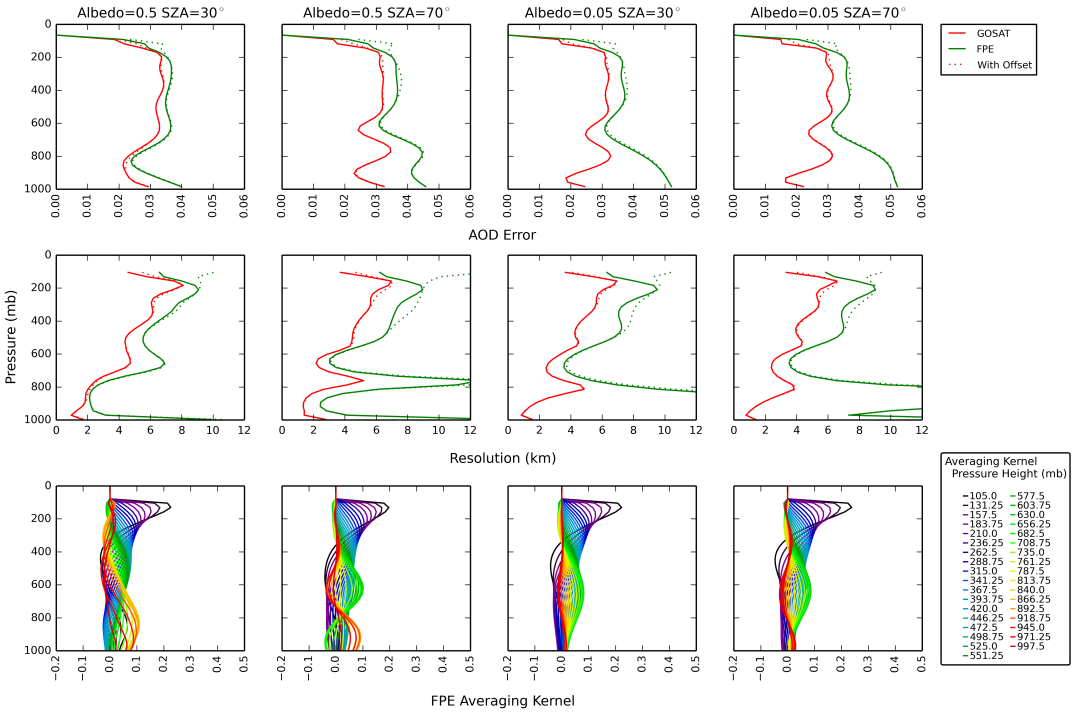

Figure 5.9: As Figure 5.8 but for scenario B

the averaging kernels for the retrieval. In all but the first case, there is very little sensitivity to the near surface layers, though this improves slightly as the aerosol moves higher. The impact of offset is more keenly felt for the FPE, perhaps more keenly than any of the previous instruments, though its effect is restricted to the upper atmosphere and is less of an issue for LAOD, with resolution sharply affected in the high SZA high albedo case.

As previously concluded, full profile retrievals are limited in their usefulness as the vertical resolution is often poor and errors high. To get a better understanding of the relative performance of the FPE the profiles were integrated over the 0-2 km and 2-5 km ranges as well as over the total column, in a repeat of Figures 3.7 and 3.8 and are shown in Figures 5.10 and 5.11 for scenarios A and B respectively. Also shown are aerosol combinations which will be discussed later on.

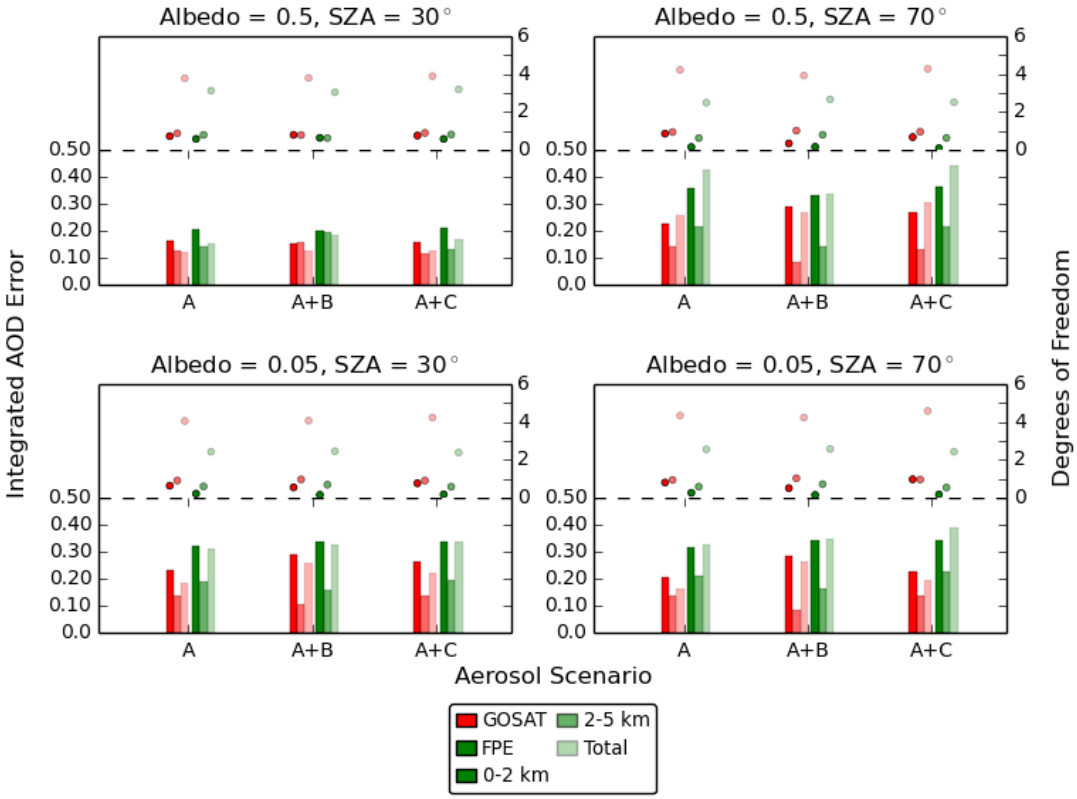

Figure 5.10: AOD error and DoF for the profile retrieval of scenario A for albedos of 0.5 and 0.05, SZAs of 30° and 70° when integrated over the 0-2 km and 2-5 km ranges as well as the total column. Combined aerosol retrievals are also shown for scenarios A+B and A+C, offset is included. Different shades of the same colour represent differing integrated ranges

Comparing GOSAT (red) to FPE (green) we can still see a disparity between them in both AOD error and DoF. Discounting the top left panel where they compare well with each other, the FPE shows a consistently higher error across all three integration ranges, although the 2-5 km integrated AOD is only weakly affected. The DoF for the boundary layer is often close to zero, whereas the 2-5km range is much closer, if not equal, to one. Because the error in the boundary layer is so high with such poor information content, one can assume that the majority of the error in the total column comes from the poor accuracy in the boundary layer. We can

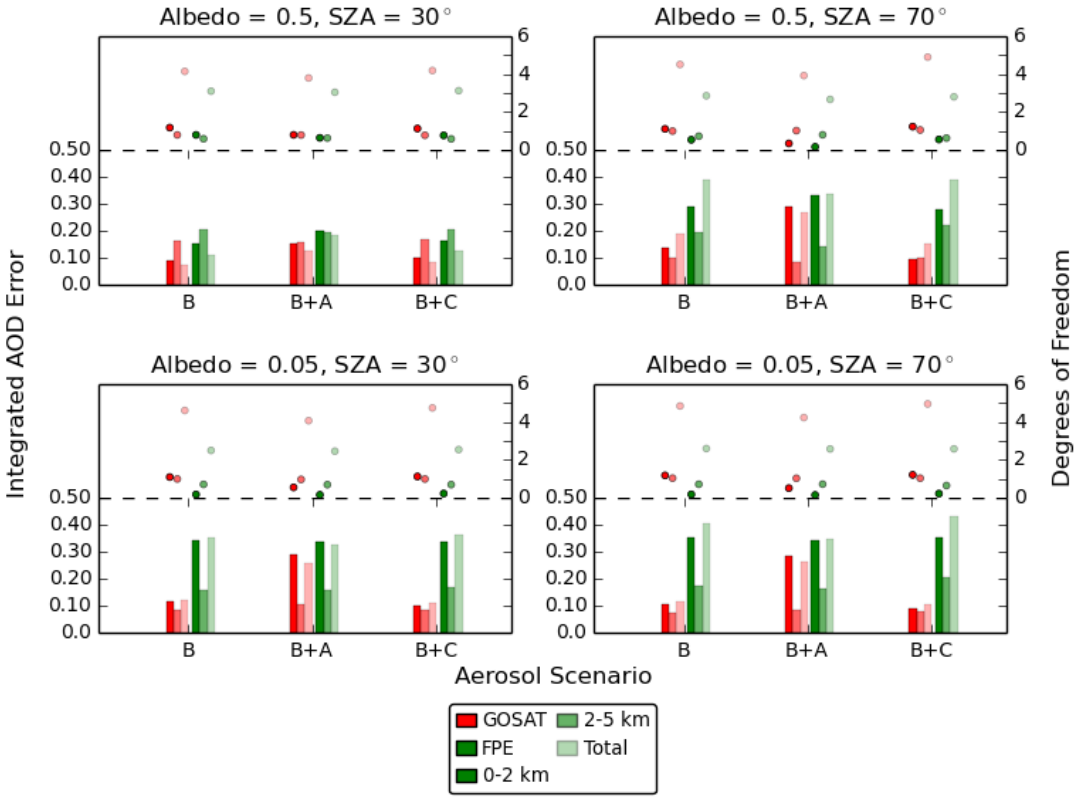

Figure 5.11: As Figure 5.10, but for scenarios B, B+A and B+C, noting that B+A is exactly the same as A+B.

also see more clearly that when the aerosol is moved to 3 km in altitude the impact is far less than for GOSAT, where a marked reduction in boundary layer error is observed. FPE in this instance only shows noticeable improvement over the brighter surface albedo, where boundary layer DoFs increase to one and there is minor error reduction.

The impact of additional aerosol layers upon the AOD error and DoF is also shown in the afore mentioned figures. What stands out is that for the FPE, the additional aerosol layer cause only minor increases in AOD error and DoF, with both instruments beginning to converge. However this 'advantage' needs to be taken carefully, the errors in absolute terms are already much greater than GOSAT,

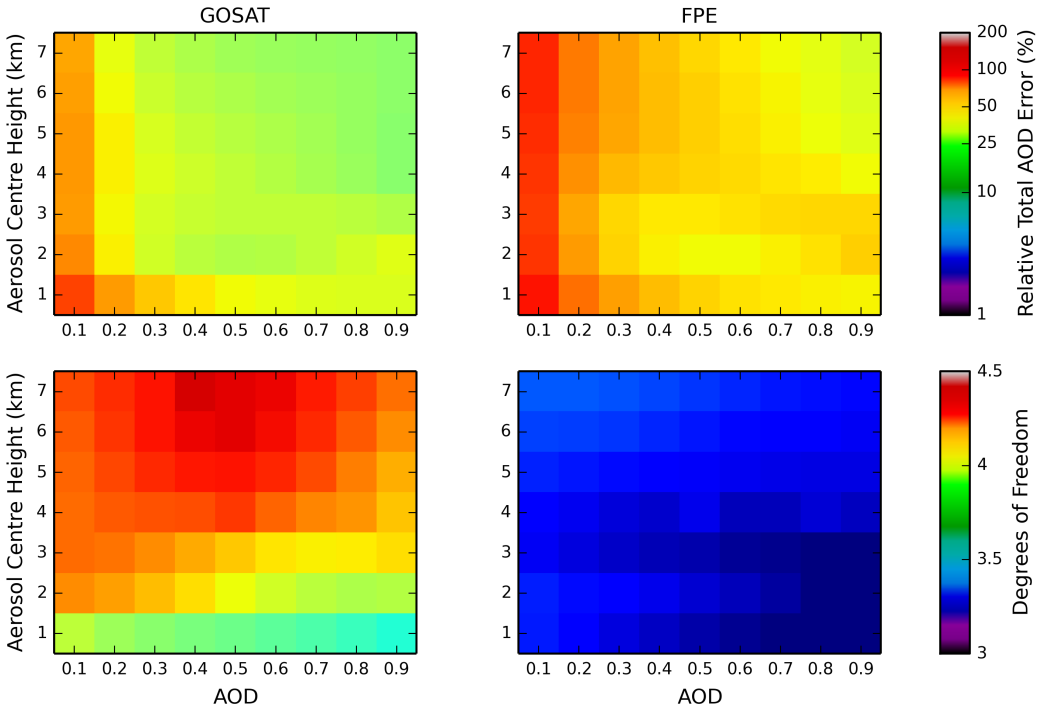

Figure 5.12: Total AOD error (given as a relative error) and DoF as a function of aerosol centre height and AOD, for an albedo of 0.5 and SZA of 30° for GOSAT and FPE.

even with GOSAT losing accuracy due to additional layers. Again though it is clear that it is advantageous to use a low SZA and high albedo, where the extra layers have little effect.

The lack of improvement with increasing aerosol height is further born out in Figure 5.12 where the total AOD error and DoF is plotted as a function of aerosol centre height and AOD for both instruments.

GOSAT shows a strong and consistent improvement with increasing aerosol height, both in AOD error and DoF with errors reducing by up to half and DoFs increasing by one. In contrast FPE shows very little variation with height, with a

maximum increase of 0.25 DoF and errors reducing by a few percent. The variation with AOD is however more consistent with the best performance occurring at higher AODs. In this case the FPE is far more comparable to the low resolution high SNR instrument Sentinel-5 P (S5P) as shown in the equivalent Figure 3.11.

5.5.1 Impact of Albedo

As previously discussed, albedo a priori uncertainty has a large impact on the retrieval performance. This is particularly acute in the case of the FPE where we have observed a marked increase in retrieval error nearer the surface. To quantify the impact of albedo constraints upon the FPE retrieval, Figure 5.13 shows a repeat of the simulations in Section 3.1.4.2 but for the FPE with GOSAT for comparison, where we show the total AOD error for different albedo a priori uncertainties for scenario A.

The trends born out are the same as previously studied, a tighter constraint rapidly improves the retrieval performance after a cut off of 0.2 and 0.04 for the longer and shorter path lengths respectively. However the magnitude of the improvement is substantially larger for the FPE, with errors reducing to below 25% of their initial value, from 0.4 to 0.06 for the high SZA cases and 0.35 to 0.05 for the low SZA, low albedo case. The last case, high albedo and low SZA, behaves much more similarly to GOSAT, which is expected given the comparable performances observed previously. One other important thing to note is that in all cases the error stabilises at tighter constraints, i.e. the retrieval performance does not improve. With the cases in Chapter 3, for all instruments this limit was an error in the region of 0.01 - 0.02. The FPE however shows a slightly higher saturation, at approximately 0.05-0.06. This would then appear to be a fundamental limitation in the design of the FPE at this stage, though we do know from Figure 5.2 that

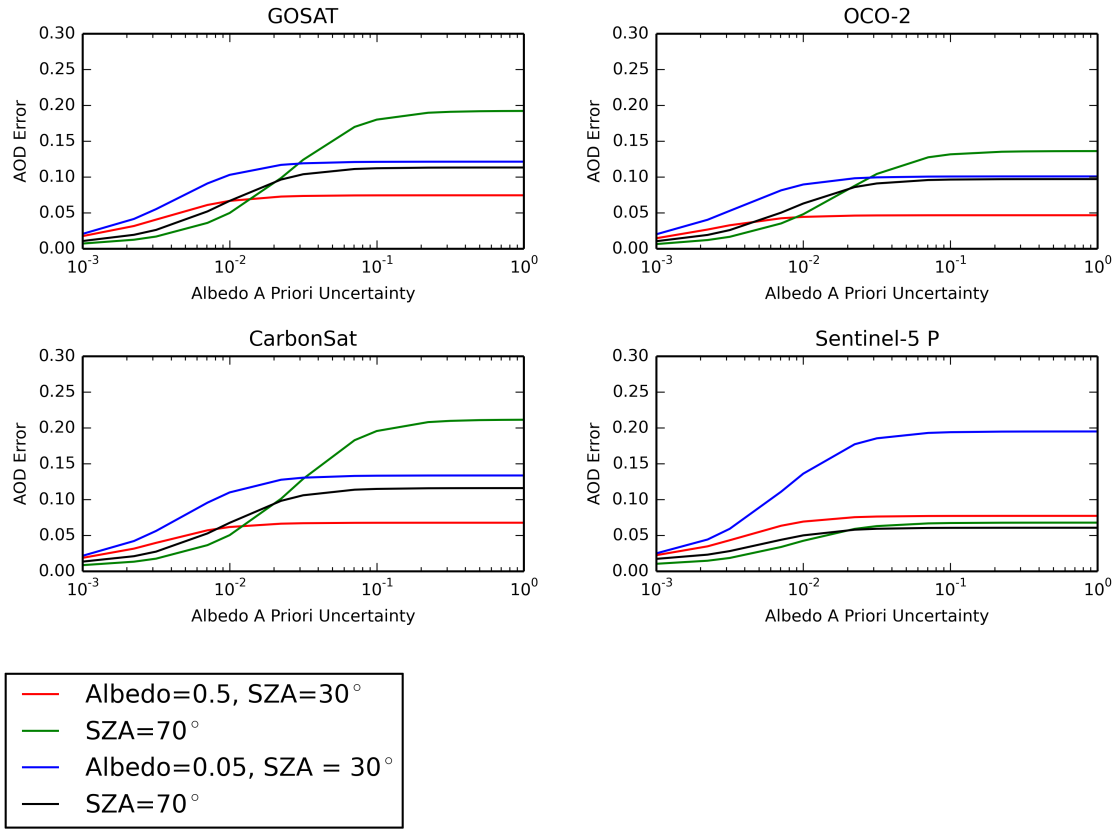

Figure 5.13: Total AOD error as a function of a priori albedo uncertainty, for an albedo of 0.5 and SZA of 30°, for scenario A aerosol (height 1 and width 1 km, AOD 0.3) for GOSAT and FPE.

AOD error can be further improved by increasing the SNR, well below the nominal requirement of 0.05.

To further investigate the nature of the improvement of retireval performance with increasing albedo constraint we have taken the above simulations for the FPE and investigated the impact upon the LAOD error and vertical resolution rather than the total AOD, both shown in Figure 5.14.

Both the LAOD and resolution show expected behaviour, in that the improvement is most dramatic nearer the surface, with almost no change above 600 mb. However there are some interesting features. Considering the LAOD with the tight-

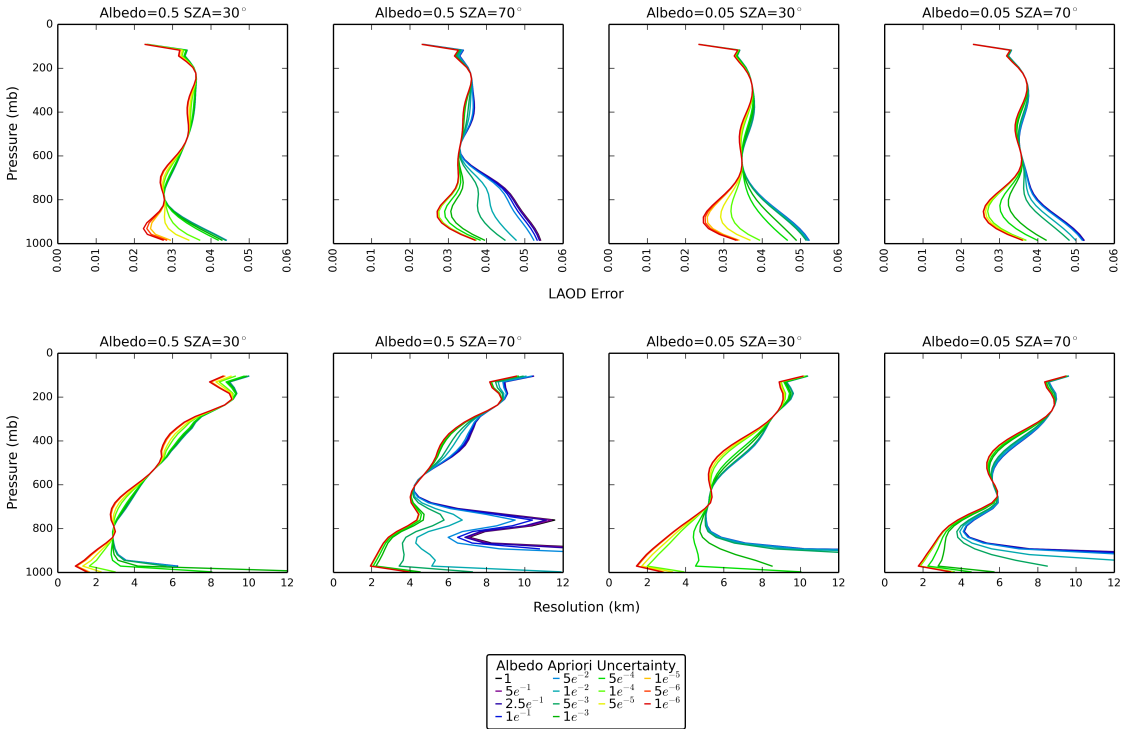

Figure 5.14: LAOD error and resolution as a function of a priori albedo uncertainty, for an albedo of 0.5 and SZA of 30°, for scenario A aerosol (height 1 and width 1 km, AOD 0.3) for FPE.

est constraint we can see that the performance at the surface becomes limited, and it is at the location of the aerosol that the improvement continues, perhaps going some way to explain the saturation at the tighter constraints discussed earlier. This feature is also observed in terms of resolution, with a slight worsening of resolutions at the very near surface. The resolution also demonstrates how severe the impact of poor albedo constraints are when considering the lower atmosphere, where previously the resolution was extremely poor (>12 km) in some cases, but can rapidly be improved to 2-4 km though the very near surface will remain a challenge.

5.6 Experimental Results

With the FPE and other components assembled it was necessary to conduct a series of performance tests on the individual components, and on the instrument as a whole. In order to undertake these tests a simple piece of code was adapted that controlled the output of the ADC by setting its gain and readout rate. It was also severely edited to allow for the data to be handled more efficiently and for processing at a later date. The extra efficiency was needed as the original programs would display significant slow down, often taking tens of seconds to read data what should only take fractions of a second. By optimising the code in this way we could be more certain that the time encoded actually corresponded to the correct event time and improved the experiment duration, which was critical in the first two experiments undertaken. In both of the experiments here after described the readout noise was low, typically at well below 1% and so the detector performance is not the main concern. The focus is the experimental procedure and results and systematic errors as a result of the design of the system.

5.6.1 Monochromator Experiments

The first two tests were to validate the coating transmission data shown in Figure 5.5, in what we call the reflectivity validation, and to repeat the same experiment but on a much finer scale, known as the instrument line shape characterisation experiment. These would serve to verify the suppliers information, and to help quantify the various inaccuracies of the experimental configuration as well as determine the transmission profile of the FPE. To do this would require a wavelength tunable light source. As a tunable laser was out of the question financially, a white light source coupled with a scanning monochromator was used. The experimental set up is identical to that of the schematic in Figure 5.1 with the input optics consisting of a

lamp, lens and monochromator configuration. The lamp used was a 200 W Quartz-Tungsten-Halogen (QTH) lamp, which radiated isotropically meaning that a large proportion of its output power was wasted. To counter this, a lens arrangement was used such that a larger solid angle was subtended and fed into the monochromator.

The monochromator used was a Cornerstone 260 1/4 m spectrograph which effectively operates like a grating spectrometer (see Figure 5.15). The light is incident upon two mirrors before the grating. The angle at which different wavelengths are transmitted depends on the angle of incidence. When the spectrum is incident upon the exit aperture, the effect of varying the grating angle is to vary the wavelength observed at that point. The light is then collimated with a final lens to reduce the dispersion caused by the grating, and fed through the FPE and then to detector 2. The output from detector 2 is then analysed by the data acquisition device (DAQ; 12 bit ADC) and computer arrangement. After some initial experimentation it was apparent that the light source was unstable over time, typically increasing in output over several minutes. As it was unsafe to leave the light source on for a substantial period of time to allow it to stabilise (the maximum time it should be allowed on should not exceed 10 minutes), an additional detector, detector 1, was employed to monitor the power output of the lamp, and was read simultaneously with detector 2.

As it was not possible to measure the individual spectral properties of the lamp, monochromator and detector, the combined spectrum was measured as an initial test of the system. In this case the FPE has been removed from the chain. At each spectral step the intensity was measured every 10 ms for half a second, and the result was then averaged out to reduce any noise. This process was repeated 8 times, averaged, and the results displayed in Figure 5.16.

The voltage received varies with the wavenumber as expected and roughly follows

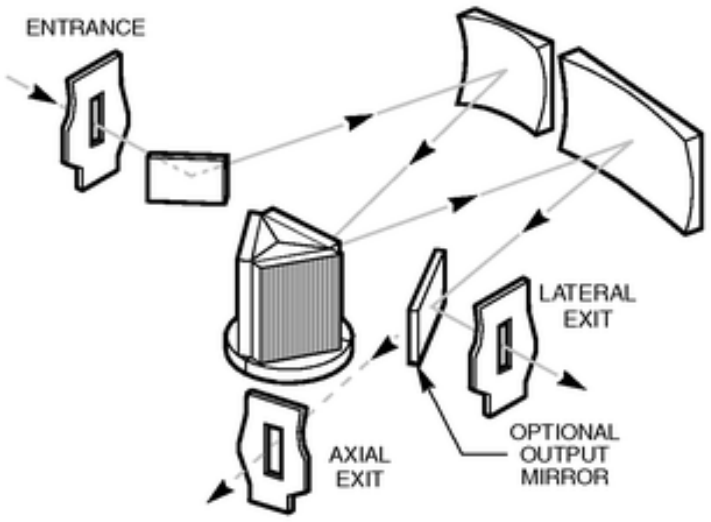

Figure 5.15: Optical design of the Cornerstone 260 1/4m monochromator. Credit: Newport /Oriel Instruments

a Planck function determined by the temperature of the lamp, the peak of which (as estimated from supplier information) is at 11100 cm^{-1} though this is expected to vary with the lower voltage used. The sharp drop and then recovery in signal observed from 15000-15500 cm^{-1} is a Wood's anomaly which is described by the theory of surface plasmon excitation (Hessel and Oliner, 1965).

5.6.1.1 Reflectivity Validation

The same experiment as that just described is effectively repeated, but this time with the inclusion of the FPE in the instrument path and using a smaller spectral range. In order to better constrain the impact of non-uniformity in the spectra, the spectra without the FPE were measured several times in order to ratio out the non-FPE spectral features and give the FPE spectrum in terms of transmission. Again this process was repeated to reduce errors and shown in Figure 5.17 in comparison to the supplied data.

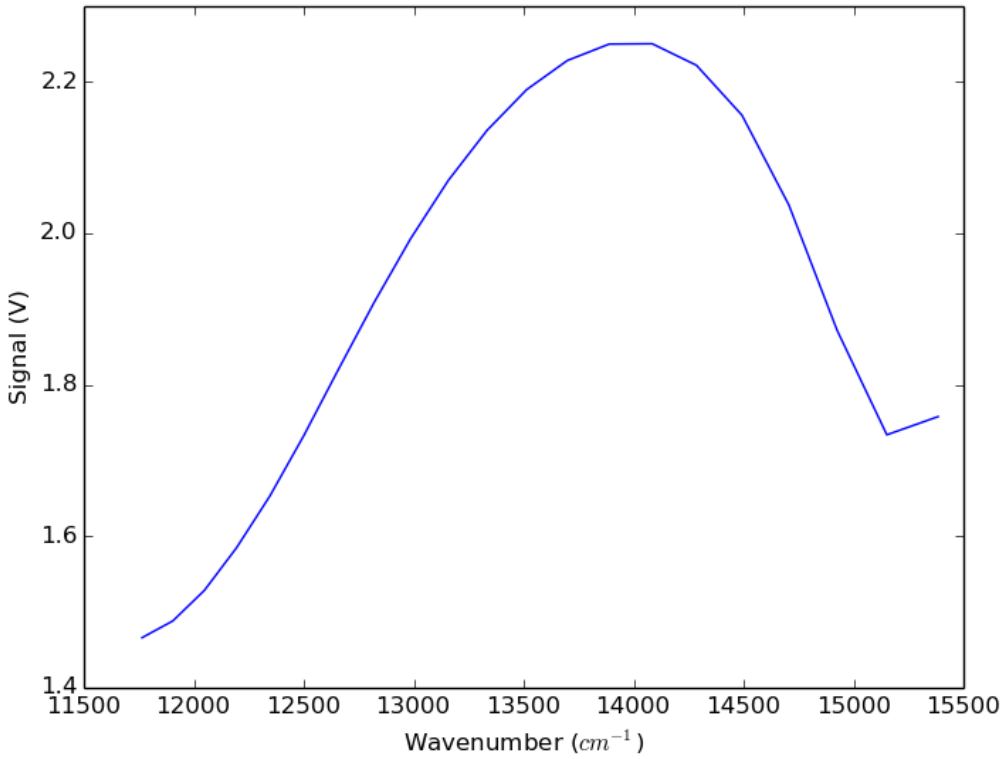

Figure 5.16: Spectrum of the QTH lamp convolved with the spectral response of the detector and monochromator

As can be seen the general form of the experimental data fits that of the suppliers, with a minimum transmission between 12500 and 13500 cm^{-1}. However there is a discrepancy in the extent of the minimum transmission and its sharpness. The suppliers have a much clearer minimum at 13000 cm^{-1} and has approximately 3% less transmission. The difference here will come from a number of sources, firstly poorer collimation than in the suppliers experiment, which will result in broader transmission lines, and secondly from the monochromator transmitting a range of wavelengths rather than the single wavelength assumed in the supplier data, as well as inconsistent wavelengths transmitted in the calibration compared to when the FPE was transmitted. Despite its flaws, it shows that the FPE is indeed behaving

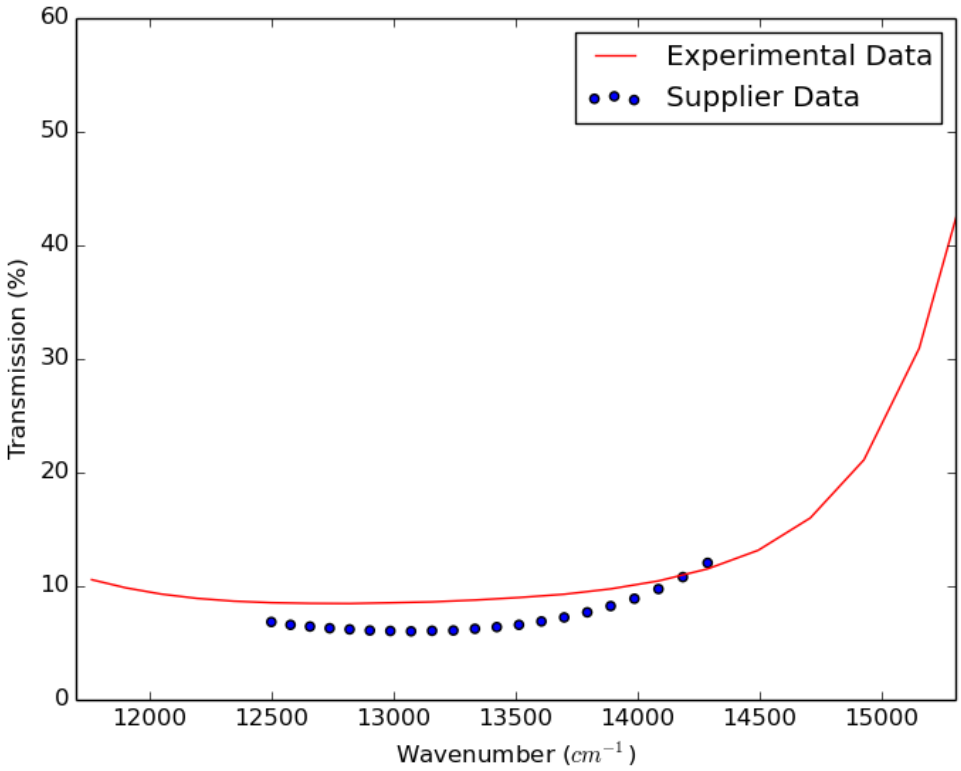

Figure 5.17: Transmission of the FPE as a function of wavenumber over a large range

largely as we imagined it too and that this rather crude arrangement could well be improved.

5.6.1.2 Instrument Line Shape Characterisation

Given the flaws identified in the reflectivity validation, it would be a challenge to accurately measure the transmission peaks of the FPE within the spectral range we are interested in, 13045 - 13105 cm^{-1}. However as the experiment was already set up, it was carried out anyway, and as a minimum would identify further weaknesses in the lamp-monochromator arrangement and provide a basis to design a better experiment. In this test, the same experiment was repeated but on a much finer scale

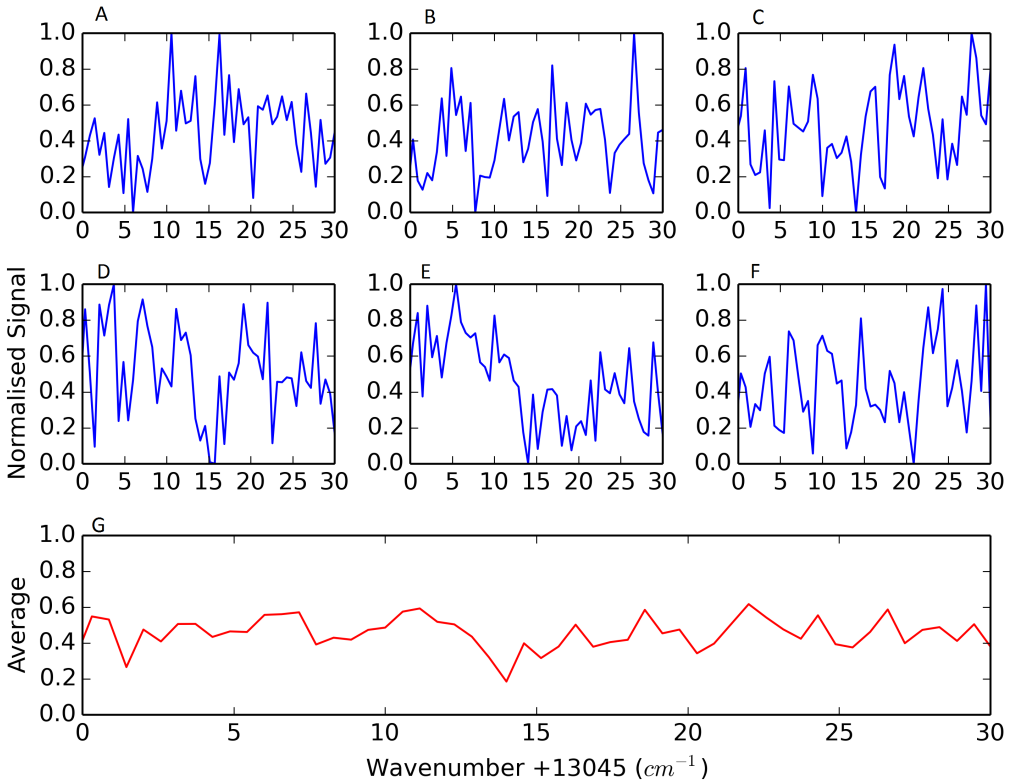

Figure 5.18: Transmission of the FPE as a function of wavenumber over a range of 30 cm^{-1}, for 6 experiments and averaged in the bottom panel

and again calibrated regularly to remove inconsistencies. The results are presented individually here in Figure 5.18 in order to highlight some of the problems with the experiment, and are normalised for clarity.

What we would ideally expect with a relatively broad light source (i.e. a light source comparable to, if not broader than the FSR) incident upon the FPE is generally high transmission with sharp drops as the light source lines up with the gaps between transmission lines, with these drops in signal separated by the FSR. Indeed we do see that occasionally in the results, i.e. panels b,c and d but the accuracy in wavelength is poor and clearly the repeatability appears to be weak. Therefore we can conclude from this that the wavelength selected by the monochromator is not

consistent in each case and is perhaps a combination of a random and systematic error (as they appear consistent in each experiment, but not with each other). If the result was purely random error, by averaging them out we should arrive at a reasonable approximation of the ILS. It could be concluded from some of the peaks that the FSR is around 10 cm^{-1} but not with any degree of certainty. As such, to make any progress in determining the line shape of the FPE an alternative light source with a high resolution and stability is needed.

5.6.2 Laser Diode

A laser diode was purchased that emits a relatively stable spectrum of light at 784 nm with a FWHM of approximately 1.5 nm in a Lorentzian distribution, which is roughly equivalent to 3 FSRs. The suppliers calibration of the diode is shown in Figure 5.19.

Although the laser is broader than the FSR, its shape will allow much more variability in the observed signal compared to the broad and near constant output from the lamp / monochromator system. The stability of the laser is not perfect, its output power is stable to less than 2% with the wavelength dependent upon the temperature of the diode, variations of the order of a few degrees can vary the central transmission wavelength by 1 nm. Additionally the line shape will vary with temperature according to supplier information. Regardless of the power and wavelength stability, determining the exact ILS through the FSR and reflectivity properties would be impossible with a fixed wavelength laser. However it will allow for an investigation into the scanning mechanism by observing the change in FPE intensity with the voltage across the PEA.

The experiment was set up similarly to the monochromator experiment, with the laser taking the place of the lamp and monochromator. In addition, the lens

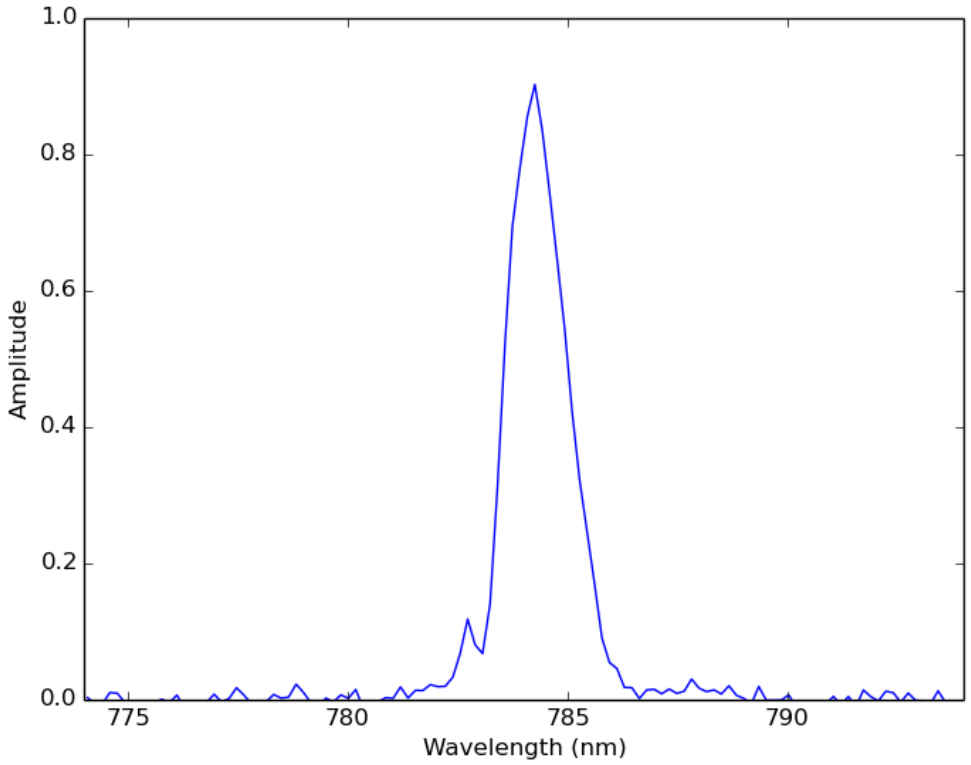

Figure 5.19: Laser diode line shape as supplied by ThorLabs

was placed after the FPE in the instrument chain as the laser was already highly collimated but relatively broad. This focused the resulting beam onto the detector, thereby increasing the signal. The voltage was supplied to the FPE by an amplifier which was in turn supplied by the DAQ. This had the advantage that the read out could be coupled directly to the supplied voltage.

The FPE suppliers state that for a maximum displacement of 12 μm, 150 V needed to be supplied. Assuming a linear relationship between voltage and displacement, we can calculate using Equation 4.8 that for one FSR a voltage change of a approximately 5 V is required. Therefore in order to observe several FSRs, 20 V was applied across the FPE in steps of 0.0125 V, taking 512 measurements at each point at a frequency of 1 kHz, taking approximately half a second in total for each

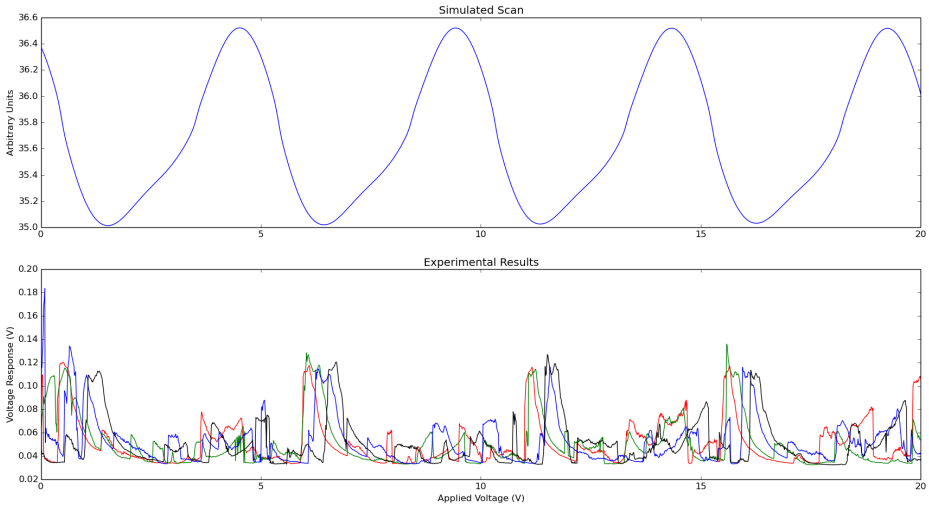

Figure 5.20: Results of 20 V scans of the FPE with the laser diode (bottom) compared to an ideal simulation using an FSR of 10 cm^{-1}

sample. To give the results more context, a simple simulation was conducted which convolved the laser line shape with an idealised transmission profile of the FPE using the same increase in FPE spacing. This is only used as an approximation of the resulting intensity in order to identify and validate the experimental structures in intensity. The results of this experiment, repeated 4 times in succession (denoted by red, green, blue, black in the order that they were performed), along with the simulation results are shown in Figure 5.20.

The structure of the simulation is typified by sharp peaks in intensity and broad troughs, with the peaks originating from increased alignment with the lasing wavelength. When we compare this to the four experimental results we do indeed see this variation, along with an additional smaller peak in-between the stronger lines. This corresponds to the slight peak observed in the simulation which in turn results from the secondary peak observed in Figure 5.19. Secondly we can clearly see that these strong peaks occur 4-5 times, again in accordance to the model. In broad terms then

we can confirm then that the FPE and laser combination is working as expected, however perfectly reproducing the model results would require a far more accurate understanding of the laser output (i.e. by monitoring its spectrum simultaneously) and a far higher degree of stability in its power output. It would also require far more knowledge of the FPE and the arrangement as previously discussed. However that wasn't the aim here; the aim was to further understand the performance of the scanning mechanism. This can be studied by looking at the results in more detail. Firstly we can see that the peak-to-peak voltage is not quite linear, with the voltage required decreasing with each peak. This will in part be driven by the decrease in FSR with increasing spacing but there is also some non-linearity expected in the voltage response. Accurately attributing this effect using this arrangement was not possible. We can also see that there is a hysteresis as expected, as the same voltage applied in a successive scan does not reproduce the same response; a clear drift is observed from red (1st) to black (4th), with the later experiments requiring a higher voltage. However the peak intensities are largely consistent, meaning that the proposed technique of self-calibrating the spectrum could still be possible.

We can also investigate the creep effect observed when holding the PEA at a specific voltage for a long duration. Though our measurements time are short, it is worth a brief discussion, as is any latency in the PEA expansion which should according to the suppliers be lower than a frequency of 10 kHz. The raw data for each experiment is shown at 1 V intervals in Figure 5.21.

As can be seen, though there is a large amount of fluctuation, there is no significant drift in the voltage or any lag in reaching the stable level, suggesting that creep is not an issue within these short integration times, and that latency is not an issue either. However, the latter could easily be masked by the instability of the intensity, indeed it is clear that in general there is a high amount of variability across each

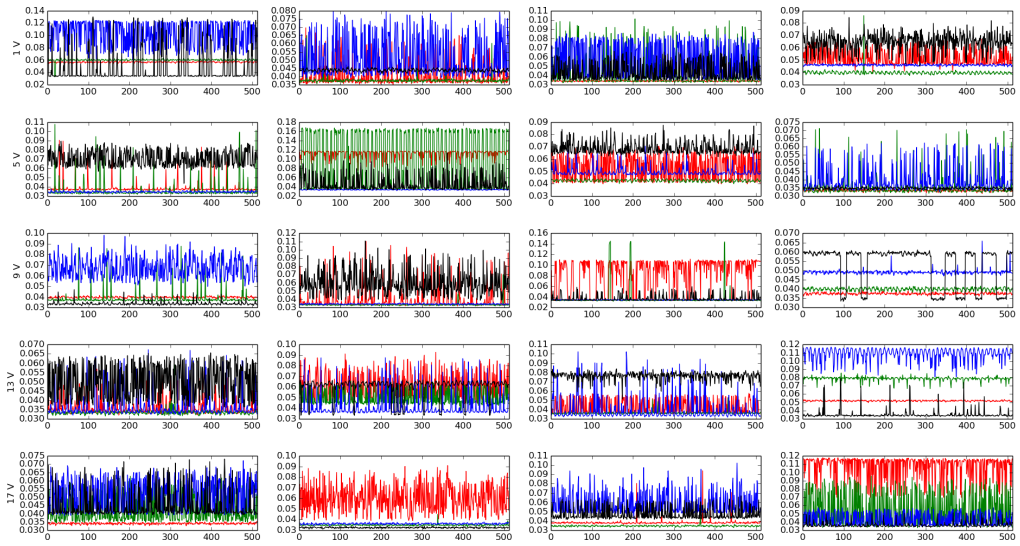

Figure 5.21: Output voltage as a function of measurement number within each step

step. The standard deviation at each step is shown in Figure 5.22 along with the cases where the error is below 10%. By comparing to Figure 5.20 we can see that the highest deviations occur within and close to the transmission peaks, particularly on the low voltage side of the peak. This could potentially be caused by instability in the secondary structure of the laser line shape. However the general observations are still present in the filtered data, and in many ways clearer.

In summary, the laser diode experiment verified the expected scanning behaviour of the FPE PEA system and confirmed the possibility of using the self-calibration method. To build upon this a more accurate understanding of the laser source is required, and ideally this source should be tunable across the O_2 A-Band. This would allow for the determination of the physical FSR, as in the monochromator experiment, rather than its voltage counterpart. The extra stability or active monitoring would allow for a more accurate study of the effects of hysteresis and the non-linearity of the voltage to displacement relationship.

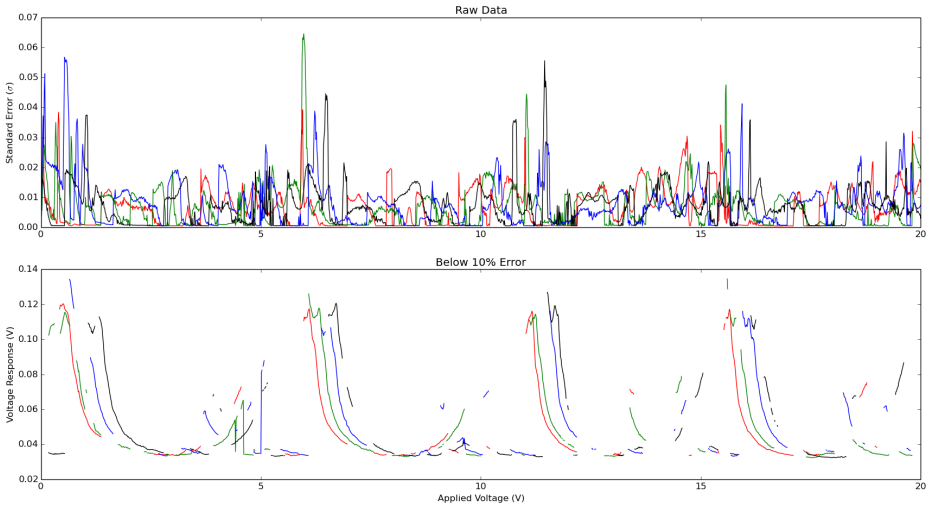

Figure 5.22: Standard deviations 20 V scans of the FPE with the laser diode (top) and the results filtered down to a below 10% error

5.7 Summary and Conclusions

A method of optimization was developed and used to obtain key parameters of the FPE design for aerosol retrievals in the O_2 A-Band, a FSR of 10 cm^{-1} and a reflectivity of 0.9. The resulting data from the FPE was then combined with detector data to develop a model instrument. This model instrument was then used in simulations of a spaceborne FPE, in line with previous studies presented in Chapter 3.

To summarise the simulations it has been shown that the spaceborne FPE will struggle below 600 mb, though this is minimised when the SZA is low and albedo is high due to the substantial gain in SNR. We observed that with increasing aerosol height the performance does not improve to the same extent as GOSAT, much the same as S5P, again if the albedo was increased or the SNR increased, perhaps by increasing the integration time or by using a more expensive detector, an improvement could be had as confirmed in the optimization process. Multiple aerosols however

present a far more similar problem to GOSAT and the previous instruments studied, with only minor degradations observed..

However even though these results are not overly promising, they are for a spaceborne FPE and can be significantly improved. In addition the performance of a groundbased FPE was shown to be more adept at retrieving AOD at relativly low SNRs, and with the removal of surface albedo as a source of uncertainty, and a greater sensitivity to the lower atmosphere, more accurate retrievals of boundary layer aerosol should be possible. In addition the design constraints are much more forgiving, particularly in reflectivity, and integration time can easily be increased, as is not the case for a spaceborne instrument.

With the design optimised and the performance assessed, the FPE was acquired and a number of preliminary experiments were undertaken. The first experiment involved the use of a lamp coupled to a monochromator. This allowed the verification of the reflectivity curve of the FPE when taking into account some non-idealisms of the experiment, however it was far too inaccurate to determine the ILS. A second experiment using a laser diode was performed with the aim to assess the behaviour of the PEA. Although there were several short comings, the experiment was successful in demonstrating that the hysteresis of the PEA, although noticeable, would hopefully be constrainable in the self-calibration scheme that has been devised. It was also found that the latency as expected was low and that creep within the time scale was minimal. Moreover this period of experimentation has led to the important development of several pieces of control code that are used in the gathering of data as well as establishing an instrument configuration that can both be used in further and more accurate experimentation. Such experiments would involve the use of a tunable and accurate laser to establish the ILS of the FPE and to investigate the noise properties more thoroughly.

Chapter 6

Groundbased Simulations

Following on from Chapters 3 and 5 this chapter focus on similar, but groundbased retrieval simulations. Spacebased profile retrievals of aerosols have been shown to have difficulties within the boundary layer due to strong correlations with the surface albedo and in some cases weak weighting functions, particularly for higher resolution instruments. For instruments at the surface the albedo effect is removed, although it will be expected to play a very minor role as will fluorescence by increasing scattering back into the detector by the aerosol layer. The sensitivity of the retrieval in this case should be strongly in favour of the boundary layer and lower troposphere due to the observed intensity resulting entirely from scattering events, which would largely be at low altitudes by aerosol. The downside of this approach is a decrease in signal. The drop in observed intensity comes from the fact that a groundbased instrument will be measuring scattered light only, a spacebased instrument will in addition to scattered light, measure light reflected from the surface, thereby increasing the SNR. The impact on information content is less clear as although in the groundbased case the aerosol layer is only traversed once, all of the intensity that is observed is scattered light.

To initially assess the groundbased retrieval performance we can look at the

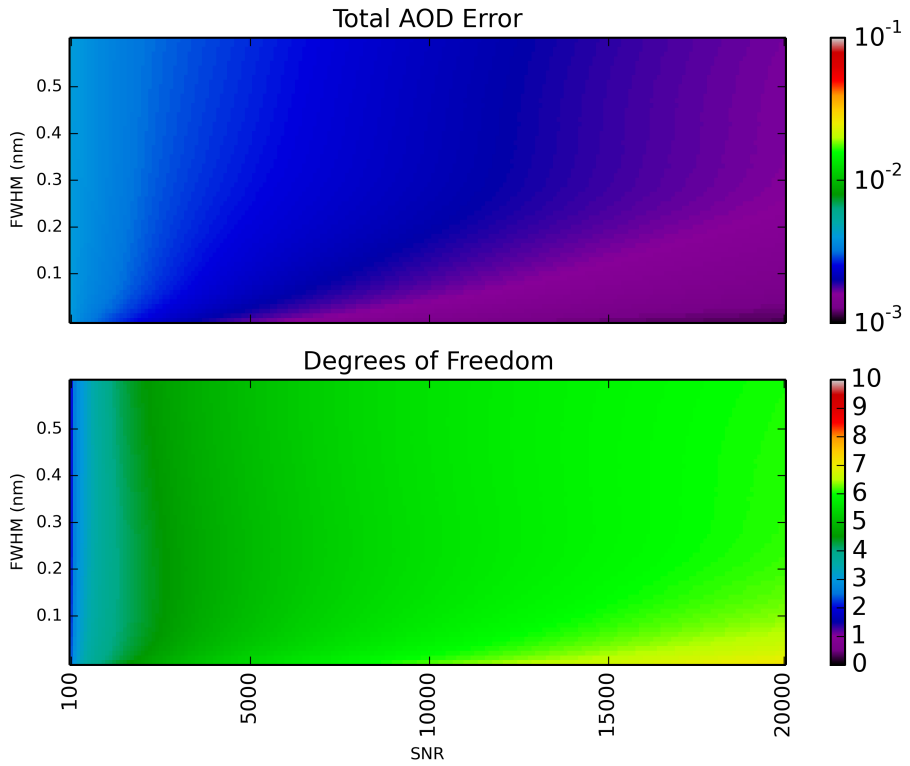

Figure 6.1: Total AOD error (top left panel) and DoF (bottom left panel) for the aerosol profile retrieval for scenario A, SZA 30° and albedo 0.5 as a function of continuum SNR and spectral resolution (as given by the FWHM of the ILS).

change in the degrees of freedom and AOD as a function of the key instrument parameters as in Chapter 3. For grating and Fourier transform spectrometer (such as GOSAT) these parameters are spectral resolution and SNR. The results for scenario A using the same procedure but for a groundbased instrument are shown in Figure 6.1 which shows the case for a groundbased zenith viewing instrument.

As can be seen there is dependence on both the SNR and resolution though it must be noted that the magnitude of the variation is typically small compared to the spacebased case presented previously. An increase in SNR of 5000 only achieves a DoF gain of 1 or an AOD error improvement of a third. Even if the SNR and

resolution were at their highest values, only 7 DoFs will be achieved, in comparison to the 10 shown for the spacebased instrument, at one tenth of the maximum SNR. The AOD error however is consistently lower than the spacebased case, with errors all below 0.1, with the minimum values approaching 0.01. The same can be said of the FPE as was previously mentioned in Chapter 5. However, much simpler instruments such as radiometers can obtain AOD to this level of accuracy, therefore it is the vertical information that we are most interested in.

Therefore to improve information content for groundbased observations we have to look at dramatically improving the SNR through far longer integration times than the 4 seconds used here, or by looking at alternate techniques such as multiple angles or the use of polarization. But before considering these aspects, a more rigorous assessment is given to better understand the characteristics of groundbased measurements of aerosol.

From the studies presented in Chapter 3 we concluded that GOSAT was not the ideal choice for aerosol retrievals compared to grating spectrometers such as OCO-2 and is not a typical choice for groundbased measurements. However, it is used here for comparison to the FPE for consistency with Chapter 5. The first section will look at the profile retrieval of aerosol using a FPE or GOSAT as uplooking devices, hereafter known as FPE-G and GOSAT-G before developing this and looking at the potential performance gains of using multiple angles as in Frankenberg et al. (2012) or polarization Boesche et al. (2008) compared to zenith viewing instruments..

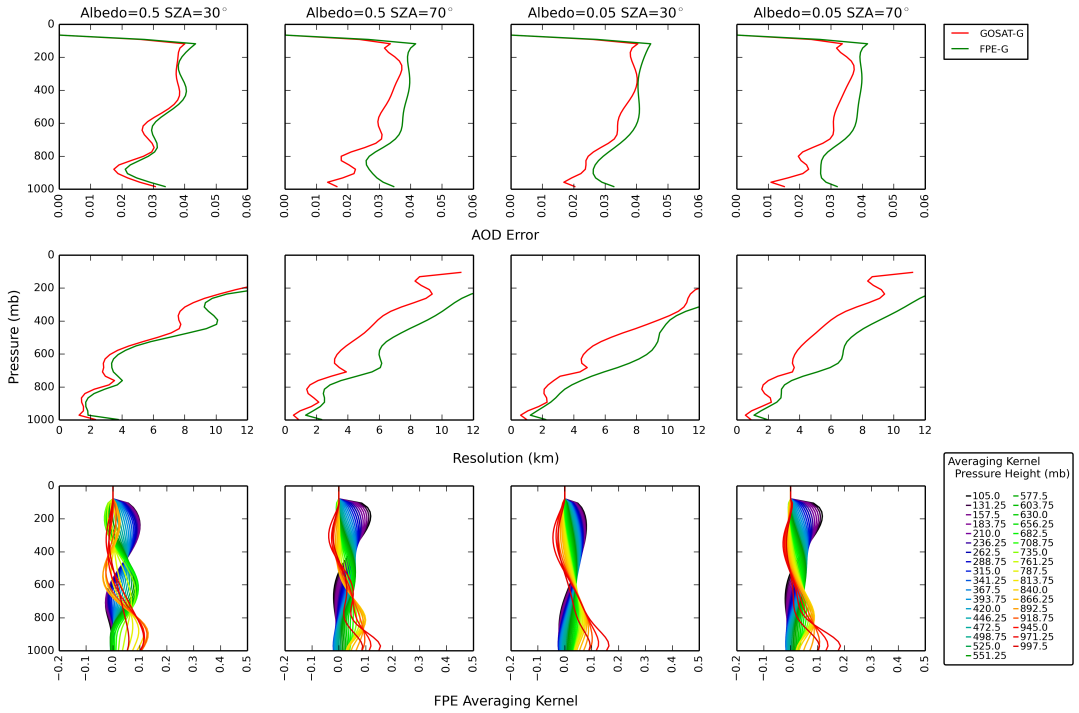

Figure 6.2: Error of LAOD (top panels) and vertical resolution (middle) as a function of pressure using the aerosol profile retrieval of scenario A for GOSAT-G and the FPE-G for groundbased measurements. The bottom row displays the corresponding averaging kernels for the FPE-G. Note the top four pressure levels are not shown.

6.1 Zenith Viewing

6.1.1 Single Aerosol Layer

Repeats of previous retrieval simulations have been undertaken but in this case considering the down-welling radiation instead of the up-welling. The same noise models as previously described have been used for consistency but for a groundbased instrument the SNR could be greatly improved by increasing the integration time. The first simulations consider single aerosol scenarios A and B and are shown in Figures 6.2 and 6.3.

As can be seen for Scenario A, the LAOD error (top row) is lower than 0.04

in all cases and significantly lower at the location of the aerosol layer. Comparing the instruments we see that in all but the case of high albedo, low SZA, the LAOD error from GOSAT-G is markedly better than the FPE-G. At high altitudes (above 600 mb) the LAOD error varies from 0.03 to 0.04 for GOSAT-G, the variation for FPE is minimal with values almost constant at 0.04. Below 600 mb the LAOD error is far more varied. LAOD decreases to 0.02, 0.025 at 800 mb for GOSAT-G and FPE-G respectively, after this the instruments diverge. FPE-G increases in LAOD error towards the surface where as GOSAT-G shows another local maximum and minimum before following FPE-G in increasing LAOD error nearer the surface.

Of interest also is the impact of surface albedo. At higher SZA, the change in the LAOD error is small when comparing the two albedos, at low SZA however, the changes are much more noticable, particularly for GOSAT-G. In this instance when the albedo reduces, so too does the LAOD error near the surface (by up to 0.01), caused by the decrease in light reflected from the surface scattering back to the instrument. As the albedo is not retrieved this induces an error in the near surface measurements, though in reality this could be removed by well characterising the albedo in the proximity of the instrument. FPE-G behaves slightly differently in that the very near surface LAOD is consistent over both albedos, however the minimum LAOD that occurs between 800 mb and 1000 mb decreases at higher albedo.

Overall, as expected, the LAOD error is far better for groundbased instruments compared to spacebased instruments where the LAOD error struggled to get below the required 0.05 level. However we also expect that the vertical information, described here by the vertical resolution will be degraded.

The resolution at low altitude is promisingly below 2 km, however this only lasts until 800 mb at best. Above 800 mb the resolution decays with only the high albedo, low SZA case showing promise and it achieves a 4 km resolution up to

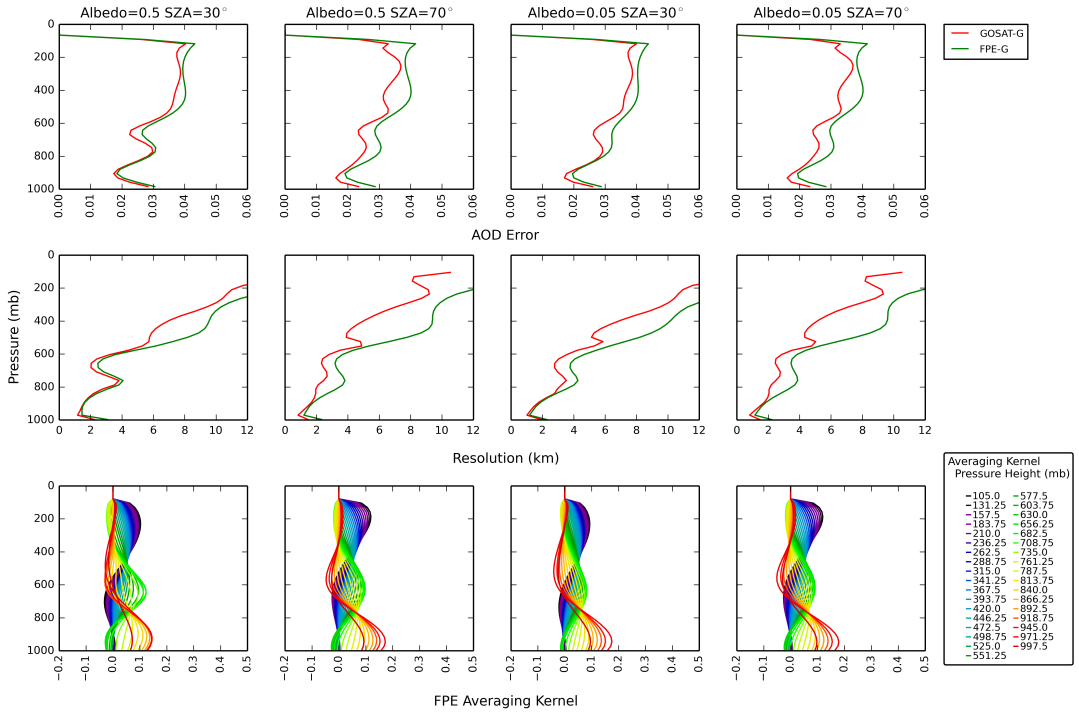

Figure 6.3: Error of LAOD (top panels) and vertical resolution (middle) as a function of pressure using the aerosol profile retrieval of scenario B for GOSAT-G and the FPE-G for groundbased measurements. The bottom row displays the corresponding averaging kernels for the FPE-G. Note the top four pressure levels are not shown.

approximately 600 mb (4 km). FPE-G performs similarly to GOSAT-G below 900 mb, as the altitude increases, the difference between the two increases with GOSAT-G maintaining a resolution of better than 6 km up to 500 mb whereas FPE-G decays far more rapidly. Compared to the spaceborne examples the high altitude resolution is substantially poorer (above 10 km), though this is made up for by the superior low altitude performance. This is to be expected as for groundbased instruments, as previously mentioned will be far more sensitive to the lower atmosphere.

The FPE-G averaging kernels are far broader then previous examples shown, illustrating the expected loss in information content, though there is evidence to suggest the retrieval of three or possibly four distinct layers.

When the aerosol is present at a higher altitude as in scenario B, Figure 6.3, we see a significant improvement in the relative performance of FPE-G and GOSAT-G. LAOD error for FPE-G is significantly reduced down to 0.02 at low altitude with the very near surface LAOD error below 0.03. In contrast GOSAT-G exhibits higher LAODs than in scenario A with minimums increasing to just below 0.02 and the near surface to 0.025. Between 800 and 600 mb both instruments improve their performance, above which the errors are largely unchanged. Resolution is far less affected in comparison so LAOD error although there is an improvement in all cases between 800 mb and 600 mb. Contrastingly a more sudden increase is observed above this height. These observations are explained by the aerosol layer effectively acting as the light source; the observed intensity corresponds directly to light scattered by the aerosol layer. The effect of albedo is minimised, again through increasingly unlikely additional scattering. Compared to the previous case, the difference between the viewing scenarios has been reduced, with all cases much more comparable to the 'optimum' case of high albedo and low SZA.

In the same manner as in Chapter 3 and 5, we assess these simulations more quantitatively by integrating over the 0-2 km, 2-5 km and total column height ranges. The results of which are shown in Figures 6.4 and 6.5 for scenarios A and B respectively along with combined aerosols scenarios that will be discussed in Section 6.1.2.

Firstly note that total AOD error shown is magnified by a factor of 10, meaning that in all cases, the total error is less than 0.005 (<2%). This dramatic reduction in error compared to the spacebourne examples is driven by strong negative covariances across the column. Positive covariances are prominent in the adjacent few pressure levels, however beyond this immediate range, the negative covariances of similar magnitude take over. This explains why the AOD error for integrated layers of

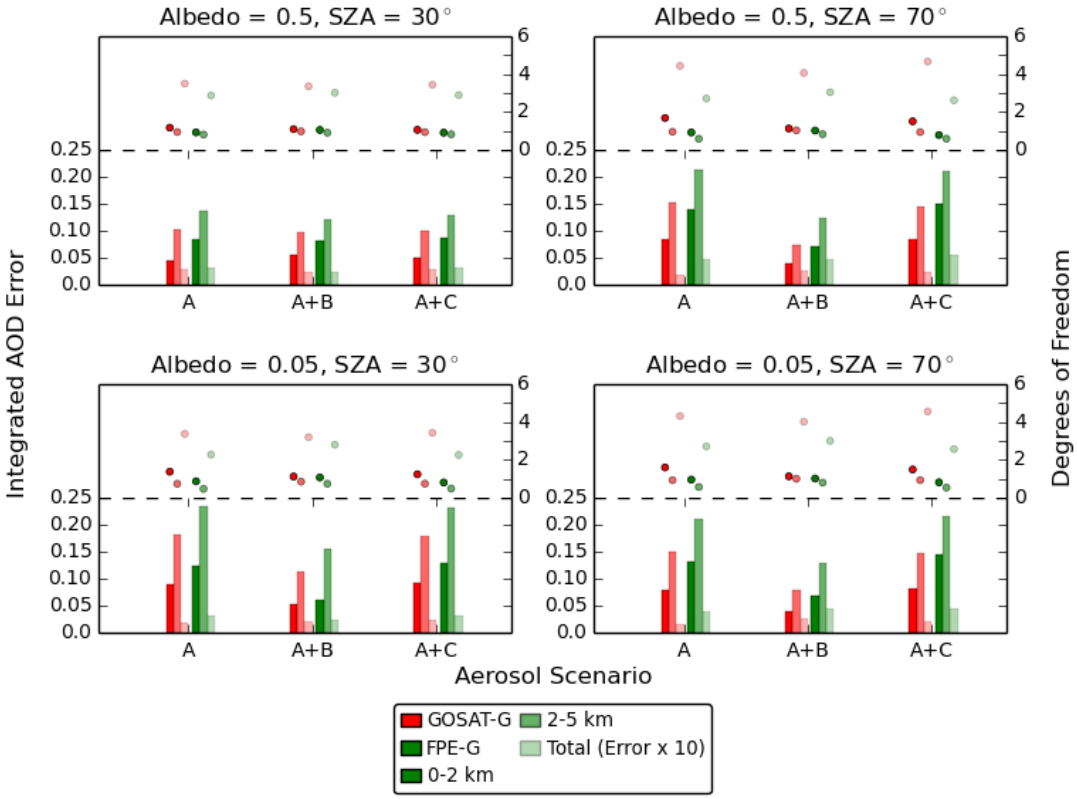

Figure 6.4: AOD error and DoF for the profile retrieval of scenario A for albedos of 0.5 and 0.05, SZAs of 30° and 70° when integrated over the 0-2 km and 2-5 km ranges as well as the total column. Combined aerosol retrievals are also shown for scenarios A+B and A+C. Differing shades of the same colour denote different integrated ranges

0-2 km and 2-5 km are not substantially reduced in the same way. The reason for the strong negative correlations is that all of the signal received by the instrument consists of scattered light, there is no direct sunlight. Thus, the total column of aerosol can be incredibly well retrieved in comparison to the spacebased cases.

In scenario A the total retrieved AOD error decreases with decreasing albedo for both instruments. The scale of this reduction is less than 0.002 for both FPE-G and GOSAT-G, with the difference minimised at higher SZA. Increasing the SZA also reduces the total AOD error for GOSAT-G by approximately 0.002 at high

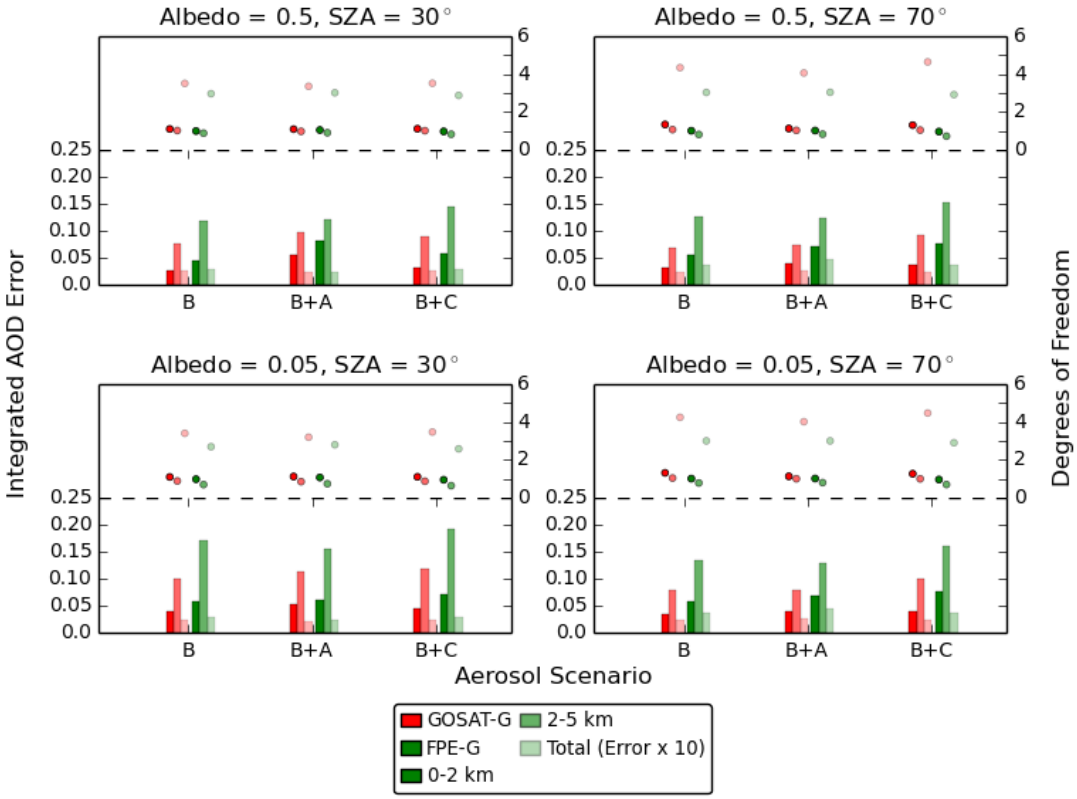

Figure 6.5: As Figure 6.4, but for scenarios B, B+A and B+C, noting that B+A is exactly the same as A+B.

albedo but minimally at low albedo. FPE-G on the other hand shows an increase in total AOD error with increasing SZA by a similar magnitude. Comparing the two instruments we see that the total error for GOSAT-G is always lower than FPE-G, with values lower than 0.0015 compared to 0.0025. They are far more comparable at low SZA, particularly at high albedo, however at high SZA GOSAT-G is typically better than half of FPE-G. The smaller integration ranges behave in much the same way but with far higher values in AOD error compared to the total error, with the FPE-G reaching over 0.2 in the 2-5 km range for Scenario A. The 0-2 km range is typically below 0.15 and as low as 0.05 in the case of GOSAT-G at high albedo and low SZA. FPE-G is always approximately 0.05 higher than GOSAT-G in the 0-2 km

layer and 0.06 in the 2-5 km layer though this difference reduces with high albedo and low SZA.

The total degrees of freedom in the upper parts of the figures, follows a similar trend. For GOSAT-G the total DoF is roughly 4 throughout but increases to almost 5 at high SZA. FPE-G on the other hand only obtains 2-3 DoF throughout, with far less of an increase, if any, with increasing SZA. If we then look at the 0-2 km and 2-5 km layers we can see where this increase in information content for GOSAT-G comes from. It is clear that an increase in boundary layer DoF is responsible with it increasing by almost one at high albedo with increasing SZA, obtaining two DoF overall. More generally though we can see that in all cases a minimum of one DoF can be retrieved in the 0-2 km, suggesting that this layer can be independently retrieved. The 2-5 km layer on the other hand varies more noticeably, FPE-G retrieved between 0.5 and 1 DoF, with the high albedo, low sza proving to be the best case. GOSAT-G on the other hand again almost constantly has a full DoF in this layer.

In Scenario B we observe a far more consistent set of errors and DoF. The total AOD error is always below 0.005 and the differences between FPE-G and GOSAT-G are minor, particularly at low SZA, at high SZA GOSAT-G is better by approximately 0.001. Again we see a total DoF of 3 for in all scenes for FPE-G with an advantage of 0.5-1.5 for GOSAT-G. In terms of the smaller integrated ranges we see that the DoFs is 1 in each range with GOSAT-G only enhanced by a maximum of 0.5. This means that the gain in total DoF at high SZA is likely to come from increased information from above 5 km. The corresponding errors are reduced in the 0-2 km layer compared to Scenario A with both instruments achieving errors below 0.05, though at high SZA FPE-G exceeeds this slightly with errors of 0.06. The 2-5 km layer is also substantially reduced from Scenario A though errors are

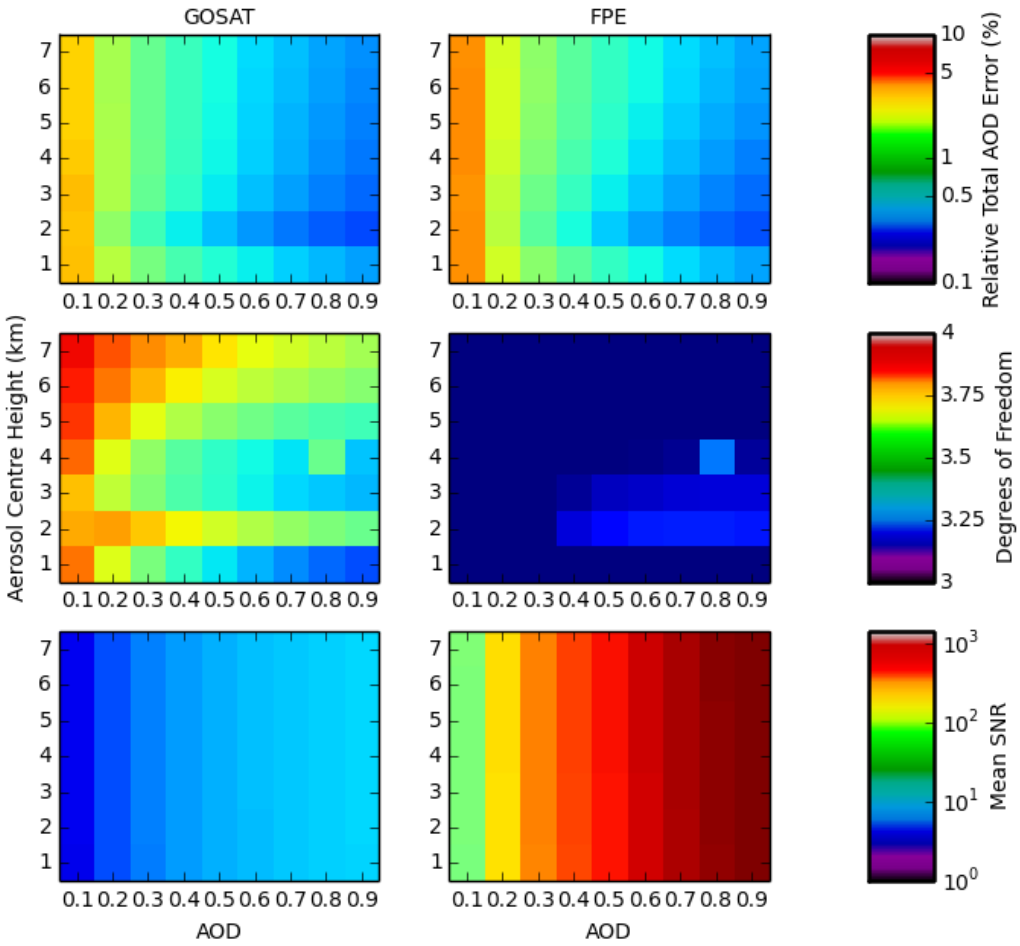

Figure 6.6: Total AOD error (given as a relative error), DoF and mean SNR as a function of aerosol centre height and AOD, for an albedo of 0.5 and SZA of 30° for GOSAT-G and FPE-G-G.

still high, with FPE-G now typically below 0.15 and GOSAT-G below 0.1.

To assess the effect of aerosol centre height on the total AOD error, we created a figure similar to that shown in Chapter 3 where we display the relative AOD error, degrees of freedom and SNR, as a function of AOD and centre height for our two groundbased instruments, Figure 6.6.

The top row, shows the relative total AOD error. We find that the performance

of the FPE-G and GOSAT-G are similar with GOSAT-G showing a consistently slightly better retrieval performance, most notably at low AOD, though this is still in terms of fractions of a percent. As a function of height we find little variations, though there is a minor improvement as the aerosol moves through the 2-5 km range. Lastly there is a consistent improvement in total AOD error with increasing AOD as anticipated.

The degrees of freedom is shown in the middle row of panels. The FPE-G DoF appears to be near constant in comparison to GOSAT-G, with a only a minor increase from an average value of approximately 3.1 to 3.2 at high AOD for 2-4 km, with no otherwise discernible trends. GOSAT-G on the other hand is far more varied with a typical increase in DoF (though it is still relatively small) with altitude and a strong decrease with increasing AOD. The maximum observed DoF for GOSAT-G therefore occurs at low AOD and high altitude, and reaches close to 4 DoF, with typical values around 3.5.

These variations are related to the increase in SNR with increasing AOD as shown in the bottom row of Figure 6.6. The SNR increases due to the increase in scattered light intensity. FPE-G varies by an order of magnitude from low AOD to high AOD, which is more than double the variation observed for GOSAT-G. The cause of this is that any variation in GOSAT-Gs SNR is amplified by the integrating nature of the FPE. The variation in SNR however does not however explain the variation with altitude observed in the DoF, particularly for GOSAT-G. This lack of variation in absolute terms is due to the lack of variation in Jacobians for varying optical depths and heights which is evidenced in Figures 6.7 to 6.9 which shows the Jacobians for an AOD of 0.7 for aerosol heights 1-3 km. These are additionally shown to highlight the cause of the increase in information content observed for GOSAT-G at 2km. The GOSAT-G Jacobians are shown only for a pair of absorption lines for clarity.

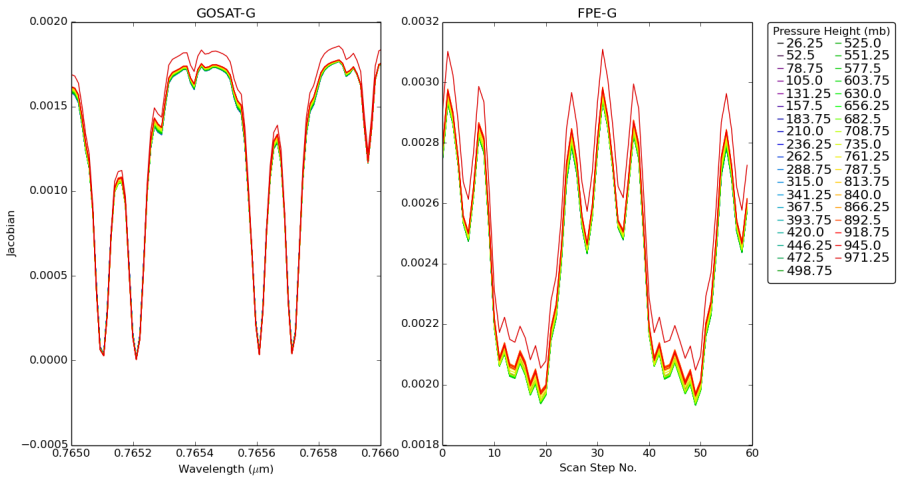

Figure 6.7: Jacobians for GOSAT-G and FPE-G at an AOD of 0.7, height 1 km under the same circumstances as Figure 6.6. GOSAT-G Jacobians are shown only for a pair of absorption lines for clarity.

From these Jacobians we can observe that as the aerosol height increases the low altitude Jacobians decrease, meaning the measurements are becoming less sensitive to the aerosols in these regions. However as aerosol height increases the individual layers become more distinct thus adding additional information. The result is that a peak in information content is achieved at a specific height which balances the two effects, as shown in Figure 6.6 noticably for GOSAT-G. Physically this comes from the increasing aerosol height allowing for more of the atmosphere to be probed by providing scattered light at a higher altitude, however less of this scattered light will be observed.

6.1.2 Two Aerosol Layers

Simulations involving the presence of two aerosol layers are also shown in Figures 6.4 and 6.5. The performance of the two instruments follows almost exactly the same pattern as the single aerosol layers shown (A and B) though the different

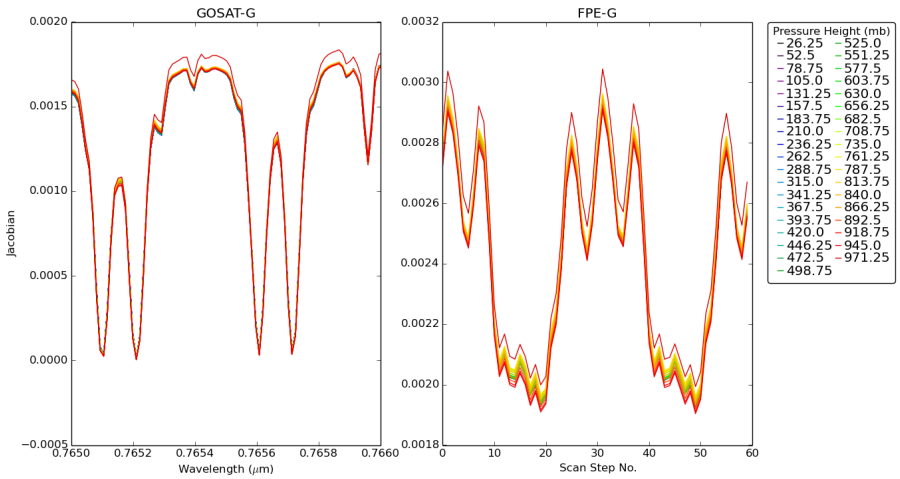

Figure 6.8: As in Figure 6.7 but for an aerosol height of 2 km.

aerosol combinations lead to differing results. The combination A and B often leads to a lower error compared to A alone, with reductions in the 0-2 km and 2-5 km layers, the total error however tends to increase. In all cases the errors are similar, the 0-2 km layer is again below 0.05 and 0.06 for GOSAT-G and FPE-G with vary little variation across all scenes. At 2-5 km the errors are more varied with slightly higher (0.01) values at low SZA though the impact of albedo is minor. On average the values in the 2-5 km range are lower than the single aerosol layer case A at a maximum of 0.12 and 0.1 for FPE-G and GOSAT-G. In terms of DoF we see a slight decrease in 0-2 km DoF from that obseverd for a single aerosol, particularly relative to Scenario A. The 2-5 km and total DoF is only minorly reduced, if at all, by 0.5.

The cases of A+C or B + C, the impact of the cirrus layer is only minor, small increases in error compared to the single cases are observed. However there is a slight increase in the total DoF due to the cirrus layer informing on higher altitude levels in the atmosphere. Relative to the space based case the impact of this cirrus layer is far less of an issue in the retrieval of tropospheric aerosols, which is of course expected because of the lack of sensitivity to the upper atmosphere for groundbased

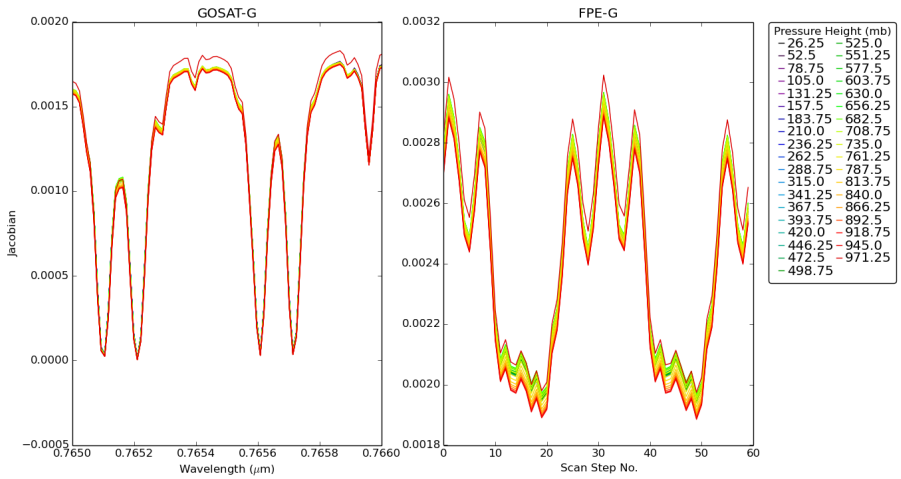

Figure 6.9: As in Figure 6.7 but for an aerosol height of 3 km.

measurements.

6.2 Off-Zenith Measurements

Varying the viewing angle can provide more information on the vertical distribution of aerosols. This is due to higher VZAs (closer to the horizon) corresponding to a lower altitude scattering height as illustrated in Figure 6.10. This figure also demonstrates that at higher VZAs a greater optical thickness will be observed and so alter the resulting information content.

We can evaluate what each angle is capable of by altering the previously used arrangement has been made; the SZA is close to zero and the VZA is varied for GOSAT-G and FPE-G with scenarios A (Figure 6.11) and B (Figure 6.12). Note that we treat the atmosphere as plane-parallel, which would introduce uncertainty for particularly high VZAs in reality.

As can be seen in both figures, the higher VZAs consistently out perform the lower VZA cases. VZA 85° always has the lowest error and the best resolution (<0.03

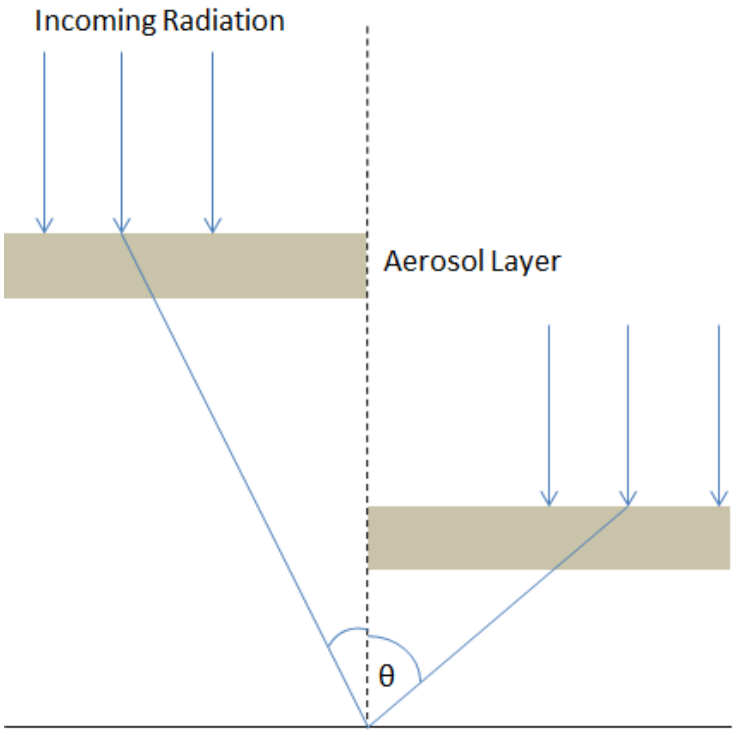

Figure 6.10: Groundbased geometry illustrating the dependence upon aerosol height and VZA, denoted by θ

and 1 km respectively) when the aerosol is within the boundary layer. However when aerosol at higher altitudes are considered, other high VZAs come into play, particularly in the FPE-G, with angles as low as 50° becoming useful, i.e. they have better errors and resolution. This benefit becomes much clearer as the aerosol is moved higher to 3km in scenario B. It is clear that our initial expectation is correct; higher VZAs give the best results near the surface, lower angles show increased performance at high altitudes.

To further quantify the variation in AOD error and DoF due to differing VZAs we can integrate the the previous profiles over the usual ranges, 0-2 km, 2-5 km and the total column, as well as the 5-10 km range for some extra detail. These are shown for scenarios A and B in Figures 6.13 and 6.14.

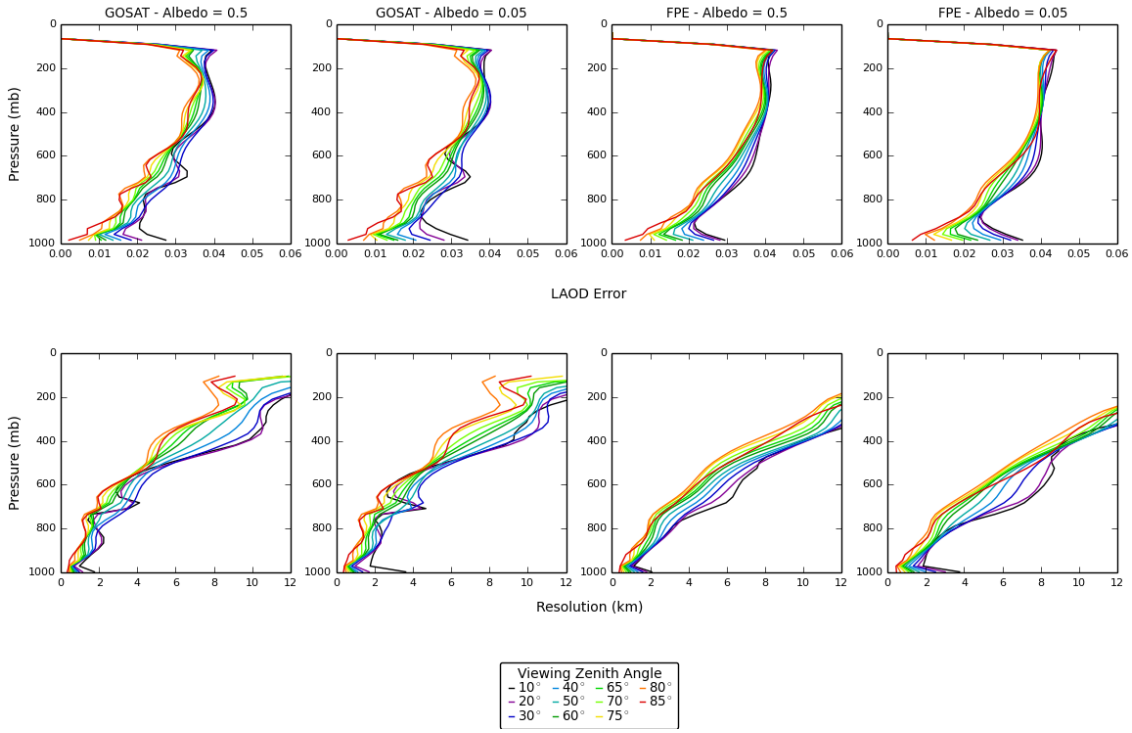

Figure 6.11: Error of LAOD (top panels) and vertical resolution (middle) as a function of pressure using the aerosol profile retrieval of scenario A for GOSAT-G and the FPE-G for groundbased measurements and viewing angles, solar zenith angle is 0°.

For scenario A we can see that the general trend in all the error quantities is to decrease error with increasing VZA, as expected from the previous figures with the higher VZAs increasingly looking into the aerosol layer. There is a slight increase in error going from 80° to 85°, which is stronger in both relative and absolute terms for lower albedo, which is further emphasised for Scenario B.

The total error decreases with increasing VZA but only from approximately 0.003 to 0.0015 with GOSAT-G and FPE-G showing only subtle differences. The total DoF however shows far more variation between the two instruments, both increase near linearly but with GOSAT-G reaching 6 DoF compared to FPE-G which achieves between 3.8 and 4.5 DoF.

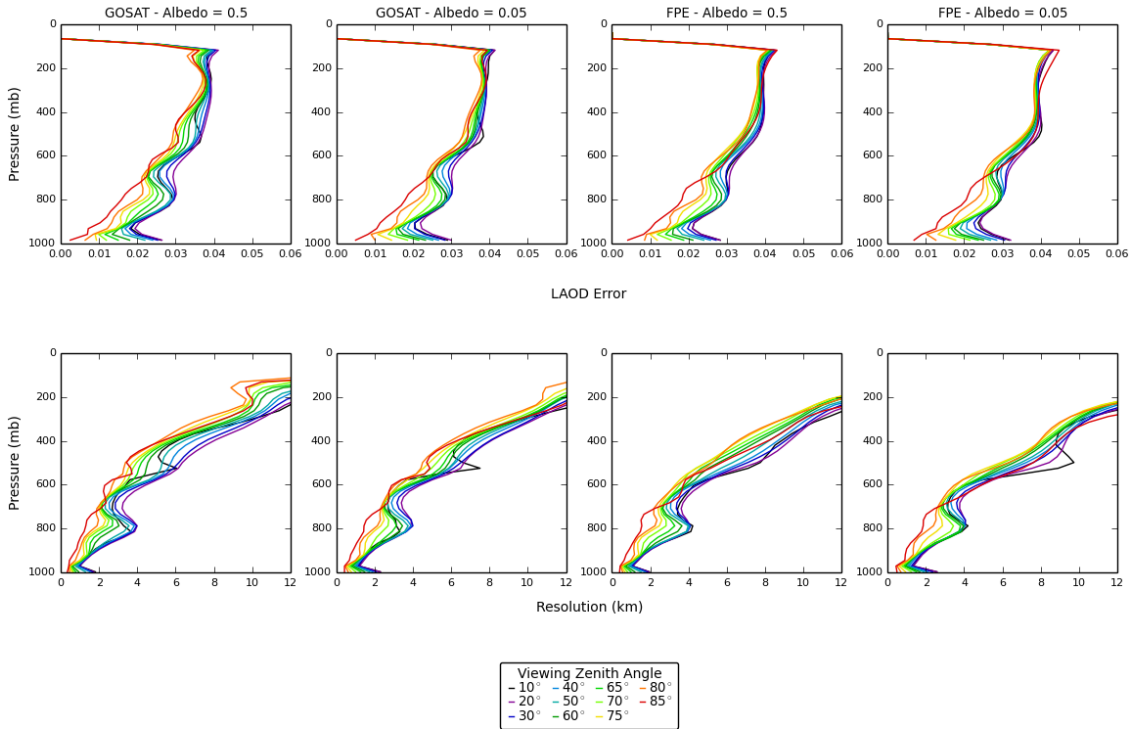

Figure 6.12: Error of LAOD (top panels) and vertical resolution (middle) as a function of pressure using the aerosol profile retrieval of scenario B for GOSAT-G and the FPE-G for groundbased measurements and viewing angles, solar zenith angle is 0°.

The 0-2 km range is by far the lowest of the sub sections in terms of of AOD error, and can reach below the required 0.05 error if the VZA is suitably high, however it is noticeably affected by albedo, particularly at low angles and for FPE-G where errors are higher at low albedo. The DoF increases upto 2 and 3 for FPE-G and GOSAT-G and the impact of albedo is more constant with a reduction of 0.2 across all angles for low albedo. We can see that a large part of the increase observed in the total DoF with increasing angle is accounted for by the increase in the 0-2 km range.

The 2-5 km and 5-10 km layers behave similarly in both AOD error and DoF. The 2-5 km layer was shown to achieve errors below 0.1 and 0.15 for GOSAT-G and

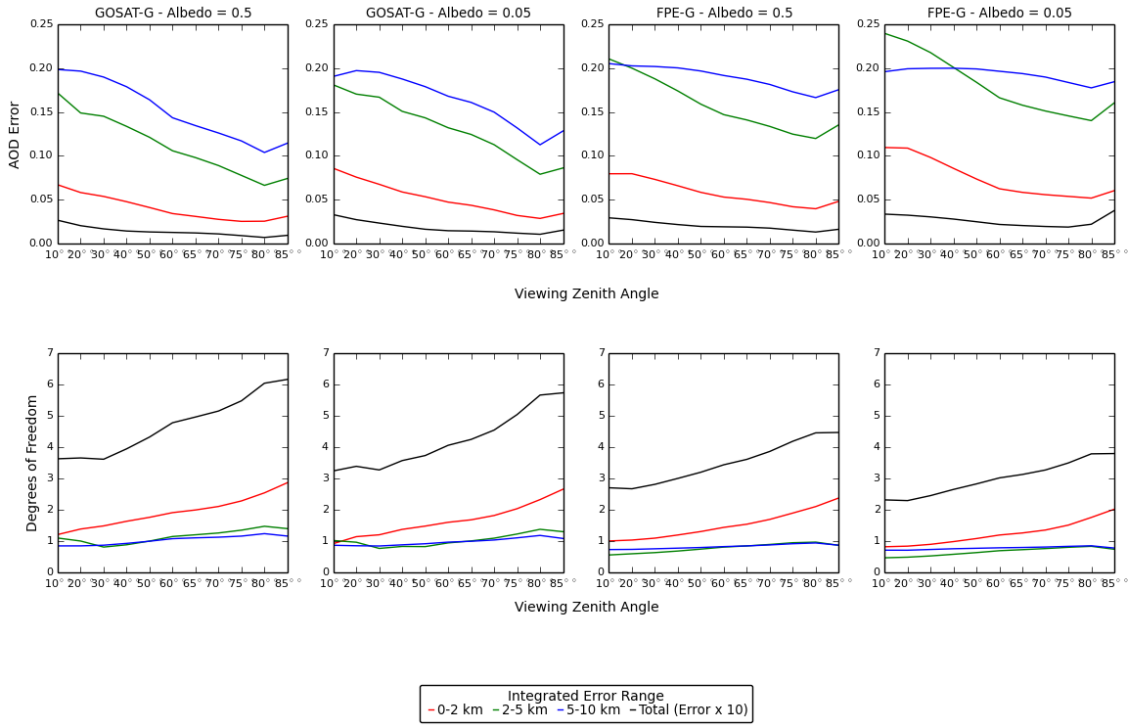

Figure 6.13: Integrated Error and Degrees of Freedom for scenario A as a function of viewing angle.

FPE-G at high VZAs and are far less noticeably affected by albedo as compared to the 0-2 km layer. The DoF does increase with increasing angle but the the scale of this is of order 0.1 for GOSAT-G and less so for FPE-G, approximately 1 DoF is consistently obtained though slightly less for FPE-G. The 5-10 km DoF is similarly unaffected by VZA and albedo and the FPE-G error is particularly unchanged with albedo. The scale of variation in the retrieved errors here is far less for FPE-G with only a reduction of 0.025 at higher angles, though GOSAT-G still shows a strong reduction but in absolute terms the errors are still high.

In Scenario B (Figure 6.14) we observe the same trends as previously discussed. The notable differences are a much higher increase in total DoF, in part due to the 0-2 km layer but also more strongly by 2-5 km layer. We also see that the 2-5 km

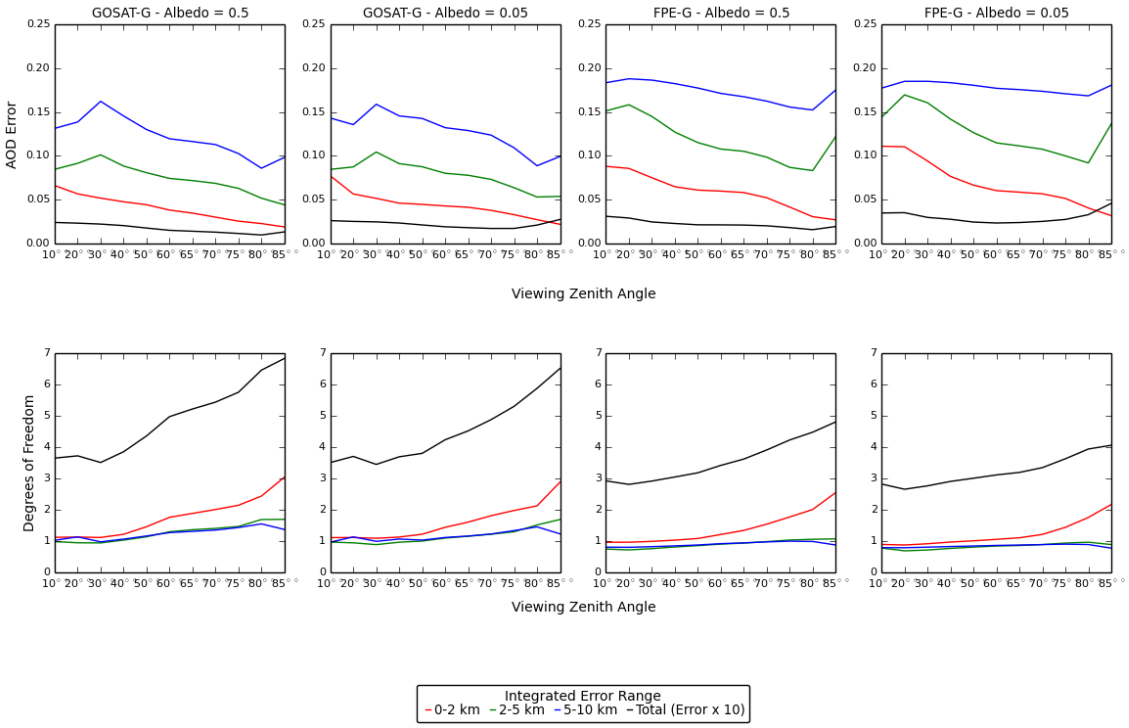

Figure 6.14: Integrated Error and Degrees of Freedom for scenario B as a function of viewing angle.

layer is more often more precisely retrieved by angles less than 85° but still relatively high, though in the 0-2 km layer it is clearly the strongest performer. The result is that the general trend of decreasing total error with increasing VZA observed in Scenario A is weaker, with the lowest errors occurring at slightly lower angles.

From these initial observations we can conclude that increasing the VZA will drastically improve the information content relative to the zentih viewing case as DoFs as high as 5 or 6 for FPE-G and GOSAT-G. To investigate this further we can look at how the SNR and Jacobians change with different VZAs as they will determine the AOD errors and information content respectively.. The mean SNR as a function of VZA and albedo for scenarios A and B and are shown in Figure 6.15.

SNR decreases as a function of VZA before increasing at high angles. The de-

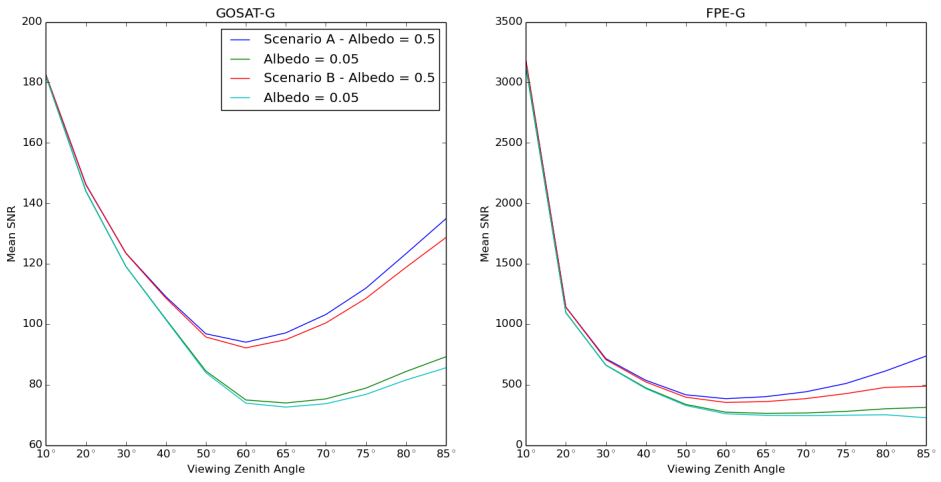

Figure 6.15: Mean SNR as a function of VZA and albedo for scenarios A and B using FPE-G and GOSAT-G.

crease is driven by the decreasing phase function with the increase resulting from higher angles observing more of the aerosol layer at lower altitude, hence why it is tempered in Scenario B. Additionally as the VZA increases the impact of albedo becomes increasingly apparent along with the aerosol height as expected. The effect of aerosol height is lessened for FPE-G as is the subsequent increase in SNR. This helps to explain the substantial uplift in performance at higher angles and the difference between the retrieval performance for the different albedos as well as the lesser variability for FPE-G.

A sample of the Jacobians comparing 30°, 70° and 85° for Scenarios A and B and 0.5 albedo is shown in Figures 6.16 and 6.17. For Scenario A with increasing VZA we see two things; firstly the Jacobians weaken which is governed by the decrease in signal and secondly that the lower altitude Jacobians become increasingly well seperated. This results in a much stronger dependence upon the lower aerosol levels at 85°, though at 85° we also observe that the mid to upper altitude Jacobians are less well resolved, explaining the increase in performance at higher altitudes for

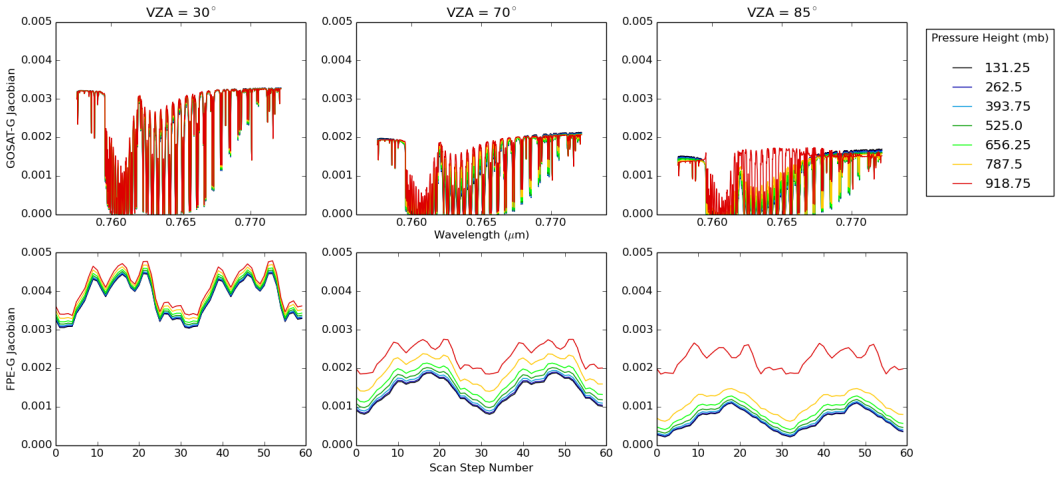

Figure 6.16: Jacobians comparing 30°, 70° and 85° for Scenario A and 0.5 albedo for GOSAT-G (top) and FPE-G (bottom).

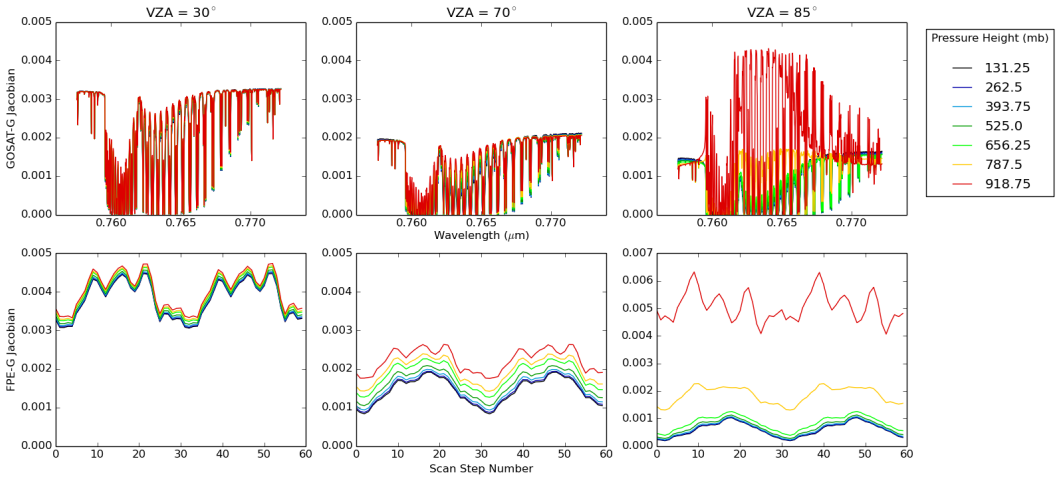

Figure 6.17: Jacobians comparing 30°, 70° and 85° for Scenario B and 0.5 albedo for GOSAT-G (top) and FPE-G (bottom).

angles such as 70°. In Scenario B shows similar trends however the scale of the improvement in the Jacobians at low altitude are substantially larger.

6.2.1 Combined Angles

As mentioned, combining different viewing angles can increase the information content of the aerosol profile. The previous plots of LAOD and resolution (Figures 6.11 and 6.12) showed that VZAs of 80° and 85° provided detail at lower altitudes whereas lower angles such as 70° improved the knowledge of higher altitude aerosols. As such combining these different angles would improve the overall information content compared to any single angle.

The measurements are combined by merging the Jacobians and recomputing the errors and degrees of freedom. To do this the Jacobians are concatenated together, the measurement errors are also combined and then the averaging kernel ($\mathbf{A}$) and a posteriori covariance matrix ($\hat{S}$) are computed using Equations 2.34 and 2.33 respectively. To ensure like for like comparisons, single angle cases must be concatenated with themselves, or have their SNRs improved by the square root of the number of angles combined due to the increase in integration time. We use the first approach.

Figures 6.18 and 6.19 demonstrate this approach for selected VZAs of 85°,80°,75°,70°, 30° and the combined measurement for Scenarios A and B. The 30° is chosen as an extreme value to help constrain high altitude aerosols. The figures show the LAOD error and resolution for each measurement angle for GOSAT-G and FPE-G.

In the majority of cases, as we expect, the combined measurement provides the best performance in both LAOD and resolution. Considering Scenario A (Figure 6.18), we observe that improvement compared to the single angles of the combined measurement is only minor for GOSAT-G. Only very subtle changes from 80° or 85° are observed, the most notable of which is below 800 mb, where the aerosol is located. However FPE-G shows improvements of up to 0.005 in this region and maintains a much greater improvement thorughout the column, particularly at 750 mb and 600 mb. We also see that at a high altitudes (above 400 mb) with low

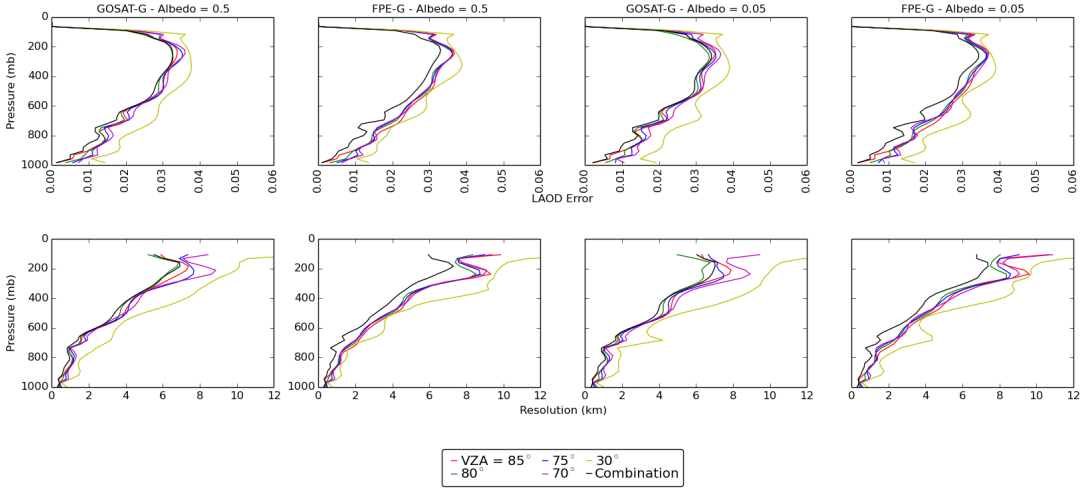

Figure 6.18: LAOD and resolution profiles for single angles and the combined measurement for Scenario A and 0.5 and 0.05 albedo for GOSAT-G and FPE-G.

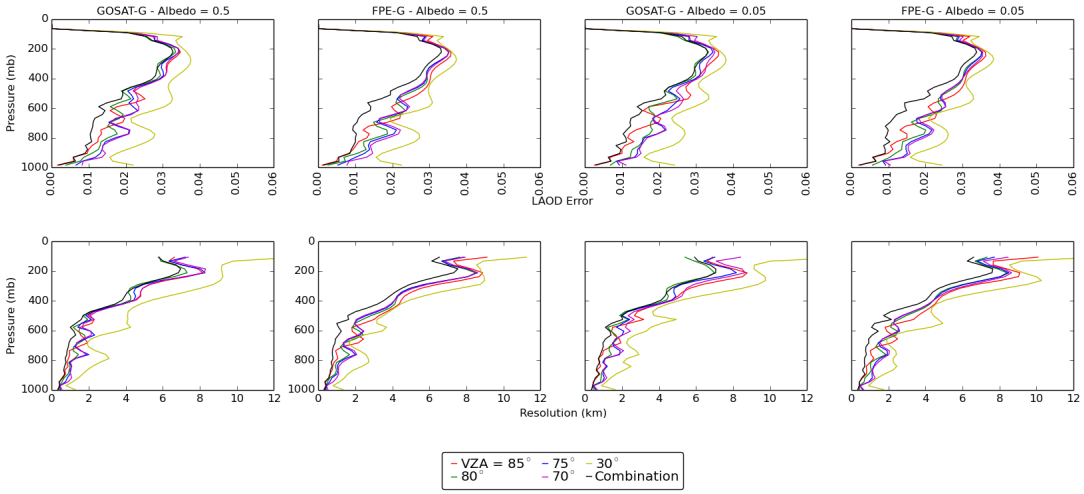

Figure 6.19: LAOD and resolution profiles for single angles and the combined measurement for Scenario A and 0.5 and 0.05 albedo for GOSAT-G and FPE-G.

albedo, the combined AOD of GOSAT-G is not better than the 80° profile. This is the result of the inclusion of poorer angles, i.e. 30°, though this is not observed in FPE-G. The vertical resolution in the bottom row of panels shows a similar trend. The improvement due to combinging angles is not appreciable for GOSAT-G relative

to the higher angles, however FPE-G is significantly benefited with improvements of up to 1 km. The result is that FPE-G is far more comparable to GOSAT-G than was previously presented.

When the aerosol is moved higher in Scenario B we observe a substantial increase in the improvement for GOSAT-G by 0.005 in LAOD and 0.25 km in resolution. Additionally the high altitude levels in the low albedo case show a far weaker advantage of the 80° profile to the combined. FPE-G again shows a strong improvement, with a reduction of approximately 0.01 in LAOD and 1 km in resolution at 600 mb in both cases.

To further quantify the advantages and disadvantages of measurement combination we can integrate the errors as repeatedly demonstrated. These are shown in Figures 6.20 and 6.21 for Scenarios A and B respectively.

Firstly it can be seen that for the single angle cases, the behviour is unchanged from the previous cases with all errors reduced and DoFs increased as one would expect with what is in effect a five fold increase in signal. However when we consider the combined case we see that all AOD errors are lower than in any other case and the DoFs are higher. This boost in performance is less apparent for GOSAT-G where the DoF increases by a maximum of 1 in scenario B compared to the next highest value at 85°, whereas for the FPE-G the increase in information content is typically 2 DoF in either scenario. The AOD errors repeat this trend but the scale of the improvement is much more restricted in the boundary layer, though the 2-5 and 5-10 km ranges do show improvement with a reduction of upto 50% for the FPE-G.

The gain in DoF and improvement in error looks to come mostly from the 2-5 km range, particularly in scenario B, with the other two ranges contributing slightly to the increase. To investigate this further we can study the averaging kernels as

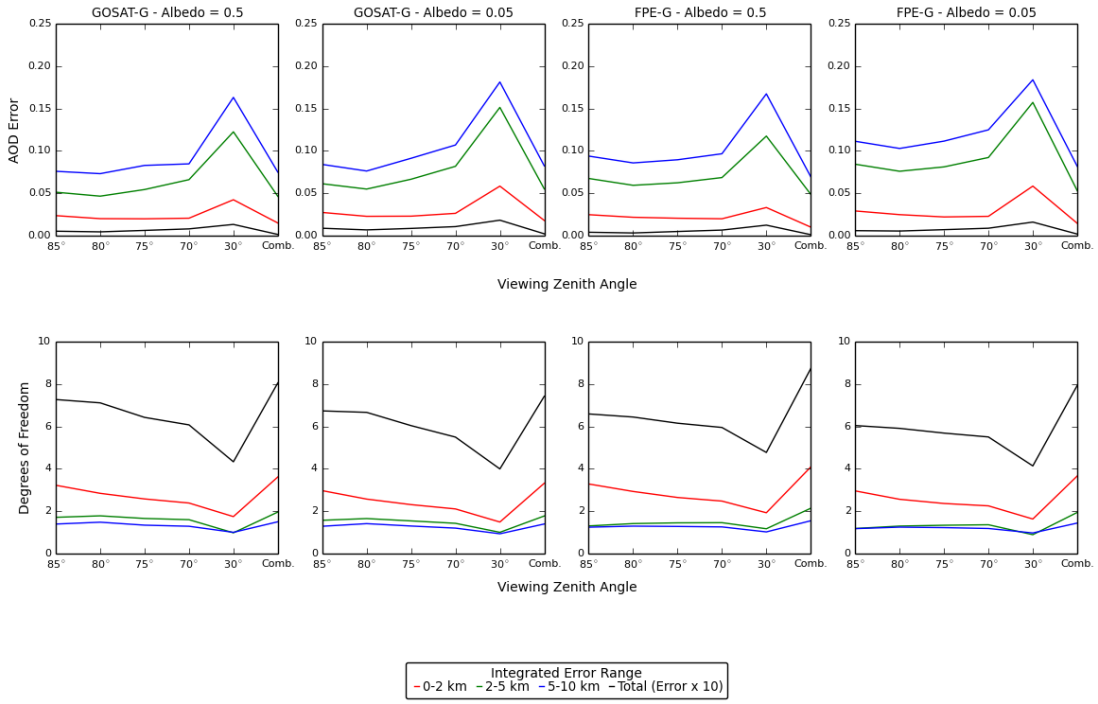

Figure 6.20: AOD errors and degrees of freedom for selected self-concatenated angles and combined together for scenario A.

we have done previously. An example is shown in Figure 6.22, which shows the averaging kernels for the FPE-G for scenario A with an albedo of 0.5. Firstly as one would expect we do see increasing values of the kernels as the angle increases to 85°, though the magnitude of this decreases for the higher (green to blue) kernels. However when the retrievals for the multiple angles are combined, the 800-600 mb kernels are greatly enhanced in this range, more so than for any other single height, thus explaining the previous gain in the 2-5 km integrated range.

6.2.1.1 Two Aerosol Layers

We now look at how combining observations of various VZAs will impact upon the retrieval of aerosols when two aerosol layers are present. Given what we have observed about the relationships between aerosol height and VZA we can expect

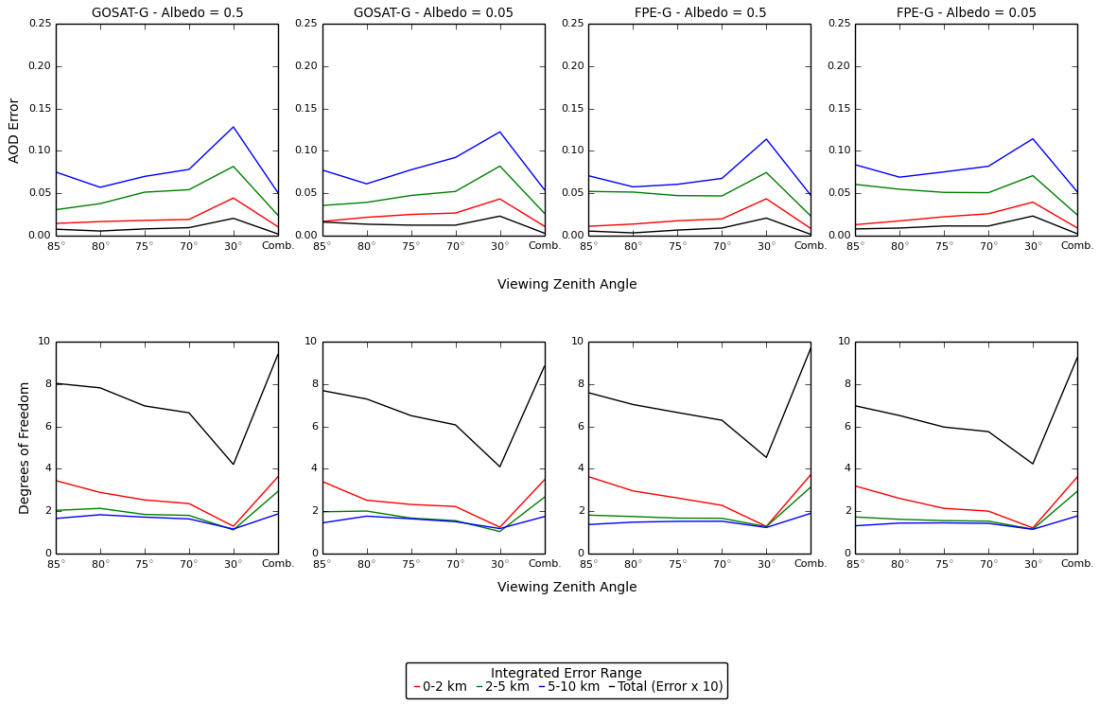

Figure 6.21: As with Figure 6.20 but for scenario B.

to see some variety in the information content location for single angles, and when combined it might be possible to significantly improve the retrieval performance and to obtain good separation between the layers. Figures 6.23 - 6.25 show the results for such simulations for scenarios A+B, A+C and B+C.

Considering firstly A+B (Figure 6.23) we observe that again the combined measurements produce the lowest AOD errors in all ranges. Of the single angles, the lowest errors consistently occur for 70° to 80° with FPE-G favouring higher angles than GOSAT-G. The single angles show similar trends to Figures 6.20 and 6.21 with the additional layer increasing the error for the 2-5 km and 5-10 km ranges at 85° though decreases at 30°. The total DoF for combined measurements is slightly lower then in Scenario A, resulting from a decrease in the 0-2 km layer, the 2-5 km layer is however slightly increased. Adding an extra layer above Scenario A does

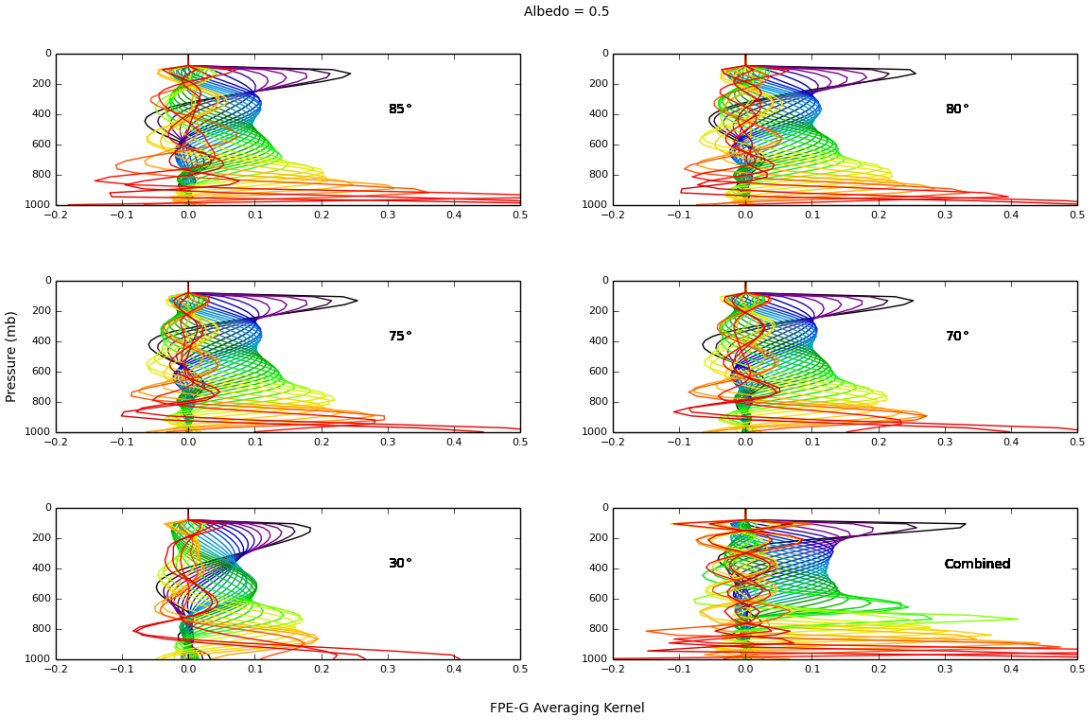

Figure 6.22: Averaging kernels for FPE-G, scenario A, albedo = 0.5.

not substantially alter the retrieval performance for the combined measurements or single angle measurements, except for 30° and 85°.

Following on from this is Figure 6.24, which shows scenario A+C. Compared to Scenario A we see an increase in error for the single angles across all ranges. However when combined, the 5-10 km error is reduced, by 0.025 in some cases. This reduction in error corresponds to an increase in DoF by almost 1 in the 5-10 km layer. Accordingly the total DoF also increases with FPE-G approaching 10 DoF and GOSAT-G exceeding 8 at high albedo.

The last example, and perhaps the most extreme given the improvements observed with higher altitude aerosols, is the case for Scenario B+C in Figure 6.25. The 0-2 km error is largely unaffected by the addition of the cirrus layer to scenario B, however the 2-5 km and particularly the 5-10 km ranges suffer in precision, par-

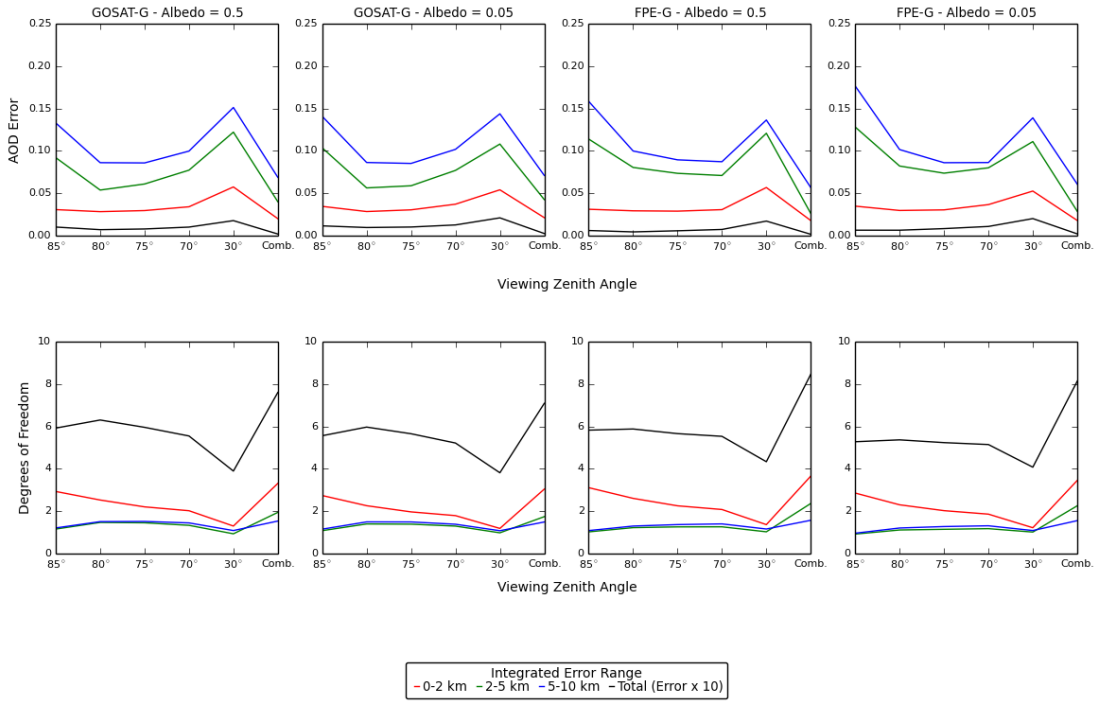

Figure 6.23: AOD errors and degrees of freedom for selected self-concatenated angles and combined together for scenario A+B.

ticularly at the higher VZAs. The DoFs for single angles are not greatly affected either, though when combined we again see an improvement in the DoF by 1, with the increase coming from the 5-10 km layer.

When VZA retrievals are combined, the addition of aerosol layers increases the DoF in the range of the layer, often by a full DoF with combined errors decreasing accordingly. This is in contrast to single VZAs which tend to be adversely affected by additional layers.

6.3 Polarisation

Another avenue to explore is the use of polarisation. Here we investigate the merits of measuring the parallel and perpendicular linear polarisations simultaneously in

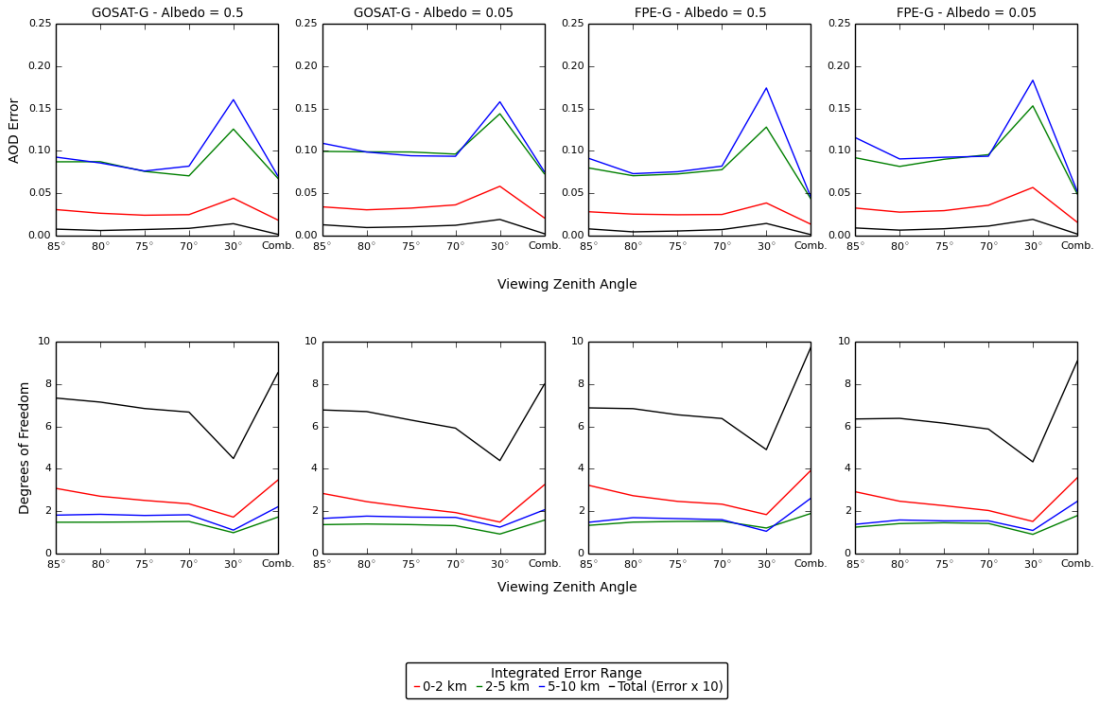

Figure 6.24: As with Figure 6.23 but for scenario A+C.

comparison to measuring unpolarised light. The degree of polarisation depends upon physical properties of the aerosol type and the viewing geometry. If the aerosol type is known, as we have often assumed to be the case, the degree of polarisation should inform us on the height of the scattering event. Furthermore, by using differing angles we should be further able to constrain the aerosol distribution. Figure 6.26 shows the degree of linear polarisation as a function of scattering angle for the 13 aerosol types discussed in Kahn et al. (2001).

As can be seen there is high variability in the degree of polarisation with aerosol type, particularly as the scattering angle increases to 100° (where polarisation is strongest) and in the back scattering at close to 180°. Smaller particles, such as groups 4 and 5, tend to polarise more strongly, and therefore behave more similarly to Rayleigh scattering which polarises completely at 90°. At low scattering angles,

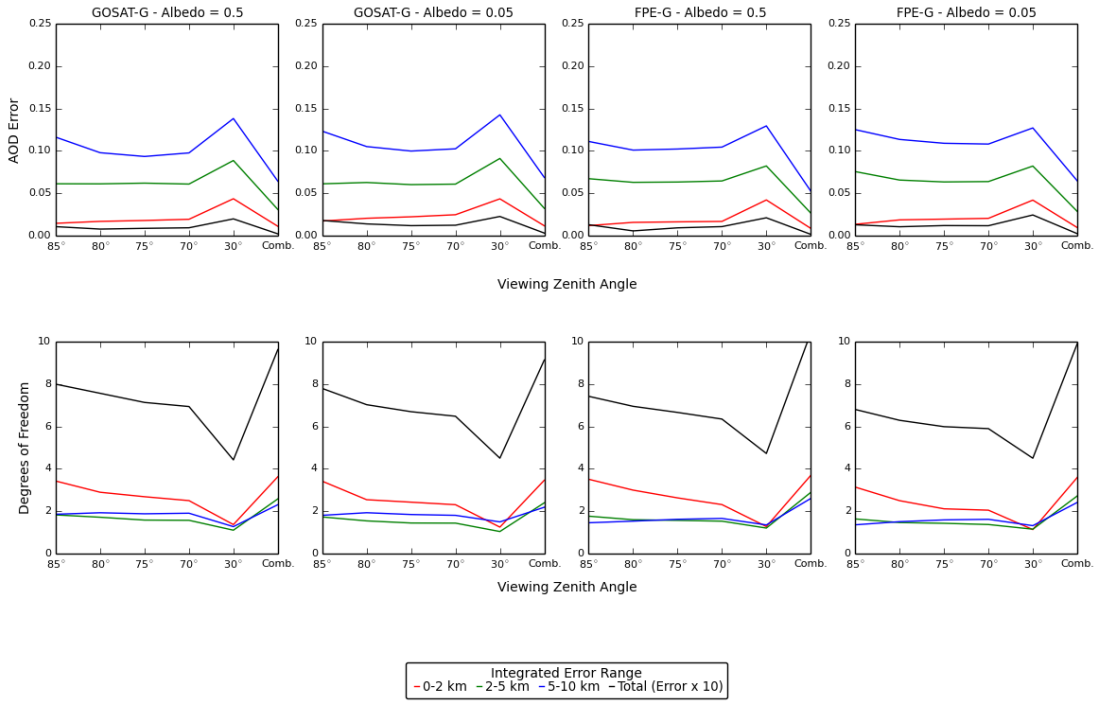

Figure 6.25: As with Figure 6.23 but for scenario B+C.

the degree of polarisation is low, as such there should be no advantage in using polarisation. However if the scattering angle is increased, i.e. the VZA is increased relative to the SZA, then not only will there be an advantage in using polarisation, there will be an increased dependence on aerosol mixture. Aerosol mixture 2b has been used throughout this thesis and so is used again here. As its polarising effect is not strong, a maximum of -0.1 we do not anticipate its effect on the aerosol error profile to be strong.

Figures 6.27 and 6.28 show the LAOD error profiles for FPE-G and GOSAT-G for Scenarios A and B, as well as a 7 km high 1 km wide layer of 0.3 AOD, for several VZAs and an albedo of 0.5.

For the 20° VZA case we see almost no difference between polarisations for both instruments, which is not surprising given the low scattering angle. At the other

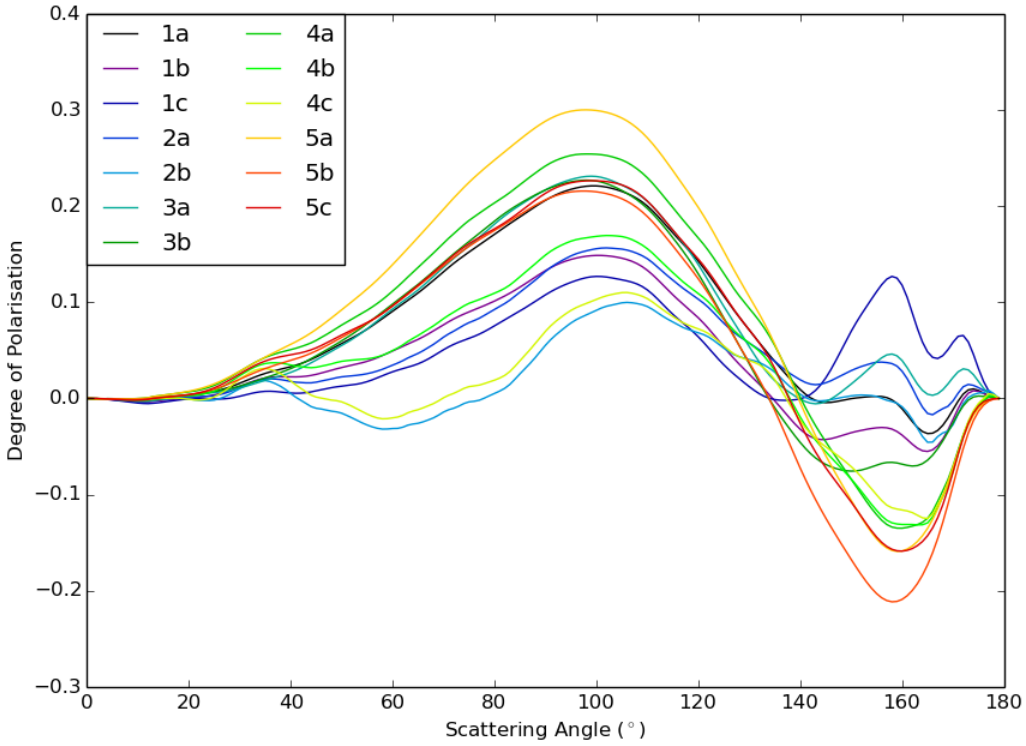

Figure 6.26: Degree of linear polarisation as a function of scattering angle for the 13 Kahn mixtures, adapted from Natraj (2008)

extreme is the case of 80° where the scattering angle is close to the strongly polarising 100°, but again we see only minor differences between the LAOD error profiles, which increase slightly with increasing aerosol altitude. In between is the 50° case where for the FPE-G we see substantially more variation where as for GOSAT-G we see slightly less than the 80° case. The variations in error tend to occur between 600 and 200 mb with the two polarised cases varying as to which one provides a lower error.

The vertical resolution is also plotted in Figures 6.29 and 6.30 in order to assess the differences in information content. GOSAT-G shows almost no variation with polarisation direction for all heights and VZAs with FPE-G only showing some

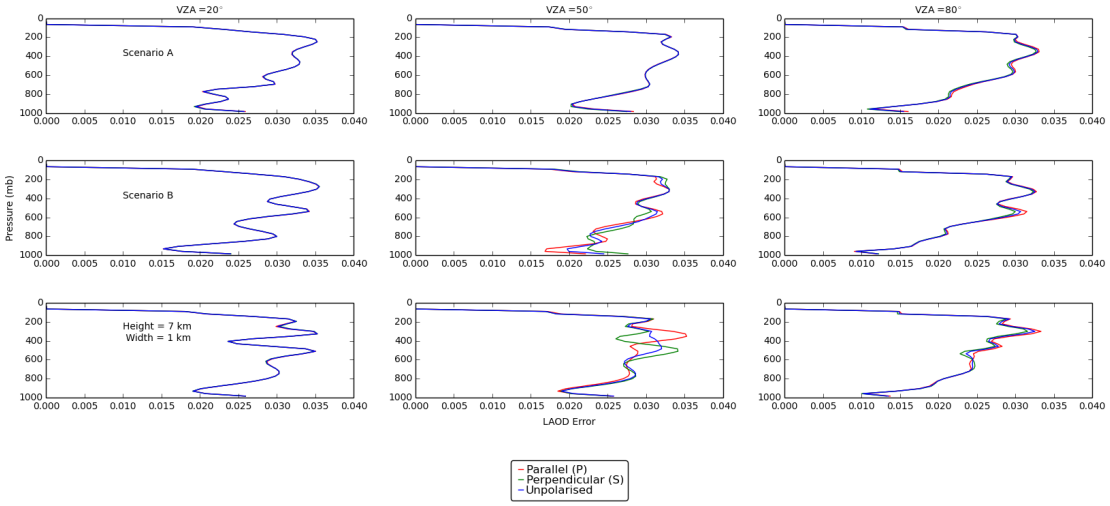

Figure 6.27: FPE-G LAOD error as a function of polarisation type, VZA and aerosol height, AOD = 0.3, Albedo = 0.5

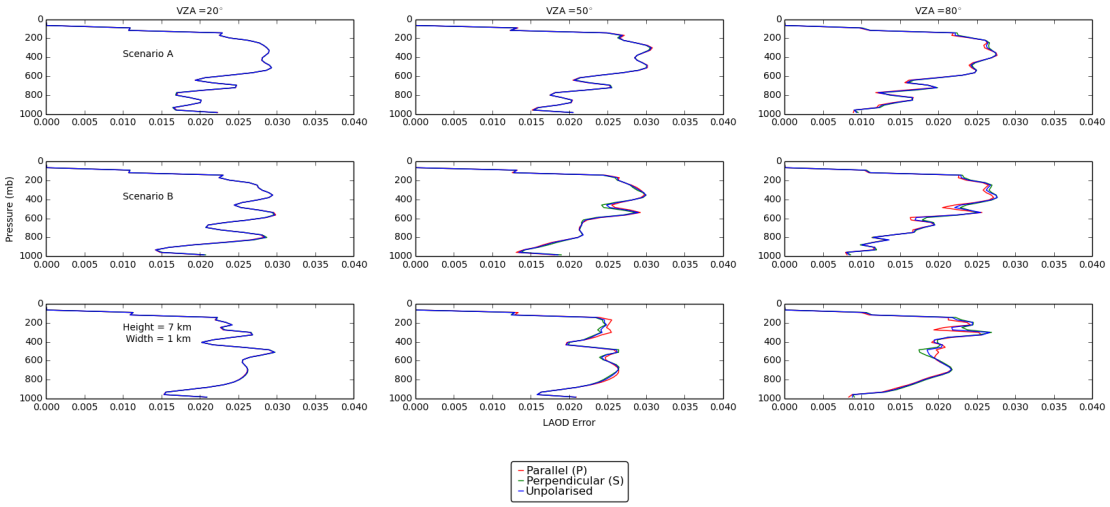

Figure 6.28: GOSAT-G LAOD error as a function of polarisation type, VZA and aerosol height, AOD = 0.3, Albedo = 0.5

advantage at VZA° and at 7 km aerosol altitude in the height range 600-200 mb although the improvement is less than 0.5 km, with substantial degradations of a km or more possible if taken in isolation. In summary the usefulness of polarisation in determining the aerosol distribution is questionable in the case of the 2b aerosol

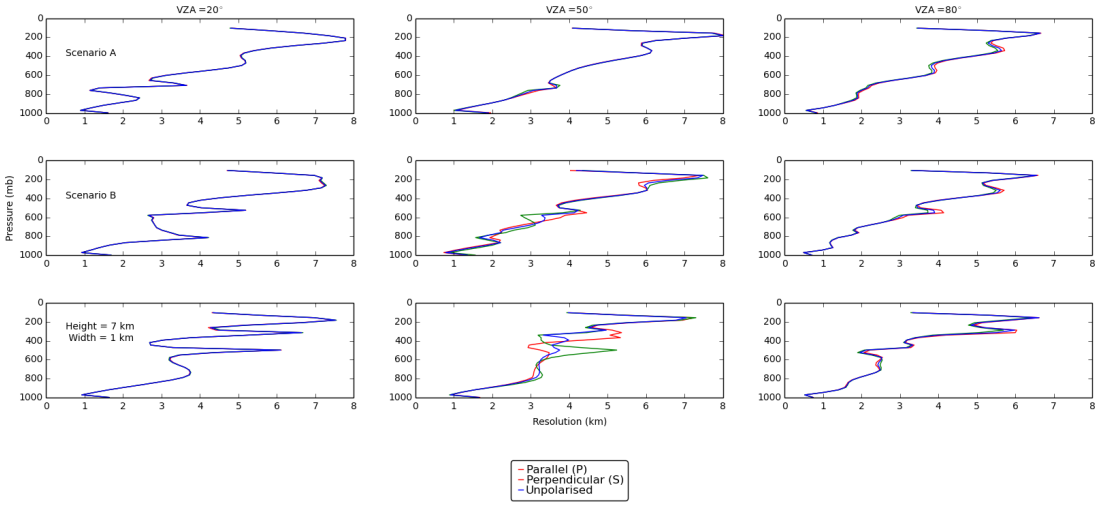

Figure 6.29: FPE-G resolution as a function of polarisation type, VZA and aerosol height, AOD = 0.3, Albedo = 0.5

mixture. As a demonstration the LAOD profiles are shown in Figure 6.31 and the resolution in Figure 6.32 for GOSAT-G but in the case of aerosol mixture 4c, the most strongly polarising aerosol mixture. Again we see only very little variation in the LAOD profiles so we can conclude that the aerosol mixture isn't the issue here. The problem would be that the polarising effects of Rayleigh scattering are too dominant at these VZA and therefore aerosols act as depolarisers, but only to minimal effect. Higher scattering angles (i.e. observing back scattered light) could improve the observations. This would be due to the additional negative lobe observed in the degree of linear polarisation having a greater impact than the Rayleigh scattering as it is far weaker at such high angles.

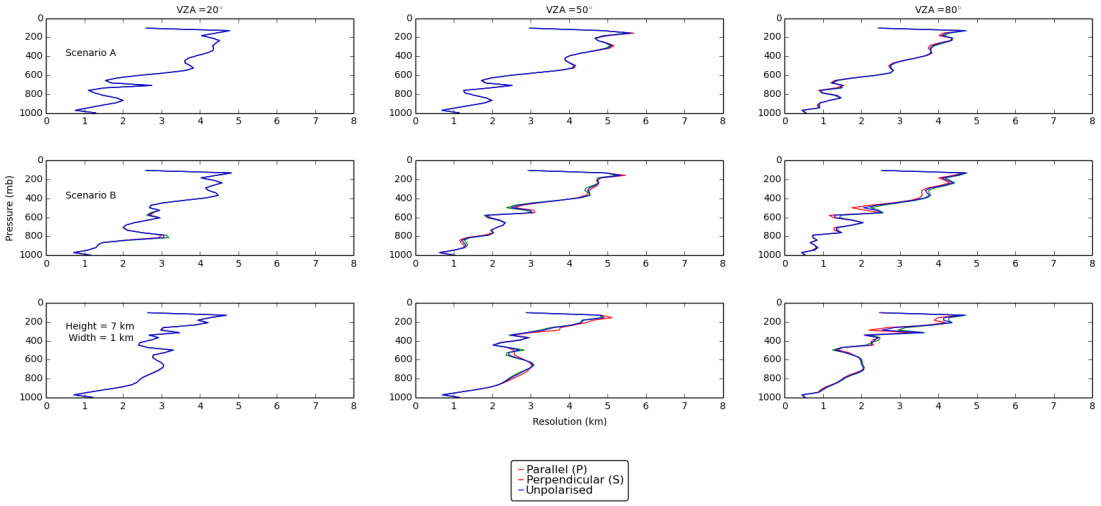

Figure 6.30: GOSAT-G resolution as a function of polarisation type, VZA and aerosol height, AOD = 0.3, Albedo = 0.5.

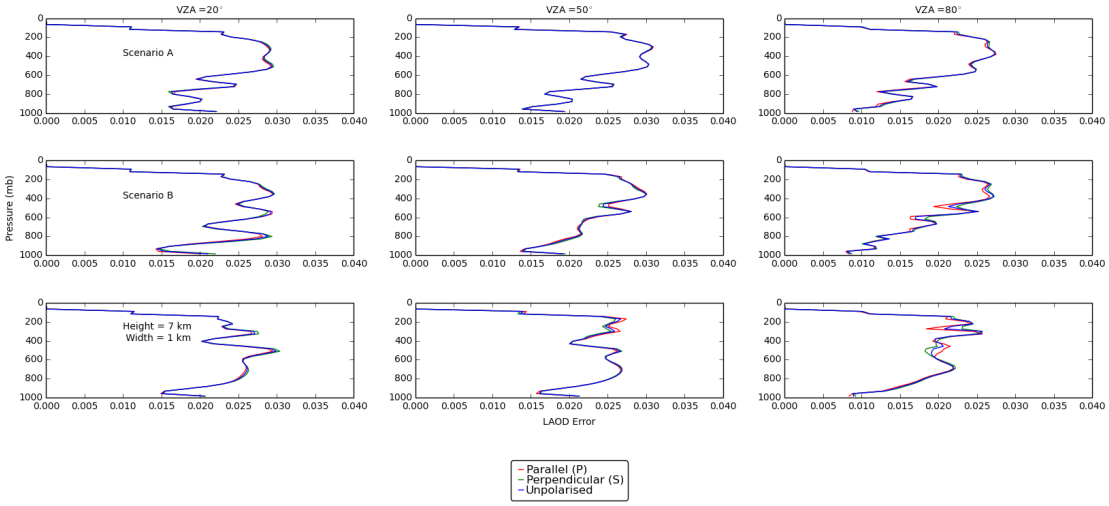

Figure 6.31: GOSAT-G LAOD error as a function of polarisation type, VZA and aerosol height, AOD = 0.3, Albedo = 0.5. for the strongly polarising aerosol mixture, 4c

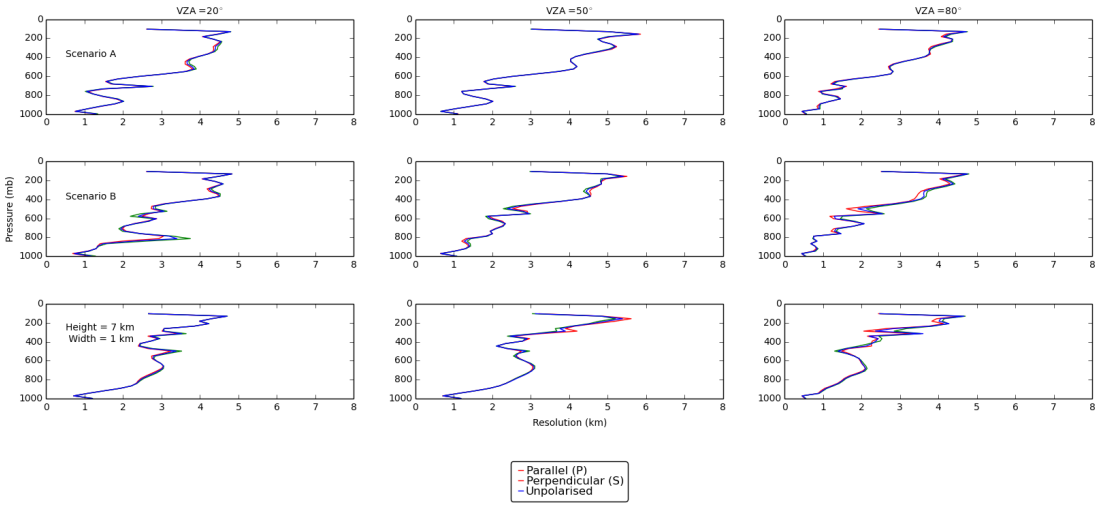

Figure 6.32: GOSAT-G resolution as a function of polarisation type, VZA and aerosol height, AOD = 0.3, Albedo = 0.5,for the strongly polarising aerosol mixture, 4c

6.4 Summary and Conclusions

Groundbased retrievals of aerosols in the O_2 have been studied using simulations involving groundbased versions of the GOSAT and FPE discussed earlier. Initial results found that purely zenith viewing systems, would only observe 3-4 degrees of freedom though will be able to retrieve total AOD to very high precision. This low information content was a result of the observations looking through aerosol layer to the minimum extent The low total AOD errors were a result of strong negative correlations across the profile, which again are a result of observing scattered light only. However it should be noted that this can be achieved by far simpler instruments such as radiometers.

By varying the observing angle we have shown that is possible to dramatically increase the information content of the retrieval. This increase was typically found at and below the aerosol layer as higher VZAs looked into more of the aerosol layer, and so obtain far more information. This was further improved by the addition of extra layers at higher altitudes which increase the amount of scattered light available. Angles in the region of 70° to 85° were shown to be particularly effective for both GOSAT-G and FPE-G where DoFs were increased upto 6 and 5 respectively. This was in part due to an increase in SNR with very high VZA and due to the varying height sensitivities at differing angles. AOD in both the integrated regions were shown to be greatly improved with 0-2 km error reducing to below the 0.05 threshold with a full DoF increase to 2 relative to the zenith case. Higher altitudes prove problematic as a result of a lack of scattered light being generated, however the addition of a cirrus layer did provide some improvement.

Combining several angles also proved to be beneficial with dramatic improvements in the LAOD and resolution (of up to 0.005 and 1 km) for FPE-G, however the benefits were far less for GOSAT-G. Though as the aerosol height increases the

advantages for GOSAT-G become more apparent. When integrated the improvements became more clear with the total DoF exceeding 8 for single layers and 10 for multiple layers. Far higher than anything observed for the spacebased observations. The improvements to FPE-G meant that it was far more comparable to GOSAT-G which was consistently better in the single angle cases. FPE-G clearly lost out in due to its integrated nature compared to the high resolution of GOSAT-G, however the latter's low SNR allowed the FPE-G to remain competitive.

The advantages of studying the polarisation spectra were also studied. It was concluded that while some aerosol types are strong polarisers, compared to the Rayleigh polarisation they act as depolarisers and therefore have only a minor impact upon the LAOD error and resolution. However the degree of polarisation was also strong at high scattering angles, at which point the polarisation from Rayleigh scattering would be weaker, and would perhaps therefore provide additional information on the aerosol profile.

Chapter 7

Conclusions and Outlook

7.1 Summary of Conclusions

The purpose of this thesis was to develop a Fabry-Pérot Etalon spectrometer for observations of aerosol in the O_2 A-Band. Which would be accompanied by a rigorous assessment of current and forthcoming spaceborne instruments in their ability to retrieve aerosols both in simulations and real observations.

The study of the current and upcoming missions was undertaken in Chapter three in two parts, the first of which involved theoretical studies of GOSAT, OCO-2, CarbonSat and Sentinel-5 P with the second half looking at real retrievals from GOSAT. The first section concluded the effectiveness of existing and upcoming instruments seems limited but could provide a powerful means of measuring uplifted aerosol and in the case of S-5 P or CarbonSat, provide imaging of such plumes. However high SNR as for S-5 P, proves beneficial for boundary layer aerosol at the expense of vertical information. This problem was largely driven by strong correlations between the AOD and the surface albedo. Applying tighter constraints on the albedo will help this situation but the required a priori uncertainty in the surface albedo has to be very low, up to 2 % which is not practical.

Higher altitude performance is promising and can be reinforced by the application of a parametrised aerosol distribution. However this method will result in misleading and erroneous retrievals if there are multiple layers present, or if the aerosol has a substantially different distribution, though this could be mitigated by retrieving two layers simultaneously.

Assumptions of aerosol properties, surface pressure and temperature were also assessed. In surface pressure and aerosol mixture additional errors could be as high as 40% though surface pressure could be retrieved simultaneously at the expensive retrieval error. Aerosol properties on the other hand could be constrained by additional measurements from instruments such as CALIPSO or by modelling. Low altitude temperature bias was far less of an issue with errors less than 8 % and could be further minimised by meteorological data.

The second part of Chapter three applied this to real retrievals of aerosol using GOSAT. These initial observations confirmed a lot of our conclusions on the impact of surface albedo correlations, low AOD and the performance of GOSAT. When the data is filtered however for low correlations and high error reduction, significant improvement in the correlations between GOSAT AOD and ARM AOD was found. This shows that when the conditions are right, the retrieval algorithm performs well however the loss in data is large and as such further work needs to be done to fully assess GOSATs performance.

Chapter five dealt with the design, optimisation and testing of a Fabry-Pérot Etalon spectrometer. The overall design was kept simple and the key parameters; the free spectral rand and reflectivity, were optimised using the the same simulations as previously described. These parameters were found to be 10 cm^{-1} for the FSR and 0.9 for the reflectivity, though the latter was deliberately over estimated in order to allow some flexibility. The FPE was then simulated in the same manner as in

Chapter 3. Its performance was found to be comparable to that of S-5 P at high altitudes and struggles below 600 mb. However its sensitivity to additional aerosol layers are far more comparable to the other instruments.

A limited programme of experiments were undertaken on the FPE. These experiments were far from ideal but confirmed the reflectivity curve of the FPE and more crucially demonstrated the performance of the PEA. The hysteresis was found to be noticeable but constrainable and as such a self-calibration scheme could be employed. Moreover this series of experimentation has led to the development of several useful pieces of control software and the establishment of an instrument configuration that can be used in future experiments.

Chapter six presented a study of groundbased in a similar vein to Chapter three. However it also investigated the impact of using differing viewing angles, combining them or by studying the polarisation of the observed spectra. In all cases the total optical depth was retrieved to high precision, less than 0.005 which is a substantial improvement from the spacebased examples. However this could be achieved with simpler instruments. The real importance is the vertical capabilities in information content and LAOD, and typically for the zenith viewing instruments this was poor, with only 3-4 DoF available for FPE-G and GOSAT-G.

The vertical information is greatly improved by the use of higher VZAs, which are closer to the horizon. Such angles observed more of the aerosol layer and therefore the gain DoF is high and is restricted to at and below the height of the aerosol layer. As a result a full DoF can be gained in the boundary layer with total DoF rising to 6. Combining several angles also proved to be beneficial with dramatic improvements in the LAOD and resolution (of up to 0.005 and 1 km) for FPE-G, however the benefits were far less for GOSAT-G. Though as the aerosol height increases the advantages for GOSAT-G become more apparent.

Lastly advantages of studying the polarisation spectra were also studied. It was concluded that while some aerosol types are strong polarisers, compared to the Rayleigh polarisation they act as depolarisers and therefore have only a minor impact upon the LAOD error and resolution. However at high scattering angles an advantage could be had but requires further study.

7.2 Outlook

Chapter three was fairly broad in its scope and several areas for future research were identified. Firstly the GOSAT retrievals could readily be expanded to a global scale which would provide more ideal scenarios and greatly improve the number of observations available after filtering. In addition the data from OCO-2 (and further down the line, S-5 P and hopefully GOSAT) will be available in the coming months which we know will provide a substantially higher performance. Additional theoretical studies could also be undertaken to study medium albedos (0.2-0.3) in greater detail, as it is at these albedos that significant problems in the AOD retrieval are found. The parametrised retrieval could be expanded upon and retrieving multiple layers investigated along with differing distributions, such as an exponential decay in AOD with height.

The groundbased simulations could also be improved upon by investigating a higher number of angles, such as those between 70° and 85° in order to further assess the optimum combination of angles. The differing phase functions of the aerosol mixtures also play a roll in performance of the different angles, so a comprehensive study of the effects of different mixtures would be worthwhile. In terms of polarisation it would be interesting to study the back scattered light from aerosol due to Rayleigh polarisation being minimised and particular types still being polarising. Further down the line it would of great interest to attempt real groundbased

retrievals using ideally the FPE that has been developed, this could then be readily compared to other groundbased instruments.

The development of the FPE is progressing well but unfortunately budget constraints have really held it back. In an ideal world a highly accurate, tunable diode laser would be used to fully calibrate the FPE. This would allow for the ILS and noise model to be fully characterised. Following on from this would be some initial attempts at groundbased retrieval as have just been mentioned. In order to reach that point a more robust instrument set up would be required, ideally involving the use of fibre optics as originally requested.

Bibliography

Abel, S., Highwood, E., Haywood, J., and Stringer, M. (2005). The direct radiative effect of biomass burning aerosols over southern africa. *Atmospheric Chemistry and Physics*, 5(7):1999–2018.

Ackerman, A. S., Toon, O. B., Taylor, J. P., Johnson, D. W., Hobbs, P. V., and Ferek, R. J. (2000). Effects of aerosols on cloud albedo: Evaluation of twomey's parameterization of cloud susceptibility using measurements of ship tracks. *Journal of the Atmospheric Sciences*, 57(16):2684–2695.

Al-Bender, F., Lampaert, V., and Swevers, J. (2005). The generalized maxwell-slip model: a novel model for friction simulation and compensation. *Automatic Control, IEEE Transactions on*, 50(11):1883–1887.

Aminou, D. (2002). Msg's seviri instrument. *ESA Bulletin(0376-4265)*, (111):15–17.

Andreae, M. and Rosenfeld, D. (2008). Aerosol–cloud–precipitation interactions. part 1. the nature and sources of cloud-active aerosols. *Earth-Science Reviews*, 89(1):13–41.

Angelino, S., Suess, D. T., and Prather, K. A. (2001). Formation of aerosol particles from reactions of secondary and tertiary alkylamines: Characterization by aerosol time-of-flight mass spectrometry. *Environmental science & technology*, 35(15):3130–3138.

Atherton, P., Taylor, K., Pike, C., Harmer, C. F., Parker, N., and Hook, R. (1982). Taurus: a wide-field imaging fabry-perot spectrometer for astronomy. *Monthly Notices of the Royal Astronomical Society*, 201:661–696.

Atwell, B. J., Kriedemann, P. E., and Turnbull, C. G. (1999). *Plants in action: adaptation in nature, performance in cultivation*. Macmillan Education AU.

Bailey, J. (2013). A low-cost portable fibre-optic spectrometer for atmospheric absorption studies. *Atmospheric Measurement Techniques Discussions*, 6(1).

Bates, T., Anderson, T., Baynard, T., Bond, T., Boucher, O., Carmichael, G., Clarke, A., Erlick, C., Guo, H., Horowitz, L., et al. (2006). Aerosol direct radiative effects over the northwest atlantic, northwest pacific, and north indian oceans: estimates based on in-situ chemical and optical measurements and chemical transport modeling. *Atmospheric Chemistry and Physics*, 6(6):1657–1732.

Bates, T. S., Huebert, B. J., Gras, J. L., Griffiths, F. B., and Durkee, P. A. (1998). International global atmospheric chemistry (igac) project's first aerosol characterization experiment (ace 1): Overview. *Journal of Geophysical Research: Atmospheres (1984–2012)*, 103(D13):16297–16318.

Bellouin, N., Boucher, O., Haywood, J., and Reddy, M. S. (2005). Global estimate of aerosol direct radiative forcing from satellite measurements. *Nature*, 438(7071):1138–1141.

Bernath, P. F., McElroy, C., Abrams, M., Boone, C. D., Butler, M., Camy-Peyret, C., Carleer, M., Clerbaux, C., Coheur, P.-F., Colin, R., et al. (2005). Atmospheric chemistry experiment (ace): mission overview. *Geophysical research letters*, 32(15).

Bezy, J., Delwart, S., and Rast, M. (2000). Meris-a new generation of ocean-colour sensor onboard envisat. *ESA bulletin*, 103:48–56.

Birmili, W., Stratmann, F., and Wiedensohler, A. (1999). Design of a dma-based size spectrometer for a large particle size range and stable operation. *Journal of Aerosol Science*, 30(4):549–553.

Boesche, E., Stammes, P., Preusker, R., Bennartz, R., Knap, W., and Fischer, J. (2008). Polarization of skylight in the o_2 a band: effects of aerosol properties. *Applied optics*, 47(19):3467–3480.

Bond, T. C. (2001). Spectral dependence of visible light absorption by carbonaceous particles emitted from coal combustion. *Geophysical research letters*, 28(21):4075–4078.

Bond, T. C., Anderson, T. L., and Campbell, D. (1999). Calibration and intercomparison of filter-based measurements of visible light absorption by aerosols. *Aerosol Science & Technology*, 30(6):582–600.

Born, M. and Wolf, E. (2002). Principles of optics 7th ed. *Cambridge University*.

Bösch, H., Baker, D., Connor, B., Crisp, D., and Miller, C. (2011). Global characterization of co2 column retrievals from shortwave-infrared satellite observations of the orbiting carbon observatory-2 mission. *Remote Sensing*, 3(2):270–304.

Bösch, H., Toon, G., Sen, B., Washenfelder, R., Wennberg, P., Buchwitz, M., De Beek, R., Burrows, J., Crisp, D., Christi, M., et al. (2006). Space-based near-infrared co2 measurements: Testing the orbiting carbon observatory retrieval algorithm and validation concept using sciamachy observations over park falls, wisconsin. *Journal of Geophysical Research: Atmospheres (1984–2012)*, 111(D23).

Bovensmann, H., Burrows, J., Buchwitz, M., Frerick, J., Noël, S., Rozanov, V., Chance, K., and Goede, A. (1999). Sciamachy: Mission objectives and measurement modes. *Journal of the Atmospheric Sciences*, 56(2):127–150.

Buchwitz, M., Reuter, M., Bovensmann, H., Pillai, D., Heymann, J., Schneising, O., Rozanov, V., Krings, T., Burrows, J., Boesch, H., et al. (2013). Carbon monitoring satellite (carbonsat): assessment of atmospheric co 2 and ch 4 retrieval errors by error parameterization. *Atmos Meas Tech*, 6:3477–3500.

Burrows, J. P., Weber, M., Buchwitz, M., Rozanov, V., Ladstätter-Weißenmayer, A., Richter, A., DeBeek, R., Hoogen, R., Bramstedt, K., Eichmann, K.-U., et al. (1999). The global ozone monitoring experiment (gome): Mission concept and first scientific results. *Journal of the Atmospheric Sciences*, 56(2):151–175.

Buscaglione, F. and Maresi, L. (2011). Gmes sentinel-5 precursor - s5p system requirement document (srd). 4.

Buseck, P. R. and Adachi, K. (2008). Nanoparticles in the atmosphere. *Elements*, 4(6):389–394.

Canagaratna, M., Jayne, J., Jimenez, J., Allan, J., Alfarra, M., Zhang, Q., Onasch, T., Drewnick, F., Coe, H., Middlebrook, A., et al. (2007). Chemical and microphysical characterization of ambient aerosols with the aerodyne aerosol mass spectrometer. *Mass Spectrometry Reviews*, 26(2):185–222.

Choi, G. S., Kim, H.-S., and Choi, G. H. (1997). A study on position control of piezoelectric actuators. In *Industrial Electronics, 1997. ISIE'97., Proceedings of the IEEE International Symposium on*, pages 851–855.

Clegg, S. and Abbatt, J. (2001). Oxidation of so 2 by h 2 o 2 on ice surfaces at 228 k: a sink for so 2 in ice clouds. *Atmospheric Chemistry and Physics*, 1(1):73–78.

Cogan, A. (2012). *Atmospheric carbon dioxide retrieved from the Greenhouse gases Observing SATellite; Method, comparisons and algorithm development.* PhD thesis.

Cogan, A., Boesch, H., Parker, R., Feng, L., Palmer, P., Blavier, J.-F., Deutscher, N. M., Macatangay, R., Notholt, J., Roehl, C., et al. (2012). Atmospheric carbon dioxide retrieved from the greenhouse gases observing satellite (gosat): Comparison with ground-based tccon observations and geos-chem model calculations. *Journal of Geophysical Research: Atmospheres (1984–2012)*, 117(D21).

Connor, B. J., Bösch, H., Toon, G., Sen, B., Miller, C., and Crisp, D. (2008). Orbiting carbon observatory: Inverse method and prospective error analysis. *Journal of Geophysical Research: Atmospheres (1984–2012)*, 113(D5).

Corradini, S. and Cervino, M. (2006). Aerosol extinction coefficient profile retrieval in the oxygen a-band considering multiple scattering atmosphere. test case: Sciamachy nadir simulated measurements. *Journal of Quantitative Spectroscopy and Radiative Transfer*, 97(3):354–380.

Courtial, J., Patterson, B., Harvey, A., Sibbett, W., and Padgett, M. (1996). Design of a static fourier-transform spectrometer with increased field of view. *Applied optics*, 35(34):6698–6702.

Crisp, D., Atlas, R., Breon, F.-M., Brown, L., Burrows, J., Ciais, P., Connor, B., Doney, S., Fung, I., Jacob, D., et al. (2004). The orbiting carbon observatory (oco) mission. *Advances in Space Research*, 34(4):700–709.

Crisp, D., DeCola, P. L., and Miller, C. E. (2008). Nasa orbiting carbon observatory: measuring the column averaged carbon dioxide mole fraction from space. *Journal of Applied Remote Sensing*, 2(1):023508–023508.

Crisp, D., Fisher, B. M., O'Dell, C., Frankenberg, C., Basilio, R., Bösch, H., Brown, L. R., Castano, R., Connor, B., Deutscher, N. M., Eldering, A., Griffith, D., Gunson, M., Kuze, A., Mandrake, L., McDuffie, J., Messerschmidt, J., Miller, C. E., Morino, I., Natraj, V., Notholt, J., O'Brien, D. M., Oyafuso, F., Polonsky, I., Robinson, J., Salawitch, R., Sherlock, V., Smyth, M., Suto, H., Taylor, T. E., Thompson, D. R., Wennberg, P. O., Wunch, D., and Yung, Y. L. (2012). The acos co_2 retrieval algorithm part ii: Global xco_2 data characterization. *Atmospheric Measurement Techniques*, 5(4):687–707.

Demtröder, W. (1982). *Laser spectroscopy*, volume 3. Springer.

Dentener, F. J. and Crutzen, P. J. (1993). Reaction of n2o5 on tropospheric aerosols: Impact on the global distributions of no x, o3, and oh. *Journal of Geophysical Research: Atmospheres (1984–2012)*, 98(D4):7149–7163.

Dicke, R. (1953). The effect of collisions upon the doppler width of spectral lines. *Physical Review*, 89(2):472.

Du, H. (2004). Mie-scattering calculation. *Applied optics*, 43(9):1951–1956.

Dubuisson, P., Frouin, R., Dessailly, D., Duforêt, L., Léon, J.-F., Voss, K., and Antoine, D. (2009). Estimating the altitude of aerosol plumes over the ocean from reflectance ratio measurements in the o_2 a-band. *Remote Sensing of Environment*, 113(9):1899–1911.

Ehsani, A., Reagan, J., and Erxleben, W. (1998). Design and performance analysis of an automated 10-channel solar radiometer instrument. *Journal of Atmospheric and Oceanic Technology*, 15(3):697–707.

Fellgett, P. (1949). On the ultimate sensitivity and practical performance of radiation detectors. *JOSA*, 39(11):970–976.

Fernald, F. G., Herman, B. M., and Reagan, J. A. (1972). Determination of aerosol height distributions by lidar. *Journal of Applied meteorology*, 11(3):482–489.

Ferrare, R., Melfi, S., Whiteman, D., Evans, K., Poellot, M., and Kaufman, Y. (1998). Raman lidar measurements of aerosol extinction and backscattering: 2. derivation of aerosol real refractive index, single-scattering albedo, and humidification factor using raman lidar and aircraft size distribution measurements. *Journal of Geophysical Research: Atmospheres (1984–2012)*, 103(D16):19673–19689.

Fischer, H., Birk, M., Blom, C., Carli, B., Carlotti, M., Clarmann, T. v., Delbouille, L., Dudhia, A., Ehhalt, D., Endemann, M., et al. (2008). Mipas: an instrument for atmospheric and climate research. *Atmospheric Chemistry and Physics*, 8(8):2151–2188.

Frankenberg, C., Butz, A., and Toon, G. (2011). Disentangling chlorophyll fluorescence from atmospheric scattering effects in o2 a-band spectra of reflected sun-light. *Geophysical Research Letters*, 38(3).

Frankenberg, C., Hasekamp, O., O'Dell, C., Sanghavi, S., Butz, A., and Worden, J. (2012). Aerosol information content analysis of multi-angle high spectral resolution measurements and its benefit for high accuracy greenhouse gas retrievals. *Atmospheric Measurement Techniques*, 5(7):1809–1821.

Funk, O. (2000). *Photon pathlengths distributions for cloudy skies: Oxygen A-band measurements and radiative transfer model calculations*. PhD thesis.

Gantt, B., Meskhidze, N., Facchini, M., Rinaldi, M., Ceburnis, D., and O'Dowd, C. (2011). Wind speed dependent size-resolved parameterization for the organic mass fraction of sea spray aerosol. *Atmospheric Chemistry and Physics*, 11(16):8777–8790.

Gittins, C. M., Lawrence, W. G., and Marinelli, W. J. (1998). Frequency-agile bandpass filter for direct detection lidar receivers. *Appl. Opt.*, 37(36):8327–8335.

Grehan, G. and Gouesbet, G. (1979). Mie theory calculations: new progress, with emphasis on particle sizing. *Applied optics*, 18(20):3489–3493.

Guenther, A., Jiang, X., Heald, C., Sakulyanontvittaya, T., Duhl, T., Emmons, L., and Wang, X. (2012). The model of emissions of gases and aerosols from nature version 2.1 (megan2. 1): an extended and updated framework for modeling biogenic emissions.

Hanel, R. A. (1961). Determination of cloud altitude from a satellite. *Journal of Geophysical Research*, 66(4):1300–1300.

Hansen, A., Rosen, H., and Novakov, T. (1984). The aethalometeran instrument for the real-time measurement of optical absorption by aerosol particles. *Science of the Total Environment*, 36:191–196.

Hansen, J., Sato, M., and Ruedy, R. (1997). Radiative forcing and climate response. *Journal of Geophysical Research: Atmospheres (1984–2012)*, 102(D6):6831–6864.

Harrison, R. M. and Yin, J. (2000). Particulate matter in the atmosphere: which particle properties are important for its effects on health? *Science of the total environment*, 249(1):85–101.

Haywood, J. and Boucher, O. (2000). Estimates of the direct and indirect radiative forcing due to tropospheric aerosols: A review. *Reviews of Geophysics*, 38(4):513–543.

Heald, C. L. and Spracklen, D. V. (2009). Atmospheric budget of primary biological aerosol particles from fungal spores. *Geophysical Research Letters*, 36(9).

Heaps, W. S. and Kawa, S. R. (2002). Fabry-perot interferometer for column co2. In *NASA Earth Science Technology Conference*.

Heidinger, A. K. and Stephens, G. L. (2000). Molecular line absorption in a scattering atmosphere. part ii: Application to remote sensing in the o2 a band. *Journal of the atmospheric sciences*, 57(10):1615–1634.

Helbert, J., Laforie, P., and Miche, P. (1977). Conditions of pressure scanning of a fabry-perot interferometer over a wide spectrum range. *Applied optics*, 16(8):2119–2126.

Hernandez, G. (1980). Measurement of thermospheric temperatures and winds by remote fabry-perot spectrometry. *Optical Engineering*, 19(4):518–532.

Hernández, G. (1988). *Fabry-Perot Interferometers*, volume 3. Cambridge University Press.

Hervig, M. and Deshler, T. (2002). Evaluation of aerosol measurements from sage ii, haloe, and balloonborne optical particle counters. *Journal of Geophysical Research: Atmospheres (1984–2012)*, 107(D3):AAC–3.

Herzberg, G. (1950). Molecular spectra and molecular structure. vol. 1: Spectra of diatomic molecules. *New York: Van Nostrand Reinhold, 1950, 2nd ed.*, 1.

Hessel, A. and Oliner, A. (1965). A new theory of woods anomalies on optical gratings. *Applied Optics*, 4(10):1275–1297.

Hicks, B., editor (1994). *Report of the WMO workshop on the measurement of atmospheric optical depth and turbidity*, volume 101.

Hobbs, P. V. (1993). *Aerosol-cloud-climate interactions*, volume 54. Academic Press.

Holben, B., Eck, T., Slutsker, I., Tanr, D., Buis, J., Setzer, A., Vermote, E., Reagan, J., Kaufman, Y., Nakajima, T., Lavenu, F., Jankowiak, I., and Smirnov, A. (1998). Aeronet - a federated instrument network and data archive for aerosol characterization. *Remote Sensing of Environment*, 66(1):1–16.

Hollstein, A. and Fischer, J. (2014). Retrieving aerosol height from the oxygen a band: a fast forward operator and sensitivity study concerning spectral resolution, instrumental noise, and surface inhomogeneity. *Atmospheric Measurement Techniques*, 7(5):1429–1441.

Huneeus, N., Schulz, M., Balkanski, Y., Griesfeller, J., Prospero, J., Kinne, S., Bauer, S., Boucher, O., Chin, M., Dentener, F., et al. (2011). Global dust model intercomparison in aerocom phase i. *Atmospheric Chemistry and Physics*, 11(15).

Hunt, W. H., Winker, D. M., Vaughan, M. A., Powell, K. A., Lucker, P. L., and Weimer, C. (2009). Calipso lidar description and performance assessment. *Journal of Atmospheric & Oceanic Technology*, 26(7).

Hutley, M. C. (1982). Diffraction gratings. *Techniques of Physics, London: Academic Press, 1982*, 1.

Ingmann, P., Veihelmann, B., Langen, J., Lamarre, D., Stark, H., and Courrèges-Lacoste, G. B. (2012). Requirements for the gmes atmosphere service and esa's implementation concept: Sentinels-4/-5 and-5p. *Remote Sensing of Environment*, 120:58–69.

Jacobson, M. Z. (2001). Strong radiative heating due to the mixing state of black carbon in atmospheric aerosols. *Nature*, 409(6821):695–697.

Jacquinot, P. and Dufour, C. (1948). Conditions optiques d'emploi des cellules

photo-electriques dans les spectrographes et les interferometres. *J. Res. CRNS*, 6:91–103.

Jensen, K. D. (2004). Flow measurements. *Journal of the Brazilian Society of Mechanical Sciences and Engineering*, 26:400 – 419.

Jimenez, J. L., Jayne, J. T., Shi, Q., Kolb, C. E., Worsnop, D. R., Yourshaw, I., Seinfeld, J. H., Flagan, R. C., Zhang, X., Smith, K. A., et al. (2003). Ambient aerosol sampling using the aerodyne aerosol mass spectrometer. *Journal of Geophysical Research: Atmospheres (1984–2012)*, 108(D7).

Kahn, R., Banerjee, P., and McDonald, D. (2001). Sensitivity of multiangle imaging to natural mixtures of aerosols over ocean. *Journal of Geophysical Research: Atmospheres (1984–2012)*, 106(D16):18219–18238.

Kahn, R. A., Li, W.-H., Moroney, C., Diner, D. J., Martonchik, J. V., and Fishbein, E. (2007). Aerosol source plume physical characteristics from space-based multiangle imaging. *Journal of Geophysical Research: Atmospheres (1984–2012)*, 112(D11).

Kaizuka, H. and Siu, B. (1988). Simple way to reduce hysteresis and creep when using piezoelectric actuators. *Japanese Journal of Applied Physics, Part 2: Letters*, 27(5):773–776.

Kasischke, E. S. and Penner, J. E. (2004). Improving global estimates of atmospheric emissions from biomass burning. *Journal of Geophysical Research: Atmospheres (1984–2012)*, 109(D14).

Kaufman, Y. (1994). Size distribution and scattering phase function of aerosol particles retrieved from sky brightness measurements. *Journal of Geophysical Research*, 99(D5):10,341–"10,356".

Kelly, F. J. (2003). Oxidative stress: its role in air pollution and adverse health effects. *Occupational and environmental medicine*, 60(8):612–616.

Kobayashi, N., Inoue, G., Kawasaki, M., Yoshioka, H., Minomura, M., Murata, I., Nagahama, T., Matsumi, Y., Tanaka, T., Morino, I., et al. (2010). Remotely operable compact instruments for measuring atmospheric co 2 and ch 4 column densities at surface monitoring sites. *Atmospheric Measurement Techniques*, 3(4):1103–1112.

Kriebel, K. T. (1976). On the variability of the reflected radiation field due to differing distributions of the irradiation. *Remote Sensing of Environment*, 4:257–264.

Kroll, J. H. and Seinfeld, J. H. (2008). Chemistry of secondary organic aerosol: Formation and evolution of low-volatility organics in the atmosphere. *Atmospheric Environment*, 42(16):3593–3624.

Kuze, A., Suto, H., Nakajima, M., and Hamazaki, T. (2009). Thermal and near infrared sensor for carbon observation fourier-transform spectrometer on the greenhouse gases observing satellite for greenhouse gases monitoring. *Applied optics*, 48(35):6716–6733.

Liou, K.-N. (2002). *An introduction to atmospheric radiation*, volume 84. Academic press.

Liu, P., Leaitch, W., Strapp, J., and Wasey, M. (1992). Response of particle measuring systems airborne asasp and pcasp to nacl and latex particles. *Aerosol science and technology*, 16(2):83–95.

Liu, Y. and Daum, P. H. (2000). The effect of refractive index on size distributions

and light scattering coefficients derived from optical particle counters. *Journal of Aerosol Science*, 31(8):945–957.

Llewellyn, E., Lloyd, N., Degenstein, D., Gattinger, R., Petelina, S., Bourassa, A., Wiensz, J., Ivanov, E., McDade, I., Solheim, B., et al. (2004). The osiris instrument on the odin spacecraft. *Canadian Journal of Physics*, 82(6):411–422.

Llewellyn-Jones, D., Edwards, M., Mutlow, C., Birks, A., Barton, I., and Tait, H. (2001). Aatsr: Global-change and surface-temperature measurements from envisat. *ESA bulletin*, 105:11–21.

Lohmann, U. and Feichter, J. (2005). Global indirect aerosol effects: a review. *Atmospheric Chemistry and Physics*, 5(3):715–737.

Long, D. A. and Hodges, J. T. (2012). On spectroscopic models of the o2 a-band and their impact upon atmospheric retrievals. *Journal of Geophysical Research: Atmospheres (1984–2012)*, 117(D12).

Marenco, F., Santacesaria, V., Bais, A. F., Balis, D., di Sarra, A., Papayannis, A., and Zerefos, C. (1997). Optical properties of tropospheric aerosols determined by lidar and spectrophotometric measurements (photochemical activity and solar ultraviolet radiation campaign). *Applied Optics*, 36(27):6875–6886.

Martin, M. V., Logan, J., Kahn, R., Leung, F., Nelson, D., and Diner, D. (2010). Smoke injection heights from fires in north america: analysis of 5 years of satellite observations. *Atmos. Chem. Phys*, 10(4):1491–1510.

Martin, R. V., Jacob, D. J., Yantosca, R. M., Chin, M., and Ginoux, P. (2003). Global and regional decreases in tropospheric oxidants from photochemical effects of aerosols. *Journal of Geophysical Research: Atmospheres (1984–2012)*, 108(D3).

Mauldin III, L., Zaun, N., McCormick Jr, M., Guy, J., and Vaughn, W. (1985). Stratospheric aerosol and gas experiment ii instrument: A functional description. *Optical Engineering*, 24(2):242307–242307.

Maxwell, K. and Johnson, G. N. (2000). Chlorophyll fluorescencea practical guide. *Journal of experimental botany*, 51(345):659–668.

Mie, G. (1976). Contributions to the optics of turbid media, particularly of colloidal metal solutions. *Contributions to the optics of turbid media, particularly of colloidal metal solutions Transl. into ENGLISH from Ann. Phys.(Leipzig), v. 25, no. 3, 1908 p 377-445*, 1:377–445.

Müller, J.-F., Stavrakou, T., Wallens, S., Smedt, I. D., Roozendael, M. V., Potosnak, M., Rinne, J., Munger, B., Goldstein, A., and Guenther, A. (2008). Global isoprene emissions estimated using megan, ecmwf analyses and a detailed canopy environment model. *Atmospheric Chemistry and Physics*, 8(5):1329–1341.

Murphy, D., Cziczo, D., Froyd, K., Hudson, P., Matthew, B., Middlebrook, A., Peltier, R. E., Sullivan, A., Thomson, D., and Weber, R. (2006). Single-particle mass spectrometry of tropospheric aerosol particles. *Journal of Geophysical Research: Atmospheres (1984–2012)*, 111(D23).

Murphy, D., Thomson, D., and Mahoney, M. (1998). In situ measurements of organics, meteoritic material, mercury, and other elements in aerosols at 5 to 19 kilometers. *Science*, 282(5394):1664–1669.

Myhre, G., Samset, B., Schulz, M., Balkanski, Y., Bauer, S., Berntsen, T., Bian, H., Bellouin, N., Chin, M., Diehl, T., et al. (2013). Radiative forcing of the direct aerosol effect from aerocom phase ii simulations. *Atmospheric Chemistry and Physics*, 13(4):1853–1877.

Nakajima, T., Takamura, T., Yamano, M., Shiobara, M., Yamauchi, T., Goto, R., and Murai, K. (1986). Consistency of aerosol size distributions inferred from measurements of solar radiation and aerosols. *Meteorological Society of Japan*.

Nakajima, T., Tanaka, M., and Tamauchi, T. (1983). Retrieval of the optical properties of aerosols from aureole and extinction data. *Applied Optics*, 22(19):2951–2959.

Nakajima, T., Tonna, G., Rao, R., Boi, P., Kaufman, Y., and Holben, B. (1996). Use of sky brightness measurements from ground for remote sensing of particulate polydispersions. *Applied Optics*, 35(15):2672–2686.

Namdeo, A., Colls, J., and Baker, C. (1999). Dispersion and re-suspension of fine and coarse particulates in an urban street canyon. *Science of the total environment*, 235(1):3–13.

Natraj, V. (2008). *Radiative transfer modeling for the retrieval of CO2 from space*. PhD thesis, California Institute of Technology.

O'Brien, D. and Mitchell, R. (1992). Error estimates for retrieval of cloud-top pressure using absorption in the a band of oxygen. *Journal of applied meteorology*, 31(10):1179–1192.

O'Dell, C. W. (2010). Acceleration of multiple-scattering, hyperspectral radiative transfer calculations via low-streams interpolation. *Journal of Geophysical Research: Atmospheres (1984–2012)*, 115(D10).

O'Dowd, C. D., Aalto, P., Hmeri, K., Kulmala, M., and Hoffmann, T. (2002). Aerosol formation: Atmospheric particles from organic vapours. *Nature*, 416(6880):497–498.

Padgett, M. and Harvey, A. (1995). A static fourier-transform spectrometer based on wollaston prisms. *Review of scientific instruments*, 66(4):2807–2811.

Parker, R., Bösch, H., Cogan, A., Fraser, A., Feng, L., Palmer, P. I., Messerschmidt, J., Deutscher, N., Griffith, D. W., Notholt, J., et al. (2011). Methane observations from the greenhouse gases observing satellite: Comparison to ground-based tccon data and model calculations. *Geophysical Research Letters*, 38(15).

Peters, A., Wichmann, H. E., Tuch, T., Heinrich, J., and Heyder, J. (1997). Respiratory effects are associated with the number of ultrafine particles. *American journal of respiratory and critical care medicine*, 155(4):1376–1383.

Peters, T. M. and Leith, D. (2003). Concentration measurement and counting efficiency of the aerodynamic particle sizer 3321. *Journal of Aerosol Science*, 34(5):627–634.

Peters, T. M., Ott, D., and O'SHAUGHNESSY, P. T. (2006). Comparison of the grimm 1.108 and 1.109 portable aerosol spectrometer to the tsi 3321 aerodynamic particle sizer for dry particles. *Annals of Occupational Hygiene*, 50(8):843–850.

Petzold, A. and Schönlinner, M. (2004). Multi-angle absorption photometrya new method for the measurement of aerosol light absorption and atmospheric black carbon. *Journal of Aerosol Science*, 35(4):421–441.

Pope III, C. A. and Dockery, D. W. (2006). Health effects of fine particulate air pollution: lines that connect. *Journal of the Air & Waste Management Association*, 56(6):709–742.

Prather, K. A., Nordmeyer, T., and Salt, K. (1994). Real-time characterization of individual aerosol particles using time-of-flight mass spectrometry. *Analytical Chemistry*, 66(9):1403–1407.

Purser, R. and Huang, H. (1993). Estimating effective data density in a satellite retrieval or an objective analysis. *Journal of applied meteorology*, 32(6):1092–1107.

Raes, F., Bates, T., McGovern, F., and Van Liedekerke, M. (2000). The 2nd aerosol characterization experiment (ace-2): general overview and main results. *Tellus B*, 52(2):111–125.

Ramanathan, V., Chung, C., Kim, D., Bettge, T., Buja, L., Kiehl, J., Washington, W., Fu, Q., Sikka, D., and Wild, M. (2005). Atmospheric brown clouds: Impacts on south asian climate and hydrological cycle. *Proceedings of the National Academy of Sciences of the United States of America*, 102(15):5326–5333.

Ramanathan, V., Crutzen, P., Kiehl, J., and Rosenfeld, D. (2001a). Aerosols, climate, and the hydrological cycle. *science*, 294(5549):2119–2124.

Ramanathan, V., Crutzen, P. J., Lelieveld, J., Mitra, A., Althausen, D., Anderson, J., Andreae, M., Cantrell, W., Cass, G., Chung, C., et al. (2001b). Indian ocean experiment: An integrated analysis of the climate forcing and effects of the great indo-asian haze. *Journal of Geophysical Research*.

Ramanathan, V., Ramana, M. V., Roberts, G., Kim, D., Corrigan, C., Chung, C., and Winker, D. (2007). Warming trends in asia amplified by brown cloud solar absorption. *Nature*, 448(7153):575–578.

Rank, D. and Shearer, J. (1956). Linear gas mass flow device with applications to interferometry. *JOSA*, 46(6):463–464.

Ritter, K. and Wilkerson, T. (1987). High-resolution spectroscopy of the oxygen a-band. *Journal of Molecular Spectroscopy*, 121(1):1–19.

Rodgers, C. D. et al. (2000a). *Inverse methods for atmospheric sounding: theory and practice*, volume 2. World scientific Singapore.

Rodgers, C. D. et al. (2000b). *Inverse methods for atmospheric sounding: theory and practice*, volume 2. World scientific Singapore.

Rozanov, V. V. and Kokhanovsky, A. A. (2004). Semianalytical cloud retrieval algorithm as applied to the cloud top altitude and the cloud geometrical thickness determination from top-of-atmosphere reflectance measurements in the oxygen a band. *Journal of Geophysical Research: Atmospheres (1984–2012)*, 109(D5).

Russell, J. M., Gordley, L. L., Park, J. H., Drayson, S. R., Hesketh, W. D., Cicerone, R. J., Tuck, A. F., Frederick, J. E., Harries, J. E., and Crutzen, P. J. (1993). The halogen occultation experiment. *Journal of Geophysical Research: Atmospheres (1984–2012)*, 98(D6):10777–10797.

Sanders, A. and De Haan, J. (2013). Retrieval of aerosol parameters from the oxygen a band in the presence of chlorophyll fluorescence. *Atmospheric Measurement Techniques*, 6(10):2725–2740.

Satheesh, S., Torres, O., Remer, L., Babu, S. S., Vinoj, V., Eck, T., Kleidman, R., and Holben, B. (2009). Improved assessment of aerosol absorption using omi-modis joint retrieval. *Journal of Geophysical Research: Atmospheres (1984–2012)*, 114(D5).

Schmid, B., Mtzler, C., Heimo, A., and Kmpfer, N. (1997). Retrieval of optical depth and particle size distribution of tropospheric and stratospheric aerosols by means of sun photometry. *IEEE Transactions on Geoscience and Remote Sensing*, 35(1):172–182.

Seaton, A., Godden, D., MacNee, W., and Donaldson, K. (1995). Particulate air pollution and acute health effects. *The Lancet*, 345(8943):176–178.

Seinfeld, J. H. and Pandis, S. N. (2012). *Atmospheric chemistry and physics: from air pollution to climate change*. John Wiley & Sons.

Shepherd, G., Lake, C., Miller, J., and Cogger, L. (1965). A spatial spectral scanning technique for the fabry-perot spectrometer. *Applied Optics*, 4(3):267–272.

Shiobara, M., Hayasaka, T., Nakajima, T., and Tanaka, M. (1991). Aerosol monitoring using a scanning spectral radiometer in sendai, japan. *Meteorological Society of Japan*.

Siddans, R., Latter, B., and Kerridge, B. (2007). Study to consolidate the uvs mission requirements for the oxygen a-band. *EUMETSAT Rep. EUM/CO/05/1411/SAT*.

Spracklen, D., Jimenez, J., Carslaw, K., Worsnop, D., Evans, M., Mann, G., Zhang, Q., Canagaratna, M., Allan, J., Coe, H., et al. (2011). Aerosol mass spectrometer constraint on the global secondary organic aerosol budget. *Atmospheric Chemistry and Physics*, 11(23):12109–12136.

Spurr, R. (2008). Lidort and vlidort: Linearized pseudo-spherical scalar and vector discrete ordinate radiative transfer models for use in remote sensing retrieval problems. In *Light Scattering Reviews 3*, pages 229–275. Springer.

Spurr, R., Kurosu, T., and Chance, K. (2001). A linearized discrete ordinate radiative transfer model for atmospheric remote-sensing retrieval. *Journal of Quantitative Spectroscopy and Radiative Transfer*, 68(6):689–735.

Stocker, T. F., Qin, D., Plattner, G.-K., Tignor, M., Allen, S. K., Boschung, J., Nauels, A., Xia, Y., Bex, V., and Midgley, P. M. (2013). Climate change 2013: The physical science basis. *Intergovernmental Panel on Climate Change, Working*

Group I Contribution to the IPCC Fifth Assessment Report (AR5)(Cambridge Univ Press, New York).

Tanre, D., Devaux, C., Herman, M., Santer, R., and Gac, J. (1988). Radiative properties of desert aerosols by optical ground-based measurements at solar wavelengths. *Journal of Geophysical Research*, 93(D11):14,223–"14,231".

Uchino, K. (1997). *Piezoelectric actuators and ultrasonic motors*, volume 1. Springer.

Van Gulijk, C., Marijnissen, J., Makkee, M., Moulijn, J., and Schmidt-Ott, A. (2004). Measuring diesel soot with a scanning mobility particle sizer and an electrical low-pressure impactor: performance assessment with a model for fractal-like agglomerates. *Journal of Aerosol Science*, 35(5):633–655.

Vogt, R., Crutzen, P. J., and Sander, R. (1996). A mechanism for halogen release from sea-salt aerosol in the remote marine boundary layer.

Volz, F. (1959). Photometer mit selen-photoelement zurspektralen messung der sonnenstrahlung und zer bestimmung der wallenlangenabhangigkeit der dunsttrubung. *Arch. Meteor. Geophys Bioklim.*

White, R. (1989). *Chromatography/Fourier transform infrared spectroscopy and its applications*, volume 10. CRC Press.

WHO (2009). *Global health risks: mortality and burden of disease attributable to selected major risks*. World Health Organization.

Wild, M., Folini, D., Schär, C., Loeb, N., Dutton, E. G., and König-Langlo, G. (2013). The global energy balance from a surface perspective. *Climate dynamics*, 40(11-12):3107–3134.

Wilson, E. L., Georgieva, E. M., and Heaps, W. S. (2007). Development of a fabry–perot interferometer for ultra-precise measurements of column co2. *Measurement Science and Technology*, 18(5):1495.

Winker, D. M., Vaughan, M. A., Omar, A., Hu, Y., Powell, K. A., Liu, Z., Hunt, W. H., and Young, S. A. (2009). Overview of the calipso mission and caliop data processing algorithms. *Journal of Atmospheric & Oceanic Technology*, 26(11).

Wiscombe, W. J. (1980). Improved mie scattering algorithms. *Applied optics*, 19(9):1505–1509.

Xu, B., Cao, J., Hansen, J., Yao, T., Joswia, D. R., Wang, N., Wu, G., Wang, M., Zhao, H., Yang, W., et al. (2009). Black soot and the survival of tibetan glaciers. *Proceedings of the National Academy of Sciences*, 106(52):22114–22118.

Yamamoto, G. and Wark, D. (1961a). Discussion of the letter by ra hanel,determination of cloud altitude from a satellite. *Journal of Geophysical Research*, 66(10):3596–3596.

Yamamoto, G. and Wark, D. (1961b). Discussion of the letter by ra hanel,determination of cloud altitude from a satellite. *Journal of Geophysical Research*, 66(10):3596–3596.

Yee, J.-H., Morgan, M. F., DeMajistre, R., Talaat, E. R., Garten, J. F., Swartz, W. H., and Skinner, W. R. (2004). Geostationary imaging fabry-perot spectrometer (gifs). In *Fourth International Asia-Pacific Environmental Remote Sensing Symposium 2004: Remote Sensing of the Atmosphere, Ocean, Environment, and Space*, pages 14–22. International Society for Optics and Photonics.

Young, A. T. (1981). Rayleigh scattering. *Applied Optics*, 20(4):533–535.